

**Modelling and Design of Advanced
High Speed Vertical Cavity
Semiconductor Lasers**

Naser Albugami

PhD

University of York

Electronic Engineering

October 2017

Dedicated to my family:
mother, father and siblings

ABSTRACT

Vertical-cavity surface-emitting laser (VCSEL) constructions capable of direct modulation at bit rates in excess of 40 GBit/s have attracted considerable attention for future high speed long- and medium-haul networks. The two main approaches to realising this goal are, firstly, the improvement in the direct current modulation laser performance, with 40 GBit/s direct modulation having been demonstrated recently, and, secondly, using advanced modulation schemes. These, in turn, fall into two major categories: firstly, modulation of the photon lifetime in the cavity as an alternative to current modulation, and, secondly, current modulation enhanced by photon-photon resonance in a specialised laser structure (e.g. using an external cavity [1], or a laser array [2]). Theoretical models describing both of these solutions have been developed, but appear to have certain limitations which will be discussed later in the thesis, and no systematic analysis and comparison of modulation properties of advanced modulation scheme had been performed, to the best of my knowledge. This was the purpose of my PhD project.

In order to understand the performance of the photon lifetime modulation for Compound Vertical Cavity Surface Emitting Semiconductor Lasers more accurately, a model involving careful analysis of both amplitude and frequency (phase) of laser emission, as well as the spectrally selective nature of the laser cavity, is required. We have developed such a model and used it to describe the laser operation and predict the performance beyond current experimental conditions in both large and small signal modulation regimes for the first time according to our knowledge.

Finally, we studied the alternative method of ultrafast modulation of VCSELs, consisting of current modulation enhanced by photon-photon resonance. The analysis concentrates on the version of the method involving an in-plane integrated extended cavity. A new model is developed to overcome the limitations of existing models and to allow better understanding of the dynamic of the in-plane laser cavity.

LIST OF CONTENTS

ABSTRACT.....	3
LIST OF CONTENTS	4
LIST OF TABLES.....	8
LIST OF FIGURES.....	9
ACKNOWLEDGEMENTS.....	20
DECLARATION	21
1. INTRODUCTION.....	22
2. LITERATURE REVIEW	25
2.1 Optimisation of VCSELs structure for high bit rate modulation: (current modulation) ...	25
2.1.1 Oxide-confined 850 nm VCSELs	25
2.1.2 The influence of the aperture size and photon lifetime	26
2.1.3 Shallow surface etching	27
2.1.4 Single-Mode High-Speed 1.5- μm VCSELs.....	30
2.2 Dual active cavity lasers: (current modulation)	32
2.2.1 Modulation with two active cavities.....	32
2.2.2 Modulation of two cavities out of phase simultaneously.....	33
2.3 Electroabsorption modulators: (photon lifetime modulation).....	35
2.3.1 Forward bias and reverse bias	35
2.3.2 Duocavity VCSEL for resonance-free modulation	37
2.3.3 Reliability performance.....	43
2.4 Electrooptic modulators: (photon lifetime modulation)	44

2.4.1	Modulation of reflectance of multistack mirrors forming the VCSEL cavity: general idea and theoretical analysis in literature	45
2.4.2	A resonant cavity design and non-absorbing modulator subsection	48
2.4.3	VCSEL with electrooptically modulated vertical resonator and a stopband edge tunable DBR	53
2.4.4	Rate equation analysis of a VCSEL with electrooptically modulated mirror: simulated eye diagrams	55
2.4.5	Experimental results on electrooptically modulated VCSELs in the literature.....	58
2.4.6	Small-signal modulation of EO modulated VCSELs	59
2.4.7	Using QD stack instead of quantum wells in the top cavity	61
2.4.8	Elimination of parasitics-related limitations in electrooptic modulation. Traveling wave electrode design	62
2.5	In-plane external cavity and optically injected current-modulated laser.....	66
2.5.1	General considerations and theoretical work so far.....	66
2.5.2	Experimental results	78
2.5.3	VCSELs with external optical injection.....	81
3.	THEORETICAL ANALYSIS OF COMPOUND CAVITY ELECTROOPTICALLY MODULATED LASERS. GENERAL CONSIDERATIONS AND STANDARD RATE EQUATION MODELLING	85
3.1	General considerations.....	85
3.2	The model	86
3.3	The formulation of the model.....	90
3.4	Small Signal Analysis	96
3.5	Large Signal Analysis	99
3.6	Chapter summary.....	107

4.	THE MODIFIED RATE EQUATION MODEL.....	109
4.1	Introduction	109
4.2	Checking the modified rate equations model	113
4.3	Small signal analysis	116
4.4	Large signal analysis	122
4.5	Chapter summary.....	138
5.	IN-PLANE EXTERNAL CAVITY LASER	141
5.1	Introduction	141
5.2	Preliminary analysis using the Lang-Kobayashi model	141
5.3	Electromagnetic Model.....	146
5.4	Small Signal Analysis	165
5.5	Large Signal Analysis	172
5.6	Chapter summary.....	177
6.	CONCLUSIONS AND MAIN RESULTS.....	179
7.	APPENDIX.....	181
7.1	SIOE15 abstract.....	181
7.2	SIOE15 poster.....	182
7.3	The departmental poster	183
7.4	YDS16 abstract	184
7.5	YDS16 poster	185
7.6	PIERS 2017 abstract	186
7.7	VCSEL day poster.....	187
7.8	2017 paper (page 1 Of 19).....	188

7.9	EMSS paper (page 1 Of 7).....	189
	REFERENCES.....	190

LIST OF TABLES

Table 1: Compound VCSEL parameters.....	95
Table 2: VCSEL cavity parameters	163
Table 3: Laser amplifier cavity parameters	164

LIST OF FIGURES

Figure 1: Back-to-back configuration BTB optical eye diagrams for 9 mm diameter oxide-confined InGaAlAs VCSEL at 25 and 40 Gbits/s modulation at fixed bias current [3]	26
Figure 2: Measured 3dB modulation bandwidth and K-factor as function of the oxide aperture size for 850 nm InGaAlAs VCSELs with low (a) and high (b) mirror losses at 20°C [13].....	27
Figure 3: Small signal modulation response for high photon lifetime VCSEL at different bias currents [5]	28
Figure 4: Small signal modulation response (S21) for low photon lifetime VCSEL at different bias currents [5]	28
Figure 5: Calculated top DBR loss rate as a function of etch depth into the top DBR [6]	30
Figure 6: Calculated photon lifetime as a function of etch depth [6]	30
Figure 7: Schematic image of a VCSEL with two dielectric DBRs [26].....	31
Figure 8: Device structure for the CRVCL showing electrical biasing [29].....	32
Figure 9: Comparison of CRVCL and conventional VCSEL response [29].....	33
Figure 10: Operation principle of the push-pull modulation in a composite-resonator vertical-cavity laser [4]	34
Figure 11: Comparison between current modulation and push-pull modulation simultaneously [4].....	35
Figure 12: Schematic of a coupled resonator vertical-cavity laser (CRVCL) [34].....	35
Figure 13: Light output from the CRVCL for various forward bias passive [34].....	36
Figure 14: The change the optical path length when the current is applied into the passive cavity [34]	37
Figure 15: Light output from the CRVCL under reverse bias operation [34]	37
Figure 16: Schematic diagram of the device layout, showing two device sections [37].....	38
Figure 17: Modulation response for a direct current modulated, intracavity loss modulated, and dual cavity devices. 20 db/decade roll-off above 5 GHz is due to RC parasitic metallization [37]	39

Figure 18: Device high frequency modulation response at room temperature [37].....	40
Figure 19: A 10 Gbit/s eye diagram of dual cavity device showing an open eye [37]	40
Figure 20: Calculated reflection and transmission spectra of a Fabry-Perot cavity with variable intracavity absorption [37].....	41
Figure 21: Modulation response of a dual-cavity devices at different modulator voltages. Change of modulator voltage causes shift of optical cavity position, thus detuning from ideal situation (red curve). Detuning may result in optical feedback-related modulation being in-phase (purple) or 180° shifted (blue) with decoupled mode modulation [37]	42
Figure 22: Change in output power of 6 μm diameter oxide-confined InGaAlAs 850 nm VCSELs measured at 20 °C as a function of ageing time at 95 °C in [39]	44
Figure 23: Modulation different types [7]	47
Figure 24: Basic EOM/VCSEL structure [reference]. The sizes of most figures can be reduced a bit [12].....	48
Figure 25: The coupling diagram between VCSEL cavity and electro-optic modulator [12]....	49
Figure 26: Optical power vs VCSEL current; solid lines: Optical output power characteristics of the EOM VCSEL are shown for different voltages applied to the EOM section. Dashed lines: Corresponding photocurrent due to absorption within the EOM section [11].....	49
Figure 27: Static performance of an EOM/VCSEL at different reverse biases applied to the modulator section (large detuning between the cavities) [12]	51
Figure 28: Spectra of a single-mode EOM/VCSEL device at different reverse biases applied to the modulator section (large detuning between the cavities) [12].....	52
Figure 29: Optical modulation performance of the EOM/VCSEL [12]	52
Figure 30: Electrooptically modulated VCSEL based on resonantly coupled cavities. (a) Optical reflection spectrum of the modulator cavity; open circle corresponds to the lasing wavelength. (b). Upon an applied bias, the modulator reflectivity dip matches the lasing wavelength, increasing the light output power. Dashed line, cavity out of resonance; solid line, cavity in resonance. (c) Profiles of the refractive index and electric field strength in the VCSEL	

optical mode. (d). Top part of the device: profiles of the refractive index and electric field strength in the VCSEL mode in the open state (solid line) and closed state (dashed line) [47]	53
.....	53
Figure 31 : Electrooptically-modulated VCSEL based on stopband edge-tunable DBR. (a) Reflectivity spectrum of a EOM DBR near the stopband edge. Filled circle refers to the lasing wavelength. (b) Shift of the EOM DBR stopband edge reflectivity spectrum upon applied bias. Reflectivity spectrum at zero bias, solid line; reflectivity spectrum at applied bias, dashed line. A transparent DBR with a low reflectivity (filled circle) becomes non-transparent with a high reflectivity (open circle). (c) Profiles of the refractive index and electric field strength in the VCSEL optical mode. (d). Top part of the device: profiles of the refractive index and electric field strength in the VCSEL mode in the open state (solid line) and closed state (dashed line) [14]	54
.....	54
Figure 32: Modeled response of a VCSEL output power to a reflectivity modulation of the top at different values of top mirror reflectivity in the open state. Response to a bit pattern signal is presented in a form of eye diagram [14]	56
.....	56
Figure 33: Modeled response of a VCSEL output power to a reflectivity modulation of the top at different values of injection current density. Response to a bit pattern signal is presented in a form of eye diagram[14]	57
.....	57
Figure 34: A schematic structure of an EOM VCSEL with a saturable absorber [10]	58
.....	58
Figure 35: Lasing spectrum of the EOM VCSEL at $I_{1/2}$ mA and two different voltages [10]	59
.....	59
Figure 36: Performance of the RZ transmission of a signal modulated by the electro-optically modulated vertical-cavity surface-emitting laser. (a)Electric eye diagram. (b) Optical eye diagram [10].	59
.....	59
Figure 37: Intrinsic bandwidth of the EOM VCSEL at RT. Electrical parasitics are deconvoluted from the measured data yielding an intrinsic bandwidth of 56 ± 5 GHz [11]	60
.....	60
Figure 38: Threshold gains as a function of the modulation electric field E_{tCav} applied to the top-cavity with quantum wells [9]	61
.....	61

Figure 39: Threshold gains as a function of the modulation electric field E_{tCav} applied to the top-cavity with quantum dots [9]	61
Figure 40: Scheme of a bottom emitting electrooptically modulated coupled-cavity VCSEL (EOM CC-VCSEL) (a) and 3D schematic view of three-section traveling wave electrode EOM CC-VCSEL (b). The top (bottom) cavity is independently driven by voltage (current) source [53]	62
Figure 41: 3D scheme (a) and electrical equivalent circuit (b) of the active (modulating) section of the modulator cavity of the TW EOM CC-VCSEL [53]	63
Figure 42: Schemes of the two types of TW EOM structures (top) and simplified equivalent circuit of the whole segmented TW-EO modulator (bottom) [53].....	64
Figure 43: (left) Cut-off frequency $f_{cut-off}$ and maximum reflection $\max(\Gamma_S)$ as a function of load resistance Z_L for type A and type B TW electrode structures and for 3 different values of the ground slot width $W_g = 12, 18$ and 26 ; (right) Reflection Γ_S as a function of modulation frequency for type A and type B structures and for the 3 values of W_g [53]	65
Figure 44: Schematic structure of the transverse coupled cavity VCSEL [57]	67
Figure 45: IM response of conventional VCSEL (blue line) and coupled cavity VCSEL at the same coupling strength, feedback phase and different delay time [57]	69
Figure 46: IM response of conventional VCSEL (blue line) and coupled cavity VCSEL at the same delay time, feedback phase and different coupling strength [57]	70
Figure 47: Phase tolerance of the modulation bandwidth enhancement [57].....	70
Figure 48: Calculated normalized effective differential net gain a function of modulation frequency [57]	71
Figure 49: Simulation results of frequency chirp as a function of modulation frequency under different coupling strength [57].....	73
Figure 50: Phase tolerance of chirp reduction as a function of modulation frequency with a coupling strength of $1.6 \times 10^{11} \text{ s}^{-1}$ [57].....	74
Figure 51: Scheme of (a) slow-light feedback in TCC-VCSEL, and (b) structure of a fabricated [67]	75

Figure 52: IM responses when LC= 20 μm under different values of η : (a) with CPR, and (b) with PPR. The IM response of the solitary VCSEL ($\eta = 0$) is also plotted for comparison [67].	77
Figure 53: Schematic view of the 850-nm-band transverse cavity surface emitting laser [77]	79
Figure 54: Top view of one fabricated device, with a mesa footprint of only $14 \times 24 \mu\text{m}^2$ [77]	79
Figure 55: Small-signal frequency responses of the device for different cases. Feedback is enhanced by injecting a 0.3 mA current to the feedback cavity [77]	80
Figure 56: Measured large-signal response with data rate of 30 to 40 Gbps (NRZ, PRBS $2^{31} - 1$, $V_{pp} = 500$ mV). VCSEL current is 6.2mA with a passive feedback cavity. The isolation width is 3 μm . Extinction ratios are ~ 3.8 dB for all data rates [77]	81
Figure 57: The experimental configuration of the proposed 64 Gb/s PAM4 VCSEL-based FSO links with an external light injection scheme [100]	83
Figure 58: The frequency responses of the PAM4 VCSEL-based FSO links for the scenarios of free-running and injection-locked [100]	84
Figure 59: Schematic of a Compound Cavity Laser	86
Figure 60: Calculated Reflectivity versus incident light wavelength for the EO modulator cavity	87
Figure 61: The notch in Figure 60 : With absorption (solid green) without absorption (blue dash)	88
Figure 62: a simulated small-signal modulation curve for a normal VCSEL, photon lifetime is 2 ps	89
Figure 63: a simulated small-signal modulation curve for a compound VCSEL, photon lifetime is 25 ps	89
Figure 64: Calculated Reflectivity versus incident light wavelength for the EO modulator cavity	92
Figure 65: Spectral shape of the reflectance notch with $n_m=3.620$ (solid curve) and $n_m=3.621$ (dashed curve) calculated using full transfer matrix analysis	92

Figure 66: Calculated Reflectivity of the passive modulator cavity at the wavelength $\lambda \approx 0.9666 \mu\text{m}$ and at $\lambda \approx 0.9670 \mu\text{m}$ (dashed curve) vs. average refractive index of the cavity.....	93
Figure 67: Calculated Reflectivity of the passive modulator cavity for 35 periods in the intermediate reflector and different periods in the top reflector	93
Figure 68: The logic diagram blocks for the original rate equation model	97
Figure 69: Calculated small-signal response of electrooptic laser modulation at three different values of bias current.....	98
Figure 70: Calculated 3dB cut-off frequency vs bias current for small-signal response of electrooptic laser modulation	99
Figure 71: Eye diagram for 1.5mA VCSEL, 40GBit/s bit rate.....	101
Figure 72: Eye diagram for 5mA VCSEL, 40GBit/s bit rate	101
Figure 73: Eye diagram for 30mA VCSEL, 40GBit/s bit rate.....	102
Figure 74: Q-Factor for 20 GBit/s Bit Rates ($R=0.9422-0.9414=0.0008$). At Current=4.5mA, the Frequency =5GHz. At Current=15.7mA, the Frequency =10GHz	103
Figure 75: Q-Factor for 40 GBit/s Bit Rates ($R=0.9422-0.9414=0.0008$). At Current=4.5mA, the Frequency =5GHz. At Current=15.7mA, the Frequency =10GHz	103
Figure 76: Q-Factor for 80 GBit/s Bit Rate ($R=0.9422-0.9414=0.0008$). At Current=4.5mA, the Frequency =5GHz. At Current=15.7mA, the Frequency =10GHz. At Current=34.4mA, the Frequency =15GHz.....	104
Figure 77: Resonant frequency versus current for small signal.....	105
Figure 78: Q-Factor for 20 GBit/s Bit Rates ($0.949-0.941= 0.0080$).....	105
Figure 79: Q-Factor for 40 GBit/s Bit Rates ($0.949-0.941= 0.0080$).....	106
Figure 80: Q-Factor for 80 GBit/s Bit Rates ($0.949-0.941= 0.0080$).....	106
Figure 81: The initial $\Delta\omega$ [red] and the final $\Delta\omega$ [blue]	114
Figure 82: The photon density and imaginary frequency correction vs normalized time.....	115
Figure 83: Transmittance ($1-R_m$) vs frequency correction in [Hz], the Lorentzian (blue), and the exact (red)	116
Figure 84: The logic diagram blocks for the modified rate equation model	119

Figure 85: Calculated small-signal response of electrooptic laser modulation at three different values of bias current (for 35 periods in the intermediate reflector and 17 periods in the top reflector)	120
Figure 86: Calculated small-signal response of electrooptic laser modulation for different top DBR periods and 35 periods in the intermediate DBR; current 10 mA	120
Figure 87: Modulation of Refractive Index, 40 Gbit/s bit rate.....	122
Figure 88: Real and Imaginary Frequency	123
Figure 89: Amplitude Spectrum of output Field at 40 GBit/s.....	124
Figure 90: Standard rate equation model	125
Figure 91: Modified rate equation model.....	125
Figure 92: Quality factor when changing number of periods for the top reflector.....	126
Figure 93: Quality factor when changing number of periods for the intermediate reflector ..	127
Figure 94: Eye diagram for 32 periods in the intermediate reflector and 19 periods in the top reflector, I= 10 mA, 40Gbit/s	127
Figure 95: Eye diagram for 31 periods in the intermediate reflector and 19 periods in the top reflector, I= 10 mA, 40Gbit/s	127
Figure 96: Quality factor when changing number of periods for the top reflector for 8 mA bias current.....	128
Figure 97: Eye diagram for 35 periods in the intermediate reflector and 17 periods in the top reflector, I= 8 mA, 40Gbit/s.....	129
Figure 98: Eye diagram for 35 periods in the intermediate reflector and 23 periods in the top reflector, I= 8 mA, 40Gbit/s.....	129
Figure 99: Quality factor when changing number of periods for the top reflector for 10 mA bias current.....	130
Figure 100: Eye diagram for 35 periods in the intermediate reflector and 17 periods in the top reflector, I= 10 mA, 40Gbit/s.....	130
Figure 101: Eye diagram for 35 periods in the intermediate reflector and 23 periods in the top reflector, I= 10 mA, 40Gbit/s.....	130

Figure 102: Quality factor when changing number of periods for the top reflector for 12 mA bias current.....	131
Figure 103: Eye diagram for 35 periods in the intermediate reflector and 17 periods in the top reflector, I= 12 mA, 40GBit/s.....	131
Figure 104: Eye diagram for 35 periods in the intermediate reflector and 23 periods in the top reflector, I= 12 mA, 40GBit/s.....	131
Figure 105: Quality factor when changing number of periods in the top reflector and for 31 periods in the intermediate reflector and 7 mA bias current.....	132
Figure 106: Quality factor when changing number of periods in the top reflector and for 31 periods in the intermediate reflector and 10 mA bias current.....	132
Figure 107: Quality factor when changing number of periods in the top reflector and for 31 periods in the intermediate reflector and 12 mA bias current.....	133
Figure 108: Quality factor when changing number of periods in the top reflector and for 29 periods in the intermediate reflector and 8 mA bias current.....	134
Figure 109: Quality factor when changing number of periods in the top reflector and for 29 periods in the intermediate reflector and 10 mA bias current.....	134
Figure 110: Quality factor when changing number of periods in the top reflector and for 29 periods in the intermediate reflector and 12 mA bias current.....	135
Figure 111: Quality factor when changing the bias current for 40 GBit/s modulation frequency	136
Figure 112: Eye diagram for 35 periods in the intermediate reflector and 19 periods in the top reflector, I= 8 mA, 40 GBit/s	136
Figure 113: Eye diagram for 35 periods in the intermediate reflector and 19 periods in the top reflector, I= 2 mA, 40 GBit/s	136
Figure 114: Quality factor when changing the bias current for 80 GBit/s modulation frequency	137
Figure 115: Eye diagram for 35 periods in the intermediate reflector and 19 periods in the top reflector, I= 10 mA, 80 GBit/s.....	138

Figure 116: Eye diagram for 35 periods in the intermediate reflector and 19 periods in the top reflector, $I = 2$ mA, 80 GBit/s	138
Figure 117: Estimate for 3dB modulation bandwidth using the impulse response method in the Lang-Kobayashi type model for $\tau_s = 18$ ps	142
Figure 118: Stable in-plane external cavity laser $r_s = 0.6$, bias current = 1.5 mA	144
Figure 119: Unstable in-plane external cavity laser $r_s = 0.99$, bias current = 1.5 mA	144
Figure 120: Estimate for 3dB modulation bandwidth using the impulse response method in the Lang-Kobayashi type model or $\tau_s = 8$ ps	145
Figure 121: Estimate for non-flatness of damping level using the impulse response method in the Lang-Kobayashi type model for $\tau_s = 8$ ps	146
Figure 122: Schematic of the electromagnetic 2D model for a compound in-plane cavity.....	150
Figure 123: 3dB cutoff frequency vs unsaturated amplifier gain for the full model and $\tau_s = 8$ ps	155
Figure 124: The intensity dynamic unusable system when the reflectance $r_s = 0.6$, $h_u = 1.3$ for the full model and $\tau_s = 8$ ps.....	156
Figure 125: The intensity dynamic unusable system when the reflectance $r_s = 0.6$, $h_u = 1.4$, modulation index = 78% for the full model and $\tau_s = 8$ ps	157
Figure 126: The intensity dynamic unusable system when the reflectance $r_s = 0.6$, $h_u = 1.5$, modulation index = 90% for the full model and $\tau_s = 8$ ps	157
Figure 127: The intensity dynamic unusable system when the reflectance $r_s = 0.6$, $h_u = 1.6$, modulation index = 95% for the full model and $\tau_s = 8$ ps	158
Figure 128: The intensity dynamic unusable system when the reflectance $r_s = 0.6$, $h_u = 1.7$, modulation index = 97% for the full model and $\tau_s = 8$ ps	158
Figure 129: The intensity dynamic unusable system when the reflectance $r_s = 0.6$, $h_u = 1.8$, modulation index = 99% for the full model and $\tau_s = 8$ ps	159
Figure 130: The intensity dynamic unusable system when the reflectance $r_s = 0.6$, $h_u = 1.9$ for the full model and $\tau_s = 8$ ps	159

Figure 131: The intensity dynamic unusable system when the reflectance $r_s = 0.6$, $h_u = 2.0$ for the full model and $\tau_s = 8\text{ps}$	160
Figure 132: Small signal analysis for solitary laser , $ r_s =0$	166
Figure 133: Small signal analysis for In plane cavity laser $ r_s =0.6$	166
Figure 134: Estimate for 3dB modulation bandwidth using the impulse response method in the full model for $\tau_s=8\text{ ps}$	167
Figure 135: Estimate for non-flatness of damping level using the impulse response method in the full model for $\tau_s = 8\text{ ps}$	167
Figure 136: Small signal analysis for In plane cavity laser using the impulse response method in the full model for $\tau_s = 8\text{ ps}$ and $ r_s =0.75$	168
Figure 137: The intensity dynamic unusable system when the reflectance $r_s = 0.8$, $h_u = 0$ for the full model and $\tau_s = 8\text{ps}$	169
Figure 138: The intensity dynamic unusable system when the reflectance $r_s = 0.85$, $h_u = 0$, modulation index = 70% for the full model and $\tau_s = 8\text{ps}$	170
Figure 139: The intensity dynamic unusable system when the reflectance $r_s = 0.9$, $h_u = 0$, modulation index = 93% for the full model and $\tau_s = 8\text{ps}$	170
Figure 140: The intensity dynamic unusable system when the reflectance $r_s = 0.95$, $h_u = 0$, modulation index = 99% for the full model and $\tau_s = 8\text{ps}$	171
Figure 141: The intensity dynamic unusable system when the reflectance $r_s = 1.00$, $h_u = 0$ for the full model and $\tau_s = 8\text{ps}$	171
Figure 142: Large signal analysis for solitary laser , $ r_s =0$ (40 GBit/s)	172
Figure 143: Large signal analysis for In plane cavity laser, $ r_s =0.6$ (40 GBit/s)	172
Figure 144: Large signal analysis for solitary laser , $ r_s =0$ (80 GBit/s).....	173
Figure 145: Large signal analysis for In plane cavity laser $ r_s =0.6$ (80 GBit/s)	173
Figure 146: Eye diagram for the full model for $\tau_s = 8\text{ ps}$, $ r_s = 0$ (40 GBit/s) , quality factor = 1.69	174
Figure 147: Eye diagram for the full model for $\tau_s = 8\text{ ps}$, $ r_s =0.3$ (40 GBit/s) , quality factor = 1.70	174

Figure 148: Eye diagram for the full model for $\tau_s = 8$ ps, $ r_s = 0.6$ (40 GBit/s) , quality factor = 2.45	175
Figure 149: Eye diagram for the full model for $\tau_s = 8$ ps, $ r_s = 0.7$, (40 GBit/s) , quality factor = 2.39	175
Figure 150: Eye diagram for the full model for $\tau_s = 8$ ps, $ r_s = 0.8$, (40 GBit/s) , quality factor = 2.02	175
Figure 151: Estimate for 3dB modulation bandwidth using the impulse response method in the full model for $\tau_s=18$ ps	176
Figure 152: Estimate for non-flatness of damping level using the impulse response method in the full model for $\tau_s=18$ ps	177

ACKNOWLEDGEMENTS

The man who must be thanked for this work is my supervisor, Dr. Eugene Avrutin. Because of his invaluable support, patience, encouragement, enthusiasm, and immense knowledge, I was able to do this hard work. I could not have imagined having a better supervisor for my PhD. In my opinion, he is the best option for any student looking for an academic supervisor!

I would like also to extend my sincere thankfulness to my thesis supervisor, Dr. Stuart Porter for his great support and helpful comments and suggestions during my PhD. I should not forget the graduate administrator, Camilla Danese for her support. I would also like to thank my friend, Muhsen Alshaharani for his help.

DECLARATION

I declare that the work presented in this thesis is based purely on my own research, unless otherwise stated, and has not been submitted for a degree in either this or any other university. Some of the research presented in this thesis has resulted in the following publications:

- Albugami, N.F. and E.A. Avrutin, *Dynamic modelling of electrooptically modulated vertical compound cavity surface emitting semiconductor lasers*. Optical and Quantum Electronics, 2017. 49(9): p. 307.
- Albugami, N.F. and Avrutin, *Analysis of Fast Electro-optical Modulation of Vertically Integrated Coupled-cavity VCSELS*. in *Proc. Progress In Electromagnetics Research Symposium (PIERS)*. 2017. St Petersburg, Russia.
- Albugami, N.F. and E.A. Avrutin, *Dynamic modelling of electrooptically modulated compound-cavity VCSELS*. in *Proc. The VCSEL Day 2017 conference (VCSEL 2017)*. 2017. Cardiff, UK.
- Albugami, N.F. and E.A. Avrutin, *Modified Rate Equation Models For Understanding Performance Limits Of Vertical And In-Plane Compound Cavity VCSELS*. in *Proc. The European Modeling and Simulation Symposium (EMSS)*. 2017. Barcelona, Spain.
- Albugami, N.F. and E.A. Avrutin, *Electrooptically modulated coupled-cavity VCSELS: the anomalous small-signal response and the large-signal modulation properties*. in *Proc. Semiconductor and Integrated Optoelectronics (SIOE)*. 2015. Cardiff, UK.

1. INTRODUCTION

Vertical-cavity surface-emitting laser (VCSEL) constructions capable of direct modulation at bit rates in excess of 40 GBit/s have attracted considerable attention for future high speed long- and medium-haul networks. There are two main approaches to realising this goal; the first of these is the improvement in the direct modulation laser performance. For example, it was possible to have an error-free transmission up to 39 and 40 Gbit/s direct modulation working in a temperature up to 100 °C using oxide-confined 850 nm VCSELs with InGaAlAs based active regions [3]. Another method of improvement to direct (current) modulation is to modulate two active cavities simultaneously and out of phase [4]. Reducing the photon lifetime by shallow surface etching of the top mirror reflectivity can also improve the direct modulation [5, 6]. The second type of modulation is by using the modulation of the photon lifetime in the cavity as an alternative to current modulation [7-12]. Advanced semiconductor lasers involving direct modulation of the photon lifetime promise better dynamic properties than lasers with traditional current modulation because their operating speed is less limited by the electron-photon resonance. Several laser designs to implement this principle have been proposed, and initial measurements are all promising. For example, Germann and co-authors have experimentally demonstrated a modulation bandwidth of 30 Gbit/s with 100 mV change in voltage and 27 dB change in output amplitude for small signal modulation [11]. Large-signal (Non-return-to-zero) NRZ modulation at 40+ GBit/s has been confidently and repeatedly demonstrated [10]. By using a non-absorbing electro-optic modulator in the first known compound VCSEL [12], the electrical bandwidth up to 60 GHz and optical bandwidth more than 35 GHz, restricted by the photodetector response, have been achieved. Strain-compensated multiple quantum wells were used in the active gain region in the VCSEL cavity with 960 nm reference frequency and 3-4 nm blue shift in the modulator region. A more recent experimental achievement for photon lifetime modulation was conducted by utilizing the influence of the aperture size on the performance of 850 nm InGaAlAs oxide-confined VCSELs [13]. When the aperture size is decreased to an optimum value of 4-6 μm and the

photon lifetime is reduced from 4 to 1 ps, there is a saturation in the maximum 3dB modulation bandwidth at 21 GHz.

These experimental results have been supported and partly stimulated by theoretical studies using simple rate equation models [7, 11, 14]. Small-signal modulation at low frequencies has been analysed [11] and showed signs of a broad, large resonant peak consistent with the formula presented in [7]. However, experiments and large-signal simulations show that the best performance of electrooptically modulated VCSELs is realised at moderately small rather than large bias currents [14], which is completely different to the case of current modulation, and not immediately obvious from the published small-signal analysis of photon lifetime modulation [7]. We believe one reason for this is that the small-signal analysis of [7] considered the modulation of the photon density *inside the laser cavity*, rather than the measurable power outside the laser which is also influenced by the outcoupling loss modulation, particularly as the modulation cavity may have some dynamic properties of its own. Another limitation of the existing theories, whether small-signal [7] or large-signal [14] is that they are based on “traditional” rate equations for the power of the output only without considering the frequency response, whereas it is clear that in a complex resonator system such as a coupled-cavity laser, amplitude and phase/frequency modulation *have* to be intricately interrelated. These limitations are addressed, one by one, in this thesis. I start with explaining the design considered and the general limitations of the models in Chapter 3 which follows our initial work [15] in considering the laser behaviour using a traditional rate equation model and a small signal analytical approach. It is found that the concept of 3 dB cutoff frequency as a measure of modulation speed cannot be applied to electrooptically coupled-cavity VCSELs within this model, as the value of the 3dB cutoff tends to infinity beyond a certain critical current. To overcome this limitation and in general to understand the laser performance more accurately, a more complex model involving careful analysis of both amplitude and frequency/phase of laser emission, as well as the spectrally selective nature of the laser cavity, is presented in chapter 4. The model is based on the analysis for complex eigenvalues (frequency detunings and amplitude variation rates) of the compound

cavity modes and used it to describe the laser operation and predict the performance beyond current experimental conditions, under both small- and large signal modulation conditions. The photon lifetime in the modulator cavity is found to be the ultimate limitation of the modulation speed.

In chapter 2, theoretical background on both current and photon modulation for Vertical-cavity surface-emitting laser (VCSEL) is reviewed. Chapter 3 and chapter 4 describe the standard and modified rate equation models for small and large signal analysis, respectively.

Chapter 5 talks about the alternative method of ultrafast modulation of VCSELs, consisting of current modulation enhanced by photon-photon resonance. The analysis concentrates on the version of the method involving an in-plane integrated extended cavity. In this chapter, the Lang-Kobayashi model [60] (which includes a single delay term and a single modulation peak) and the multiple-pass model by Ahmed and co-authors [67] (includes two peaks) are analysed in depth. A new model is developed to overcome the limitations of these two models and to allow better understanding of the dynamic of the in-plane laser cavity. This new model can also be used to analyse the potential of the laser with a transverse external cavity as an optoelectronic microwave signal generator which can be used, for example, for microwave over fibre generator.

Chapter 6 concludes this study with the summary and comparison of all three models' results. Several future directions are also proposed at the end.

2. LITERATURE REVIEW

As mentioned in the introduction section, the main modulation methods for VCSELs are current modulation and photon modulation. In this chapter, both methods will be discussed in details.

2.1 Optimisation of VCSELs structure for high bit rate modulation: (current modulation)

The conventional way of laser modulation is direct (current) modulation. Though it has some limitations such as limited bandwidth in standard structures (around 10 GHz), it is still used commonly, and recently, structures with bandwidths exceeding 20 GHz have been developed. There are many methods to improve the modulation speed of direct modulation using optimised VCSELs structures; some methods will be discussed here in brief.

2.1.1 Oxide-confined 850 nm VCSELs

The improvement in the direct modulation laser performance, with 40 GBit/s direct modulation has been demonstrated recently by S.A. Blokhin and co-authors [3]. They achieved high performance of oxide-confined 850 nm VCSELs with InGaAlAs based active regions. Though the limitation of the performance is based on experimental setup and not by optical components, it has error-free transmission rates up to 39 Gbit/s and open eye diagrams of 40 Gbit/s frequency modulation. Figure 1 shows Back-to-back configuration (back-to-back) BTB optical eye diagrams for 9 mm diameter oxide-confined InGaAlAs VCSEL at 25 and 40 Gbits/s modulation at fixed bias current; it shows an open eye diagram for such high frequency. The rise time is less than 10ps for different temperatures. However, the applied electrical radio frequency signal can dramatically reduce the quality of the eye diagram for the laser output received signal due to their imperfections.

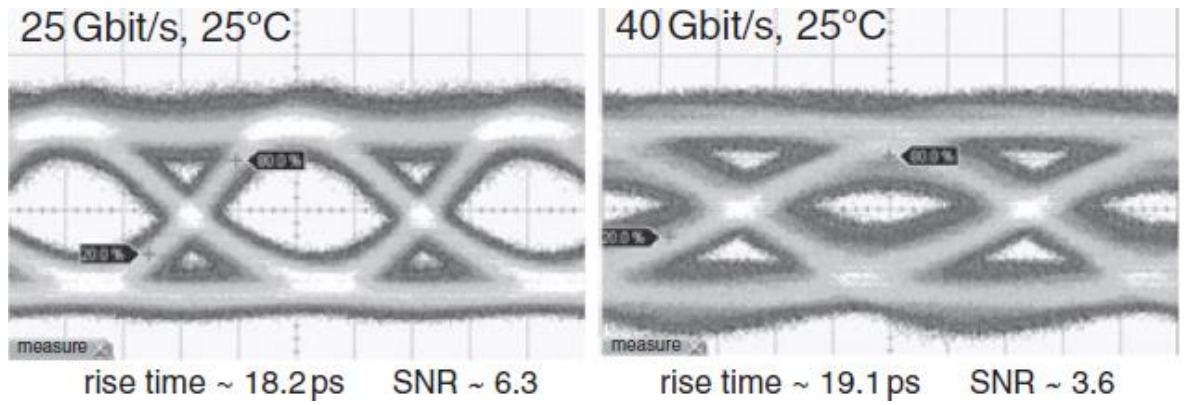


Figure 1: Back-to-back configuration BTB optical eye diagrams for 9 mm diameter oxide-confined InGaAlAs VCSEL at 25 and 40 Gbits/s modulation at fixed bias current [3]

In order to reduce parasitic effect, dielectric/planarizing BCB (bisbenzocyclobutene) material is used in the vertical cavity semiconductor emitting laser (VCSEL) design. Moreover, to easily test the VCSEL without soldering and on wafer itself, a probe is manufactured in a ground-source-ground (GSG) contact pad [16].

2.1.2 The influence of the aperture size and photon lifetime

There are many ways to increase the resonance frequency, such as by increasing the differential gain, decreasing the mode volume (aperture size) and reducing the chip parasitics [17-19]. These means can help in increasing the modulation bandwidth up to 20 GHz [20, 21] and the damping limitation can be controlled by reducing the photon lifetime [22].

A more recent experimental achievement for photon lifetime modulation was conducted by utilizing the influence of the aperture size and photon lifetime on the performance of 850 nm InGaAlAs oxide-confined VCSELs [13]. When the aperture size is decreased to an optimum value of 4-6 μm and the photon lifetime is reduced from 4 to 1 ps, there is a saturation in the maximum 3dB modulation bandwidth at 21 GHz. Figure 2 shows how the modulation bandwidth and the K-factor can be controlled by adjusting the oxide aperture radius for low and high mirror losses.

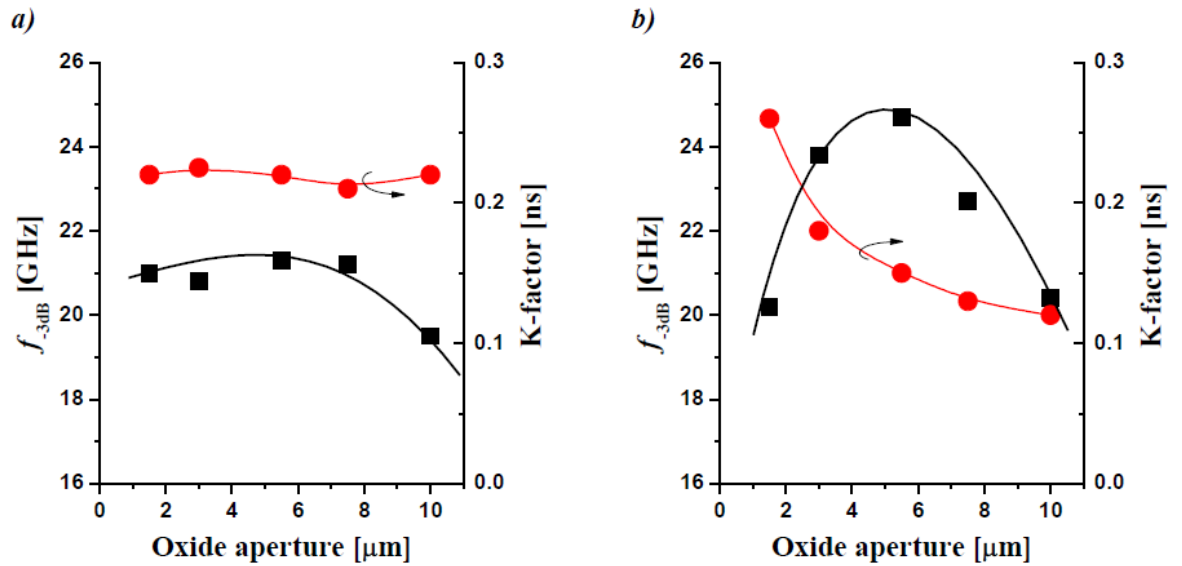


Figure 2: Measured 3dB modulation bandwidth and K-factor as function of the oxide aperture size for 850 nm InGaAlAs VCSELs with low (a) and high (b) mirror losses at 20°C [13]

2.1.3 Shallow surface etching

One of the methods to get current modulating VCSEL lasers is to reduce the photon lifetime by shallow surface etching which is controlled by the top mirror reflectivity [5]. In this method, the modulation speed and laser efficiency can be enhanced and the 3dB bandwidth can be increased up to 23 GHz for 850 nm multimode VCSELs by 50% photon lifetime reduction.

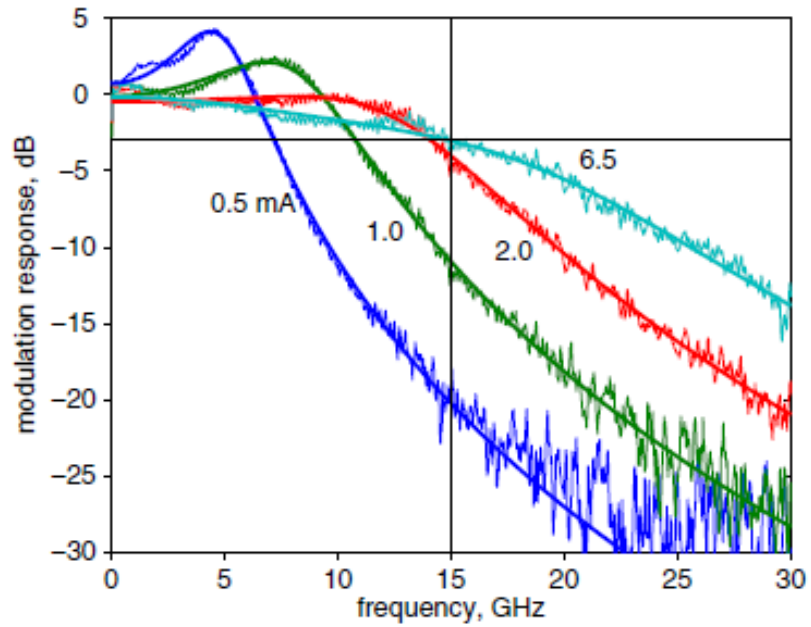


Figure 3: Small signal modulation response for high photon lifetime VCSEL at different bias currents [5]

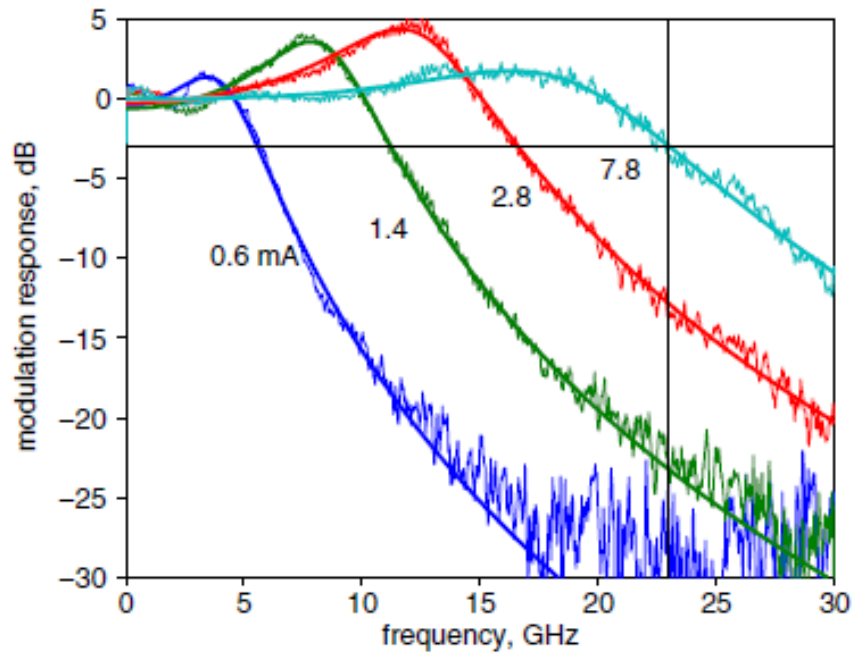


Figure 4: Small signal modulation response (S21) for low photon lifetime VCSEL at different bias currents [5]

Figure 3 and Figure 4 shows how reducing photon lifetime improves the laser performance for example the 3dB cut-off frequency can go up to 23 GHz for 7.8 mA bias current in the case of low photon lifetime. However, the 3dB- cut-off frequency is only 15 GHz for 6.5 mA bias

current in the case of high photon lifetime. This means that there is about 50% enhancement in the bandwidth which can be explained by Equations (1-3) when talking about damping factor and resonance frequency [23].

$$\gamma = Kf_r^2 + \gamma_0 \quad (1)$$

$$K = 4\pi^2\left(\tau_p + \frac{\varepsilon\chi}{v_g \partial g/\partial n}\right) \quad (2)$$

$$\omega_R^2 \approx \frac{v_g \cdot (\partial g/\partial N) \cdot N_p}{\tau_p} \Rightarrow f_{3dB} \approx \sqrt{3}f_r \Rightarrow f_{3dB} \propto \sqrt{P}; f_{3dB} \propto \sqrt{\partial g/\partial N} \quad (3)$$

Where (γ) is damping factor, (f_r) is resonance frequency, γ_0 is the damping factor offset, (ε) is the gain compression factor, (χ) is the transport factor, v_g is group velocity, and ($\partial g/\partial N$) is the differential gain.

The big improvement can be explained by the above equations: when photon lifetime (τ_p) is reduced, K factor will be reduced as well, which will reduce the damping factor according to Equation (1). The 3dB cutoff frequency (f_{3dB}) depends on the current, when the current (I) and the power (p) are high, 3dB bandwidth is high which agreed with Equation (3).

Petter Westbergh and co-authors found that there is an optimum value for the photon lifetime at which a maximum value of 23 GHz modulation bandwidth as well as 40 Gb/s error-free transmission. To find the value of the internal quantum efficiency (η_i) and the internal optical loss rate (α_i), slope efficiency (SE) must be measured as a function of mirror loss [24, 25]. Figure 5 and Figure 6 elaborate this result as they show that 60 nm is the optimum etch depth at which there is a maximum top DBR loss (0.7 ps^{-1}) and minimum photon lifetime (1.2 ps). The different etch depths used in the experiments are indicated in the graphs [6].

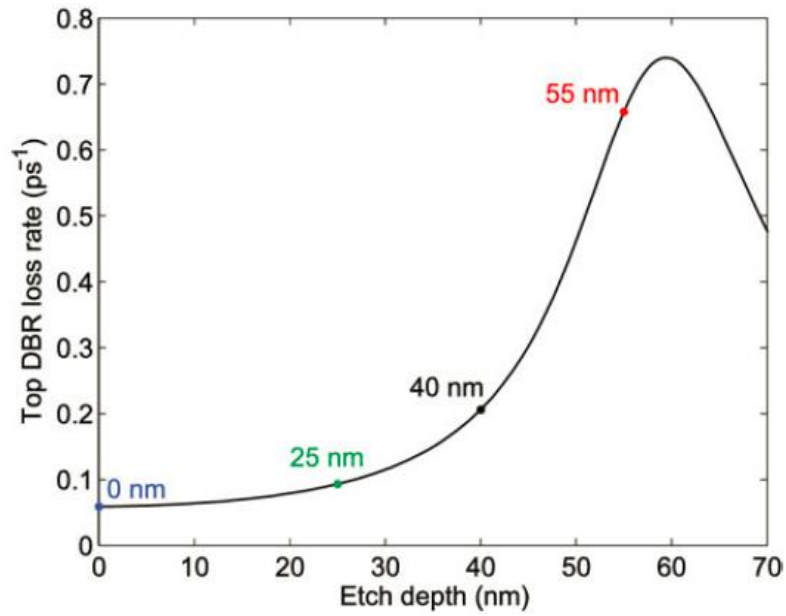


Figure 5: Calculated top DBR loss rate as a function of etch depth into the top DBR [6]

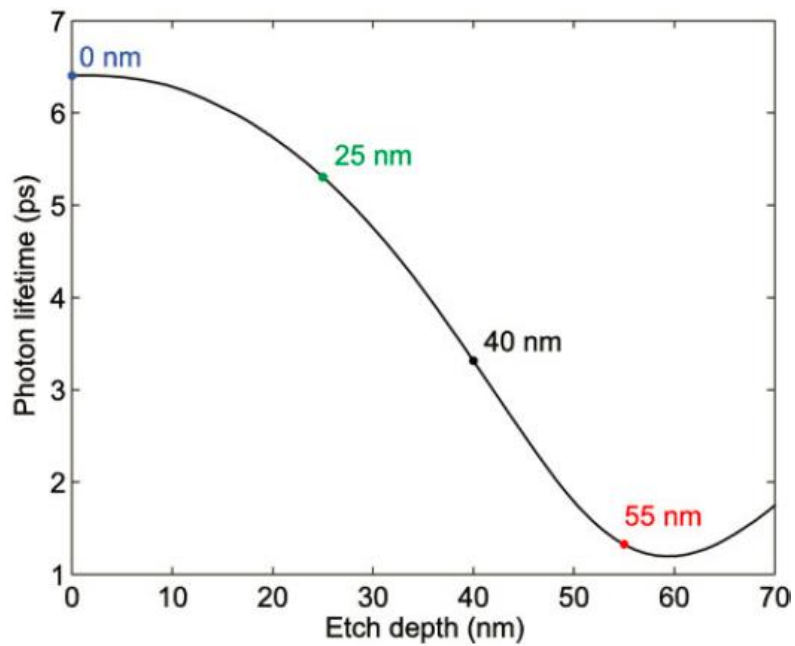


Figure 6: Calculated photon lifetime as a function of etch depth [6]

2.1.4 Single-Mode High-Speed 1.5- μm VCSELs

Silvia Spiga and co-authors have introduced the shortest semiconductor cavity InP-based VCSELs with a length of 1.5λ - single-mode lasers and two dielectric DBRs in 2017 [26]. They were able to reach a speed of 50 Gb/s NRZ modulation for back to back configuration with no

error correction and equalization. Creating an effective short cavity length can reduce the photon lifetime [27], which helps in enhancing the small-signal modulation bandwidth. This can be achieved by reducing the damping and increasing the relaxation resonance frequency for different DC currents. This design has some disadvantages, which are increasing the thermal resistance, having low threshold current density [28] and increasing electrical resistance causing high dissipated power.

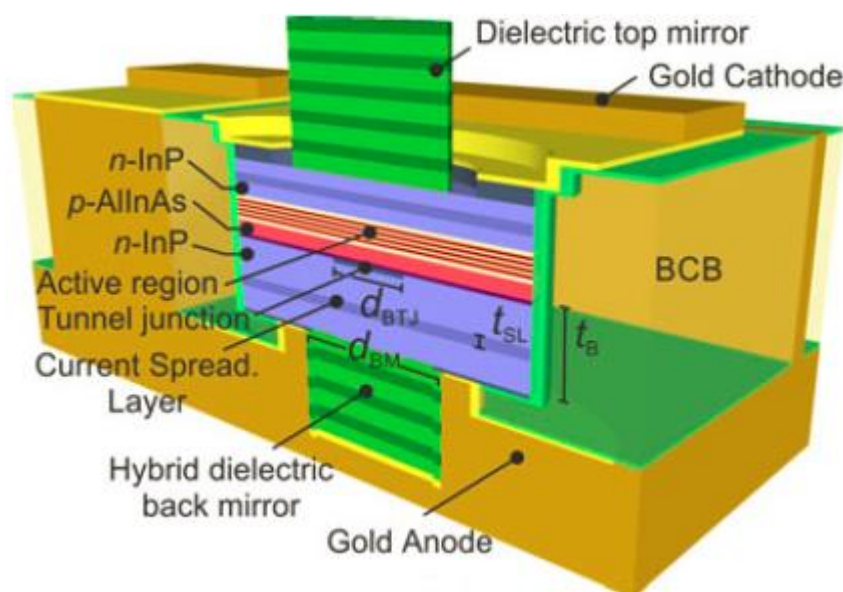


Figure 7: Schematic image of a VCSEL with two dielectric DBRs [26]

Figure 7 shows a schematic image of a VCSEL with two dielectric DBRs. The active cavity consists of seven AlGaInAs quantum wells and it is surrounded by two claddings (InP n-doped InP AlInAs highly p-doped layers). The buried tunnel junction (BTJ) is p⁺- AlGaInAs/n⁺- GaInAs and reverse-bias junction is p⁺n⁻; the earlier is for current confinement and later is for current blocking.

2.2 Dual active cavity lasers: (current modulation)

2.2.1 Modulation with two active cavities

In this design, two cavities of a VCSEL are not electrically connected, but their active regions are optically coupled [29]. It is called a composite resonator vertical cavity laser (CRVCL) and its structure is shown in Figure 8. The main principle of CRVCL is that the current in one cavity is fixed and the gain in the other cavity is changing which causes the photon density to change.

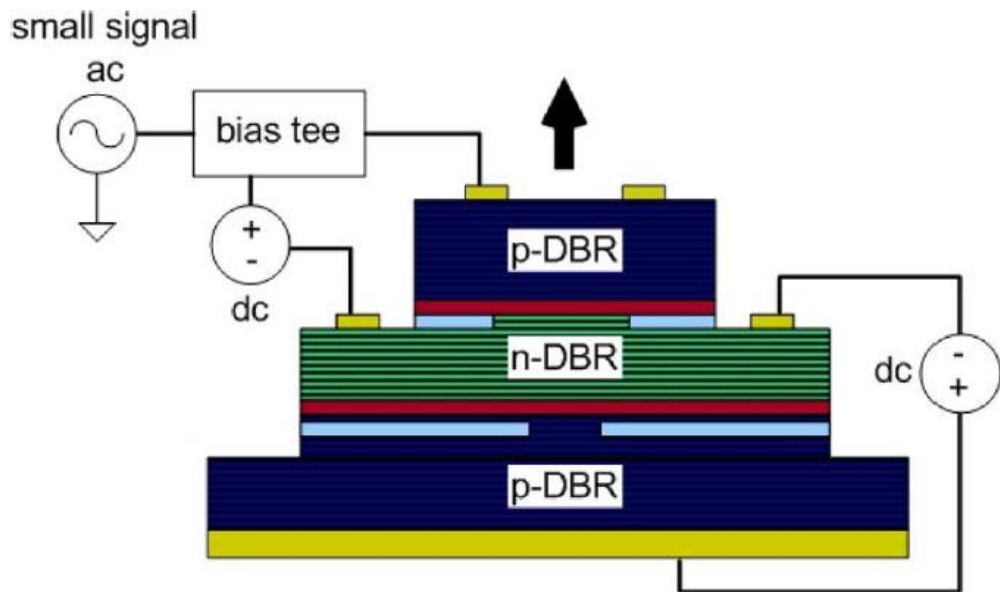


Figure 8: Device structure for the CRVCL showing electrical biasing [29]

It should be also noted that the dynamic used in the standard rate-equation assumes only one optical mode with one electron population when analysing small signal modulation response [30].

To describe the transfer function, two independent carrier densities and one photon density are analysed in the rate equations [31]. To get an optimal response of the transfer function, the differential gains and the photon density of the two active regions can be adjusted separately.

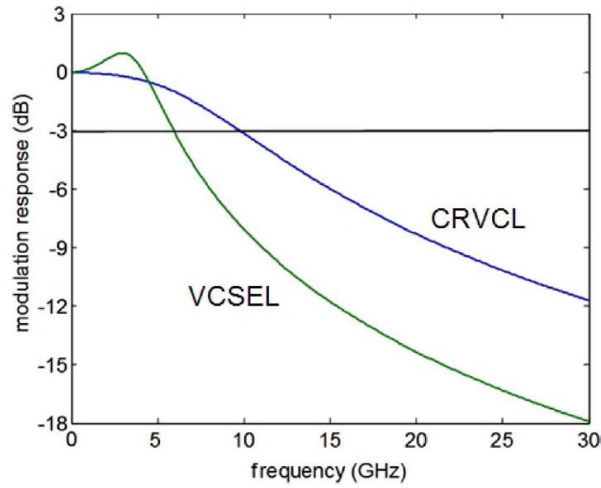


Figure 9: Comparison of CRVCL and conventional VCSEL response [29]

Figure 9 shows a comparison between CRVCL and normal VCSEL. It shows that the composite resonator has a higher bandwidth than the normal VCSEL without changing the density of photons since the relaxation oscillation frequency is strongly affected by the total photon density in the two cavities. Moreover, the 3-dB bandwidth is 12.5 GHz and the modulation current efficiency factor is 5 GHz/mA.

2.2.2 Modulation of two cavities out of phase simultaneously

This design is different from the previous design in section 2.2.1 as the two active cavities in this design are modulated out of phase simultaneously [4]. In this case, light can be produced without varying the total photon density inside the laser. This means that it can produce a high modulation bandwidth independent of the total photon density. In this case, spatially varying the longitudinal optical mode distribution causes light modulation results which means that the bottom resonator is effectively longer than the top resonator, thanks to the free carrier plasma effect [32, 33]. The free carrier plasma effect happens when a photon is absorbed by a free carrier which is already have absorbed a photon and is excited. As a result, equal amount of currents but out-of-phase are injected into both cavities as shown in the schematic of this laser in Figure 10.

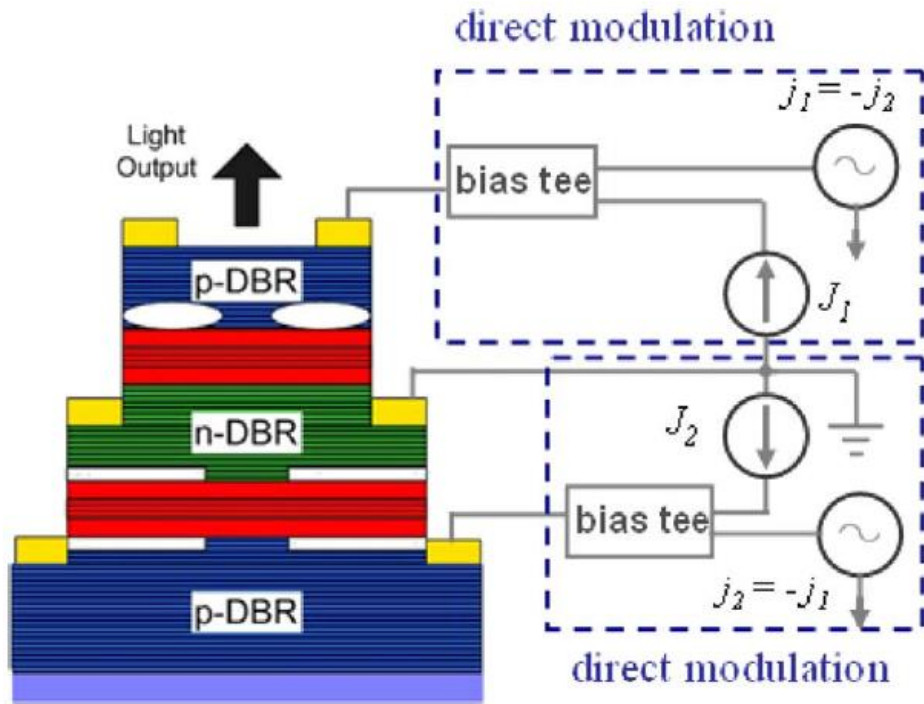


Figure 10: Operation principle of the push-pull modulation in a composite-resonator vertical-cavity laser

[4]

This compound laser is called 'push-pull' modulation which has a high-speed operation, low power consumption and 2.5 Gb/s modulation. Figure 11 shows the case when only current modulation is applied to the compound laser and when push-pull modulation is applied. It shows that the electrical bandwidth is 20 GHz for the modulation response for the top and bottom cavities; this is because of the device parasitics. They cause a dominant pole to the modulation response and limit the modulation bandwidth of the compound laser. It should be noted that in direct modulation, the bandwidth depends on relaxation oscillation peak but it does not cause any effect in the push-pull modulation.

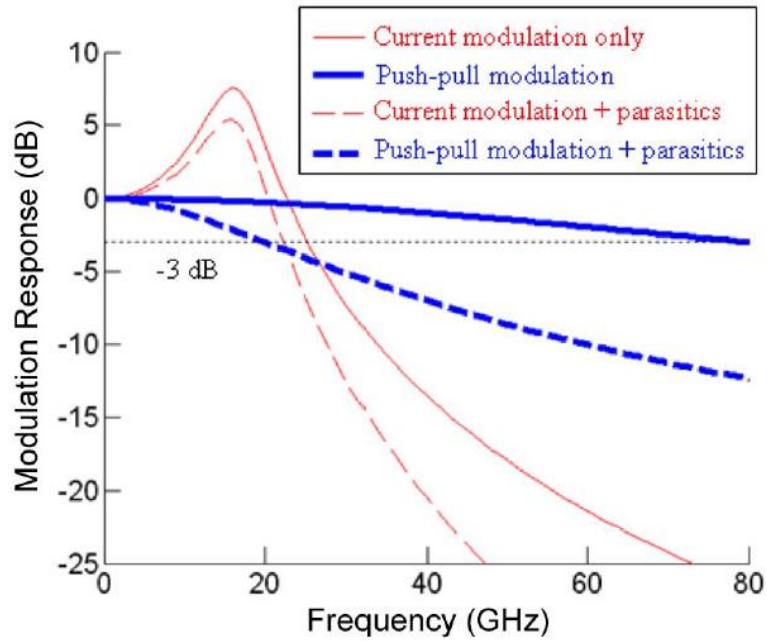


Figure 11: Comparison between current modulation and push-pull modulation simultaneously [4]

2.3 Electroabsorption modulators: (photon lifetime modulation)

2.3.1 Forward bias and reverse bias

This vertical-cavity laser with an integrated modulator is similar to the previous design in section 2.2.1 but the passive cavity is forward modulated by current or reversed modulated by voltage [34].

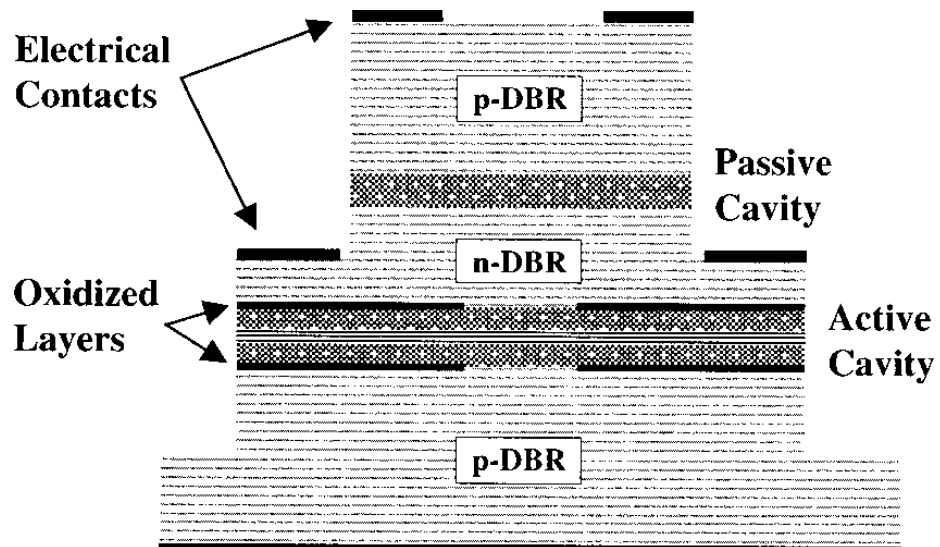


Figure 12: Schematic of a coupled resonator vertical-cavity laser (CRVCL) [34]

Figure 12 shows the main design; as it can be seen from this figure, the top and intermediate resonators have separate electrical contacts to give them independent current injection. This is also to make the device a three terminal coupled resonator vertical cavity laser (CRVCL). The output intensity is modulated by changing the cavity coupling.

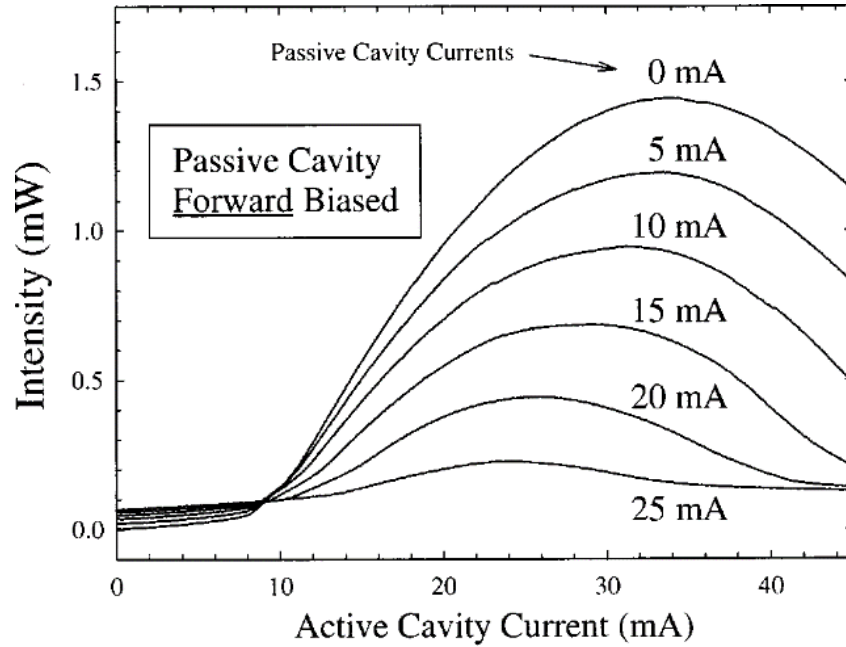


Figure 13: Light output from the CRVCL for various forward bias passive [34]

When the current applied to the passive cavity is increased, the laser intensity is decreased as shown in Figure 13. This is because the index of refraction is reduced and it changes the optical path length when the current is applied into the passive cavity as shown in Figure 14. The change of the index of refraction can go to $\Delta n = 3 \times 10^{-3}$ according to the model with plasma of charged particles in a dielectric [35]. As a result of the change of the optical path, the intensity amplitude changes and the laser output will be modulated. The sensitivity of the path length variation and the modal frequency can be controlled to have a chirpless laser output power. However, the laser output can be affected by heating which results in redshift in wavelength [36].

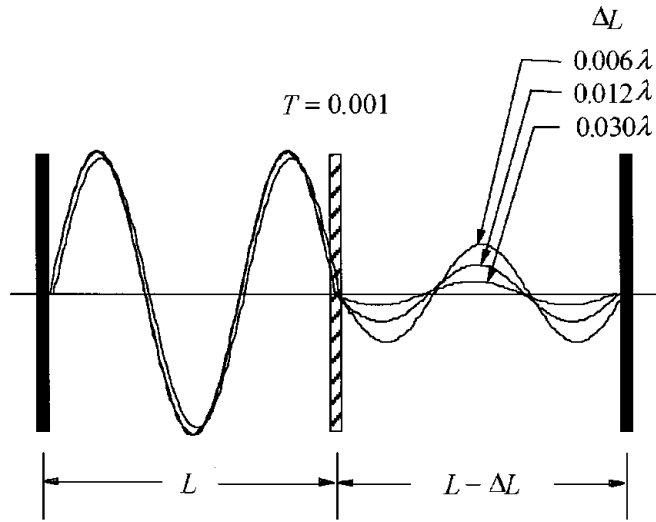


Figure 14: The change the optical path length when the current is applied into the passive cavity [34]

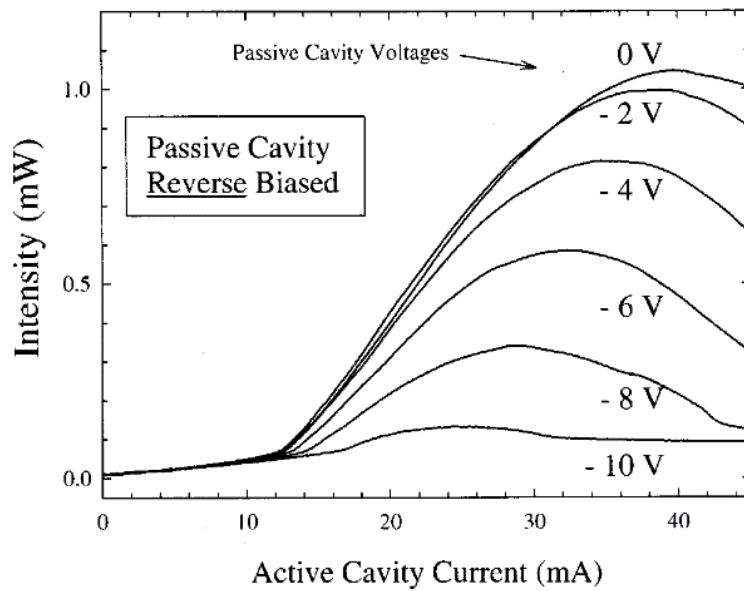


Figure 15: Light output from the CRVCL under reverse bias operation [34]

Figure 15 shows the second way to modulate laser output using the mechanism reverse bias of the passive cavity. When a bias voltage is applied to the passive cavity, the laser intensity is decreased due to electroabsorption loss in the cavity.

2.3.2 Duocavity VCSEL for resonance-free modulation

Eisden and co-authors studied the current modulation for compound vertical cavity laser from other aspects [37]. Their schematic diagram is shown in Figure 16 with 29 periods for

bottom Distributive Bragg Reflector (DBR) of n-type $\text{Al}_{0.07}\text{Ga}_{0.93}\text{As}/\text{Al}_{0.90}\text{Ga}_{0.10}\text{As}$, 32 periods of n-doped middle DBR and 9 periods of p-type top DBR [37]. The active layer consists of four quantum wells, p-type doping and with $\text{n}^{++}\text{-p}^{++}$ tunneling junction. The modulator section is $1\frac{1}{2}\lambda$ thick and it contains an embedded absorber in the i-region of p-i-n junction.

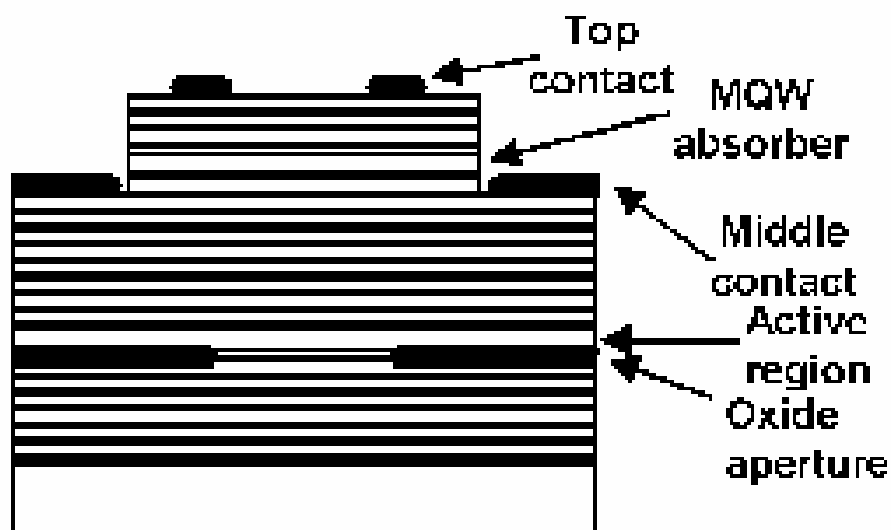


Figure 16: Schematic diagram of the device layout, showing two device sections [37]

And the middle DBR's are n-doped and the $\text{n}^{++}\text{-p}^{++}$ tunneling junction was built under the active region so the optical loss induced by free-carrier absorption of p-doped AlGaAs is reduced. As normal practice in the current modulation, the active area is connected to a bias current and the modulator section is connected to RF signal and DC bias through bias T circuit. The active region was created by wet lateral oxidation and field implantation while the modulator area was created by ion implantation.

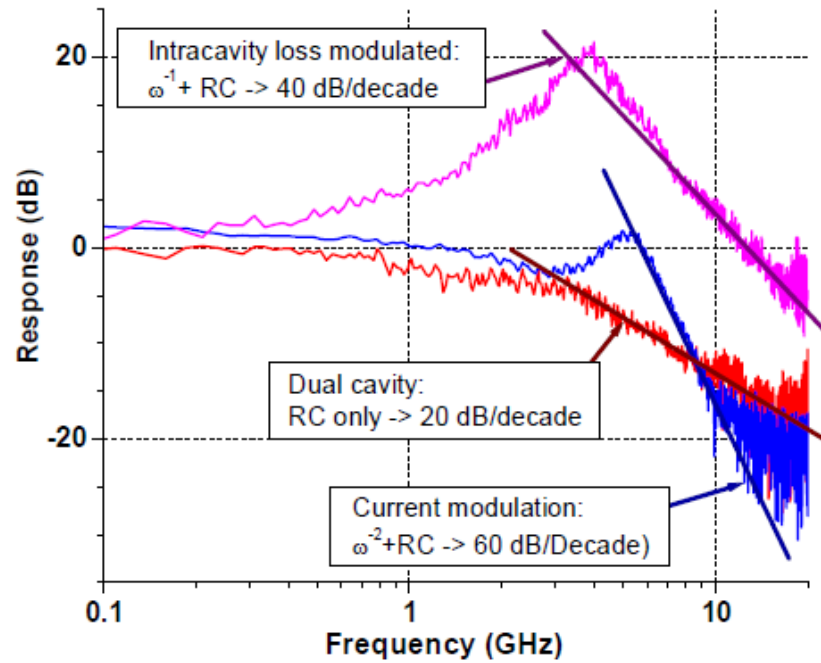


Figure 17: Modulation response for a direct current modulated, intracavity loss modulated, and dual cavity devices. 20 db/decade roll-off above 5 GHz is due to RC parasitic it metallization [37]

Figure 17 shows the three cases which can be examined by this structure. The frequency response has 20 dB/decade roll-off with 5 GHz bandwidth when the RC parasitics is only considered. This result was theoretically discovered by [7] and experimentally demonstrated by [38]. The second case has 60 dB/decade roll-off when the direct (current) modulation is considered. The last case has a response a 40 dB/decade roll-off when the intracavity loss is considered.

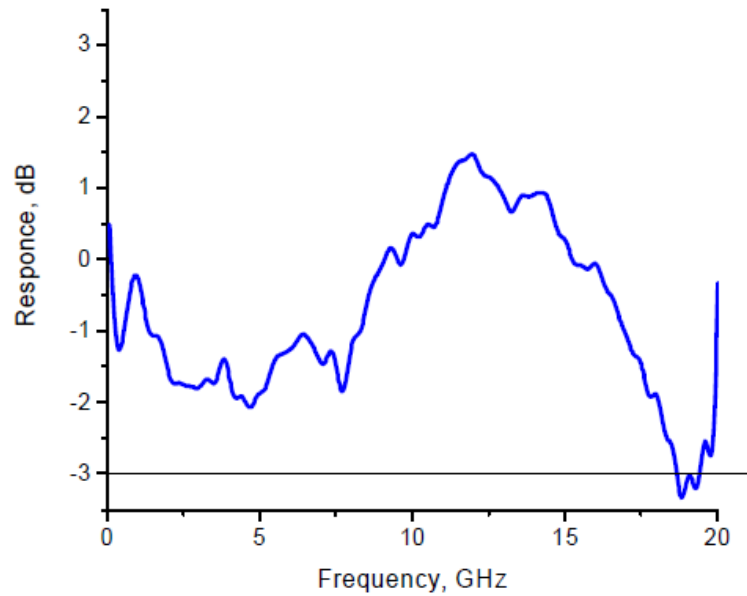


Figure 18: Device high frequency modulation response at room temperature [37]

In this design, the 3dB cut-off frequency is 19 GHz as shown in Figure 18. This means that the transfer function is flat until 19 GHz and the 3 dB cut-off can be decided by the modulator parasitics which can be calculated by the electrical equivalent circuit. Figure 19 shows an open eye electrical eye diagram for a 10 Gbit/s for compound vertical cavity laser.

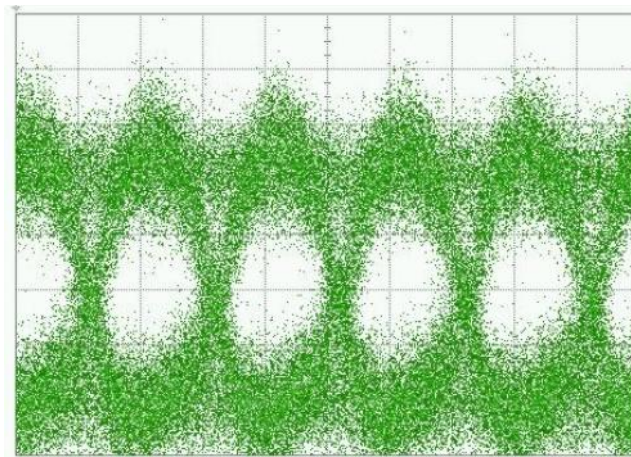


Figure 19: A 10 Gbit/s eye diagram of dual cavity device showing an open eye [37]

One of the very important results is shown in Figure 20 which shows the calculated reflection and transmission spectra of a Fabry-Perot cavity with variable intracavity absorption (0, 0.5% and 1% per round-trip). The 1-D transfer matrix [9] model was used to calculate the wavelength spectrum for these three different variable intracavity absorption. The figure shows that there is an unchangeable point in the wavelength spectrum (cross-over) at which the wavelength is fixed for different values of absorption which means that reflectivity is independent of absorption at this wavelength.

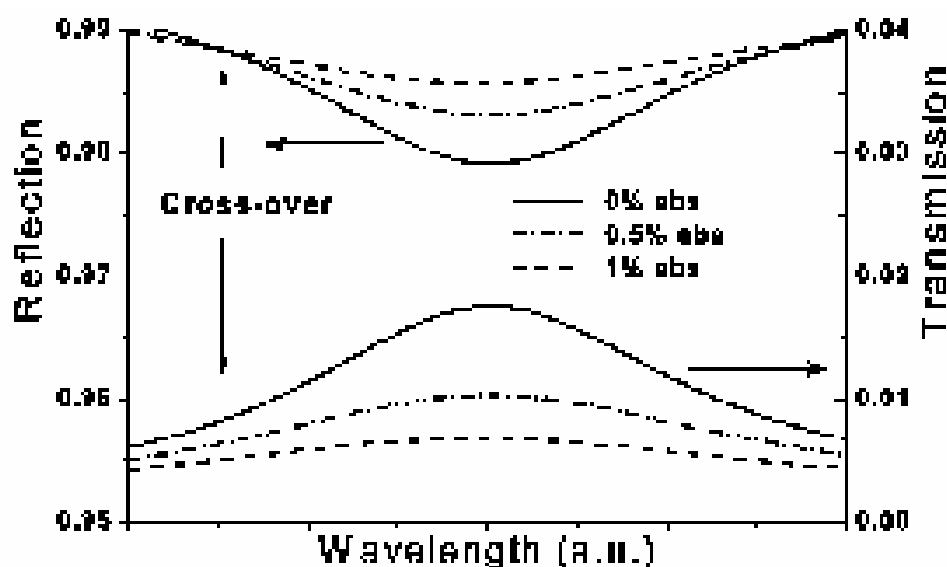


Figure 20: Calculated reflection and transmission spectra of a Fabry-Perot cavity with variable intracavity absorption [37]

The last result in this section is shown in Figure 21. The frequency response is plotted for three different bias reverse biased at the modulator section. When the voltage is reverse bias at -0.4 volts, the frequency response has a flat resonance at 10 GHz. When the voltage is revers bias at -0.1 volts, there is a peak response at 10 GHz. However, the most exciting result is that, the resonance at the frequency response is getting depressed instead of increase at 10 GHz for +0.4 volts forward bias.

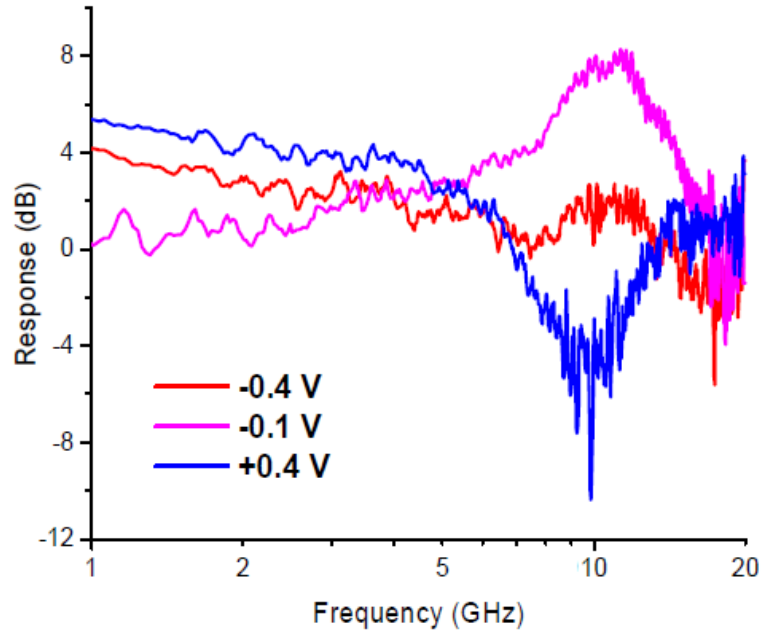


Figure 21: Modulation response of a dual-cavity devices at different modulator voltages. Change of modulator voltage causes shift of optical cavity position, thus detuning from ideal situation (red curve). Detuning may result in optical feedback-related modulation being in-phase (purple) or 180° shifted (blue) with decoupled mode modulation [37]

To explain the reason for this depressed peak in the frequency response, it should be noted that the output power is proportional to the photon concentration and output transmittance as shown in Equation (4):

$$I_{out} \sim N_p * T \quad (4)$$

In terms of modulation of small signal, Equation (4) is adjusted to Equation (5):

$$\Delta I_{out} \sim \Delta(N_p * T) = N_p * \Delta T + \Delta N_p * T \quad (5)$$

The first term in Equation (5) is $(N_p * \Delta T)$ which describes the potentially flat line while the second term $(\Delta N_p * T)$ describes resonance term of the frequency response because of the modulation of photon concentration at the output power. The art of the design of the resonant-free modulated laser is then to ensure that the second term disappears. This is done by ensuring the spectral operating point such that the *transmittance* of the top mirror does

change with electroabsorption modulation (so the first term is nonzero) but the *reflectance* (and thus the photon lifetime) does not. This is done by ensuring that the effects of the broadening of the spectral notch and the flattening of the notch, both of which happen with increased absorption, compensate each other (in other words, the laser operates at the cross-over point in Figure 20). If the reflectance does not change with a variation of absorption, this means N_p does not change, the second term in the equation disappears, and so there is no resonance in the modulation. To work at this spectral point, the correct bias on the electroabsorption modulator section bias is needed (e.g. -0.4 V in Figure 21). At +0.4 V forward bias, there is a depressed response instead of increase at 10 GHz, and at -0.1 V reverse bias, a peak response – this is depending on whether the broadening or the flattening of the peak dominates, in other words whether the reflectance increases or decreases with an increase in absorption.

2.3.3 Reliability performance

In this section, the reliability performance study of current modulation for VCSEL at 95 °C as investigated in [39] is reported. It was found that the performance of such type of lasers is stable and reliable even after a relative long time of operational test (more than 6000 hours). The VCSEL used for this experiment was 6 μm diameter oxide confined with 850 μm wavelength and the number of VCSELs were 50. To have an error-free operation, high current densities ($\sim 18 \text{ kA cm}^{-2}$) were applied. Figure 22 shows that the change of power verses the time of the operational test for the experiment. The figure shows almost a stable output power with respect to the time of the experiment. However, there was less than 5% increase of the output optical power after 6000 hours at a constant current of 5 mA. This small increase of the output power might be attributed to the ohmic contact burn in the first 2000 hours of the study.

In the beginning of the study, some VCSELs were damaged due to mechanical damages, growth and fabrication-related defects, or electrostatic discharge and they were removed from operation. However, all remaining VCSELs were reliable after 6000 hours of the start of the study.

By using new optimized oxidation methods, the oxide aperture stress can be reduced when the intermediate metastable products are removed [40, 41]. This may help in reducing the threshold current density and capacitance for VCSELs working at 850 nm wavelength and a speed of 25 Gbit/s at high temperatures.

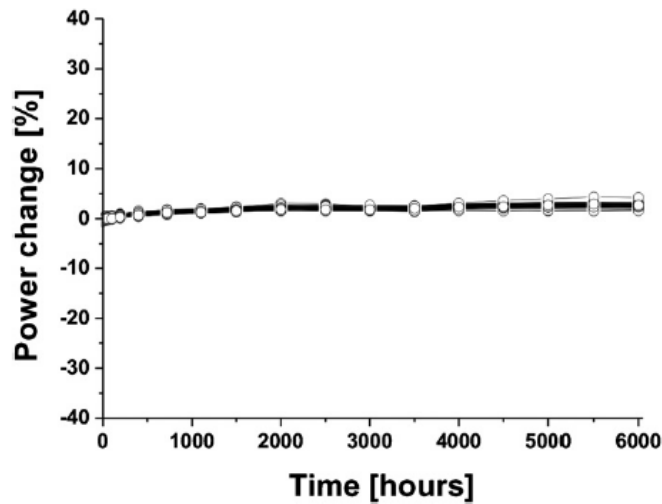


Figure 22: Change in output power of 6 μm diameter oxide-confined InGaAlAs 850 nm VCSELs measured at 20 $^{\circ}\text{C}$ as a function of ageing time at 95 $^{\circ}\text{C}$ in [39]

2.4 Electrooptic modulators: (photon lifetime modulation)

The limitations of current modulation can be overcome using modulation of the photon lifetime in the cavity as an alternative method to current modulation. This approach is potentially free from the limitations of the modulation such as the 3dB modulation frequency being limited by the electron-photon oscillation damping, since the photon lifetime modulation, unlike current one, affects the output of the laser directly as opposed to indirectly via carrier density. In the following sections, different methods of photon lifetime modulation will be discussed, including electroabsorption and electrooptical modulation.

2.4.1 Modulation of reflectance of multistack mirrors forming the VCSEL cavity: general idea and theoretical analysis in literature

A method of realisation of the cavity loss modulation was suggested a while ago in the form of electrooptic modulation of the reflectance of one of the multistack mirrors forming the VCSEL cavity [7]. When 1 V variation is applied to the electro-optically tuned distributed Bragg reflectors (DBR) in the vertical cavity semiconductor emitting laser, 12% reflectance modulation is achieved [42].

The following rate equations can be used to characterize the electron and photon densities in the VCSEL active layer:

$$\frac{dN}{dt} = J - Sg - \frac{N}{\tau_{sp}(N)} \quad (6)$$

$$\frac{dS}{dt} = \Gamma gS - \frac{S}{\tau_{ph}} + \frac{\beta_{sp}N}{\tau_{sp}} \quad (7)$$

In these equations, (N) is the carrier density, (S) is the photon density in the laser, ($J = \frac{I}{eV}$) is the electron flux per unit volume (V), (I) is the pumping current, (g) is the optical gain in the active layer, (τ_{sp}) is the radiative recombination lifetime of carriers and (τ_{ph}) is photon lifetime and (Γ) is confinement factor.

The photon lifetime is defined, in the usual way, as:

$$\tau_{ph_{out}}^{-1}(t) = \frac{v_g}{2 * L} \ln \frac{1}{R_b R_T} \approx \frac{v_g}{2 * L} (T_b + T_T)$$

Where R_b and R_T are the (intensity) reflectances of the bottom DBR and top reflector (which was assumed to be modulated), and $T_{b,T} = 1 - R_{b,T} \ll 1$ the corresponding transmittances. The nature of the top reflector (e.g. stopband or resonator modulation) and how it was modulated was not specified in the paper, but it was assumed that the modulation would be electrooptic, therefore fast.

And the following expressions for light intensity response were obtained:

$$\partial S = \frac{\Gamma \tau_{st}^{-1} \partial J - (i\omega + \tau_d^{-1} + \tau_{st}^{-1}) \partial S \tau_{ph}^{-1}}{i\omega\gamma - \omega^2 + \omega_{rel}^2} \quad (8)$$

$$\tau_{st}^{-1} \equiv \bar{S} \frac{\partial g}{\partial N} \quad (9)$$

$$\tau_d^{-1} \equiv \frac{\partial}{\partial N} \left(\frac{N}{\tau_{sp}(N)} \right) \quad (10)$$

$$\omega_{rel}^2 \approx \frac{1}{\tau_{st} \tau_{ph}} \quad (11)$$

$$\gamma = \tau_d^{-1} + \tau_{st}^{-1} + \frac{\beta_{sp} N}{\bar{S} \tau_{sp}} - \Gamma \bar{S} \frac{\partial g}{\partial S} \quad (12)$$

Where (τ_d) is the dynamical carrier lifetime, (τ_{st}) is the stimulated recombination time, (ω_{rel}) is the relaxation oscillation frequency, and (γ) is the damping factor.

Small-signal modulation curves corresponding to this modulation type were analysed and predicted to have a higher 3dB cutoff frequency than the current modulation, owing to the transfer function decaying at high frequency F values as $1/F$ (see Equation 8) rather than $1/F^2$ as is the case of current modulation.

Figure 23 shows different possibilities for modulation: when current density (J) is changing (curve 1), when either photon lifetime (τ_{ph}) or confinement factor (Γ) are changing (curve 2), when the carrier temperature (T) is changing (curve 3).

Curve 4 in Figure 23 shows the case when two independent modulation mechanisms (current density and temperature) are applied and their amplitudes and phases are adjusted [43]. In this case, high-frequency carrier density variation is isolated ($\delta n = 0$) and relaxation oscillations is eliminated which creates a flat response as in curve 4 in Figure 23 which can be used in analogue and digital circuits and networks.

Finally, when both current density and photon lifetime (or carrier temperature) are changing (curve 5-flat response). As shown in Figure 23, when current density (J) is changing (curve 1), the transfer function is decaying at high frequency ω values as $1/\omega^2$. On the other hand, the transfer function is decaying at frequency values as $1/\omega$ for photon lifetime modulation (curve 2).

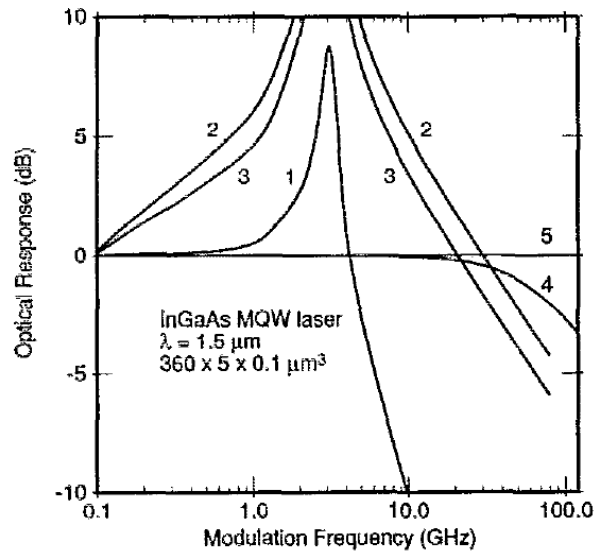


Figure 23: Modulation different types [7]

While the generic idea of dual or photon lifetime modulation has been used in subsequent work, some modifications needed to be made for its practical implementation, which also requires a modification in the theoretical approach. Most importantly, the analysis of [7] ignored the spectral selectivity and spectral position of the operating point of the laser, assuming frequency-independent modulation of reflectance and hence of photon lifetime. In practice, efficient modulation of reflectance of a DBR such as one used in a VCSEL is only possible where there is a relatively sharp spectral feature in the reflectance spectrum. Hence, two designs have been proposed, involving either a resonant subcavity with the operating point near the mode (transmission notch) of this subcavity, or alternatively stopband modulation, where the operating point is at the edge of the DBR reflectance.

2.4.2 A resonant cavity design and non-absorbing modulator subsection

In this section, a typical compound VCSEL with a non-absorbing electro-optic modulator is discussed [12]. This design of compound VCSELs can be used to transmit single mode and multimode pulses over modern multimode fibre optics (MMF) with modulation speed of 40 Gbit/s and over a distance of 400 m [44].

The main design is shown in Figure 24 with all lengths and parameters are labelled. In this design, the electrical bandwidth can go up to 60 GHz and optical bandwidth can be more than 35 GHz restricted by the photodetector response. Strain-compensated multiple quantum wells were used in the active gain region in the VCSEL cavity with 960 nm reference frequency and 3-4 nm blue shift in the modulator region. To have a non-absorbing modulator, a low Q-factor modulator was used which will have an efficient light coupling and low chirp (frequency change in time).

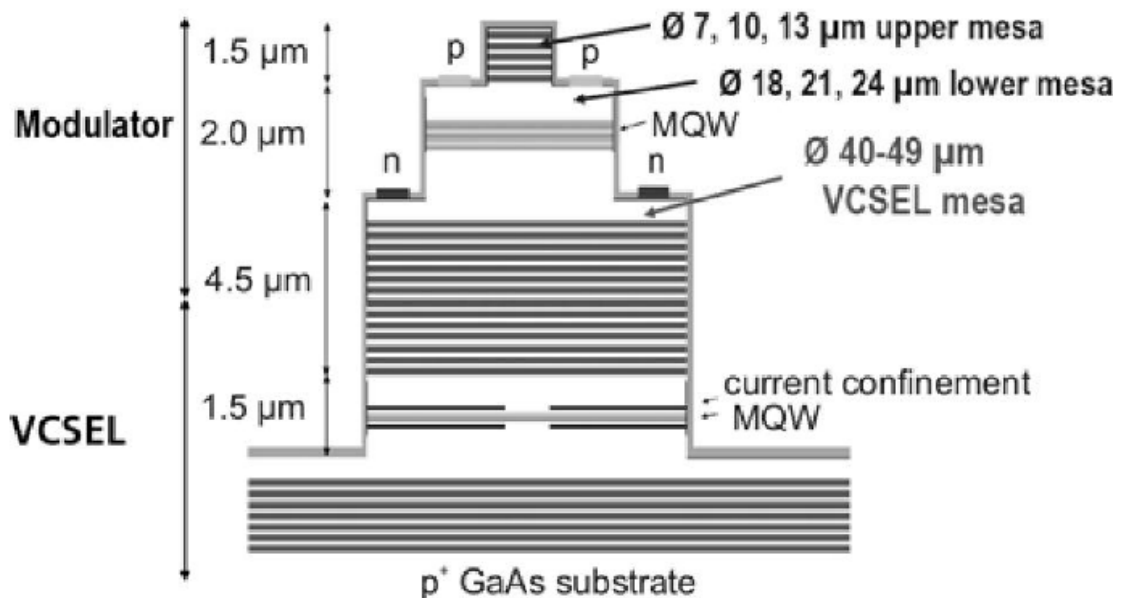


Figure 24: Basic EOM/VCSEL structure [reference]. The sizes of most figures can be reduced a bit [12]

The main idea of this new structure is that by applying a reverse bias voltage to the modulator section, the two cavities will be resonant. This is because the energy band of the

electrooptically modulated (EOM) section will be tilted [45] and adjusted to be in the same level as the energy band of the VCSEL as shown in Figure 25, thanks to the quantum confined Stark effect.

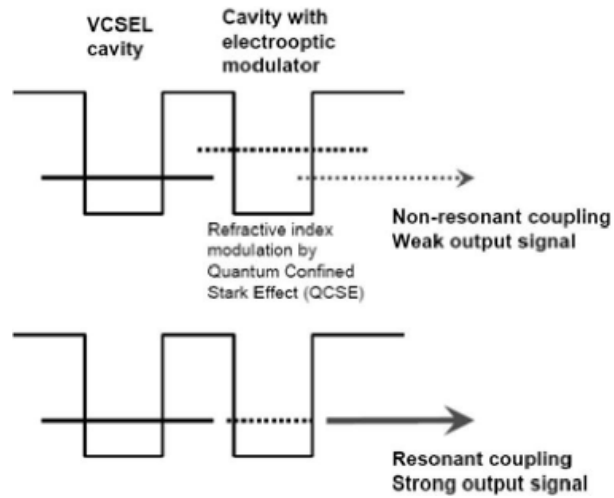


Figure 25: The coupling diagram between VCSEL cavity and electro-optic modulator [12]

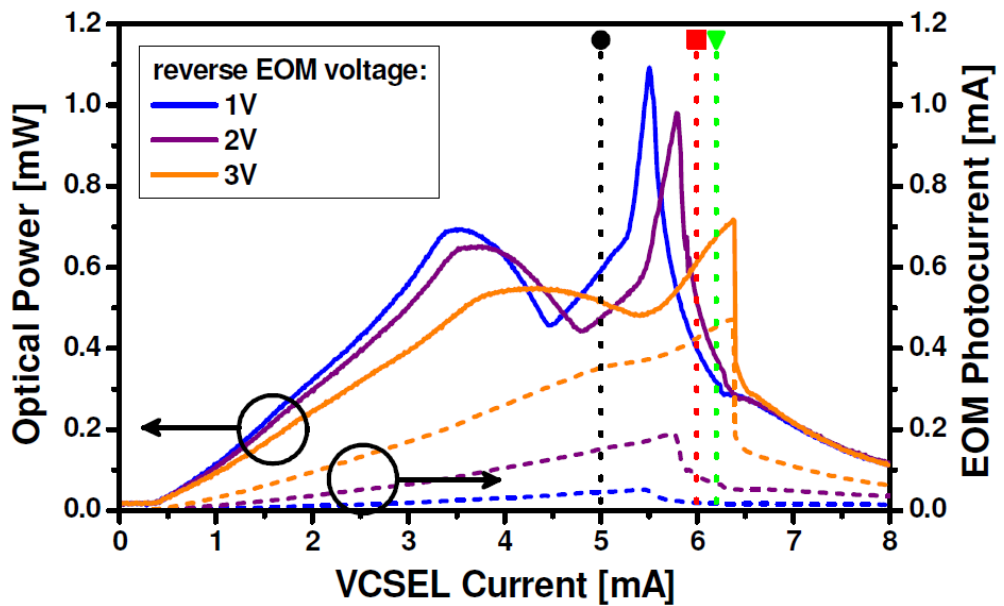


Figure 26: Optical power vs VCSEL current; solid lines: Optical output power characteristics of the EOM VCSEL are shown for different voltages applied to the EOM section. Dashed lines: Corresponding photocurrent due to absorption within the EOM section [11]

Figure 26 shows the optical power in mW as a function of bias current in mA for different reverse modulator voltage for large detuning between the VCSEL and the modulator cavity. As it can be seen in this figure that the relationship between the optical power and the laser current in the case of large detuning is non-monotonic. In this design [11], the static characteristics at room temperature are also analysed. It was found that the optical power depends non-monotonically on the VCSEL current for three different reverse EOM volts (1, 2 and 3 volts). The general characteristics is that at low currents (from 0.5 mA until 3.5 mA for 1 V and 2 V reverse EOM voltage, and 4 mA for 3 V reverse EOM voltage), the optical power increases as current increases. Then, there is a normal decrease in the optical power until 4.5 mA for 1 V and 2 V reverse EOM voltage and 5.5 mA for 3 V reverse EOM voltage. After that, there is a high increase in power for a short increase of current (about 1 mA) followed by a normal decrease in power. Figure 26 shows the details of the optical power versus VCSEL current. The change of passive cavity absorption is not the reason for the sudden and high increase in optical power between 5.5 and 6.5 mA VCSEL current rather it can be explained by the resonance between top and bottom cavities. However, when a high reverse voltage is applied, there will a high reduction for the exciton absorption peak and an alternative change in the resonance wavelength according to the change in the refractive index (positive or negative) [14, 45, 46]. The resonant output power in this design matched the typical output power for similar design [12].

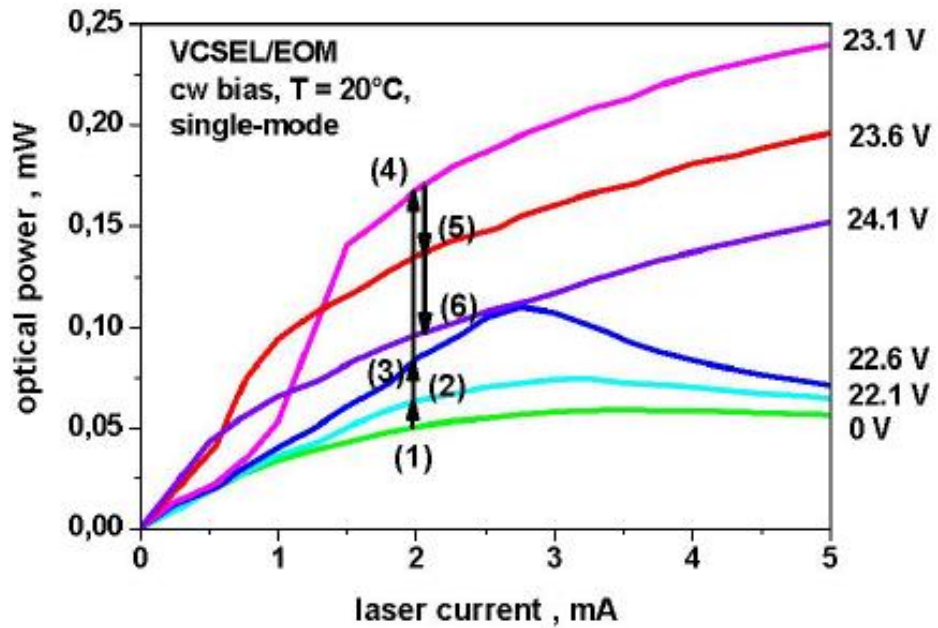


Figure 27: Static performance of an EOM/VCSEL at different reverse biases applied to the modulator section (large detuning between the cavities) [12]

Figure 27 shows the optical power in mW as a function of bias current in mA for different reverse modulator voltage for large detuning between the VCSEL and the modulator cavity. The relationship between the optical power and the laser current in the case of large detuning is monotonic except for 22.6 V reverse bias modulator voltage. The graph also shows that the maximum optical power occurs when the reverse voltage is 23.1 V when there is a strong resonance between the VCSEL and modulator cavities.

Figure 28 shows the change in wavelength (chirp) for the single mode laser device for different reverse voltages in the case of large detuning. The chirp in this model is 0.3 nm/V and it can be increased when the thickness of the modulator is reduced because the applied voltage in this case will be increased too. The threshold current, on the other hand will not be increased but the differential efficiency and the external losses will be increased as well.

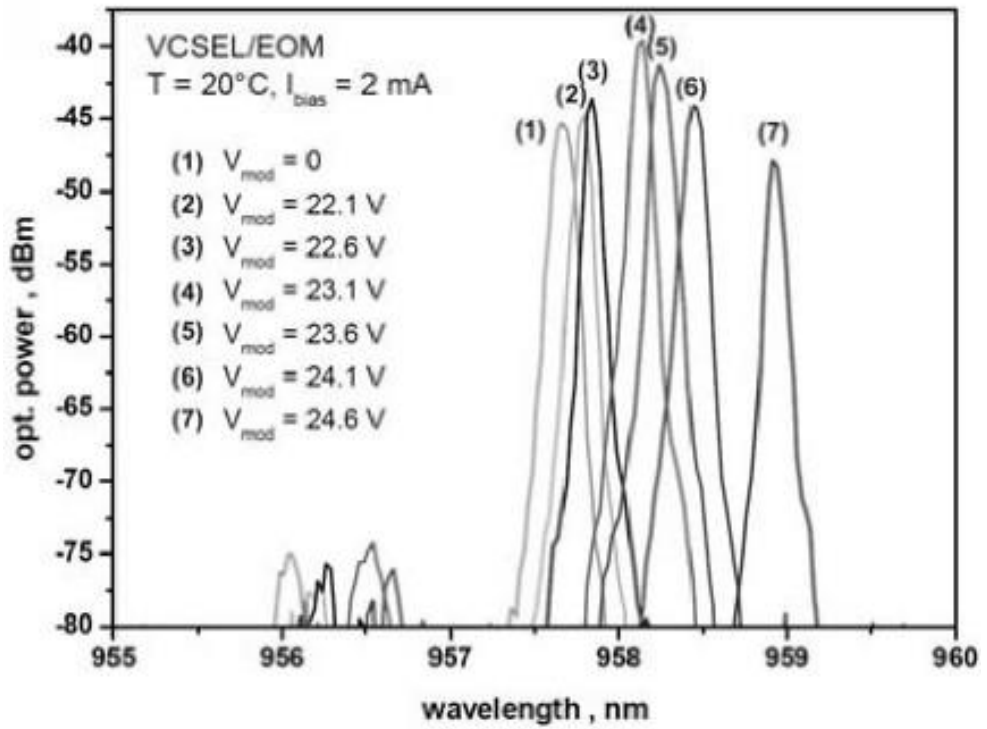


Figure 28: Spectra of a single-mode EOM/VCSEL device at different reverse biases applied to the modulator section (large detuning between the cavities) [12]

As mentioned in the start of this section, the cut-off frequency can go up to 35 GHz restricted by the photodetector response. This can be elaborated by Figure 29 which shows the small signal response of the optical intensity in dB as a function of modulation frequency.

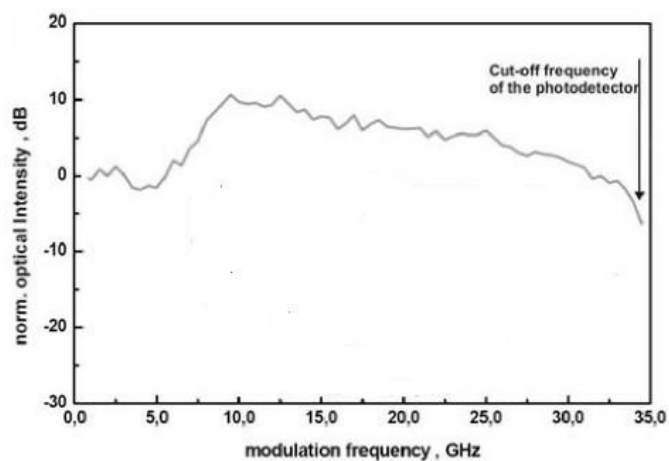


Figure 29: Optical modulation performance of the EOM/VCSEL [12]

2.4.3 VCSEL with electrooptically modulated vertical resonator and a stopband edge tunable DBR

Theoretically, the idea of cavity loss modulation mentioned in section 2.4.1 [7] inspired a large amount of further work, in which the idea of modulating a mirror reflectance has evolved into two possible routes: the coupled-cavity laser with an additional, electrooptically modulated vertical resonator [47], and a stopband edge-tunable DBR [48]. Figure 30 and Figure 31 shows electrooptically modulated vertical resonator, and a stopband edge-tunable DBR, respectively.

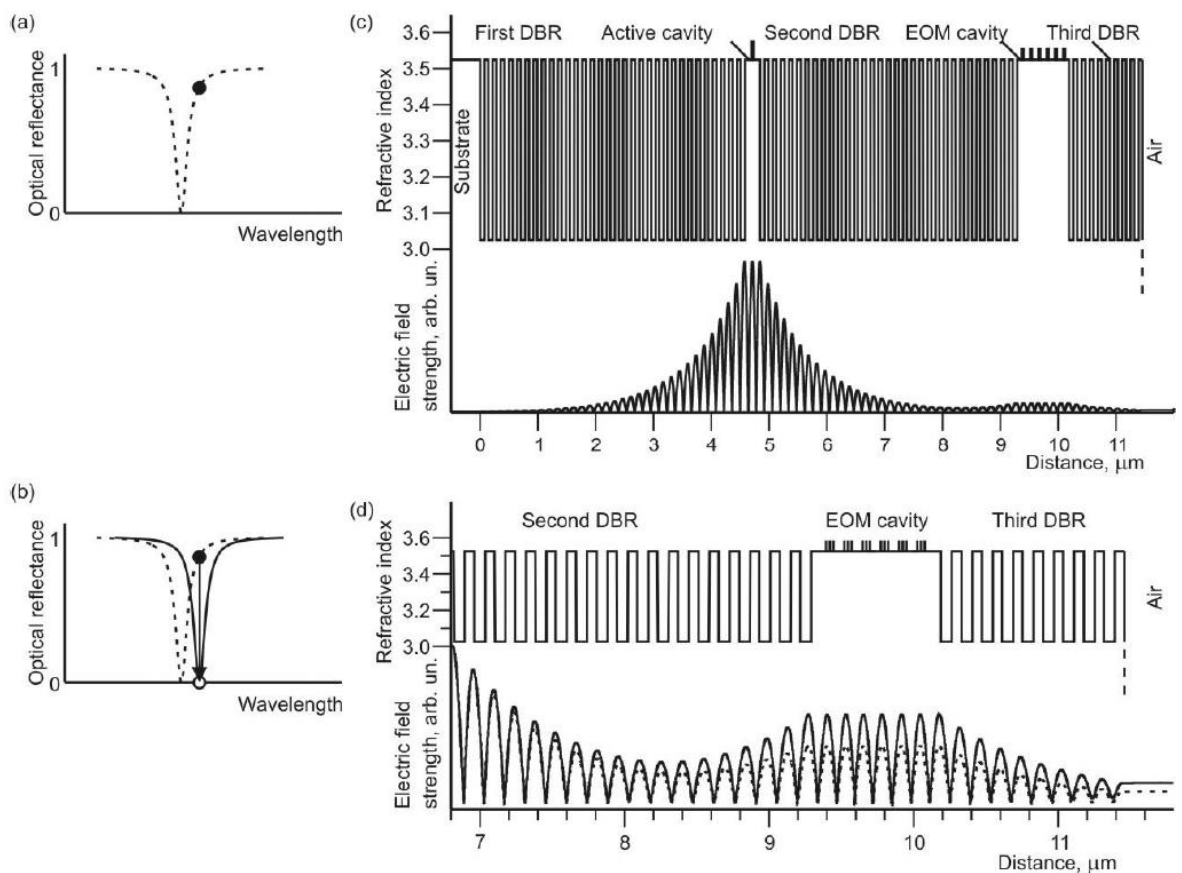


Figure 30: Electrooptically modulated VCSEL based on resonantly coupled cavities. (a) Optical reflection spectrum of the modulator cavity; open circle corresponds to the lasing wavelength. (b) Upon an applied bias, the modulator reflectivity dip matches the lasing wavelength, increasing the light output power. Dashed line, cavity out of resonance; solid line, cavity in resonance. (c) Profiles of the refractive index and electric field strength in the VCSEL optical mode. (d). Top part of the device: profiles of the refractive index and electric field strength in the VCSEL mode in the open state (solid line) and closed state (dashed line)

[47]

In electrooptically modulated vertical resonator, the top resonator is modulated using Fabry–Perot cavity with passive DBR [14]. When a reverse voltage is applied to the passive cavity, the refractive index is modulated which modulates the reflectivity seen by the active cavity in the VCSEL. The second DBR consists of 31 periods and the third DBR has 9 periods. Figure 30 (b) shows that the optical reflection spectrum of the modulator cavity; upon an applied bias, the modulator reflectivity dip (notch) shifts to higher wavelength and increase the light output power [46].

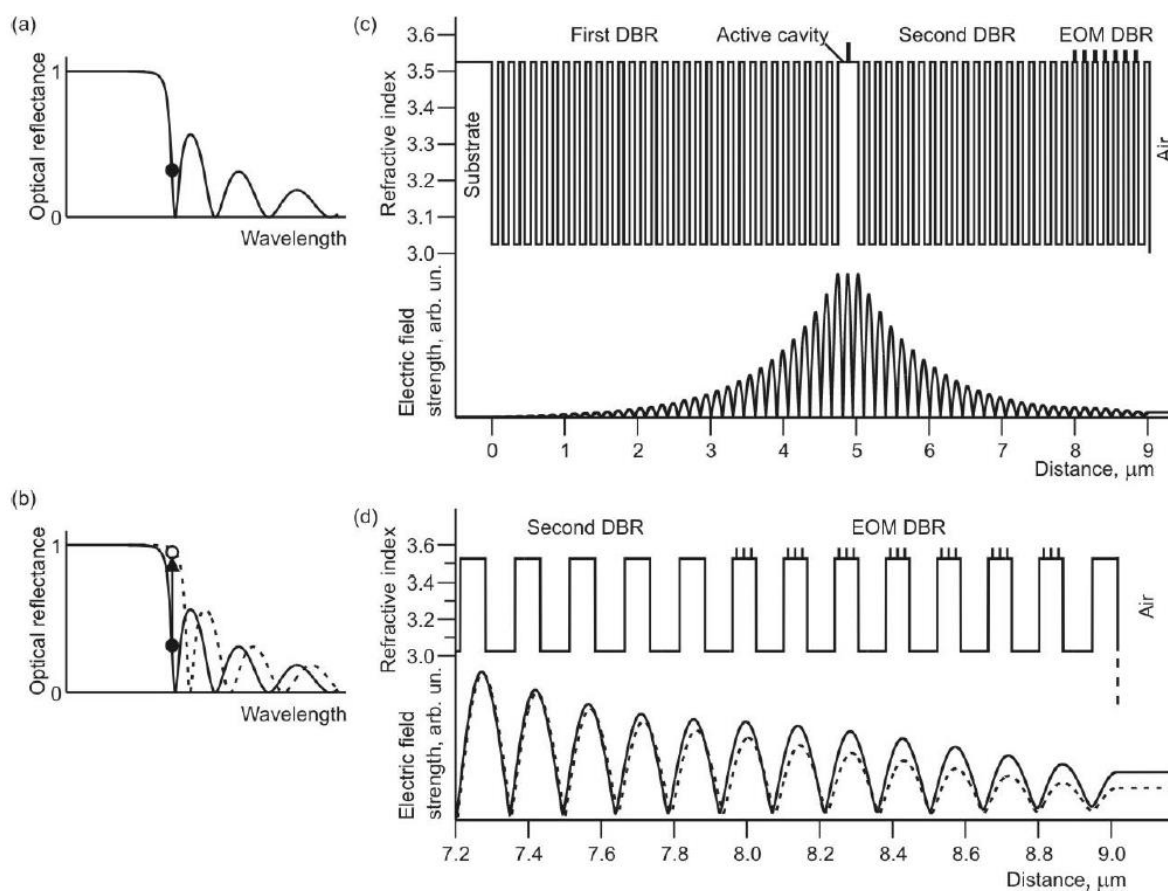


Figure 31 : Electrooptically-modulated VCSEL based on stopband edge-tunable DBR. (a) Reflectivity spectrum of a EOM DBR near the stopband edge. Filled circle refers to the lasing wavelength. (b) Shift of the EOM DBR stopband edge reflectivity spectrum upon applied bias. Reflectivity spectrum at zero bias, solid line; reflectivity spectrum at applied bias, dashed line. A transparent DBR with a low reflectivity (filled circle) becomes non-transparent with a high reflectivity (open circle). (c) Profiles of the refractive index and electric field strength in the VCSEL optical mode. (d). Top part of the device: profiles of the refractive index and electric field strength in the VCSEL mode in the open state (solid line) and closed state (dashed line) [14]

The stopband edge-tunable DBR has the same design as electrooptically modulated vertical resonator but a part of the top DBR is un-doped and QWs are placed in the layers having a high refractive index. Figure 31 shows schematically the profiles of the refractive index and electric field strength of the VCSEL mode. In this design, the side notch is modulated upon applied bias as shown in Figure 31 (b).

2.4.4 Rate equation analysis of a VCSEL with electrooptically modulated mirror: simulated eye diagrams

The authors of [7] first used a standard rate equation system, similar to Equations (6-7) with modulated photon lifetime, to simulate the small-signal response of the laser.

Later, a similar model was applied to large-signal dynamics of the laser [14]. The modulated parameter was the reflectance of the top cavity, from which the photon lifetime was calculated from Equations (6-7). The analysis thus related to both the coupled-resonator design and the stopband one, because it was the reflectance that was modulated, as in [7].

The results are presented in Figure 32 and Figure 33, both taken from [14]. The main result is that in order to achieve high quality modulation (open eye), it is advisable to keep the modulated reflectance as high as practical, so that the modulation of the photon lifetime, and hence the photon density inside the resonator, is minimised and the mirror works *almost* as an external modulator. The obvious limitation is that the reflectance of the top mirror needs to be smaller than that of the bottom mirror in order to have efficient output.

The simulations also allowed some conclusions to be made regarding the optimal pumping conditions. Specifically, Figure 32 shows that the best performance of electrooptically modulated VCSELs is realised at moderately small rather than large bias currents [14], which is completely different to the case of current modulation, and not immediately obvious from the published small-signal analysis of photon lifetime modulation [7].

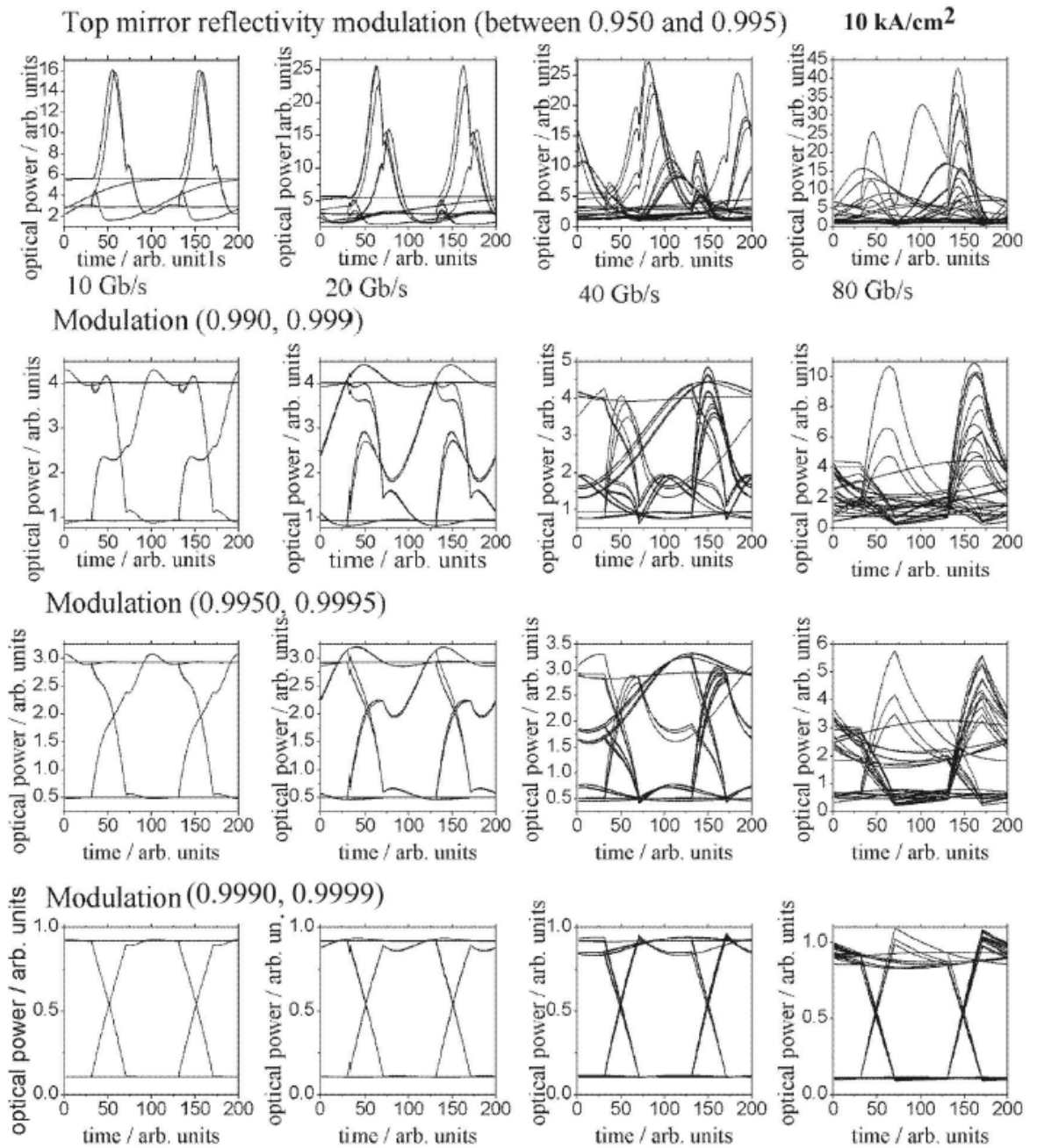


Figure 33: Modeled response of a VCSEL output power to a reflectivity modulation of the top at different values of injection current density. Response to a bit pattern signal is presented in a form of eye diagram[14]

Additionally, and possibly more predictably, as seen in Figure 33, eye diagrams are having open eyes for relatively low top mirror reflectivity modulation amplitude and lower bit rates.

2.4.5 Experimental results on electrooptically modulated VCSELs in the literature.

Experimentally, large-signal NRZ modulation at 40+ GBit/s has been confidently and repeatedly demonstrated using this type of device (see [10]). In this paper, an electrooptically (EO) modulated oxide-confined (VCSEL) is designed with an additional saturable absorber near the bottom active cavity. The passive cavity contains a type-II EO superlattice medium, which causes a strong negative EO effect in weak electric fields and short pulses in the compound laser. Figure 34 shows a schematic structure of an EOM VCSEL with a saturable absorber.

The saturable absorber works is such that: when the voltage applied to the EOM cavity in the VCSEL changes (step-like), short pulses are generated [49]. When a voltage is applied (logic one) in EOM VCSEL section, the absorption of light is decreasing and when logic zero is applied, the absorption of light is increasing (the resonant transparency [50]).

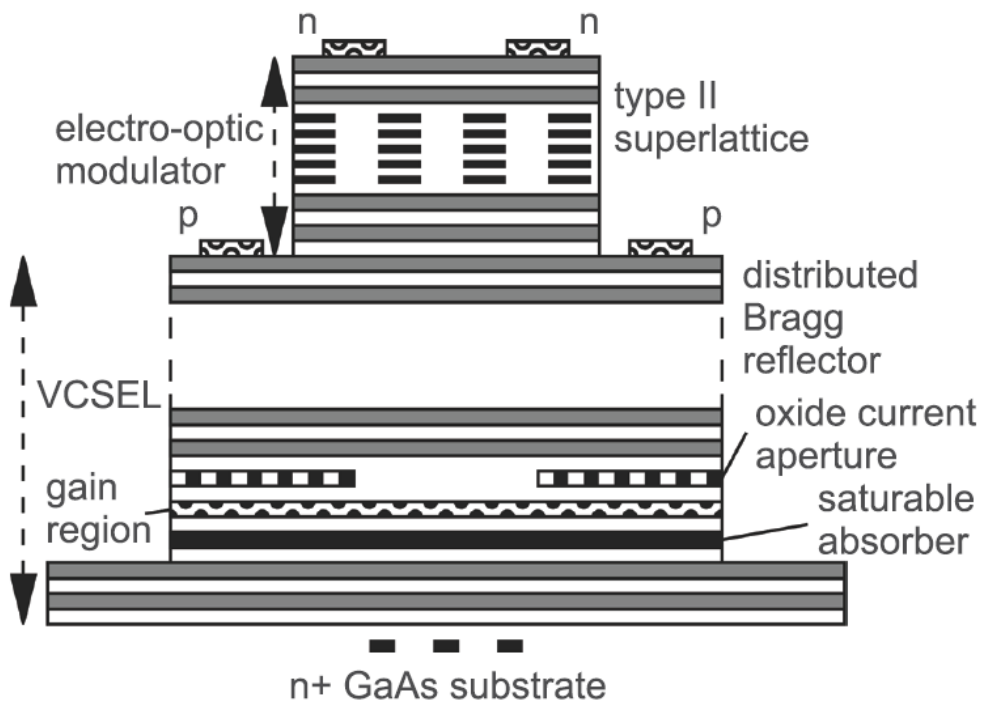


Figure 34: A schematic structure of an EOM VCSEL with a saturable absorber [10]

When a reverse bias voltage is applied to the EO section, -0.012 change in refractive index at 840 nm wavelength was estimated theoretically. The authors of [10] estimated further that this change in the refractive index would lead to a 3dB extinction ratio. The experimental extinction ratio, as shown in Figure 35, is a bit smaller (~ 2 dB) but in reasonably good agreement. In addition, the refractive index modulation achievable would lead to an open electrical and optical eye diagrams as in Figure 36.

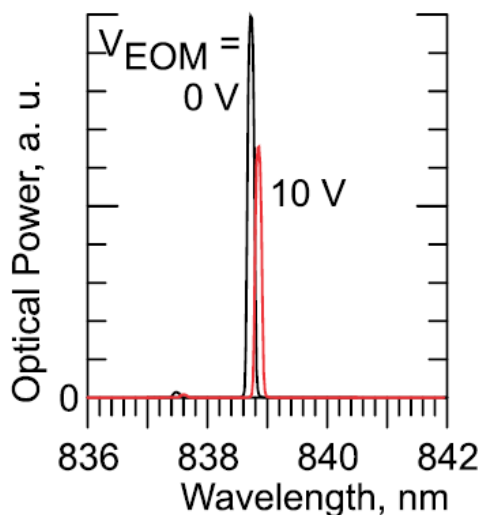


Figure 35: Lasing spectrum of the EOM VCSEL at 1/42 mA and two different voltages [10]

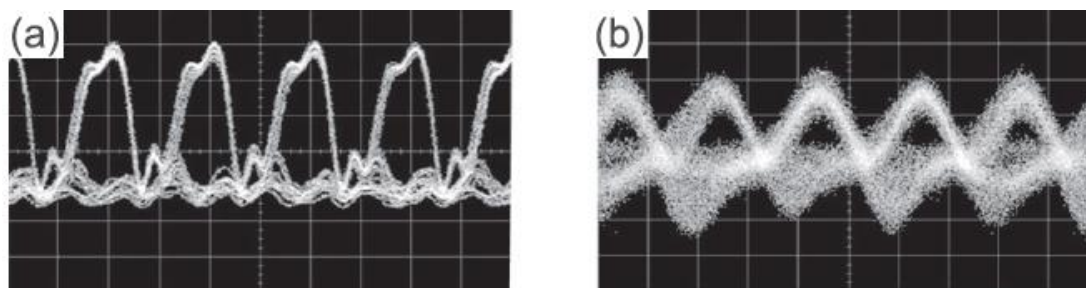


Figure 36: Performance of the RZ transmission of a signal modulated by the electro-optically modulated vertical-cavity surface-emitting laser. (a) Electric eye diagram. (b) Optical eye diagram [10].

2.4.6 Small-signal modulation of EO modulated VCSELs

Small-signal modulation at low frequencies has been experimentally analysed [11] and showed signs of a broad, large resonant peak consistent with the formula presented in [7].

Figure 37 shows the intrinsic bandwidth of the EOM VCSEL; the solid line fits with the transfer function in Equation (13) as derived in [51]:

$$S_{21}(\omega) \propto \frac{1}{\tau_p} \frac{\omega_0^2 \tau_p + i\omega}{\omega_0^2 - \omega^2 + i\omega\gamma} \quad (13)$$

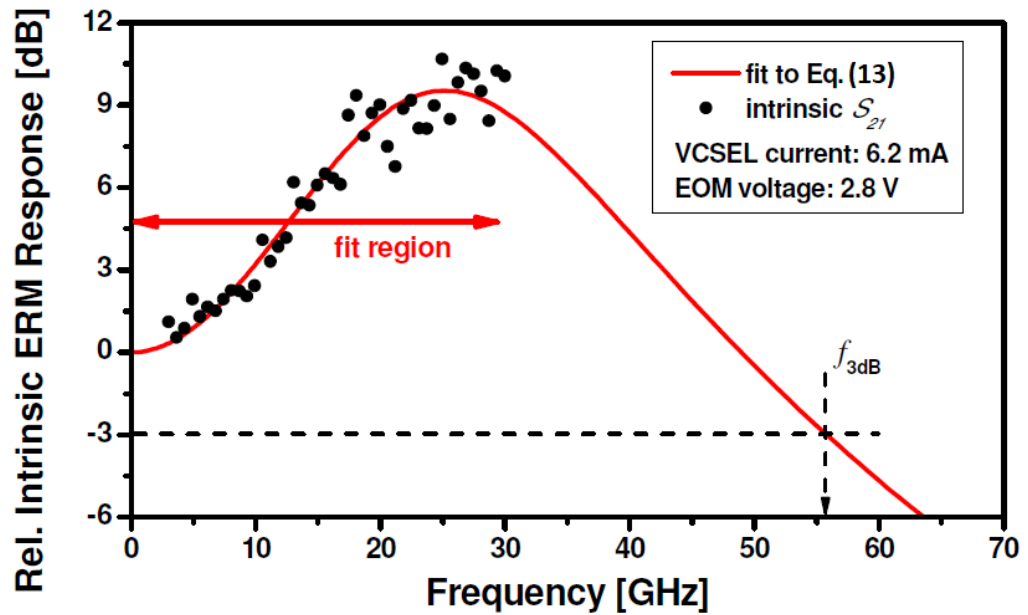


Figure 37: Intrinsic bandwidth of the EOM VCSEL at RT. Electrical parasitics are deconvoluted from the measured data yielding an intrinsic bandwidth of 56 ± 5 GHz [11]

2.4.7 Using QD stack instead of quantum wells in the top cavity

Panajotov, Zujewski and Thienpont found that the driving electrical field can be dramatically decreased if QD stack is used instead of quantum wells in the top cavity [9]. This reduction of linear electrooptical effect can be equal to the one of Lithium Niobate which can go up to $r = 3 \times 10^{-11} \text{m/V}$ [52]. For example, the threshold gain difference when quantum wells are used in the top cavity of a coupled cavity (Figure 38) can become 2.5 bigger than the one when quantum dot stack is used in the top cavity (Figure 39). This happens when same parameters are used and the effective thickness of the QD stack is 10nm to have a smaller QD filling factor.

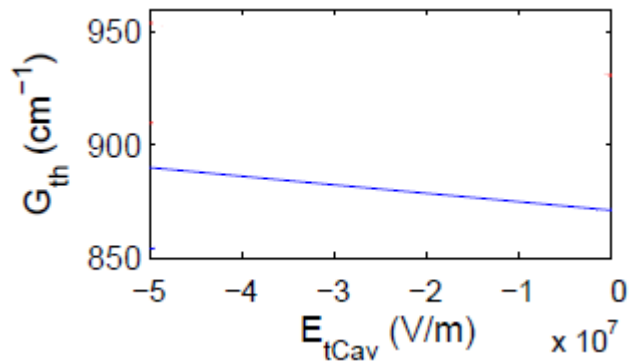


Figure 38: Threshold gains as a function of the modulation electric field E_{tCav} applied to the top-cavity with quantum wells [9]

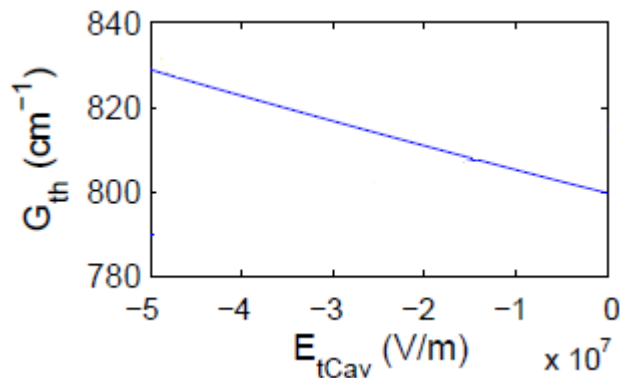


Figure 39: Threshold gains as a function of the modulation electric field E_{tCav} applied to the top-cavity with quantum dots [9]

2.4.8 Elimination of parasitics-related limitations in electrooptic modulation.

Traveling wave electrode design

In this section, we concentrated on the electromagnetic/carrier kinetic model only, not considering the electrical circuit limitations. Indeed, Zujewski and co-authors have proved that the modulation speed limitation due to associated electrical circuit, as studied in [54], of coupled-cavity vertical-cavity surface-emitting laser (CC-VCSEL) can be avoided using a traveling wave electrode design [55]).

Their work shows that the RC time constant of a traditional lumped electrode structures can be coped with and ignored. They were also able to make impedance of the modulator much less than the optimum 50Ω series resistance by segmented transmission line electrical design of the modulator which allow the electrical cutoff frequency to go up to 330 GHz [55]. In the previous design by lumped electrodes, the electrical bandwidth can go up to 100 GHz [54].

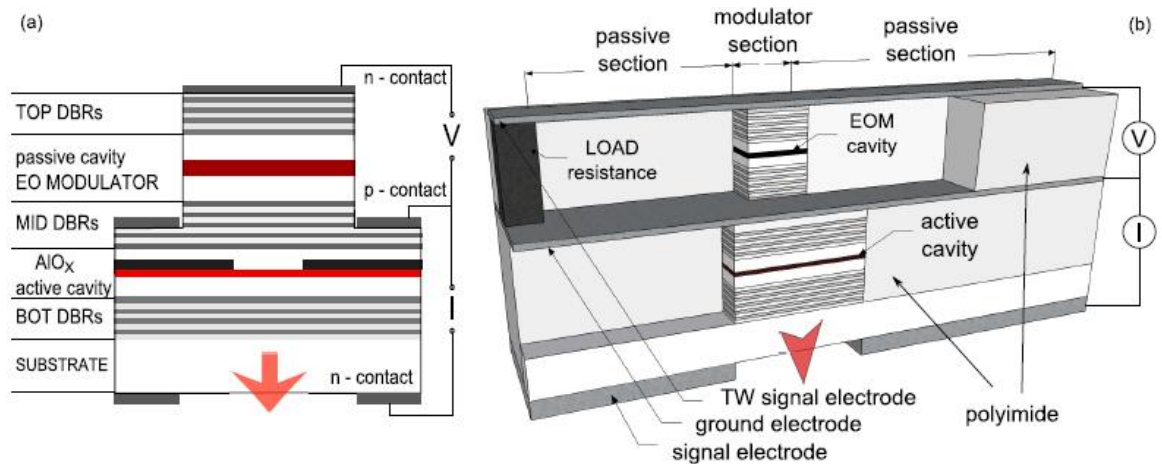


Figure 40: Scheme of a bottom emitting electrooptically modulated coupled-cavity VCSEL (EOM CC-VCSEL) (a) and 3D schematic view of three-section traveling wave electrode EOM CC-VCSEL (b). The top (bottom) cavity is independently driven by voltage (current) source [53]

Figure 40 shows the main npn bottom-emitting CC-VCSEL structure used in the compensated-parasitics travelling-wave scheme. As usual in the EO modulated design, it consists of two cavities: electro-optical modulator (EOM) and active cavities separated by the

middle DBR. It contains three DBRs: top, middle and bottom DBRs with 31, 28 and 25 pairs respectively. The middle DBR consists of two parts separated by a P current-spreading layers: 15 pairs above and 13 pairs below the contact layer.

The top cavity is connected to voltage source in the right side and load resistance in the left side. On the other side, the bottom cavity is connected to a current source to the right side. Whereas the EOM cavity is connected to traveling wave electrode (TW) electrode and is surrounded by two passive sections, the active cavity is connected to a normal signal electrode.

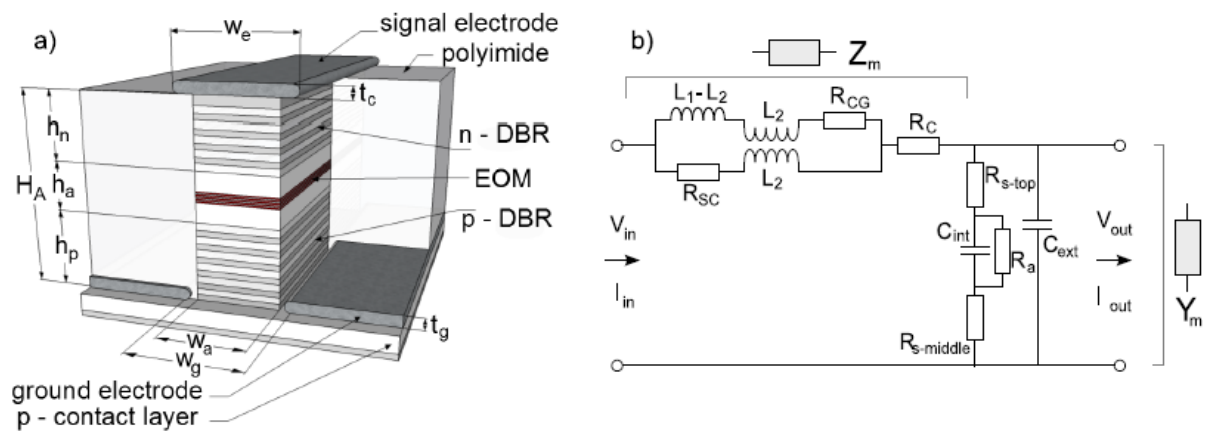


Figure 41: 3D scheme (a) and electrical equivalent circuit (b) of the active (modulating) section of the modulator cavity of the TW EOM CC-VCSEL [53]

In order to elaborate the equivalent circuit of EO modulated cavity, Figure 41 should be explained; it shows the top cavity and its electrical circuit. h_n , h_a and h_p are the lengths of the top DBR, the top modulator cavity and the 15 pairs of the middle DBR respectively and the total length is $H_A = h_n + h_a + h_p$. w_g is the ground electrode, w_a is the top cavity width, w_e is the micro stripe width and t_c and t_g are the micro stripe and the ground electrode thicknesses, respectively. The shape of the metal electrodes is elliptical as normally assumed and all calculations and parameters are taken from [56].

The electrical circuit is described in Figure 41 (b); where Z_m is the serial impedance which includes L_1 (the electrode inductance), L_2 (the inductive coupling between the substrate and

the ground electrode), R_{CG} (the ground metal loss), R_{SC} (the induced current in the substrate) and R_c (the loss dissipation in the conductor strip). Z_m is connected to R_{S-top} (the series resistance of the top and part of the middle DBR layers), Y_m (the parallel admittance), C_{int} (the intrinsic region capacitance) and C_{ext} (the strip capacitance).

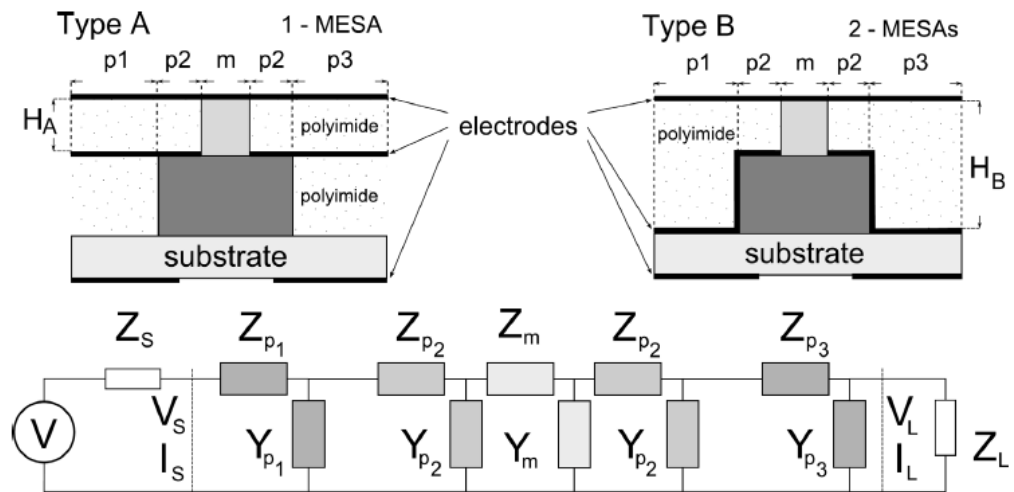


Figure 42: Schemes of the two types of TW EOM structures (top) and simplified equivalent circuit of the whole segmented TW-EO modulator (bottom) [53]

In order to calculate the electrical cut-off frequency (up to 330 GHz cut-off frequency), two structures of traveling wave EOM (type A and type B) are studied. Figure 42 shows a simplified electrical equivalent circuit of the whole segmented transmission line structure. These structures have two passive sections, the first one (p_1) is connected to a voltage source and the second one (p_3) is connected to a load resistance. The active modulator m and the passive section p_2 are located between p_1 and p_3 sections. The difference length between the radius of the active and passive cavities is called d_{p2} . For type A structure, the height of the top cavity (H_A) is equal to $H_A = h_n + h_a + h_p$ and the bottom cavity height (H_B) is equal to $H_B = H_A + H_{bottom\ mesa}$ for type B structure.

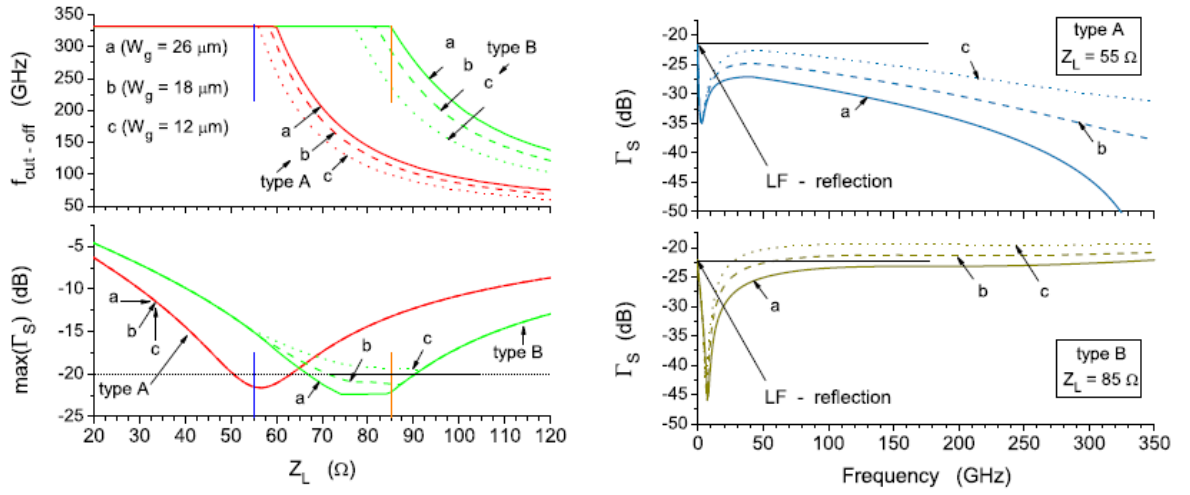


Figure 43: (left) Cut-off frequency $f_{\text{cut-off}}$ and maximum reflection $\max(\Gamma_S)$ as a function of load resistance Z_L for type A and type B TW electrode structures and for 3 different values of the ground slot width $W_g = 12, 18$ and 26 ; (right) Reflection Γ_S as a function of modulation frequency for type A and type B structures and for the 3 values of W_g [53]

Figure 43 shows that this novel design (type A and type B) proves that the electric parasitics are not a limitation on the modulation bandwidth and the cut-off frequency can go up to 330 GHz at 55Ω load resistance for type A structure and 85Ω load resistance for type B structure. Type A structure dB reflection can be less than -20 dB when the modulator cavity is 1λ long but the carrier extraction in this case can cause speed limitations. For type A and B, the speed limitations might be attributed to the carrier saturation velocity for 1.5λ long EOM cavity with $\eta_M = 77 - 89\%$ modulation efficiency. Experimentally, 52 GHz cut-off frequency has been found in the design based on electro-optic effect [11]. The result of this work allows us to disregard the electric parasitics in our modelling as discussed below, as it shows that they can be successfully overcome, so we could focus on intrinsic limitations.

2.5 In-plane external cavity and optically injected current-modulated laser

2.5.1 General considerations and theoretical work so far

Transverse coupled cavity VCSEL is a new design where the modulator mesa is manufactured to the lateral side of the VCSEL as shown in Figure 44 [57]. In a series of recent papers (e.g. [61] and [67]) it has been shown that because of the optical feedback effect, the chirp in this design can be reduced to 70% and the 3-dB-modulation bandwidth can be increased to 200% compared to the normal VCSEL. The detailed review is given below, but the qualitative explanation is that the presence of the external reflectance changes the nature of the relaxation oscillation process, which no longer involves just electron-photon resonance but also photon-photon resonance, the characteristic frequency of which is the inverse of the round-trip period of light in the external cavity. In addition, it was shown that the optical feedback effect can be seen as equivalent to an increase in the differential net gain, and as the relaxation oscillation frequency (and hence modulation cutoff) is proportional to the square root of the differential gain, this helps in creating high speed and low chirp transverse coupled cavity VCSELS. The relaxation oscillation frequency is not the only factor for determining the 3-dB modulation bandwidth which is below 20 GHz for normal VCSEL. Other important factors of modulation speed are parasitic capacitance and heating effect. The frequency of carrier-photon resonance (CPR) can increase the frequency of carrier-photon due to the detuned-loading effect [58]. Photon-photon resonance (PPR) can be enhanced and increased by the optical feedback due to the beating between different modes in coupled cavities [59] which can enhance the modulation bandwidth in small signal responses and high-speed operations. Optical feedback can also decrease the frequency chirp (phase noise) which increases the efficiency in transmitting data through long distance fibre optics.

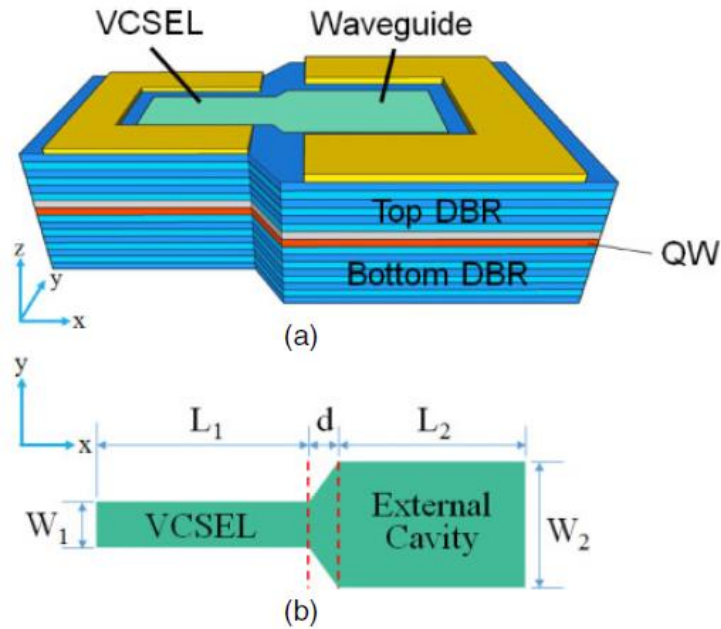


Figure 44: Schematic structure of the transverse coupled cavity VCSEL [57]

The proposed circuit in this design builds on an earlier bow-tie-shaped coupled cavity VCSEL whose 3dB bandwidth had been measured at 29 GHz. As shown in Figure 44, the transverse mode in the VCSEL can be created by the reflection at the conjunction between the VCSEL and the external cavity. The equivalent refractive is created when the transverse waves are reflected by the perfect mirror at the end of the external cavity.

The extension of the 3 dB cut off frequency is made by the few Pico seconds optical delay caused by the extended external cavity length by few μm . The chirp can be reduced by the detuned loading effect [58] at short delay index difference at the boundary creates this reflection which also can create an optical lateral confinement. This effect happens when a dispersive loss is created by the optical feedback. As a result, the frequency must be detuned away from the dispersive loss minimum which will increase the net gain since it is the gain minus loss. As mentioned before, the net gain will increase the modulation bandwidth as it is proportional to the relaxation oscillation frequency.

The following Lang-Kobayashi rate equations [60, 61] are used to model the transverse coupled cavity VCSEL. This model has some assumptions and limitations; for example, only small coupling strength and delay time can be dealt with in this model since it was assumed

that the optical feedback has only one round trip traveling path. The second assumption is that by controlling the current injection in the external cavity, the steady state feedback phase is also controlled.

$$\frac{dS(t)}{dt} = \left[\Gamma G(t) - \frac{1}{\tau_p} \right] S(t) + 2\kappa \cos\theta(t) \sqrt{S(t)S(t-\tau)} \quad (14)$$

$$\frac{d\varphi(t)}{dt} = \frac{\alpha}{2} \Gamma G_n - \kappa \sin\theta(t) \sqrt{\frac{S(t-\tau)}{S(t)}} \quad (15)$$

$$\frac{dN(t)}{dt} = \frac{\eta I}{qV} - \frac{N(t)}{\tau_s} - G(t)S(t) \quad (16)$$

Here, $S(t)$ is the photon density, $N(t)$ is the carrier density, Γ is the confinement factor, τ_p is the photon lifetime, κ is the coupling strength, α is the linewidth enhancement factor, $\varphi(t)$ is the temporal phase change, $\theta(t)$ is the feedback phase. The authors did not present a definition of this parameter, but comparing their notations with those of the original paper by Lang and Kobayashi [60], it can be recovered that:

$$\theta(t) = \varphi(t) - \varphi(t-\tau) - \varphi_\kappa$$

Where φ_κ is the argument (phase) of the complex coupling coefficient ($\kappa \exp(j\varphi_\kappa)$) determined by the subwavelength variations in the position of the external reflector.

The phase $\theta(t)$ was then, in general, a variable, with its steady state determined by the reflectance phase, reflectance strength, and the linewidth enhancement factor.

Furthermore, G_n is the net gain, I is the injection current, η is the current injection efficiency, V is the volume of the active region, τ_s is the carrier lifetime, τ is the one-round trip delay time

in the external cavity and $G(t)$ is the nonlinear material gain, which is determined from a two-parameter logarithmic approximation:

$$G(t) = \frac{v_g g}{1 + \varepsilon S(t)} \ln \left[\frac{N(t) + N_s}{N_{tr} + N_s} \right] \quad (17)$$

v_g : the group velocity in the vertical direction.

G : the material gain coefficient.

ε : the nonlinear gain coefficient.

N_s : the carrier density reduction.

N_{tr} : the transparent carrier density.

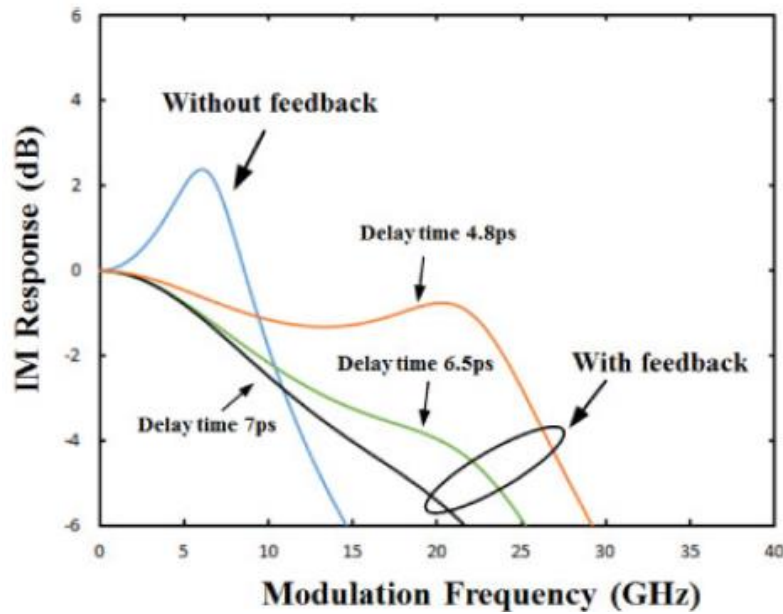


Figure 45: IM response of conventional VCSEL (blue line) and coupled cavity VCSEL at the same coupling strength, feedback phase and different delay time [57]

Figure 45 shows the small signal response as a function of modulation frequency for different delay times. The steady state feedback phase is fixed for these curves (1.08π) and the coupling strength k (radiated power per unit time) is fixed too ($\kappa = 1.5 \times 10^{11} \text{ s}^{-1}$). As shown in the figure, the modulation bandwidth is only 10 GHz without optical feedback. On the other hand, the modulation bandwidth can get up to 29 GHz when the delay time of 4.8 ps exists

which happens when the external cavity length is $4.8 \mu\text{m}$ and the group refractive index in the lateral direction is 150. When the delay time is longer (e.g. 7 ps), the modulation frequency (e.g. 14 GHz) is shorter.

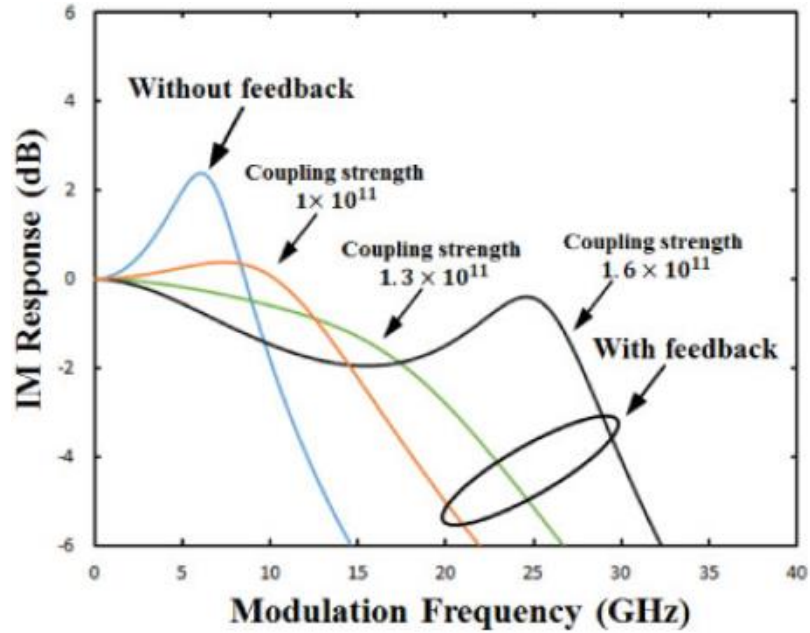


Figure 46: IM response of conventional VCSEL (blue line) and coupled cavity VCSEL at the same delay time, feedback phase and different coupling strength [57]

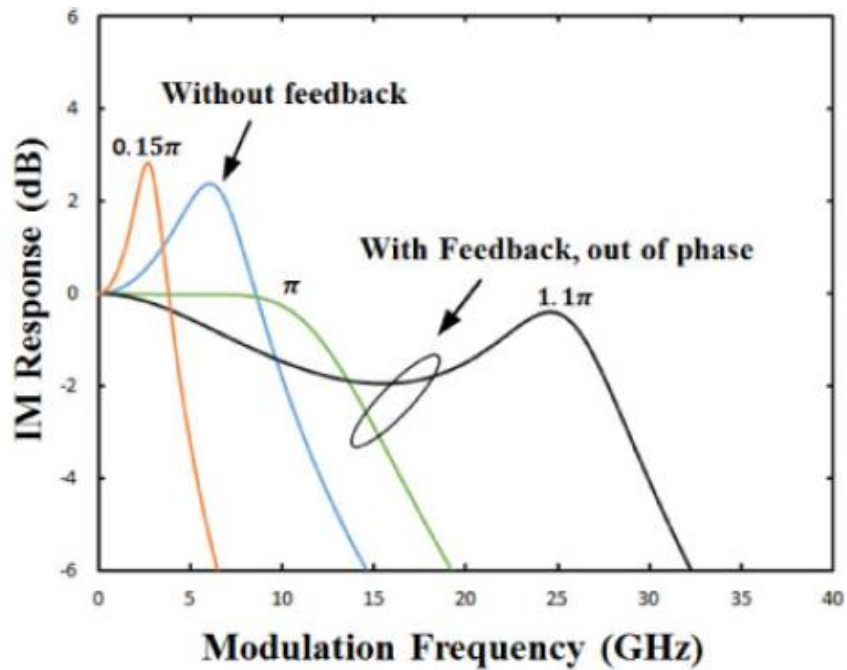


Figure 47: Phase tolerance of the modulation bandwidth enhancement [57]

Figure 46 shows the small signal response as a function of modulation frequency for different coupling strengths and at a fixed delay time of 4.7 ps and a steady state feedback phase of 1.1π . As shown in the figure, when the coupling strengths are increased, the 3-dB modulation bandwidths are increased too.

Figure 47 shows the intensity modulation response as a function of modulation frequency for different optical feedback phase. For the in- phase case (the phase angle is 0.15π which is very close to zero), the bandwidth is reduced. However, for the out- phase- case, when the phase is π , the modulation cutoff frequency is increased, and the laser has a flat response similar to that of an over-damped oscillator at moderate frequencies. By small detuning, a maximum modulation bandwidth is achieved with a feedback phase of 1.1π .

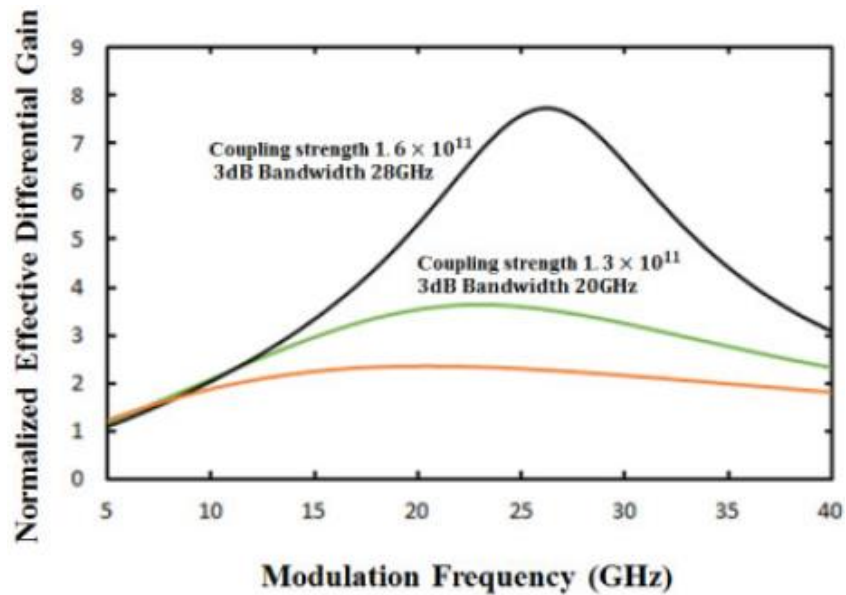


Figure 48: Calculated normalized effective differential net gain a function of modulation frequency [57]

The authors quantified their results using the concept of effective net differential gain determined as [57]:

$$g_{effective} = \frac{dG_n}{dN(t)} = \frac{d \frac{dS(t)}{dt}}{SdN(t)}$$

Here S is the steady state photon density; this parameter ($g_{effective}$) is increased in presence of feedback, and a corresponding increase in the modulation bandwidth is gained as shown in Figure 48. This is because the bandwidth is proportional to the square root of the differential net gain.

The linewidth enhancement factor α in a standard laser design is given by Equation (18):

$$\alpha = -\frac{4\pi \, dn/dN}{\lambda \, dg/dN} \quad (18)$$

Where the differential gain and the refractive index are represented by (dg/dN) and n respectively. As is known, [23], the linewidth enhancement factor quantifies the chirp in a laser structure. With this in mind, the equation above shows that when the effective differential gain is increased, the chirp can be decreased. Using the logic, the authors of [57] introduced an *effective linewidth enhancement factor* for their structure, which is not given by Equation (18) (except for a solitary laser with no feedback: $\kappa=0$) and is a function of modulation frequency, but still quantifies the chirp.

In order to numerically calculate the effective linewidth enhancement factor, the frequency-modulation- intensity-modulation (FM-IM) ratio can be used to derive the analytical expression and to calculate chirp reduction [62]. The FM-IM ratio or the chirp-power ratio (CPR) for a solitary laser can be expressed as [63, 64]:

$$CPR_{In \, a \, solitary \, laser} = \frac{v \, dn/dN \, 2\pi F_m}{n \, dg/dN \, \Gamma P}$$

Where (v) is optical frequency, (F_m) is modulation frequency, (Γ) is mode confinement factor and (P) is power.

From Equation (18), the linewidth enhancement factor α in a standard laser design is:

$$\alpha = \frac{4\pi \, dn/dN}{\lambda \, dg/dN}$$

$$\alpha = \frac{4\pi v \, dn/dN}{c \, dg/dN}$$

$$CPR_{In \, a \, solitary \, laser} = \frac{c}{2n} \alpha \frac{F_m}{\Gamma P}$$

So presumably, by the effective linewidth enhancement factor, the authors of [57] mean the following quantity:

$$\alpha_{eff} = \frac{2n\Gamma P}{cF_m} CPR$$

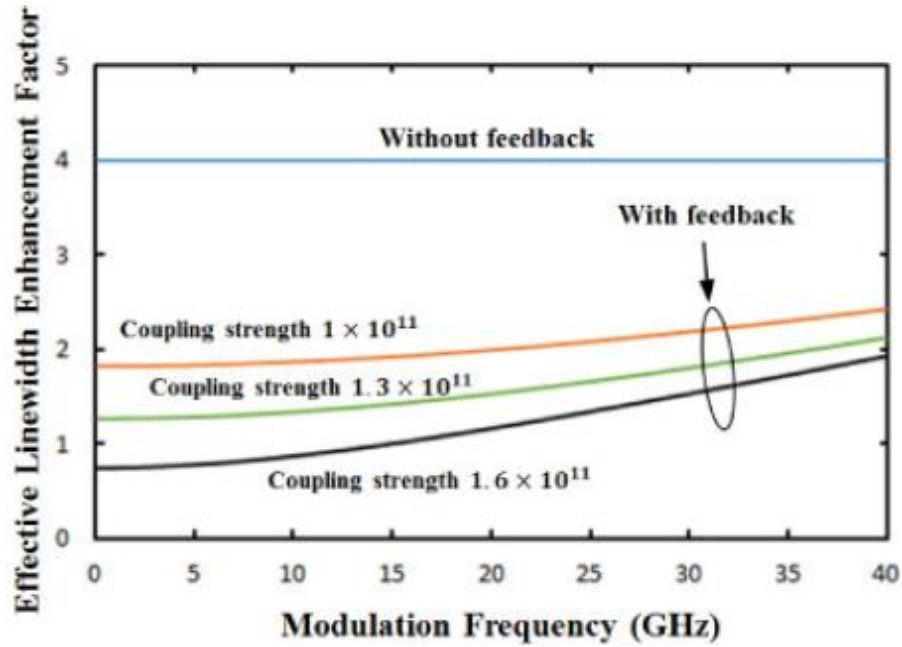


Figure 49: Simulation results of frequency chirp as a function of modulation frequency under different coupling strength [57]

Figure 49 shows the effective linewidth enhancement factor as a function of modulation frequency for different coupling lengths (using the same parameters of Figure 46). The linewidth enhancement factor is 4 without feedback and there is a reduction in chirp when the coupling strength is increased because of the increase in effective differential gain as expressed in Equation (18). However, when the modulation frequency is less than 10 GHz, the effective linewidth enhancement factor can be less than one when coupling strength $\kappa = 1.6 \times 10^{11} \text{ s}^{-1}$ (same as normal electro-absorption modulators).

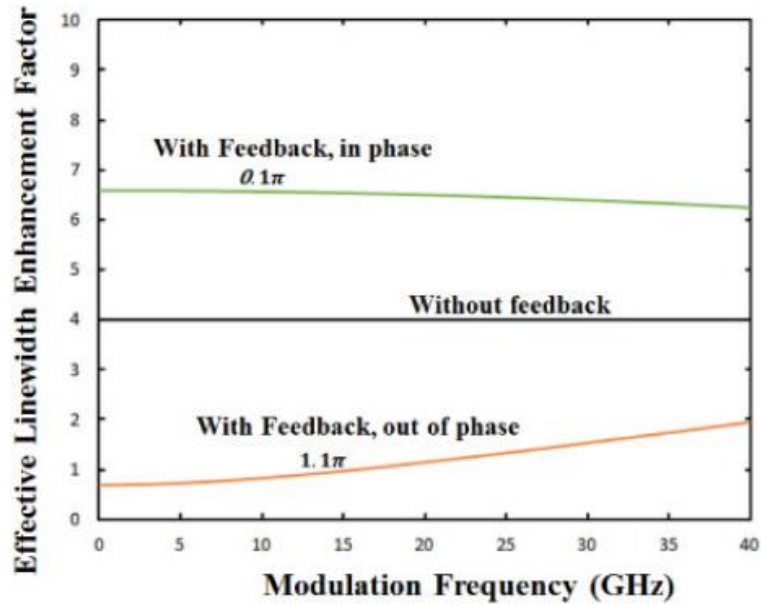


Figure 50: Phase tolerance of chirp reduction as a function of modulation frequency with a coupling strength of $1.6 \times 10^{11} \text{ s}^{-1}$ [57]

Figure 50 shows the effective linewidth enhancement factor as a function of modulation frequency for different phase angles (frequency chirps) and for a fixed coupling strength ($1.6 \times 10^{11} \text{ s}^{-1}$). The figure shows that for the case of the in- phase, the frequency chirp is increased with a very small feedback phase (about 0) and with a high effective linewidth enhancement factor. For the out- phase case, on the other hand, the bandwidth can be increased and the chirp can be reduced when the effective linewidth enhancement factor is less than one.

The simulations performed using the model described above imply that such VCSELs with a lateral external cavity or transverse coupled cavity VCSEL's are able to produce a very good bandwidth enhancement and a chirp reduction which can be used for future high-speed long- and medium-haul networks. It has to be pointed out however that the analysis performed in [57, 65, 66] has a certain internal contradiction and so has to be treated with some caution. Namely Lang-Kobayashi equations, containing a single delay term proportional to the external reflector amplitude reflectance, are derived for the conditions of *weak feedback*, - approximately corresponding to the condition $\kappa \ll 1/\tau_p$, whereas in the numerical analysis conducted in the papers, this condition is not satisfied.

The same team later tried to resolve the contradiction, by implementing a model containing multiple reflections in the external cavity, with multiple delays [67].

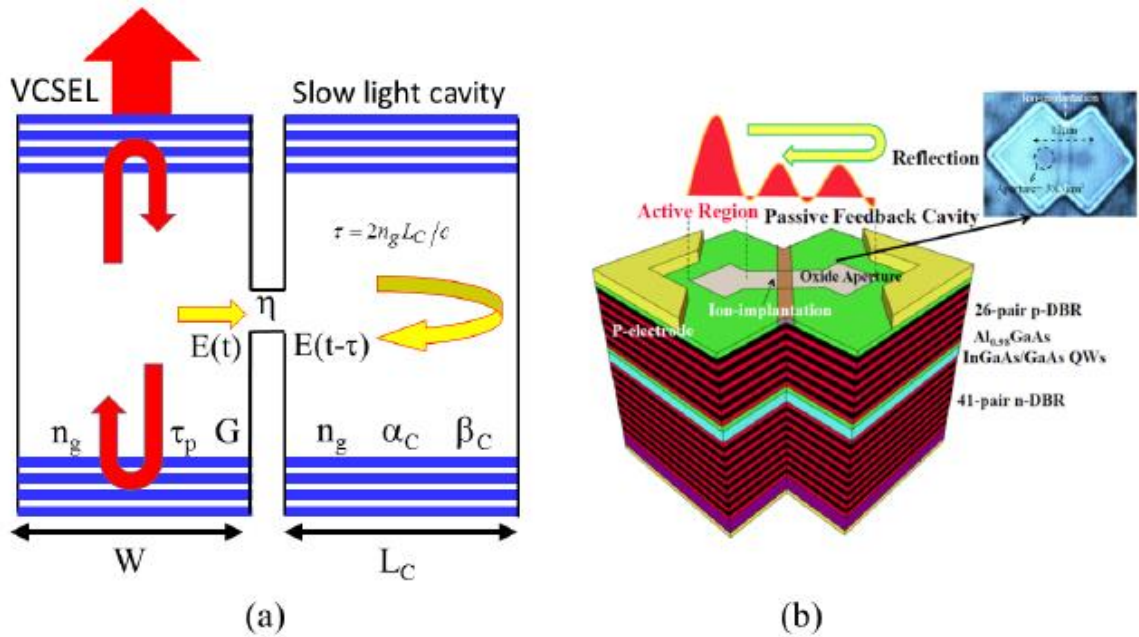


Figure 51: Scheme of (a) slow-light feedback in TCC-VCSEL, and (b) structure of a fabricated [67]

Figure 51 (a) shows the scheme of the main structure of the TCC-VCSEL and (b) shows the fabricated structure [68]. The external cavity is located to the lateral side of the VCSEL and some of the light generated in the VCSEL cavity is leaked to the lateral direction through an oxide aperture between the two cavities. According to [61], light is leaked in the lateral direction at an angle of 90° which causes slow light leaked in the external cavity. This slow light will travel through waveguide of the external cavity of length L_c and will be reflected back at the right side of the external cavity and continues to travel round trips in the same cavity with (τ) period. Where $\tau = 2n_g L_c / c$, $n_g = fn$ is the group index, c is speed of light in vacuum, n is the average material refractive index and f is the slow factor of light which can reach values of 30 to 50 according to [61]. In the external waveguide, the light will experience $e^{-2\alpha_c L_c}$ loss and $e^{-2j\beta_c L_c}$ phase delay at each round trip. Where $\alpha_c = f\alpha_m$ is lateral optical loss, α_m is the material loss, $\beta_c = 2\pi n / (\lambda f)$ is propagation constant, λ is the emission wavelength and η is the coupling ratio at which the light is injected back to the VCSEL.

In order to model the above design, rate equations for edge emitting laser with lateral optical feedback (OFB) are used as in [65]. The following rate equations must be time delayed due to the OFB which means that the electric field $E(t)$ should have a time delay parameter for each round trip:

$$\frac{dN}{dt} = \frac{\eta_i}{e} I - \frac{N}{\tau_s} - GS \quad (19)$$

$$\frac{dS}{dt} = \left[\Gamma G - \frac{1}{\tau_p} + \frac{v_g}{W} \ln|U| \right] S + \Gamma V R_{sp} \quad (20)$$

$$\frac{d\theta}{dt} = \frac{1}{2} \left(\alpha \Gamma \frac{a}{V} (N - N_{th}) - \frac{c}{n_g W} \phi \right) \quad (21)$$

Where $N(t)$ is the electron number, $S(t)$ is the photon number, $\theta(t)$, is the optical phase $\theta(t)$, G is the optical gain and is giving by the gain suppression [69] described in Equation (22):

$$G = \frac{a}{V} (N - N_T) (1 - \varepsilon S) \quad (22)$$

where a is the differential gain in the active region, V is the volume, N_T is the electron numbers at transparency, ε is the gain suppression coefficient, Γ is the confinement factor, τ_p is the photon lifetime, η_i is the injection efficiency, τ_s is the spontaneous emission electron lifetime, N_{th} is the electron number at threshold and the time-delay function $U(t-\tau)$ is giving by Equation (23):

$$U = 1 + \frac{\eta}{1-\eta} \sum_p \sqrt{1-\eta^p} e^{-2p\alpha_c L_c} e^{-j2p\beta_c L_c} \sqrt{\frac{S(t-p\tau)}{S(t)}} e^{j\theta(t-p\tau)-j\theta(t)} \quad (23)$$

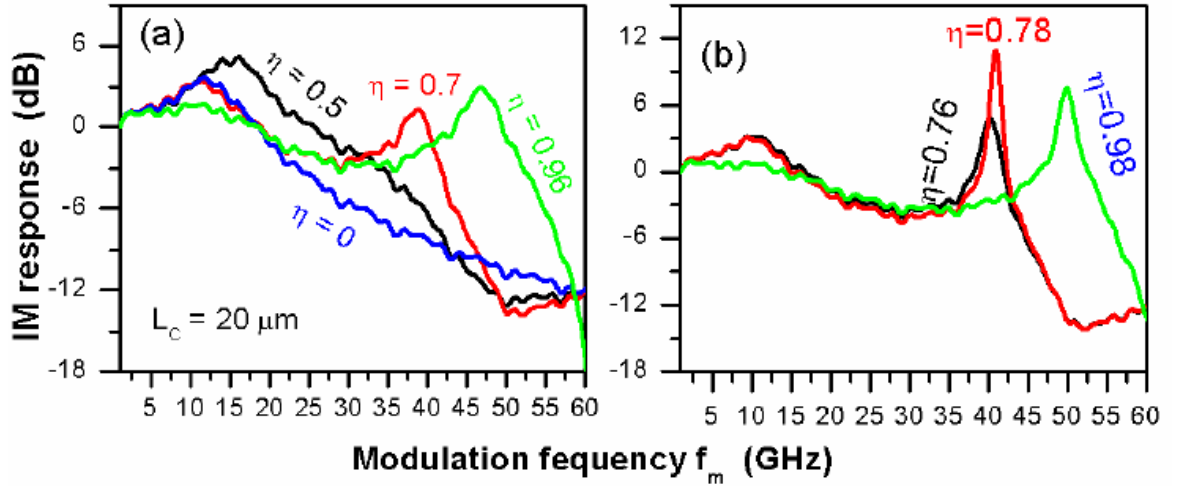


Figure 52: IM responses when $L_c = 20 \mu\text{m}$ under different values of η : (a) with CPR, and (b) with PPR. The IM response of the solitary VCSEL ($\eta = 0$) is also plotted for comparison [67]

Figure 52 shows the main results of this model considering the time delay and loss in the external cavity for each round trip. This figure shows that when the coupling ratio ($\eta=0$) in the case of normal VCSEL is without feedback, the bandwidth is 23.5 GHz and the carrier photon resonance (CPR) peak is at 12 GHz. However, when we compare these values with the others for transverse coupled cavity (TCC) VCSEL and for the case for the coupling ratio ($\eta=0.5$), for example, the bandwidth increased to 33.5 GHz and the carrier photon resonance (CPR) peak is at 16 GHz. Moreover, when $\eta=0.7$, the bandwidth becomes 42GHz which is equal to 79% more than the case without feedback and this percentage is much higher than the one expected in [61] which was only 60%.

Moreover, it can be seen that when the coupling ratio is ($\eta=0.7$), the peak for carrier photon resonance (CPR) is higher than the peak for photon-photon resonance (PPR) as in Figure 52 (a). On the other hand, when there is a small change in the coupling ratio (η from 0.7 to 0.78), the peak for photon-photon resonance (PPR) is higher than the peak for carrier photon resonance (CPR) as in Figure 52 (b). More details for the PPR effect can be found in [70-75]. These graphs were plotted for $L_c=20 \mu\text{m}$, 0.01 modulation index (m), $8 \mu\text{m}^2$ oxide aperture

and 2 mA bias current. This $8 \mu\text{m}^2$ oxide aperture is small but for the larger oxide apertures, the bandwidth can go up to 20 GHz [76].

The results above, while still encouraging, are very different from those of earlier work [57, 65, 66]. Namely, instead of a single modulation peak, shifted to higher frequencies, as in the single-pass model [57, 65, 66], the multiple-pass model predicted *two* peaks: one at the usual electron-photon relaxation frequency and the other in the microwave band, near (or at least of the same order as) the round-trip time of the external cavity (the cavity was longer than that used in the single-pass model work so the peak was at around 100 GHz). The relaxation oscillation peak could be either slightly shifted to higher frequencies or lower frequencies depending on feedback strength, as in the single-pass model (though the shift is not as significant as in early work), but the main improvement to the modulation properties came from the appearance of the second peak.

The authors presented their rate equation model without derivation, and so some uncertainty remains about its accuracy and applicability limits, and at this time there appears to be no experimental work to directly confirm the results.

2.5.2 Experimental results

In the paper of 2015 and by Xiaodong and co-authors, a transverse coupled cavity vertical cavity surface-emitting laser was experimentally demonstrated for the first time at 850 nm wavelength and 30 GHz bandwidth [77]. A three dimensional schematic of their device and a real image of their fabricated design are shown in Figure 53 and Figure 54, respectively.

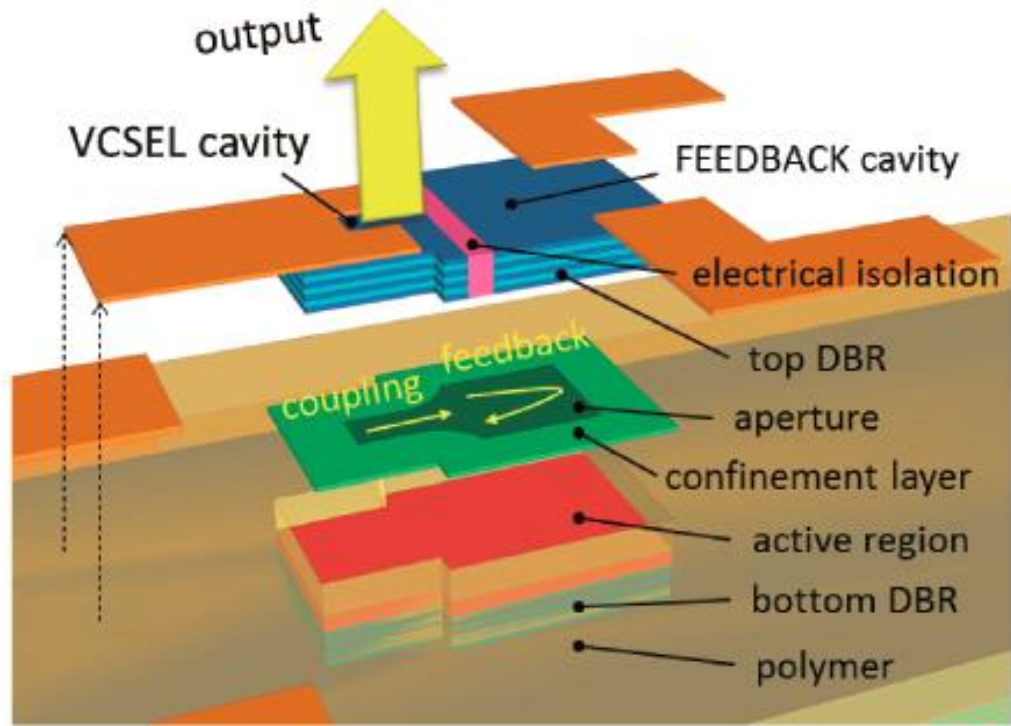


Figure 53: Schematic view of the 850-nm-band transverse cavity surface emitting laser [77]

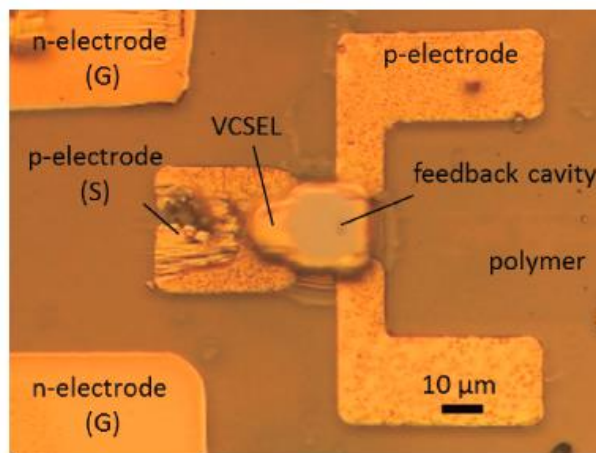


Figure 54: Top view of one fabricated device, with a mesa footprint of only $14 \times 24 \mu\text{m}^2$ [77]

The size of the VCSEL mesa size is $10 \times 14 \mu\text{m}^2$ and it is $20 \times 24 \mu\text{m}^2$ for the feedback cavity. Moreover, the width of the side oxidation and the width of electrical isolation for proton implantation are $5 \mu\text{m}$ and $3 \mu\text{m}$, respectively. The modulation can be done by pumping on the ground-signal-ground electrode using radio frequency probes.

Figure 55 shows the small signals modulation for the main design when the VCSEL is having a feedback and it has no feedback and with/without calibration response. It shows that the increase in bandwidth is three times more than the one without feedback which is the highest bandwidth reported so far (< 30 GHz). The receiver response limit can be equalized using this structure by connecting the external cavity to a current bias source as illustrated in the red line in Figure 55.

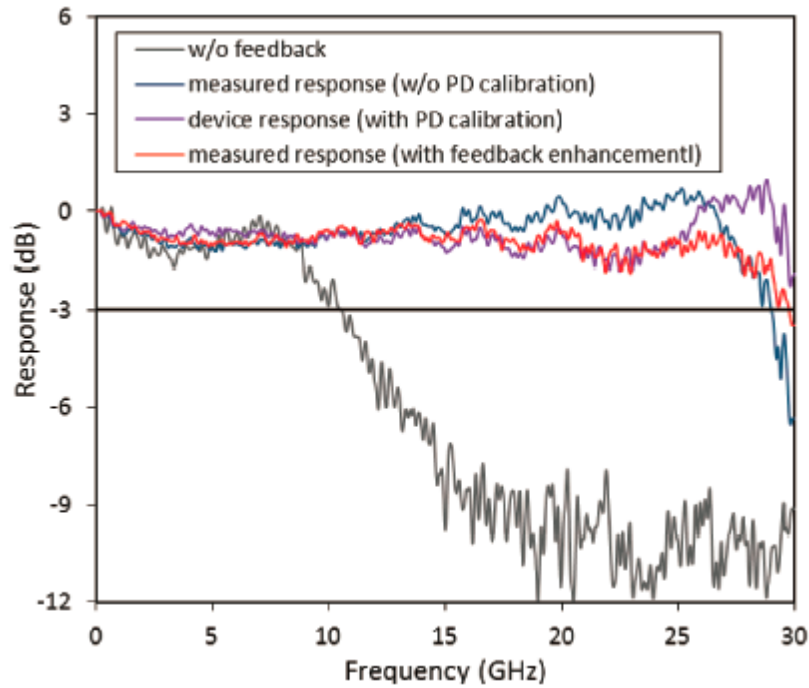


Figure 55: Small-signal frequency responses of the device for different cases. Feedback is enhanced by injecting a 0.3 mA current to the feedback cavity [77]

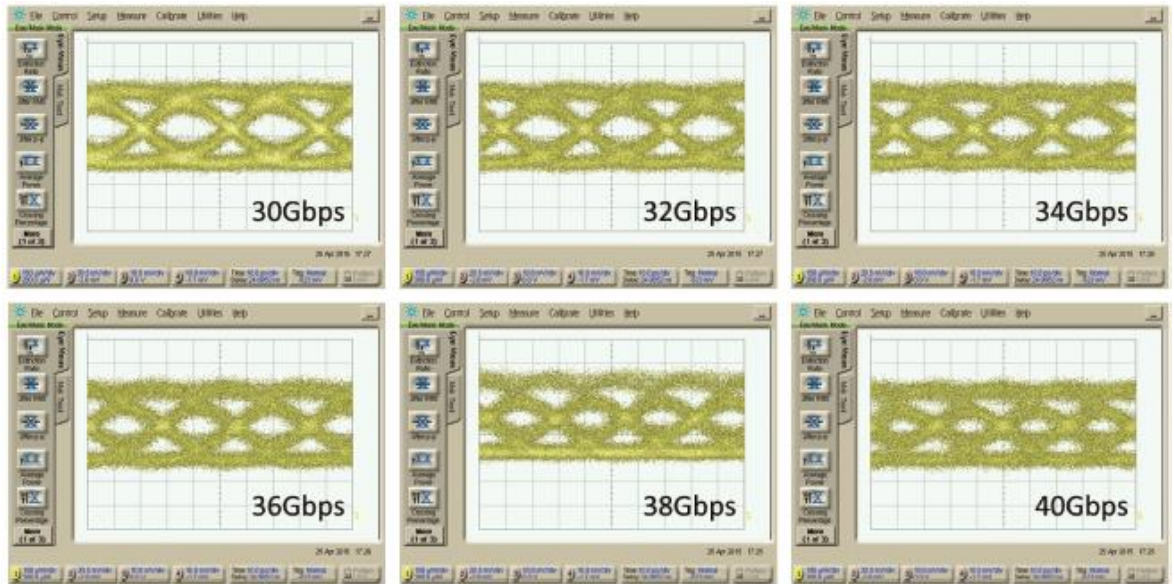


Figure 56: Measured large-signal response with data rate of 30 to 40 Gbps (NRZ, PRBS $2^{31} - 1$, $V_{pp} = 500$ mV). VCSEL current is 6.2mA with a passive feedback cavity. The isolation width is $3 \mu\text{m}$. Extinction ratios are ~ 3.8 dB for all data rates [77]

The large signal modulation can also be seen in Figure 56 in a form of eye diagrams for non-return-to-zero (NRZ), pseudo-random binary sequences (PRBS), $2^{31} - 1$ word length, 500 mV peak to peak, 6.2 mA bias current and ~ 3.8 dB extinction ratio for all bitrates. While Figure 56 shows not very clear eye diagrams at higher bitrates, it illustrates opens eyes for all bitrates (30 -40 Gbps). The reason of having not very clear eye diagram from higher bitrates is the noise associated with light fluctuations in fibre optics cables causing unstable modes [78].

2.5.3 VCSELs with external optical injection

VCSELs with external optical injection have many advantages for both fundamental and applied researches [79-87]. For example, optical injection can be used to speed up modulation, to narrow lasing spectrum and to reduce frequency chirp [79, 80, 88]. Under certain conditions, VCSELs, and in general, semiconductor lasers can practice nonlinear dynamics, such as chaos, one, two and quasi-periods [85-87, 89-93]. These nonlinear dynamics have many applications, including coding, security networks and the generation of

physical random number. Moreover, the TE and TM polarizations modes for edge-emitting semiconductor lasers and the X and Y polarization modes for VCSELS can be improved using optical injections as in [94].

To overcome the current limitations in 3dB cutoff bandwidth in optical transmission, non-return-to-zero (NRZ) and four-level pulse amplitude modulation (PAM4) are used. This can be done by combining two NRZ signals using PRBS pattern generator and forming a PAM4 signal whose bandwidth is double than the bandwidth of the NRZ signal [95-99]. One example of utilizing this principle was done Hai-Han Lu and co-authors when they were able, for the first time, to use optical injection to speed up modulation using a 64 Gb/s PAM4 VCSEL-based free-space optical (FSO) link.

Figure 57 shows their main circuit design for the 64 Gb/s PAM4 VCSEL-based FSO experimental configuration. PRBS pattern generator can produce two binary NRZ signals, 32 Gb/s, 900 and 450 mV amplitude, which then are combined into a PAM4 converter. This PAM4 converter can then add these NRZ binary signals and produce a 64 Gb/s signal. The optical injection to the VCSEL can be done by the distributed feedback (DFB) laser through a three-port optical circulator (OC). The erbium-doped fiber amplifier (EDFA) will amplify the PAM4 signal which then is attenuated by an optical attenuator (VOA). After that the signal is converted to a free-space light signal through a free space link and a pair of doublet lenses which are connected to an optical fibre which is connected to a photodiode (PD) to convert the light signal into a PAM4 signal again. At the receiver side, the digital storage oscilloscope (DSO) is used to show and analyse eye diagrams of the PAM4 signal and to process the BER, synchronization, equalization, and hard decision.

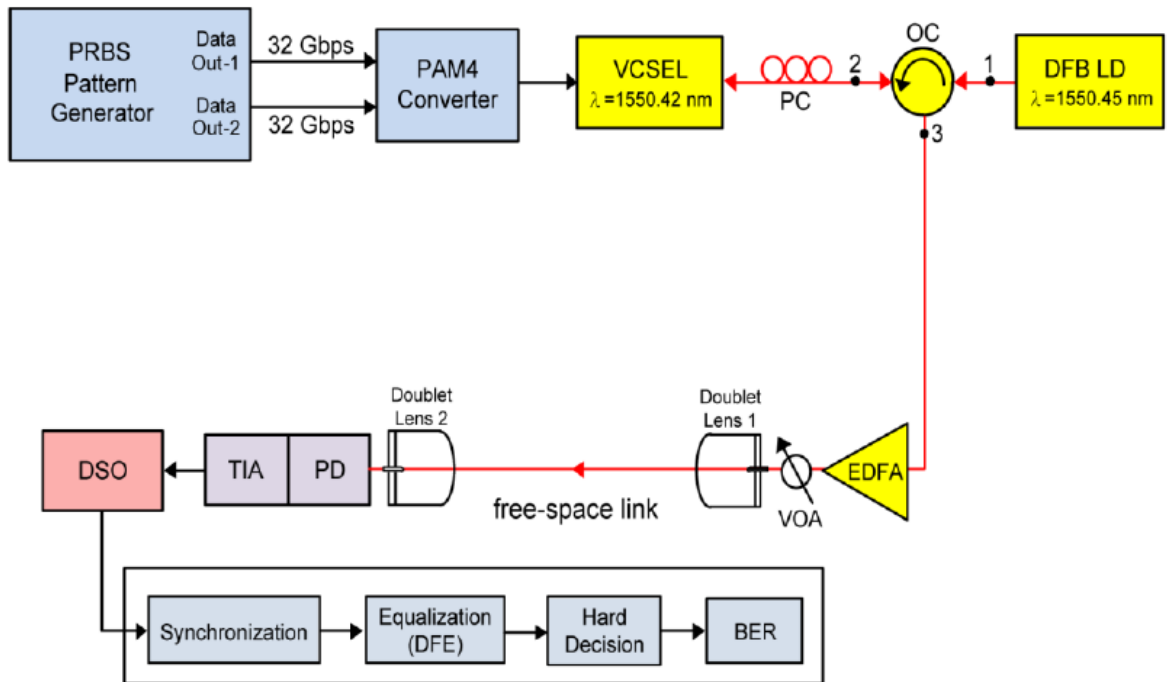


Figure 57: The experimental configuration of the proposed 64 Gb/s PAM4 VCSEL-based FSO links with an external light injection scheme [100]

Figure 58 shows how the optical injection to VCSEL has improved the bandwidth for the PAM4 signal from 11.2 GHz in the case of free running to 22.8 GHz in the case of optical injection. If we divide 22.8 GHz by 11.2 GHz, this gives us more than 2 times increase in the bandwidth but it should be noticed that 22.8 GHz PAM4 signal is equal to 64 Gb/s ($22.8 \times \sqrt{2} \times 2 = 64.5 > 64$).

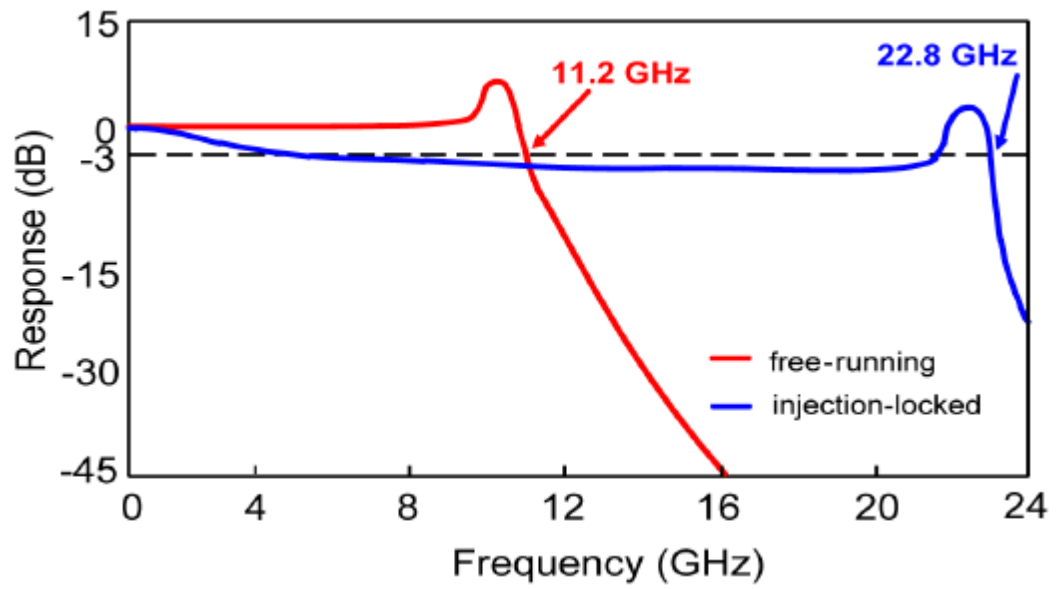


Figure 58: The frequency responses of the PAM4 VCSEL-based FSO links for the scenarios of free-running and injection-locked [100]

3. THEORETICAL ANALYSIS OF COMPOUND CAVITY ELECTROOPTICALLY MODULATED LASERS. GENERAL CONSIDERATIONS AND STANDARD RATE EQUATION MODELLING

3.1 General considerations

As discussed in the Literature review, electrooptically modulated compound-cavity lasers are among the main contenders for ultrafast modulation, but some questions concerning their physics and performance remain not answered. The purposes of the work covered in this design was therefore to:

- 1) Analyse the theoretical limits of the electrooptic modulation of compound-cavity lasers considered in Section [2.4].
- 2) To investigate their performance as regards chirp and its physical origins, and:
- 3) To come up with some recommendations concerning the laser design for high frequency modulation (e.g. number of periods in different reflectors).

The analysis starts with continuing the work started in the paper by Avrutin et al. 1993 [7] on simple rate equation analysis (Sections [2.4.1]) . We found however that, while giving some insight into the laser performance, the model is not really capable of analysing the laser performance completely, as will be discussed below.

3.2 The model

Figure 59 shows the schematic of a Compound Cavity Laser which we used in our analysis. The laser is formed by two sub-cavities.

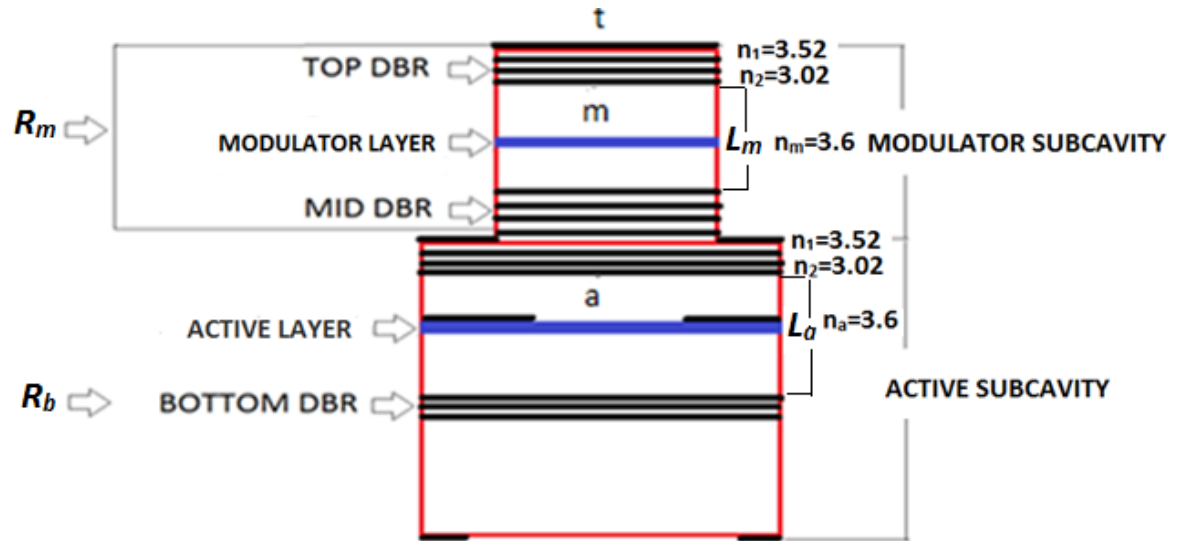


Figure 59: Schematic of a Compound Cavity Laser

The top, modulator, sub-cavity is a passive Fabry-Perot resonator whose reflectivity $R_m(t)$ is modulated via electro-optically varying the optical properties of a modulator layer contained within the sub-cavity by applying time-varying reverse bias voltage. In a typical design, the intermediate DBR has 25-35 periods of two layers of alternating composition, the top DBR consists of 15-25 periods; the resonator thus can be substantially asymmetric. As has been mentioned in the literature, the relatively low Q-factor modulator helps confine efficient light coupling and low chirp [12]. The bottom sub-cavity is the active one, containing the electrically pumped active layer and terminated by the bottom DBR whose reflectivity is assumed to be very large (about 0.999). Three electric contacts are used in our device to have a good control when changing the current in the active cavity and the reverse bias voltage for the modulator cavity as shown in Figure 59.

Throughout the analysis, we consider only refractive index modulation (no absorption modulation). Indeed, according to [14], the electrorefraction effect [45] plays a dominant role

in modulating $R_m(t)$ as compared to electroabsorption. This fact is illustrated in Figure 60 and Figure 61. Figure 60 shows the calculated reflectivity versus incident light wavelength for the EO modulator and Figure 61 shows the calculated reflectivity versus incident light wavelength for the EO modulator with and without absorption. The dash blue line represents the reflectivity R_1 without absorption and the solid green line represents the reflectivity R_1 with absorption. The two graphs are very similar which indicates that electrorefraction effect plays a dominant role in modulating $R_m(t)$ as compared to electroabsorption. However, the only difference appears in the notch which is deep and narrow when there is absorption and shallow and wide when there is no absorption. This result matches the same result by previous authors mentioned in section 2.3.2 as in Figure 20.

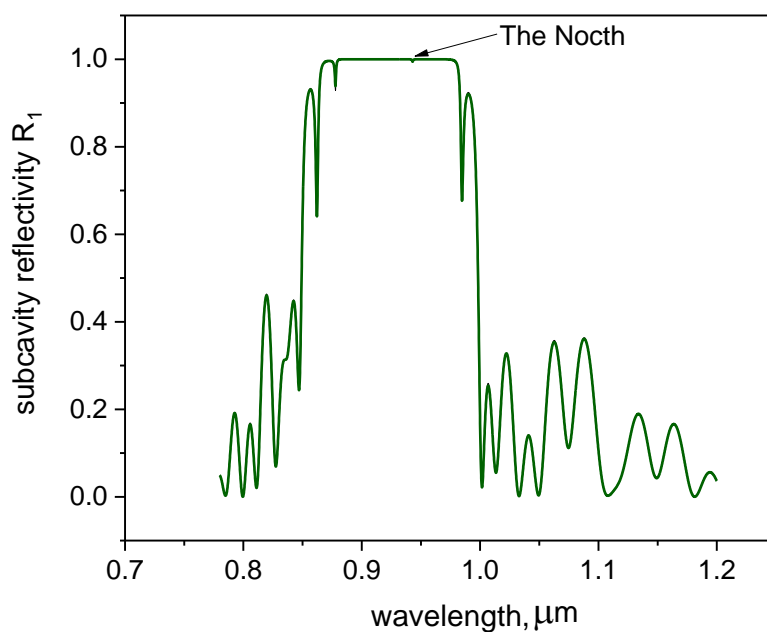


Figure 60: Calculated Reflectivity versus incident light wavelength for the EO modulator cavity

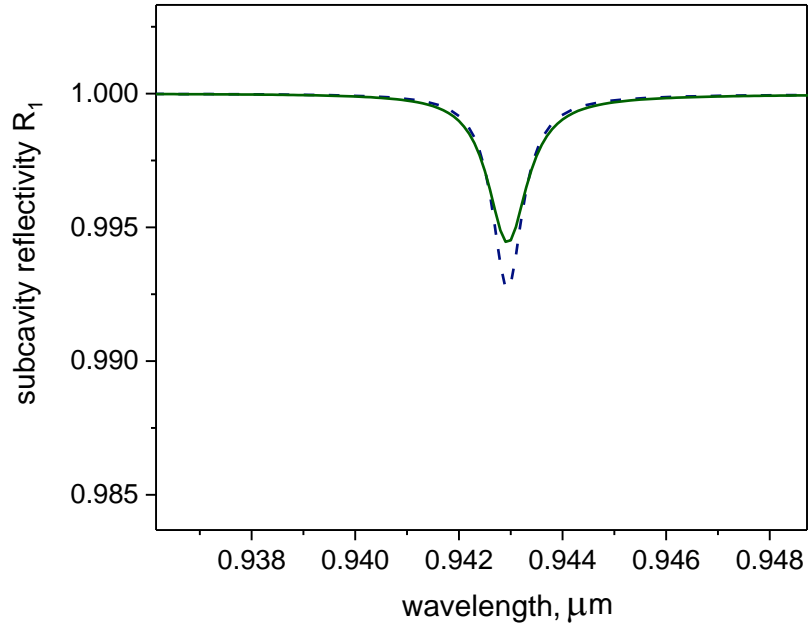


Figure 61: The notch in Figure 60 : With absorption (solid green) without absorption (blue dash)

Another noticeable difference between the normal VCSEL and our compound VCSEL is the transfer function damping parameter value. In the “off” state, the compound cavity VCSEL has a very high top reflector reflectance, meaning a long photon lifetime, which means low damping. Figure 62 and Figure 63 show the comparison between normal VCSEL and compound cavity VCSEL in regarding their damping parameter. The damping for the compound cavity VCSEL is much smaller than the damping level for the normal VCSEL.

$$\tau_{phout}^{-1}(t) = \frac{v_g}{2 * L} \ln \frac{1}{R_b R_m(t)} \approx \frac{v_g}{2 * L_a} (T_b + T_m) = \frac{0.8 \times 10^{10} \times 10^{-3}}{2 \times 10^{-4}} = 4 \times 10^9 s^{-1} \quad (24)$$

$\tau_{phout} = 25 \text{ ps}$

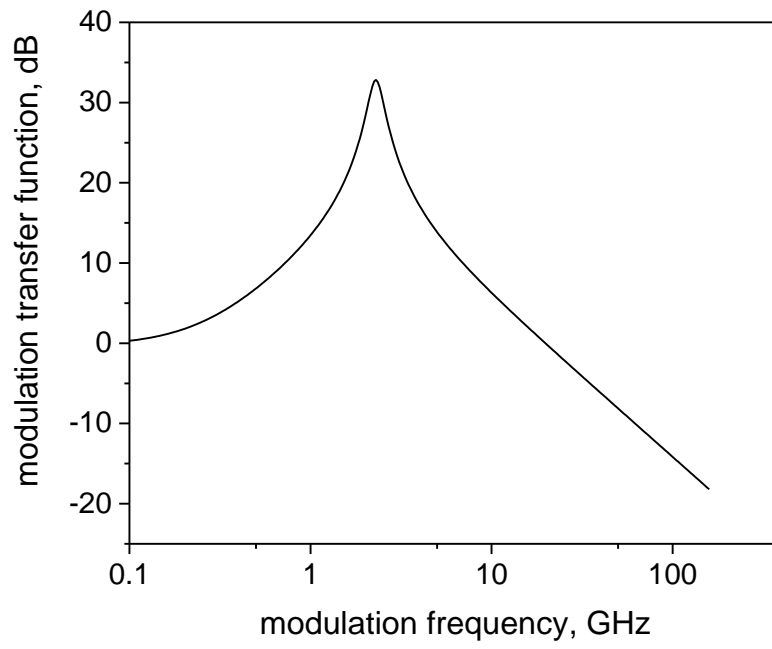


Figure 62: a simulated small-signal modulation curve for a normal VCSEL, photon lifetime is 2 ps

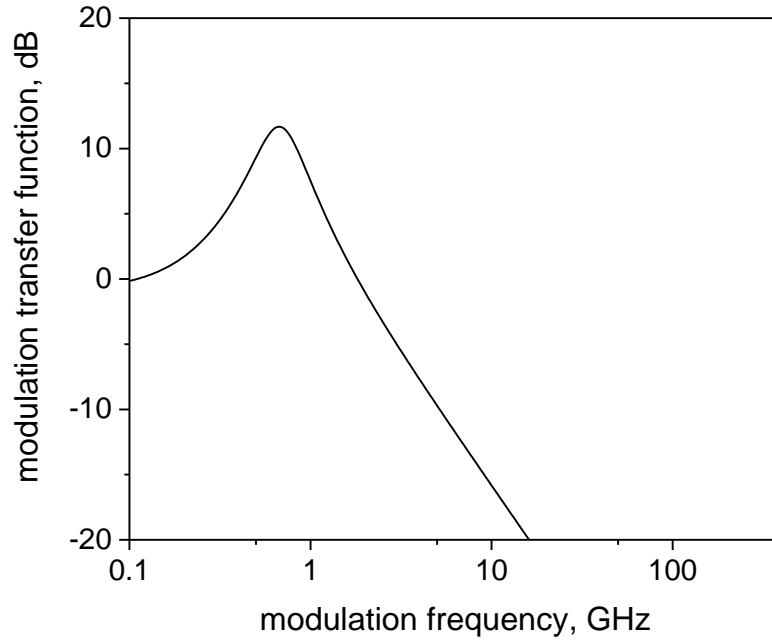


Figure 63: a simulated small-signal modulation curve for a compound VCSEL, photon lifetime is 25 ps

In a realistic design (see e.g. [14]), the mesas containing the two subcavities have different lateral diameters; however, as in previous analysis, we use a purely one-dimensional approach, which is justified because the diameter of the active part of the laser is determined by the current aperture and is thus smaller than the mesa diameter. In this design, we assumed the length confinement factor of 0.0209 and the enhancement factor due to the standing wave pattern of 1.83. As a result, the overall confinement factor in the active subcavity is assumed to be $0.0209 \times 1.83 = 0.0382$, as in [23, 101, 102].

3.3 The formulation of the model

First, I present the analysis using the standard rate equation model. This work was published in [15] and later expanded in [103]. Within the standard rate equation model, the effect of the modulator cavity is represented essentially as photon lifetime modulation. The importance of photon lifetime is known both for “standard” current modulation [6], [39] and for advanced modulation schemes. Small-signal modulation analysis was presented in [7] and large-signal modulation in [14], specifically with the compound cavity in mind, so the main emphasis in this part of our work was on improving the small-signal modulation formula taking into account modulation of both the photon density and the outcoupling loss. The rate equations system used in this part of the work is fairly standard [23], though in our case, it is useful to distinguish explicitly between the photon lifetime due to internal loss τ_{ph-in} and the photon lifetime due to outcoupling loss $\tau_{ph-out}(t)$ which is what is varied in the process of EO modulation:

$$\frac{dN}{dt} = \frac{\eta_i I}{eV} - \left(\frac{1}{\tau_{sp}(N)} + \frac{1}{\tau_{nr}} \right) N - \frac{G(N)}{1 + \epsilon N_p} N_p \quad (25)$$

$$\frac{dN_p}{dt} = \frac{\beta_{sp} N}{\tau_{sp}} + \left(\Gamma \frac{G(N)}{1 + \epsilon N_p} - (\tau_{ph-in}^{-1} + \tau_{ph-out}^{-1}) \right) N_p \quad (26)$$

$$\tau_{ph-out}^{-1}(t) = \frac{1}{2L_a} \ln \frac{1}{R_b R_m(t)} \quad (27)$$

Here, N and N_p are the the electron and photon densities, respectively, η_i is the internal quantum efficiency, I is the injected current, e is electron charge, V is the volume of the active region,

$\tau_{sp} = [B_1 N^2 / (1 + b_1 N)]^{-1}$ and $\tau_{nr} = (A_1 + C_1 N^3)^{-1}$ are the spontaneous and nonradiative recombination times of carriers, respectively, $G(N)$ is the optical gain in the active layer, ϵ is gain compression factor (see Table 1), β_{sp} is the spontaneous emission factor, Γ is the total confinement factor, L_a is the geometrical thickness of the active subbcavity, R_b is the constant bottom reflectance and R_m is the modulated reflectance of modulator subcavity, which is calculated as:

$$R_m = r_m r_m^*; \quad r_m = r_{am} + \frac{\theta_{am} \theta_{ma} r_{mt} e^{-j2K_m L_m}}{1 - r_{ma} r_{mt} e^{-j2K_m L_m}} \quad (28)$$

Here, r_{kl} and θ_{kl} are complex (and strictly speaking wavelength dependent, though the dependence is relatively weak) amplitude reflectances and transmittances of multistack DBRs, with the light incidence direction from layer k towards layer l , a being defined as inside the active cavity, m as inside the modulator cavity, and t as outside the top layer (see Figure 59) calculated at the wavelength λ .

$$K_m = \frac{2\pi n_m}{\lambda} = \frac{n_m \omega}{c}$$

K_m is the spatially average wave vector in the passive (EO modulator) cavity, n_m being the average refractive index in this cavity, and the wavelength λ (or optical frequency ω) in this simplified model is treated as a constant, and c is the speed of light in vacuum. Then, electro-optic variation of the average refractive index (nm) of the modulator cavity leads to a corresponding variation in the wave vector K which makes a change to R_m according to Equation (28); this changes the outcoupling photon lifetime $\tau_{ph-out}(t)$ as defined by Equation (27) which contributes to modulating N and N_p as described by Equation (25) and Equation (26).

Within the small signal analysis of prime interest for us here, the absolute magnitude of the variation of R_m and thus $\tau_{ph-out}(t)$ for a given variation of n_m is not relevant, but it is useful to estimate it, both for large-signal analysis and for use in subsequent parts of the thesis.

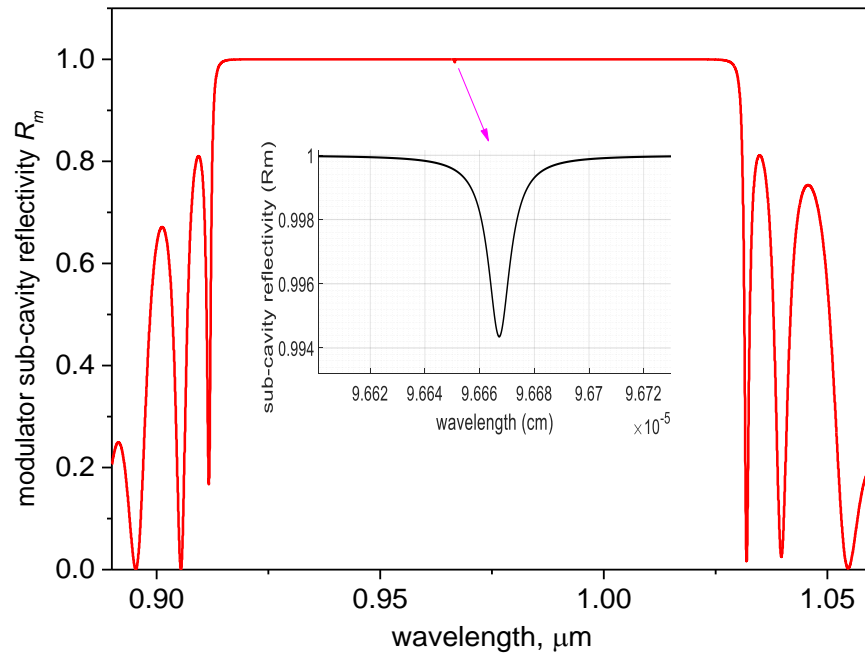


Figure 64: Calculated Reflectivity versus incident light wavelength for the EO modulator cavity

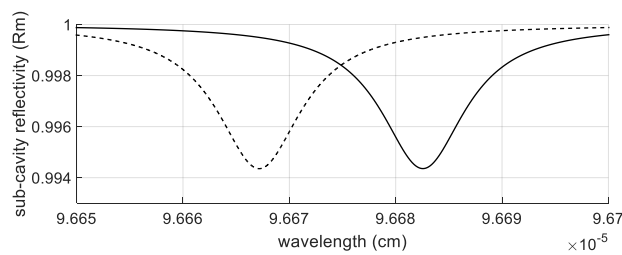


Figure 65: Spectral shape of the reflectance notch with $n_m=3.620$ (solid curve) and $n_m=3.621$ (dashed curve) calculated using full transfer matrix analysis

Figure 64 shows the calculated reflectivity versus incident light wavelength for the EO modulator cavity, for a specific case of the GaAs/Al_{0.2}Ga_{0.8}As 80Å QW laser operating at $\lambda=0.9685 \mu\text{m}$. It shows that the reflectivity R_m is very close to one for a broad range of the wavelength λ between $0.9 \mu\text{m}$ and $1.1 \mu\text{m}$ but has a narrow notch at $\lambda \approx 0.9666 \mu\text{m}$. Figure 65

illustrates how the position of the notch, and thus the reflectance in the relatively narrow range of wavelengths within it, can be modulated by changing the refractive index. It can be seen that the notch can be shifted by 1 nm when the refractive index is modulated by $\sim 10^{-3}$.

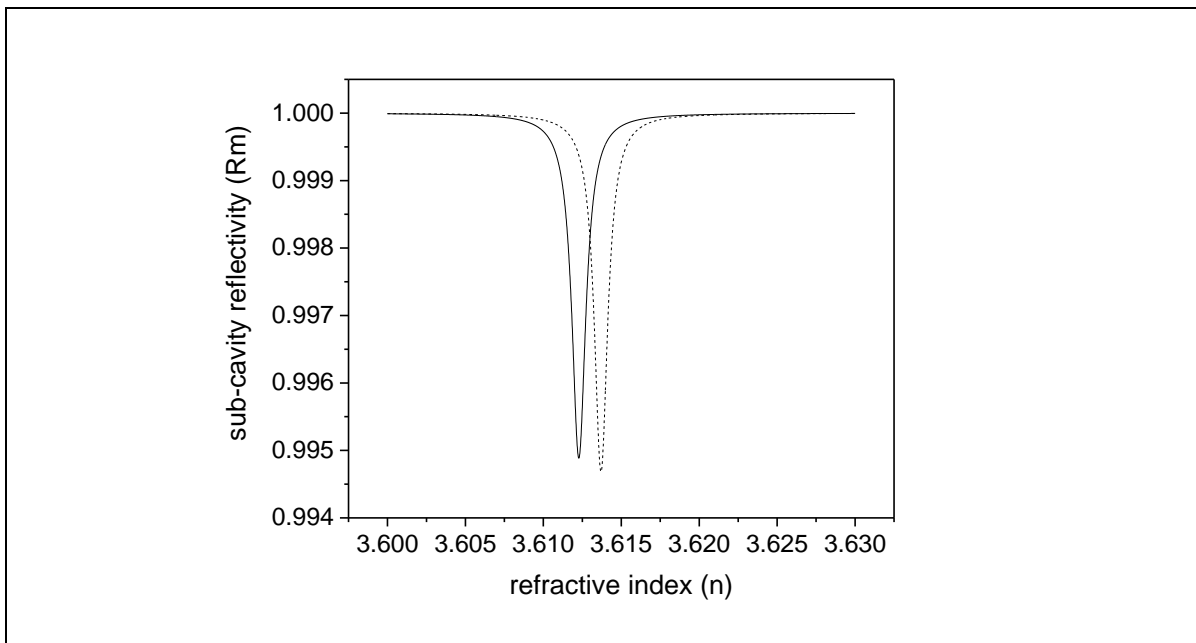


Figure 66: Calculated Reflectivity of the passive modulator cavity at the wavelength $\lambda \approx 0.9666 \mu\text{m}$ and at $\lambda \approx 0.9670 \mu\text{m}$ (dashed curve) vs. average refractive index of the cavity

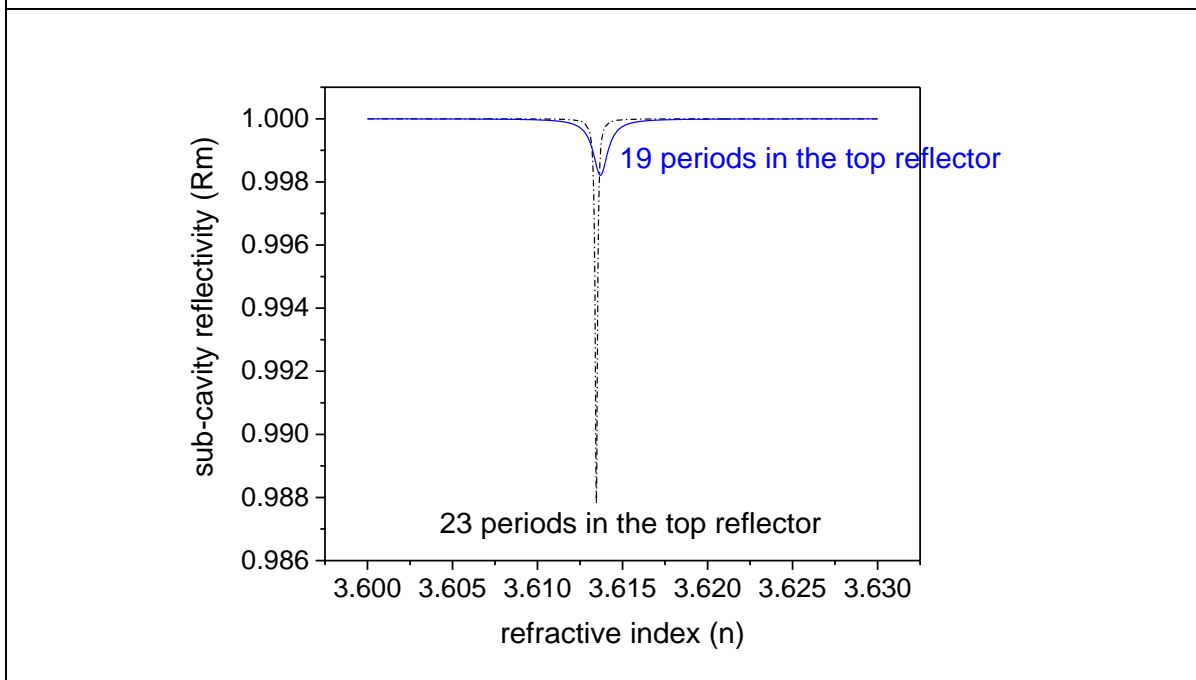


Figure 67: Calculated Reflectivity of the passive modulator cavity for 35 periods in the intermediate reflector and different periods in the top reflector

Figure 66 shows the calculated reflectivity of the passive modulator cavity versus average refractive index of the cavity. Similarly, Figure 67 shows the calculated reflectivity of the passive modulator cavity for 35 periods in the intermediate reflector and different periods in the top reflector. The results of Figure 65, Figure 66 and Figure 67 illustrate that a substantial variation of the reflectance is possible with the average refractive index varied by about $\sim 10^{-3}$, but also highlight the narrow wavelength range in which this variation occurs.

With the dynamics of the electron and photon densities being modelled using Equations (25-28), the output power can be calculated as:

$$P = h\nu_{ph}V_{opt} \tau_{ph-out}^{-1}(t) N_p(t) \quad (29)$$

Here $h\nu_{ph}=hc/\lambda$ is the photon energy (h being Planck's constant), V_{opt} is the modal volume, and τ_{ph-out}^{-1} is the outcoupling photon lifetime as defined above. The main parameters used in the simulations, together with their values where appropriate, are summarized in Table 1.

Table 1: Compound VCSEL parameters

Parameter	Symbol	Value	unit
transparency value of electron density	N_{tr}	2.6×10^{18}	cm^{-3}
linearity parameter	N_s	1.1×10^{18}	cm^{-3}
Gain constant in three-parameter approximation	g_o	3000	-
group velocity	v_g	$3 \times 10^{10} / 3.6$	cm/s
internal quantum efficiency	η	0.8	-
gain compression factor	ε	1.5×10^{-17}	cm^3
Nonradiative recombination coefficient	A_1	0.2×10^8	cm/s
bimolecular recombination coefficient	B_1	0.8×10^{-10}	cm^3/s
bimolecular recombination correction constant	b_1	1×10^{-19}	cm^3
Auger recombination coefficient	C_1	3.5×10^{-30}	cm^6/s
the geometrical thickness of the active subcavity	L_a	1.04×10^{-4}	cm
the effective thickness of the modulator	L_{eff}	1.04×10^{-4}	cm
length of modulator subcavity	L_m	1.0×10^{-4}	cm
confinement coefficient in active area	Γ_a	0.0382	-
confinement coefficient in modulator area	Γ_m	0.3	-
volume of active subcavity	V	2.4×10^{-12}	cm^3
enhancement factor due to standing wave pattern	ζ	1.83	-
internal loss	a_i	20	cm^{-1}
spontaneous emission	β_{sp}	1.2×10^{-5}	-
reflectivity of the bottom DBR	r_b	0.999	-
reflective index of the active layer	n_a	3.6	-
reflective index of the modulator layer	n_m	3.6	-
threshold current	I_{th}	0.8	mA

3.4 Small Signal Analysis

In the small signal analysis, as usual, one assumes small harmonic modulation of the modulation parameter (in our case, the reflectance R_m of the modulator subcavity) at a frequency $\Omega = 2\pi F$

$$R_m = R_{m0} + \delta R_m \exp(j\Omega t) + \text{c. c.},$$

Which results in small-signal modulation of the carrier and photon densities,

$$N = N + \delta N \exp(j\Omega t) + \text{c. c.},$$

$$N_p = N_{p0} + \delta N_p \exp(j\Omega t) + \text{c. c.}, \text{ and so } P = P_0 + \delta P \exp(j\Omega t) + \text{c. c.},$$

In the small signal approximation, $\delta N_p = \frac{\partial P}{\partial R_m} \delta R_m$,

The derivative is obtained by linearising Equations (25, 26, 29) after some manipulation, we get:

$$\frac{\partial P}{\partial R_m} = -h\nu_{ph} V_{opt} N_{p0} \frac{v_g}{2L_a} \frac{-\Omega^2 + j(\gamma_{rel} - \tau_{ph-out}^{-1})\Omega + \Omega_{rel}^2 - \tau_{ph-out}^{-1}(\tau_d^{-1} + \tau_{st}^{-1})}{-\Omega^2 + j\gamma_{rel}\Omega + \Omega_{rel}^2} \quad (30)$$

Where as usual $j = \sqrt{-1}$, h is Planck's constant, v_g is *group velocity*, ν_{ph} is the reference frequency, V_{opt} is the optical mode volume, N_{p0} is the photon density at threshold, L_a is the thickness of the active subcavity. Furthermore, Ω_{rel} and γ_{rel} , as usual in small-signal analysis, are the relaxation oscillation frequency and decay decrement:

$$\Omega_{rel}^2 \approx \frac{1}{\tau_{st}\tau_{ph}}, \tau_{st} \text{ being the stimulated carrier lifetime.}$$

$$\tau_{st}^{-1} \equiv \overline{N_p} \frac{\partial g}{\partial N}, g \text{ is the optical gain in the active layer.}$$

$$\gamma_{rel} = \tau_d^{-1} + \tau_{st}^{-1} + \frac{\beta_{sp} N}{\overline{N_p} \tau_{sp}} - \Gamma \overline{N_p} \frac{\partial g}{\partial N_p} \quad (31)$$

Where Γ is the confinement factor, $\overline{N_p}$ is the average photon density, τ_d is the dynamical carrier lifetime, $\tau_d^{-1} \equiv \frac{\partial}{\partial N} \left(\frac{N}{\tau_{sp}(N)} \right)$, τ_{sp} is the radiative recombination lifetime of carriers.

Equation (30) differs from the result presented in [7] in that it takes into account modulation of both the photon density and the outcoupling loss which is related to it. This equation thus shows the modulation, not of the photon density inside the laser, but of the measurable power outside the laser which is also influenced by the outcoupling loss modulation.

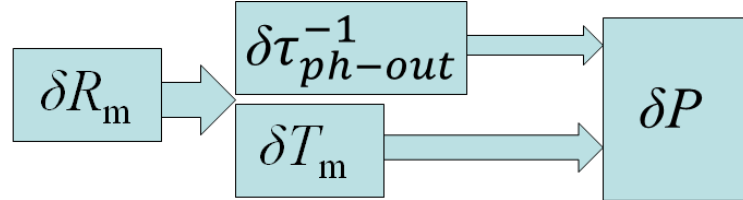


Figure 68: The logic diagram blocks for the original rate equation model

Figure 68 shows the logic diagram showing the modulation physics for the standard rate equation model. In this model, we modulate the reflectivity of the modulator subcavity (R_m), which modifies the photon lifetime (τ_{ph-out}) and the transmittance $T_m=1 - R_m$ both of which contribute to modulation of the output power (P).

From Equation (30), the 3dB cutoff frequency Ω_{3dB} for the laser considered can be derived in the following form:

$$\Omega = \sqrt{\frac{8z - 4d - 2fb + \gamma_{rel}^2 b^2 - \sqrt{(-8z + 4d + 2fb - \gamma_{rel}^2 b^2)^2 - (4 - b^2)(4z^2 - f^2)}}{8 - 2b^2}} \quad (32)$$

Where $z = \Omega_{rel}^2 - \tau_{ph-out}^{-1}(\tau_d^{-1} + \tau_{st}^{-1})$, $b = \frac{z}{\Omega_{rel}^2}$, $d = (\gamma_{rel} - \tau_{ph-out}^{-1})^2$ and $f = b\Omega_{rel}^2$.

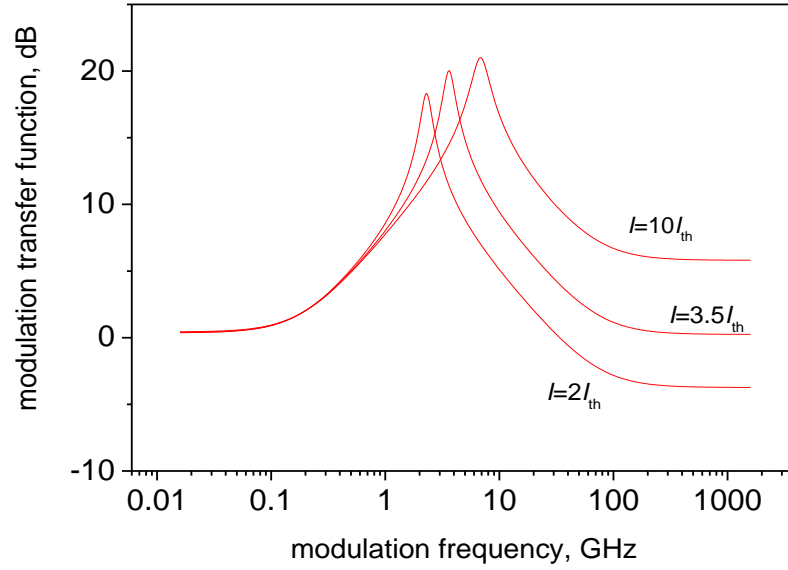


Figure 69: Calculated small-signal response of electrooptic laser modulation at three different values of bias current

Figure 69 shows calculated small-signal response of electrooptic laser modulation at three different values of bias current. It illustrates a somewhat unusual result of the analysis, namely, the fact that the concept of 3 dB cutoff frequency as a measure of modulation speed is, strictly speaking, not applicable to electrooptically modulated coupled-cavity VCSEL. Indeed, the phase relations between the modulation of the photon density (which, as shown in [7], decays as $1/\omega$ at high modulation frequencies) and the modulation of the mirror loss (which depends directly on R_m and thus, neglecting the circuit parasitics as discussed below, is modulation frequency independent) are both current and frequency dependent. As a result, at high enough currents we get a situation when at high frequencies (above the electron-photon resonance) the laser response is *higher* than at low frequencies approaching DC. In terms of the 3dB cutoff frequency, this means that this parameter tends to infinity as the current approaches a certain critical value I_{crit} which can be estimated as:

$$I_{crit} \approx I_{th} + \frac{ev_g g_{th} V \tau_d^{-1}}{\eta_i (2G'_N - \epsilon \tau_d^{-1})} \quad (33)$$

Where $\tau_d^{-1} = \frac{\partial}{\partial N} \left(\frac{N}{\tau(N)} \right)$, e is electron charge, $G'_N = v_g g'_N$ is the differential gain at ($I = I_{th}$), I_{th} and g_{th} are the current and gain at threshold, respectively, ε is the gain compression factor, V is the active layer volume and η_i is the internal quantum efficiency.

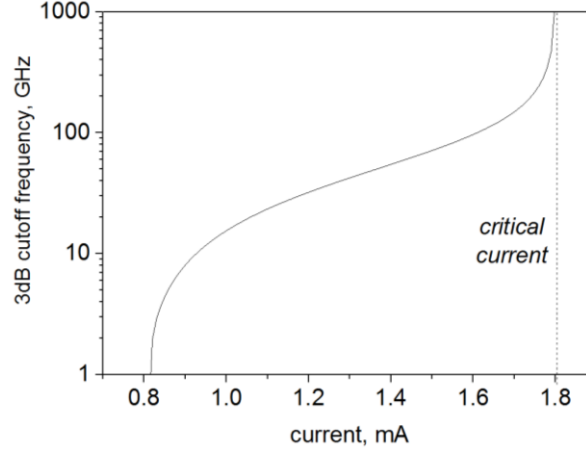


Figure 70: Calculated 3dB cut-off frequency vs bias current for small-signal response of electrooptic laser modulation

At $I > I_{crit}$, modulation frequency cannot be defined within the standard rate equation approach. In fact, as seen in Figure 70, showing the current dependence of the 3dB cutoff frequency, its values are actually unphysically high even at currents approaching, but below, I_{crit} . This is a limitation of the standard rate equation model that will be addressed below.

3.5 Large Signal Analysis

As in previous simulations using the rate equation model [7, 11, 14], we used Equations (25-29) to produce eye diagrams of large signal modulation. The diagrams (unfiltered) are shown in Figure 71, Figure 72 and Figure 73 for three values of current (1.5mA, 5mA and 30mA, respectively). Mathematically, the quality of eye diagrams is characterized by the quality factor:

$$Q = \frac{\overline{P_{(1)}} - \overline{P_{(0)}}}{\sigma_{(1)} + \sigma_{(0)}} \quad (34)$$

Where $\overline{P}_{(1)}, \overline{P}_{(0)}$ are the mean values of the power corresponding to the logical one and zero states, respectively; $\sigma_{(1)}, \sigma_{(0)}$ are the corresponding standard deviations.

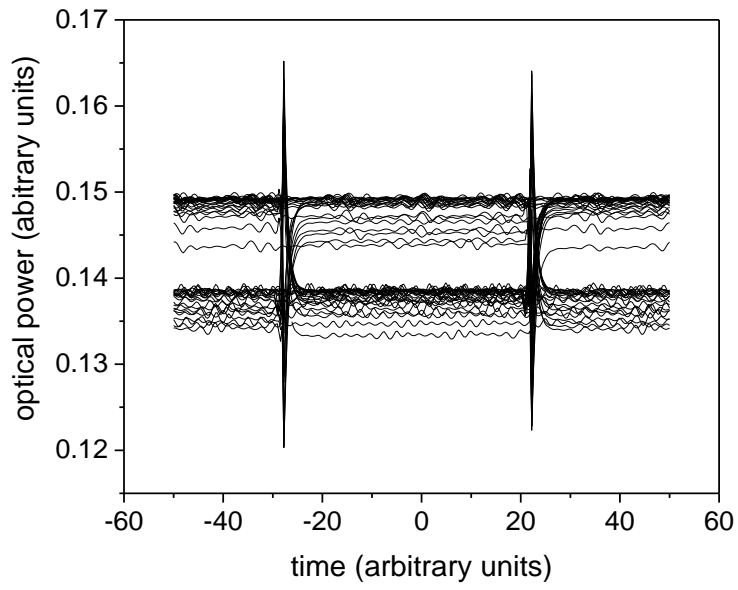


Figure 71: Eye diagram for 1.5mA VCSEL, 40Gbit/s bit rate

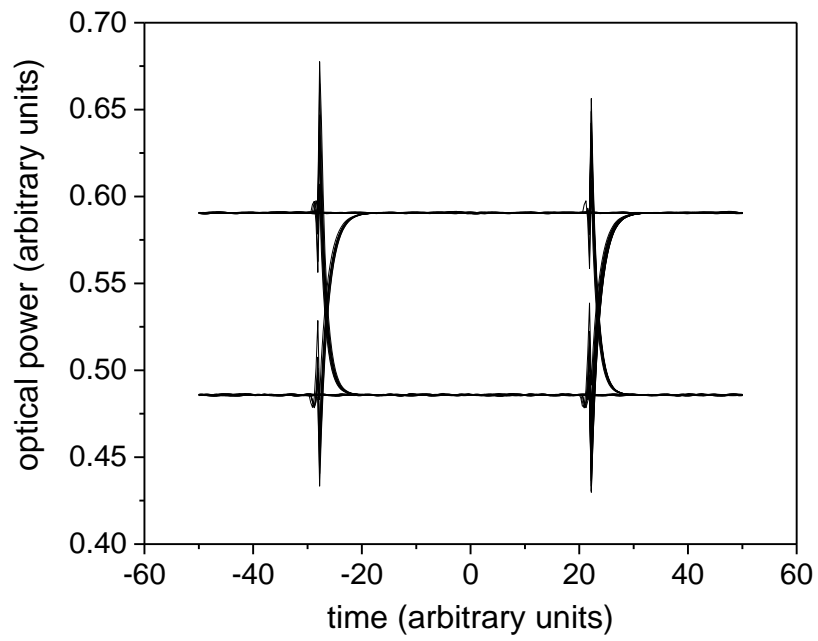


Figure 72: Eye diagram for 5mA VCSEL, 40Gbit/s bit rate

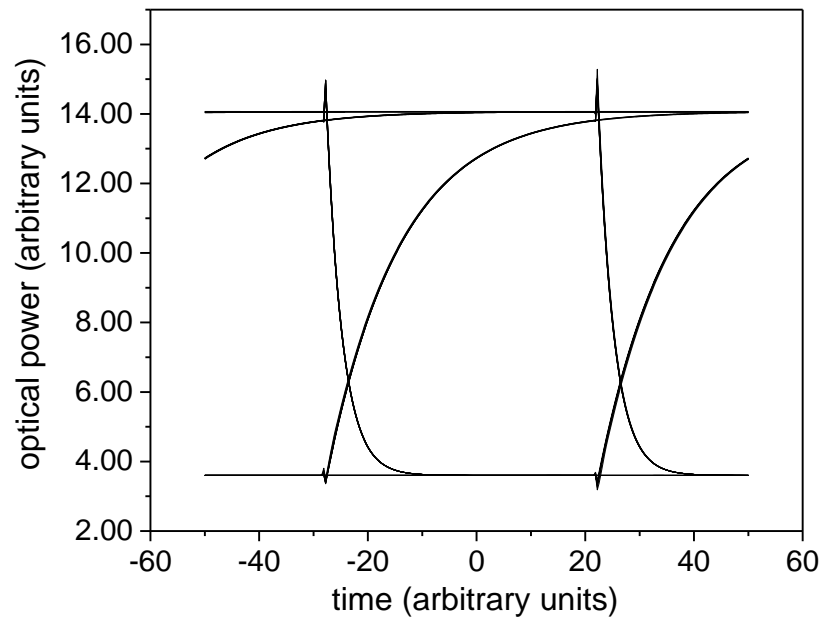


Figure 73: Eye diagram for 30mA VCSEL, 40Gbit/s bit rate

In agreement with earlier simulations using a similar model [14], we find that overall, relatively low currents tend to produce higher modulation quality. However, the quality of large signal modulation depends non-monotonically on bias current, e.g. the eye diagram quality factor for 5 mA is higher than the other two currents. This is due to the effects of the small modulation contrast at smallest currents (the numerator of Equation (34)), on the one hand, and the large switch-on and switch-off times leading to a large standard deviation of the on-state (denominator of Equation (34)); a moderate current thus offers an optimum quality of modulation.

Relatively Weak Modulation Amplitudes (reflectivity: $0.9422-0.9414=0.0008$)

In this part, the analysis is made for relatively weak modulation amplitudes (reflectivity: $0.9422-0.9414=0.0008$). The quality factors are calculated versus different bias currents for modulation frequencies are 20 Gbit/s, 40 Gbit/s and 80 Gbit/s.

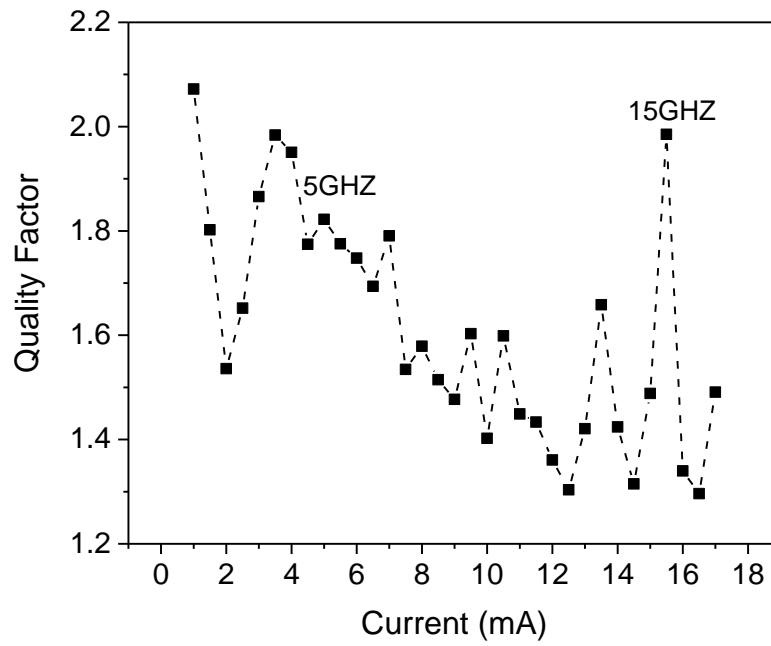


Figure 74: Q-Factor for 20 GBit/s Bit Rates ($R=0.9422-0.9414=0.0008$). At Current=4.5mA, the Frequency =5GHz. At Current=15.7mA, the Frequency =10GHz

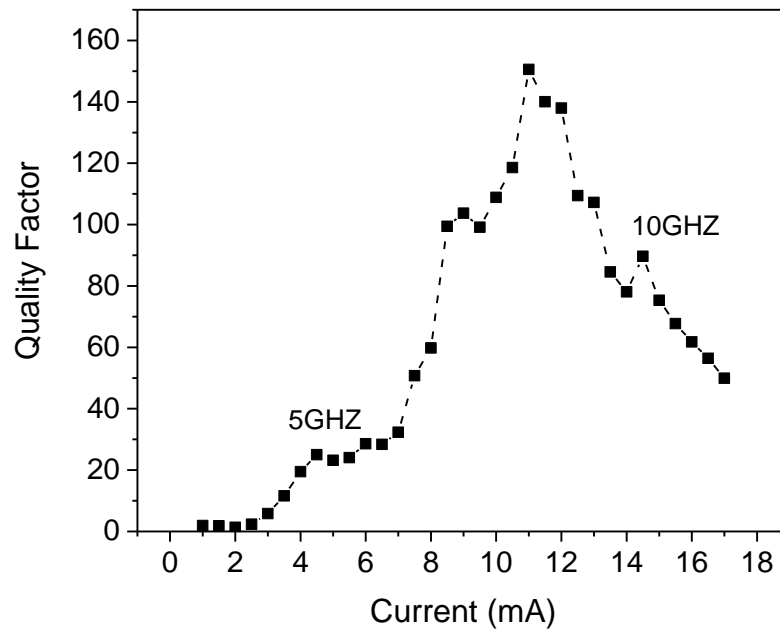


Figure 75: Q-Factor for 40 GBit/s Bit Rates ($R=0.9422-0.9414=0.0008$). At Current=4.5mA, the Frequency =5GHz. At Current=15.7mA, the Frequency =10GHz

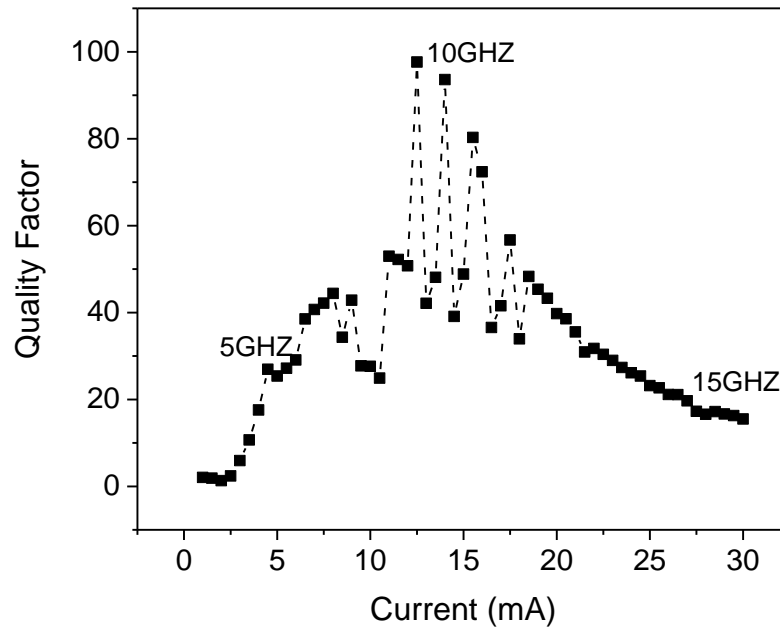


Figure 76: Q-Factor for 80 GBit/s Bit Rate ($R=0.9422-0.9414=0.0008$). At Current=4.5mA, the Frequency =5GHz. At Current=15.7mA, the Frequency =10GHz. At Current=34.4mA, the Frequency =15GHz

Figure 74, Figure 75 and Figure 76 show the quality factor versus different bias currents for relatively weak modulation amplitudes. These curves are calculated for 20 GBit/s, 40 GBit/s and 80 GBit/s modulation frequency, respectively. The figures show that quality factor of relatively weak modulation amplitudes depends non-monotonically on bias current which is improved with reflection modulation contrast. It might be attributed to sub-harmonic resonance with relaxation oscillations non-monotonic relationship between quality factor and current as shown in Figure 77. This figure shows resonance frequencies as a function of bias currents for small signal analysis. When currents in this figure are 5 mA, 15 mA and 30 mA, the corresponding frequencies in small signal analysis are 5 GHz, 10 GHz and 15 GHz, respectively. These three frequencies in the small signal analysis corresponds to three peak quality factors in the large signal analysis as shown in Figure 74, Figure 75 and Figure 76.

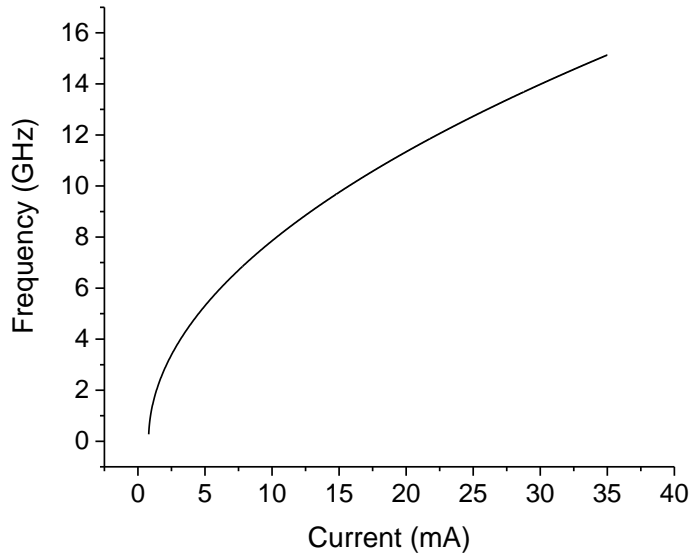


Figure 77: Resonant frequency versus current for small signal

Larger Modulation Amplitudes (reflectivity: $0.949-0.941= 0.0080$):

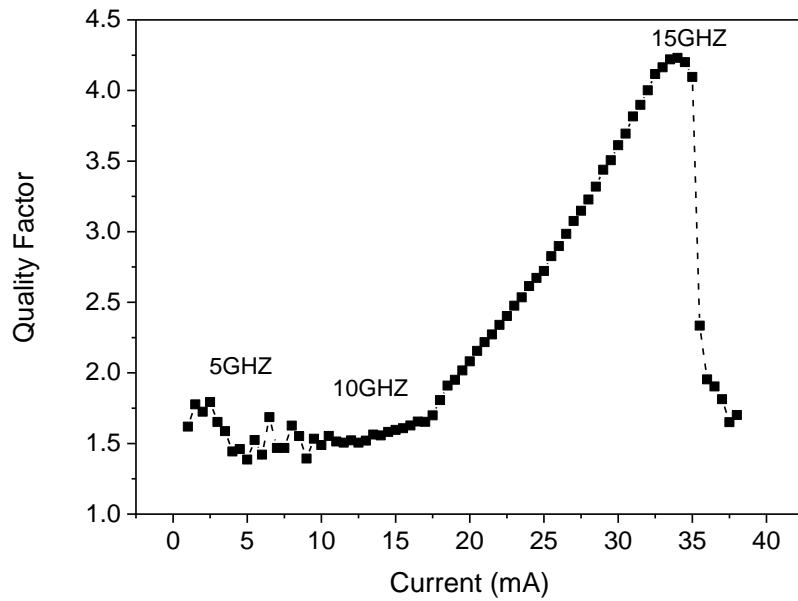


Figure 78: Q-Factor for 20 GBit/s Bit Rates ($0.949-0.941= 0.0080$)

Figure 78 shows the quality factor versus current from 1mA until 40mA for larger modulation amplitudes (reflectivity: $0.949-0.941= 0.0080$). This curve is calculated for 20

Gbit/s modulation frequency and it shows a peak at 35mA. It should be noticed that the corresponding frequency for 35mA is 15GHz for small signal response as shown in Figure 77.

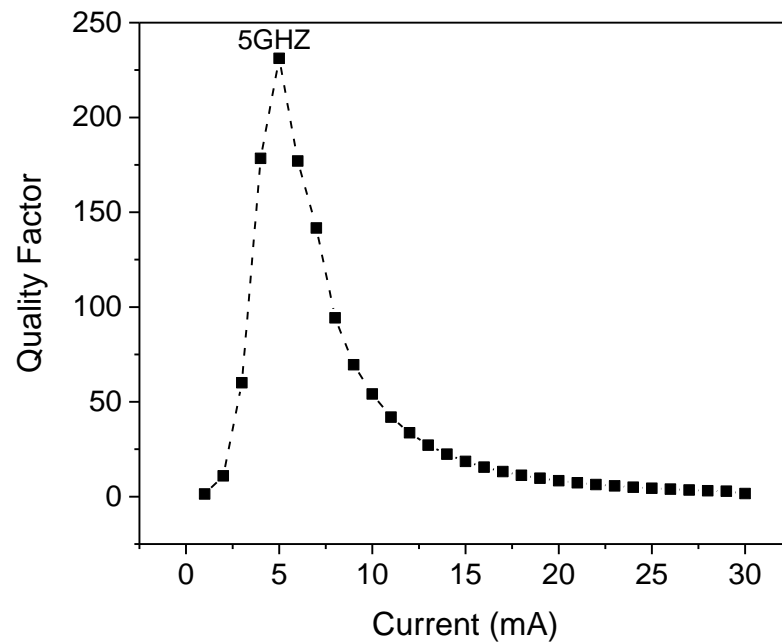


Figure 79: Q-Factor for 40 GBit/s Bit Rates (0.949-0.941= 0.0080)

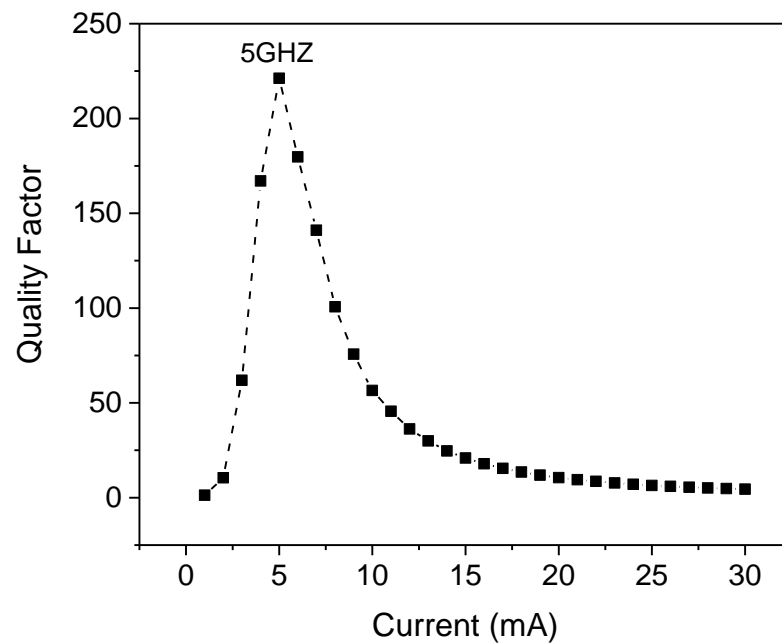


Figure 80: Q-Factor for 80 GBit/s Bit Rates (0.949-0.941= 0.0080)

Figure 79 and Figure 80 show the quality factors for varying current for 40 GBit/s and 80 GBit/s modulation frequency, respectively. Both curves are analysed for larger modulation amplitudes (reflectivity: $0.949-0.941= 0.0080$). Figure 79 and Figure 80 showed a peak in quality factors at 5mA bias current which is corresponding to 5GHz (sub-harmonic of modulation frequency) for small signal response as shown in Figure 77.

3.6 Chapter summary

In this chapter, we found that the quality factor of the eye diagrams for large signal modulation depend non-monotonically on bias current. It might be attributed to sub-harmonic resonance with relaxation oscillations non-monotonic relationship between quality factor and current. We also found that in agreement with earlier simulations using a similar model, relatively low currents tend to produce higher modulation quality and the quality of large signal modulation depends non-monotonically on bias current.

In this chapter, we model the reflectance modulation in the compound VCSEL as the photon lifetime modulation, and we found that the previous authors modelled modulation of the power inside the active region not the output power emitted from the top DBR's. We included the modulation of actual output power in the model and found that:

- No high frequency roll-off existed in small-signal modulation at $I > I_{critical}$, therefore the 3 dB cutoff frequency as a measure of laser performance could not be determined at such currents in this model.
- Quality of large signal modulation depended non-monotonically on bias current, improved with reflection modulation contrast; this can be attributed to sub-harmonic resonance with relaxation oscillations.

Since not having a 3 dB cutoff frequency is not realistic, we decided to develop the standard rate equations model into a more complex model to include the phases of the fields and also

the finite response speed of the modulator section. We also considered the selective nature of the modulator section reflectance (both its amplitude and phase) in the next chapter.

4. THE MODIFIED RATE EQUATION MODEL

4.1 Introduction

In order to understand the laser performance more accurately, and to gain some understanding of the aspects of it which the rate equation model does not capture (the linewidth broadening performance and the ultimate limitations to the modulation properties of electrooptically modulated lasers), a somewhat more complex model involving careful analysis of both amplitude and frequency/phase of laser emission, as well as the spectrally selective nature of the laser cavity, is necessary.

In designing the model, we follow the approach used previously for DFB lasers (see e.g. [101]) and for multimode compound cavity lasers (see e.g. [104]). Namely, the laser cavity is treated as a complex resonator, and a complex eigenfrequency of this resonator is found, which is then used to describe the laser dynamics. The electrooptically modulated VCSEL is very naturally suited for such an approach, because the complex resonator in this case can be defined by considering the active sub-cavity as a quasi-Fabry-Perot resonator terminated, on one side, by the bottom reflector with an amplitude reflectance r_b and on the other side, by the EO modulator subcavity treated as a passive, frequency-dependent reflector with a complex reflectance $r_m(\omega)$, where ω is the complex eigenfrequency sought. The value of $r_m(\omega)$ is calculated from Equation (28) with the average wave vector in the form of:

$$K_m(\omega) = \frac{(n_m + \Gamma_m \Delta n_{EO})\omega}{c} \quad (35)$$

Here, Δn_{EO} describes the time-dependent correction to the refractive index of the modulator layer caused by electrooptic modulation. $\Gamma_m \approx \frac{d_m}{L_m}$ (assuming the modulator layer is thick enough that the standing wave factor is near one) is the confinement factor of the modulator layer, d_m being the modulator layer thickness and L_m , the total physical thickness of the modulator cavity, including any spacer layers between the modulator layer and the DBRs but not including the penetration into mirrors. The complex eigenfrequency is then found by solving the usual threshold/resonant condition of a Fabry-Perot type cavity (due to the short cavity length, the equation has only one solution):

$$r_m(\omega)r_b(\omega) \exp \left[2 \left(-j \frac{(n_a + \Delta n_a)\omega}{c} + \Gamma_a \frac{g}{2} \right) L_a \right] = 1 \quad (36)$$

It is convenient to write this solution in terms of a frequency correction $\Delta\omega = \omega - \omega_{ref}$, where the (real) reference frequency ω_{ref} is arbitrary but can be conveniently taken, for example, as the position of the notch (Figure 64) in either on or off-state. Then, the complex instantaneous frequency correction $\Delta\omega$ is defined from a transcendental equation:

$$\Delta\omega = v_g \left[-\frac{j}{2} \left(\Gamma_a g - \frac{1}{L_a} \ln \frac{1}{r_m(\omega_{ref} + \Delta\omega)r_b} \right) - \frac{\Delta n_a \omega_{ref}}{c} + \left(\frac{q\pi}{L_a} - \frac{n_a \omega_{ref}}{c} \right) \right] \quad (37)$$

Here, Γ_a is the confinement factor for the active area, g is the time-dependent gain, n_a is the refractive index of the active layer subcavity, averaged over the length in the same way as n_m is averaged over the modulator subcavity. The refractive index varies in time primarily due to self-phase modulation in the active layer; its time-dependent part can be quantified as:

$$\Delta n_a \approx \frac{c}{2\omega_{ref}} \Gamma_a \alpha_H (g - g_{th}) \quad (38)$$

where α_H is the Henry linewidth enhancement factor in the active layer and g_{th} is the gain at threshold.

The choice of reference frequency near the modal frequency to ensure that $|\Delta\omega| \ll \omega_{ref}$ means that we can introduce a parameter q which is the number of half-wavelengths of light in material fitting (roughly) in the distance L_a . It depends on the VCSEL design, mainly the thickness L_a , and it is an integer number chosen in such a way that:

$$q \approx \frac{2n_a L_a}{\lambda} - \frac{1}{2\pi} \arg(r_m r_b) \quad (39)$$

where $\lambda = 2\pi c / \omega_{ref}$ is the operating wavelength, and r_m can be estimated in the on- or off-state.

The frequency ω (or frequency correction $\Delta\omega$) has a real part, which determines the time-dependent spectral position of the lasing mode and thus the chirp of laser emission, and an

imaginary part, which reflects the balance of gain and loss (the latter including the outcoupling loss, which is frequency dependent through $r_m(\omega)$). The imaginary part determines the dynamics of photon density (in the active cavity) N_p , giving a modified rate equation in the form:

$$\frac{dN_p}{dt} = -2 * \text{Im}(\Delta\omega(t))N_p(t) + \frac{\beta_{sp}N}{\tau_{sp}(N)} \quad (40)$$

The dynamics of the electron density is determined by Equation (25) as in the standard rate equation model. The addition of the electromagnetic Equation (40), however, offers a number of additional capabilities that are absent in the standard rate equation model. Firstly, the modified model allows us to deal with modulation of the refractive index more directly. In this model, we are modulating refractive index, not the photon lifetime as in the standard model. Secondly, by describing frequency and phases, as well as intensity, of the signal, we can evaluate the chirp and optical spectra. Finally, we can take into account the speed limitations because of the spectral selectivity of the modulator cavity (spectral width of the notch in Figure 64). The latter two points however require an additional modification to the model. Namely, in the simple rate equation model one assumes an instantaneous relation (Equation 29) between the photon density and the output power. In subsequent calculations, this led to abrupt fronts in the eye diagram as will be shown below (Figure 90). In the more accurate model, we need to replace this instantaneous relation with an additional differential equation taking into account the electromagnetic resonance in the modulator cavity as will be shown below (Figure 91). The equation is derived by considering the modulator section in frequency domain and then substituting the imaginary part of the frequency correction by a time derivative. The result is conveniently expressed as:

$$\frac{d\tilde{E}_t}{dt} = \left(-\frac{1}{2\tau_{cm}} - j \left(\Delta\omega'(t) - \Delta\omega_{n0} + \Gamma_m \frac{\Delta n_{EO}(t)}{n_g} \omega_{ref} \right) \right) \tilde{E}_t + \frac{\sqrt{2T_i T_t}}{4} \frac{v_g}{L_{eff,m}} E_a \quad (41)$$

$$\tau_{cm} = \frac{L_{eff,m}}{v_g(1 - \sqrt{R_i R_t})} \approx \frac{2L_{eff,m}}{v_g(T_i + T_t)} \quad (42)$$

Here, $\tilde{E}_t = E_t \exp(j\varphi_t)$ describes the complex amplitude of the output field emitted from the modulator subcavity (the top mirror), $E_a = \sqrt{N_p}$ is the field amplitude inside the active subcavity. Note that in the equation written in the form above, E_a is a *real* value, which means that the complex amplitude of the output light is actually $\tilde{E}'_t = \tilde{E}_t \exp(j \int \Delta\omega' dt)$, where $\Delta\omega' = \text{Re}(\Delta\omega)$ is the instantaneous frequency correction in the active cavity. Furthermore, $\Delta\omega_{n0} = \omega_{n0} - \omega_{ref}$ is the position of the notch in the modulator subcavity transmission in the absence of modulation ($\Delta_{nE0} = 0$), τ_{cm} is the effective photon lifetime in the modulator cavity (which was neglected in the simple model since it was assumed to be very fast), $R_i = |r_{ma}|^2$ and $R_t = |r_{mt}|^2$ are the intensity reflectances of the intermediate and top reflectors (the two reflectors forming the modulator cavity) respectively, $T_i = 1 - R_i$, $T_t = 1 - R_t$ are the transparencies of the intermediate and top DBR stacks, and:

$$L_{eff,m} = L_m + \frac{v_g}{2} \left(\left| \frac{\partial}{\partial \omega} \arg(r_{ma}) \right| + \left| \frac{\partial}{\partial \omega} \arg(r_{mt}) \right| \right) \Big|_{\omega_{ref}} \quad (43)$$

Is the effective thickness of the modulator section (L_m is being its physical thickness as in Section 3.2). The effective thickness is typically a fraction of a micron greater than the physical one, as it considers the penetration of the field into the mirrors. The power emitted from the laser can be calculated as:

$$P \approx v_g \hbar \omega A_x E_t^2 \quad (44)$$

Where A_x is the cross-section of the top mirror. The instantaneous frequency determining the chirp of the output laser emission is:

$$\Delta\omega_t = \frac{d}{dt} \arg(\tilde{E}'_t) = \text{Re}(\Delta\omega(t)) + \frac{d}{dt} \arg(\tilde{E}_t) \quad (45)$$

It is worth noting that an alternative formalism for describing the laser dynamics with phase included would consist of writing out an equation similar to Equation (41) for the *active* subcavity, with an injection term representing light reflected from the modulator cavity, rather than solving a transcendental Equation (37) for the instantaneous frequency. A model of that type treats the laser as a system of two subcavities, one active, one passive but

modulated, treated on the same footing. The results should be very similar to those of the current formalism so long as the dynamics of light *inside* the active cavity remain slower than the modulator cavity round-trip (which is the case for most realistic designs). We chose the formalism presented above as it represents an easy logical step from the simple rate equation model. Indeed, in the absence of the explicit expression for the frequency dependence of r_m , interrelated with the laser chirp as described by Equation (37), i.e. with a constant $\Delta\omega$, Equation (26) is reduced to Equation (40) and so the modified rate equation model is reduced to the standard rate equation one.

4.2 Checking the modified rate equations model

In order to check the accuracy of the model, the following steps were taken:

1. $\Delta\omega$ is made variable. (within the limits -10^{12} to $+10^{12}$ s⁻¹).
2. K_m , the wave vector magnitude, is calculated using the usual equation:

$$K_m = \frac{2\pi n_m}{\lambda} = \frac{n_m \omega}{c} \approx K_{ref} + \frac{\omega_{ref} \Gamma_m \Delta n + n_{ref} \Delta \omega}{c}$$

3. r_m , the reflectance coefficient, is calculated using the usual equation for a Fabry-Perot resonator reflectance:

$$R_m = r_m r_m^*; \quad r_m = r_{am} + \frac{\theta_{am} \theta_{ma} r_{mt} e^{-j2K_m L_m}}{1 - r_{ma} r_{mt} e^{-j2K_m L_m}}$$

4. $\Delta\omega$ is calculated using its definition:

$$\Delta\omega = v_g \left[-\frac{j}{2} \left(\Gamma_a g - \frac{1}{L_a} \ln \frac{1}{r_m(\omega_{ref} + \Delta\omega) r_b} \right) - \frac{\Delta n_a \omega_{ref}}{c} + \left(\frac{q\pi}{L_a} - \frac{n_a \omega_{ref}}{c} \right) \right]$$

The final $\Delta\omega$ vs the initial $\Delta\omega$ is plotted (Figure 81):

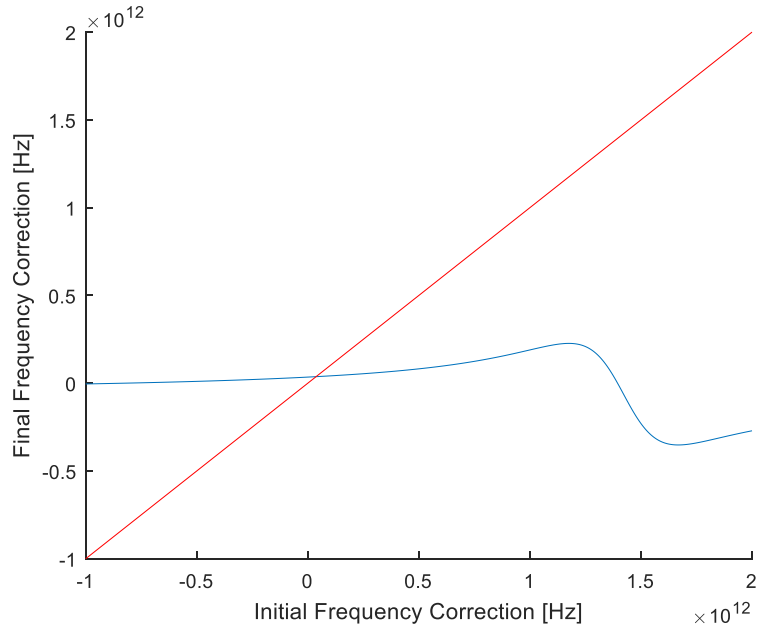


Figure 81: The initial $\Delta\omega$ [red] and the final $\Delta\omega$ [blue]

Figure 81 shows the final $\Delta\omega$ (solution) vs the initial $\Delta\omega$ vs frequency correction. The intersection between the two graphs for the final $\Delta\omega$ and the initial $\Delta\omega$ occurs at a very small frequency correction, which implies that the model is correct because the smallness of correction was one of the model assumptions.

Figure 82 shows the photon density and imaginary frequency correction vs normalized time. It shows that when the rate of change for photon density is increasing, the imaginary part of the frequency correction is negative and when the rate of change for photon density is decreasing, the imaginary part of the frequency correction is positive which copes with the rate equation for photon density:

$$\frac{dN_p}{dt} = -2 * \text{Im}(\Delta\omega(t))N_p(t) + \frac{\beta_{sp}N}{\tau_{sp}(N)}$$

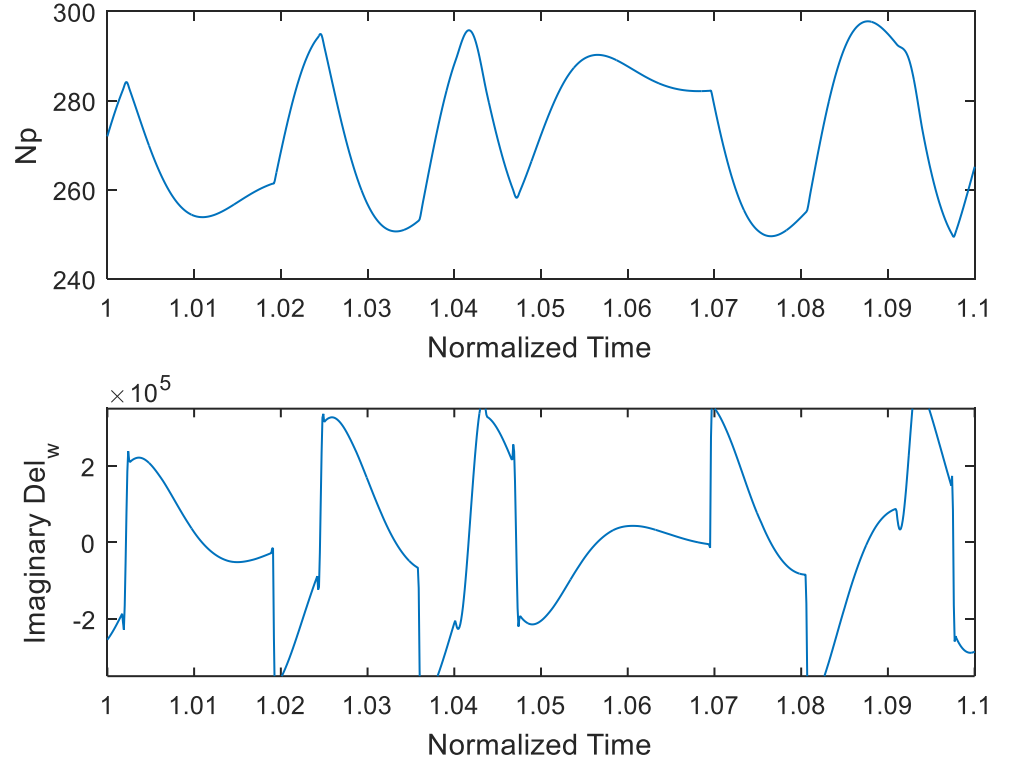


Figure 82: The photon density and imaginary frequency correction vs normalized time

Another aspect of checking the model was also taken by comparing between the Lorentzian and exact transmittance vs the frequency correction as in Figure 83. This is important for the Equation (41) describing the dynamics of the modulator section [4.1], which assumes a Lorentzian shape of the transmission peak:

$$\frac{d\tilde{E}_t}{dt} = \left(-\frac{1}{2\tau_{cm}} - j \left(\Delta\omega'(t) - \Delta\omega_{n0} + \Gamma_m \frac{\Delta n_{EO}(t)}{n_g} \omega_{ref} \right) \right) \tilde{E}_t + \frac{\sqrt{2T_i T_t}}{4} \frac{v_g}{L_{eff,m}} E_a$$

The following figure shows that both graphs are similar within a wide range of frequencies:

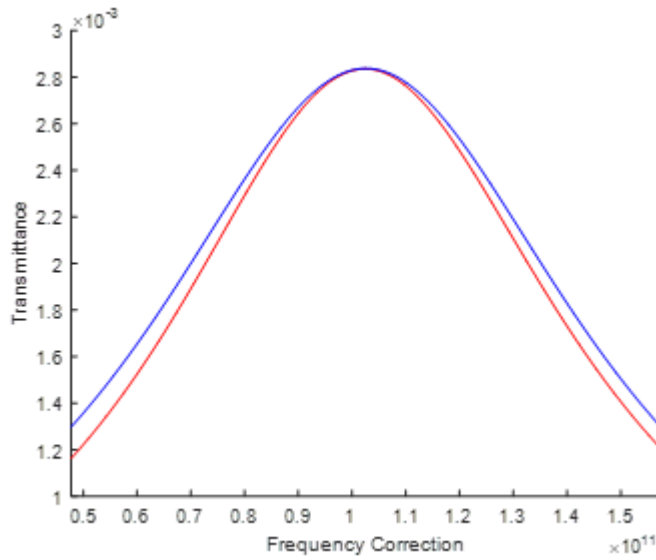


Figure 83: Transmittance ($1-R_m$) vs frequency correction in [Hz], the Lorentzian (blue), and the exact (red)

4.3 Small signal analysis

To analyse the small signal response, the dynamic variables are given small variations, as in the standard rate equation model. The origin of modulation in this case is the electrooptically modulated refractive index:

$$\Delta n_{EO} = \Delta n_{EO0} + \delta n_{EO} \exp(j\Omega t) + \text{c. c.},$$

This leads to small-signal modulation of the photon densities in the active cavity and outside the laser, as in the case of standard rate equations:

$$N = N + \delta N \exp(j\Omega t) + \text{c. c.},$$

$$N_p = N_{p0} + \delta N_p \exp(j\Omega t) + \text{c. c.}, \quad P = P_0 + \delta P \exp(j\Omega t) + \text{c. c.},$$

which in terms of internal field is expressed as:

$$\delta E_a = \frac{\delta N_p}{2\sqrt{N_p}}$$

and in addition of the lasing frequency and phase:

$$\Delta\omega = \Delta\omega_0 + \delta\omega \exp(j\Omega t) + \text{c. c.},$$

$$\Delta\varphi_t = \varphi_{t0} + \delta\varphi_t \exp(j\Omega t) + c. c.,$$

(the latter only required if small-signal chirp is analysed).

The steady state values of the carrier and photon densities N_0 and N_{p0} as well as the operating frequency $\Delta\omega_0$, have to be found from the steady state solutions of the rate equation system, including the transcendental Equation (37), and so cannot be written in a closed form. The linear differential Equation (41), on the other hand, can be easily solved in steady state, giving the transmission properties of the modulator subcavity:

$$E_{t0} = \frac{\sqrt{2T_i T_t}}{T_i + T_t} \cos \varphi_{t0} E_{a0} \quad (46)$$

Where

$$\tan \varphi_{t0} = -2\tau_{cm} \Delta\omega_i$$

And

$$\Delta\omega_i = \Delta\omega_0 + \Gamma_m \frac{\Delta n_{E00}}{n_m} \omega_{ref}$$

is the steady state detuning between the incident light and the position of the transmission notch in the modulator subcavity. A combination of the three equations above gives the steady-state relation between the internal and output intensity or power as:

$$\left| \frac{E_{t0}}{E_{a0}} \right|^2 = \frac{2T_i T_t}{(T_i + T_t)^2} \frac{1}{1 + (2\tau_{cm} \Delta\omega_i)^2} \quad (47)$$

which stems from the assumption $\Delta\omega \ll \omega_{ref}$ and is a very good approximation for the actual form presented in Figure 64 and Equation (28); note that the result differs from the transmittance of the modulator section by a factor of two, as only half of the internal intensity is travelling in the output direction.

Linearising the differential Equation (41), we can relate the small-signal modulations of light amplitude outside and inside the laser as:

$$\delta E_t = \frac{1}{\left(j\Omega + \frac{1}{2\tau_{cm}}\right)^2 + \Delta\omega_i^2} \left[\left(\frac{1}{2\tau_{cm}}\left(j\Omega + \frac{1}{2\tau_{cm}}\right) - \Delta\omega_i^2\right) \frac{\sqrt{2T_i T_t}}{(T_i + T_t)} \cos \varphi_{t0} \delta E_a + \Delta\omega_i E_{t0} \left(\delta\omega + \frac{\Gamma_m \omega_{ref}}{n_m} \delta n_{EO}\right) \right] \quad (48)$$

Linearisation of the transcendental Equation (37) gives a small-signal complex frequency variation in the form:

$$\delta\omega = -jv_g \frac{\Gamma_a(1 - j\alpha_H)\delta g + \frac{1}{2L_a} \Gamma_m \frac{\partial r_m}{\partial n_m} \delta n_{EO}}{1 + j \frac{v_g}{2L_a} \left(\frac{\partial r_b}{\partial \omega} + \frac{\partial r_m}{\partial \omega}\right) \Big|_{\omega_{ref}}} \quad (49)$$

Interestingly, although we did not explicitly introduce the effective cavity length for the active subcavity, the denominator of this equation effectively contains it. In Equation (50), the variation of gain at the modulation frequency is determined in the same way in standard rate equations, namely:

$$\delta g = \frac{a_0}{1 + \varepsilon N_p} \delta N - \frac{\varepsilon g}{(1 + \varepsilon N_p)^2} \delta N_p \quad (50)$$

Where $a_0 = \partial g / \partial N$ at threshold

Finally, the expressions for photon (and electron) density variations can be obtained in a closed form:

$$\delta N_p = - \frac{AC(j\Omega - H)N_{p0}\delta n_{EO}}{-\Omega^2 + (H - D)j\Omega - (DH + EF)} \quad (51)$$

$$\delta N = \frac{-N_p AC \delta n_{EO} F j \omega_m - N_p AC \delta n_{EO} HF}{-j\Omega^3 - (-D + 2H)j\Omega^2 + [H(H - D) - (DH + EF)]j\Omega - H(DH + EF)} \quad (52)$$

Where:

$$A = \frac{v_g}{\left(\frac{L_{eff}}{L_a}\right)^2 + \left(\frac{v_g}{2L_a} \frac{\partial r_m}{\partial \omega}\right)^2}$$

$$L_{eff,m} = L_m + \frac{v_g}{2} \left(\left| \frac{\partial}{\partial \omega} \arg(r_{ma}) \right| + \left| \frac{\partial}{\partial \omega} \arg(r_{mt}) \right| \right) \Big|_{\omega_{ref}}$$

$L_{eff,m}$ is the effective thickness of the modulator.

$$B = \frac{L_{eff}}{L_a} \Gamma + \alpha_H \frac{v_g}{2L_a} \frac{\partial r_m}{\partial \omega}$$

$$C = \frac{\Gamma_m}{L_a^2} \left(L_{eff} \frac{\partial r_m}{\partial n_m} + \frac{v_g}{2} \frac{\partial \arg(r_m)}{\partial n_m} \frac{\partial r_m}{\partial \omega} \right)$$

$$D = \frac{N_p AB \varepsilon g}{(1 + \varepsilon N_{p0})^2}$$

$$E = -\frac{N_p AB \alpha_0}{1 + \varepsilon N_{p0}} + \frac{\beta}{\tau_{cm}}$$

$$F = \frac{v_g N_p \varepsilon g}{(1 + \varepsilon N_{p0})^2} - v_g g$$

$$H = \frac{v_g N_{p0} \alpha_0}{1 + \varepsilon N_{p0}} + \frac{1}{\tau_{cm}}$$

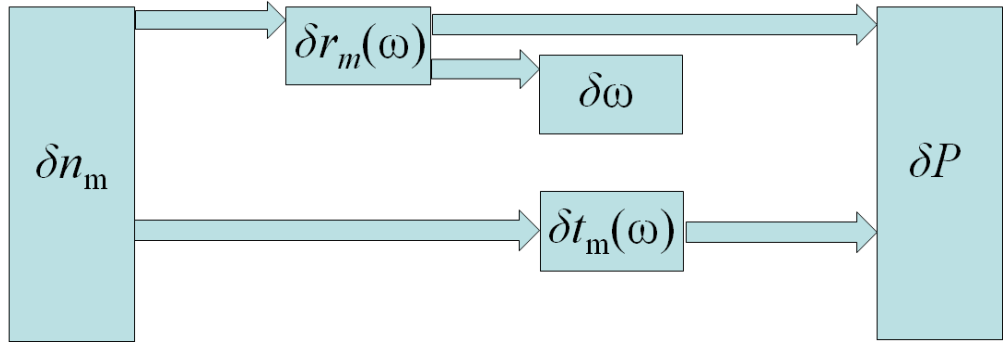


Figure 84: The logic diagram blocks for the modified rate equation model

Figure 84 illustrates the logic of the modified rate equation model. In this model, we modify the refractive index (n_m) of the modulation layer, which changes the complex reflectance and

transmittance and also modifies the operating wavelength of the laser, all of which modulate the output power (P).

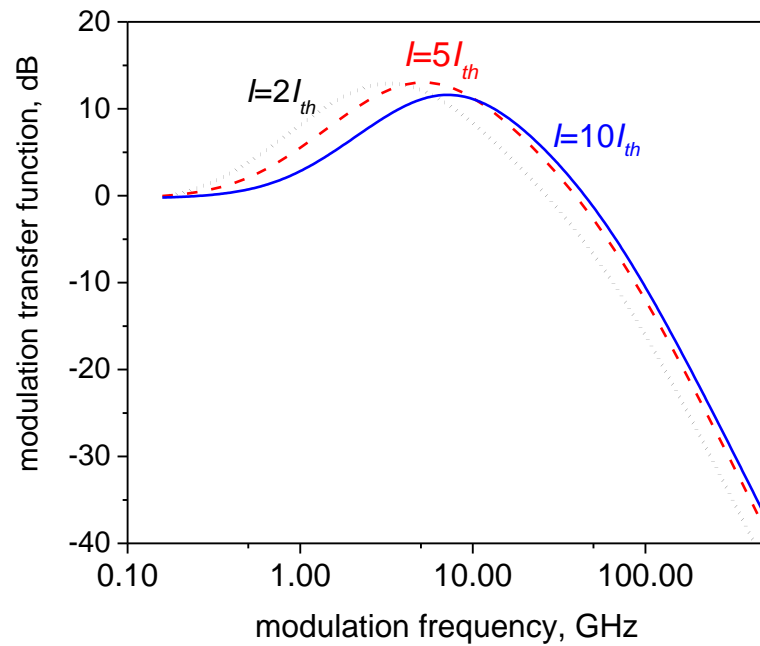


Figure 85: Calculated small-signal response of electrooptic laser modulation at three different values of bias current (for 35 periods in the intermediate reflector and 17 periods in the top reflector)

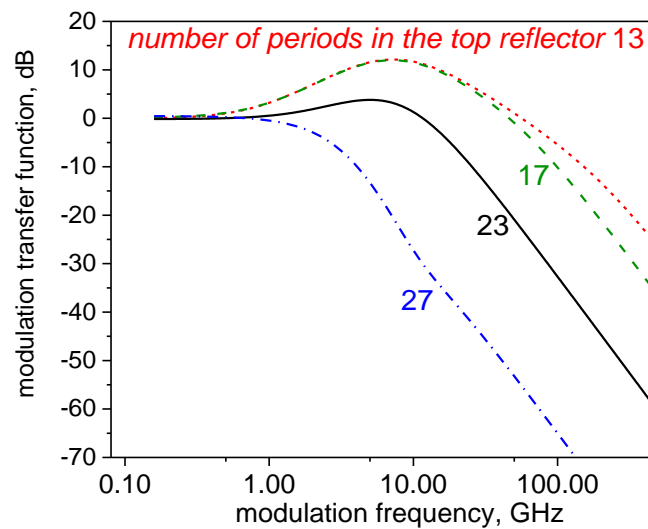


Figure 86: Calculated small-signal response of electrooptic laser modulation for different top DBR periods and 35 periods in the intermediate DBR; current 10 mA

Figure 85 shows calculated small-signal response of electrooptic laser modulation at three different values of bias current (for 35 periods in the intermediate reflector and 17 periods in the top reflector). At low modulation frequencies (below the resonant peak), the figure, with the characteristic broad resonant peak, is fairly similar to the ones calculated using the standard rate equation model (Figure 69). However at high frequencies (above the resonant peak), there is no plateau seen in Figure 69, and the 3dB cutoff modulation frequency can be determined in all designs. This is due to the limitation introduced by the modulator cavity photon lifetime.

Figure 85 also shows that the transfer function for the properly designed compound cavity laser is capable of providing 3dB cut-off frequency as high as hundreds of GHz in a broad range of currents; the cutoff frequency is a rather weak function of total power/current. The figure shows only a 100 GHz cutoff frequency but it can go up hundreds of GHz with less number of periods in the top DBR as shown in Figure 86. This can be expected since the roll-off of the modulation curve at high frequencies, and hence the 3dB cutoff frequency, are mainly determined by the lifetime of the photons in the modulator cavity which does not depend on current in the active cavity. With the laser design shown in the figure (a large intermediate reflector reflectance ensuring the external-modulator-type operation of the modulator section, and a more modest reflectance of the output reflector ensuring the value of τ_{cm} of the order of picoseconds), this limit is indeed of the order of hundreds of gigahertz, and thus not a concern for any realistic modulation scheme.

The situation can be different however with a design of the modulator section less optimised for high speed operation. Figure 86 shows that with a large (but perfectly technologically achievable) number of periods in the top reflector, when the notch in the reflectance of the modulator section (the peak in the transmittance) becomes narrow meaning a large photon lifetime in the modulator cavity, the 3dB frequency drops to ~ 10 GHz, which can be a very real limitation. At the same time, the *amplitude* of output power modulation, given the same

(small) refractive index modulation, increases with an increased number of top reflector period, though this is not shown in Figure 86 in which the transfer function is normalised to 0dB at low frequencies.

As will be discussed later, these features are seen also in the results of large signal modulation simulations (see Figure 100 and Figure 101).

4.4 Large signal analysis

For the large signal analysis, the modified rate equations are solved directly numerically using the Matlab Program (ode45 built-in function) for NRZ digital pseudorandom modulation, as in the standard rate equation model. The results are used to construct an eye diagram as seen by an ideal receiver.

In addition, since the model gives both the amplitude and phase/frequency of the output field, we can analyse the optical spectrum of the laser emission.

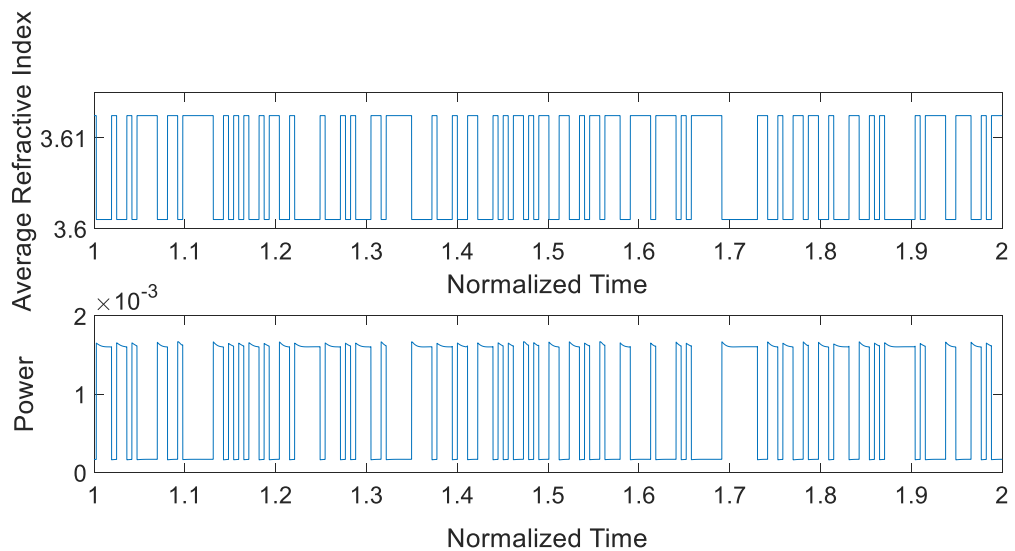


Figure 87: Modulation of Refractive Index, 40 Gbit/s bit rate

Figure 87 shows the modulation of the refractive index; it shows that when the average refractive index is high, the output power is low. Figure 88 shows the real and imaginary parts of the frequency correction as well as the reflectivity. The real part represents the detuning of frequency or the phase modulation while the imaginary part represents the rate

of change in time or amplitude modulation. The normalized time in Figure 87 and Figure 88 is calculated by dividing the time by the carrier lifetime.

$$\Delta\tilde{\omega} = \Delta\omega' + \Delta\omega''$$

$$e^{j(\omega' + j\Delta\omega'')} \geq 0 \rightarrow \text{decay}$$

$$e^{j(\omega' + j\Delta\omega'')} \leq 0 \rightarrow \text{growth}$$

In this figure, the frequency correction is about 100 GHz and it shows the imaginary part goes oscillates around zero.

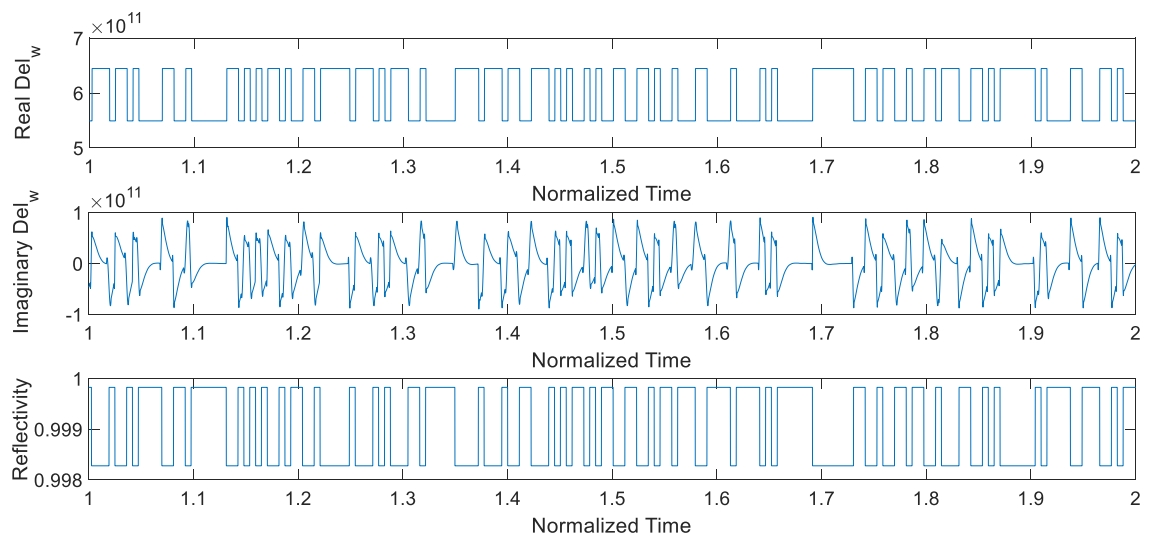


Figure 88: Real and Imaginary Frequency

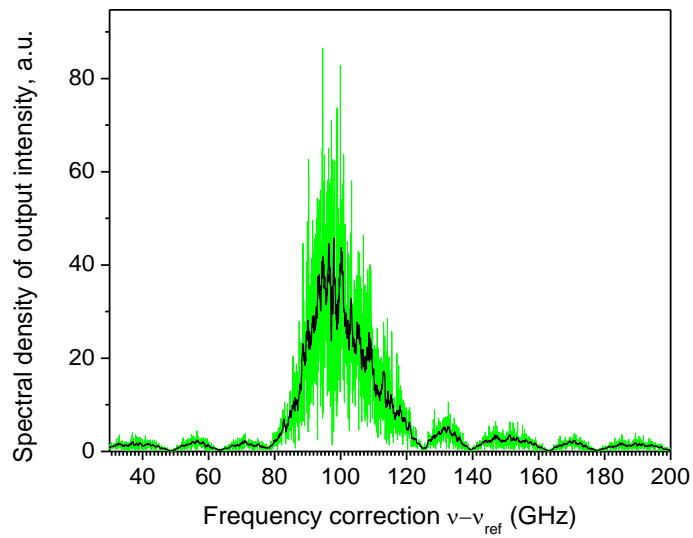


Figure 89: Amplitude Spectrum of output Field at 40 GBit/s

Figure 89 shows a typical calculated output spectrum at 40 GBit/s, with the spectrum near the main peak, with a smoothed line for easier evaluation of the spectral width. The smoothing is performed by adjacent averaging of points, as in, say, [105]. While the spectrum is somewhat asymmetric, implying that there is a bit of chirp in the output, the width at half maximum is 20 GHz, and at e^{-2} close to 40 GHz, or the bit rate, or the Nyquist limit for NRZ modulation, which implies that the chirp is low.

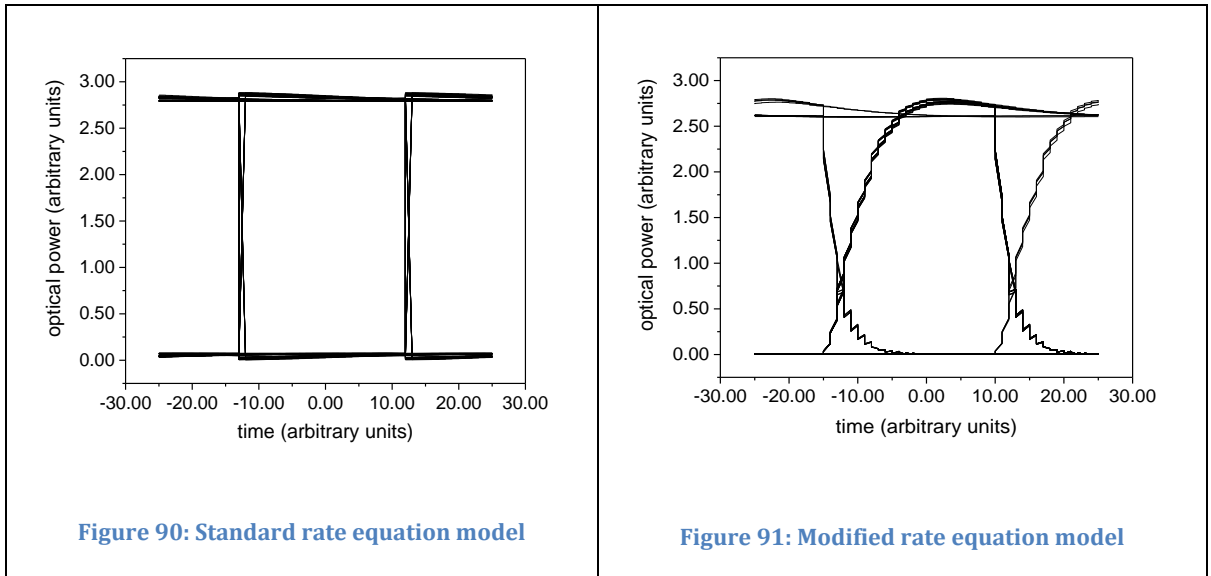


Figure 90 and Figure 91 show the eye diagrams calculated using the standard and modified rate equation models, respectively, for the same amplitude of refractive index modulation.

As can be expected, the modified RE model is free from unphysical abrupt changes from OFF to ON states; instead, it shows gradual transients with elements of oscillatory behaviour in the off state (which is associated with the frequency detuning between the light frequency and the resonator).

As in the standard RE model, we can determine the quality factor of the eye diagram using the Equation (34).

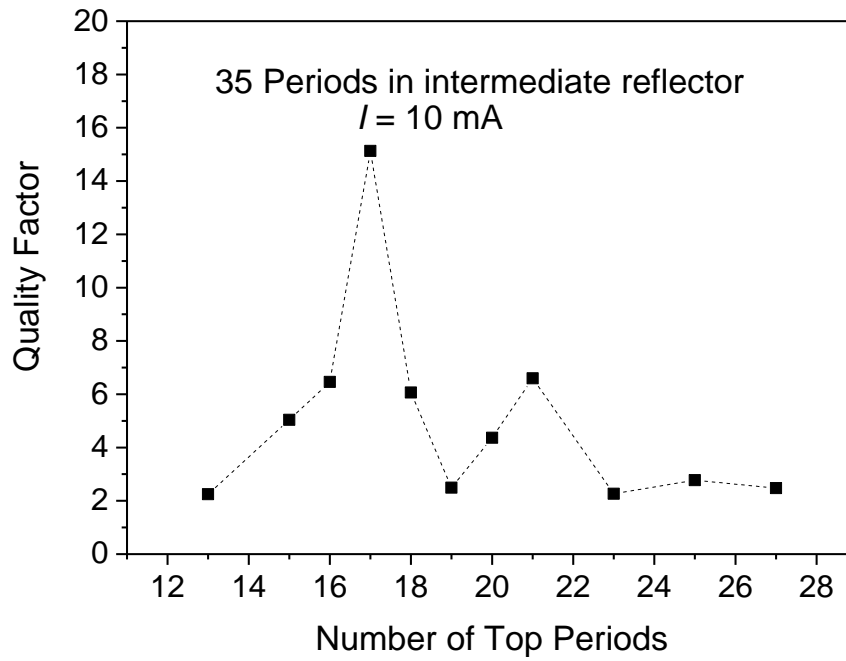


Figure 92: Quality factor when changing number of periods for the top reflector

Figure 92 shows the modulation quality factor as function of the number of layer pairs (periods) in the *top* reflector DBR stack. As seen in the figure, there is an optimum number, in this case around 17. When we increase the number of periods beyond that number, the photon lifetime in the modulator cavity is increased, leading to longer transients and closing the eye diagram, hence bad quality factor. When the number of top reflector period becomes too low, on the other hand, the modulation of power ($P_1 - P_0$) becomes lower, hence lower quality factor.

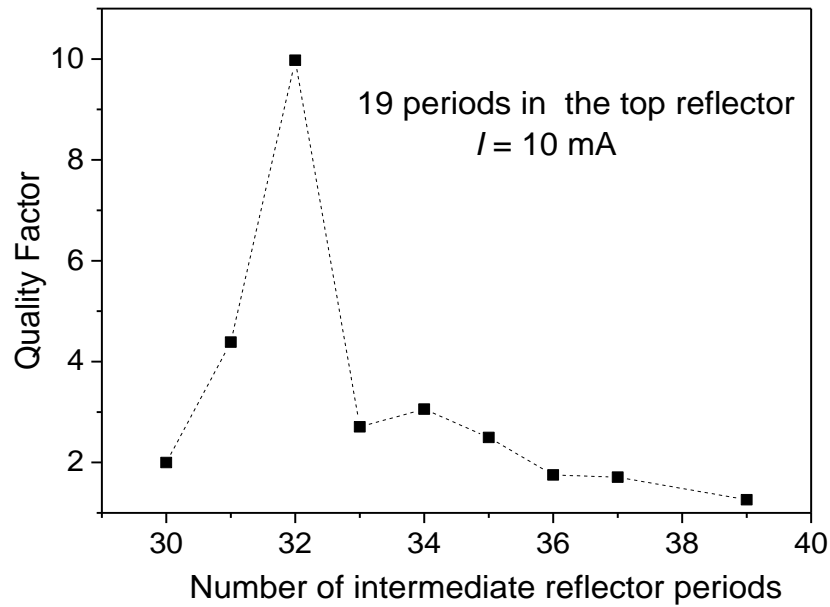


Figure 93: Quality factor when changing number of periods for the intermediate reflector

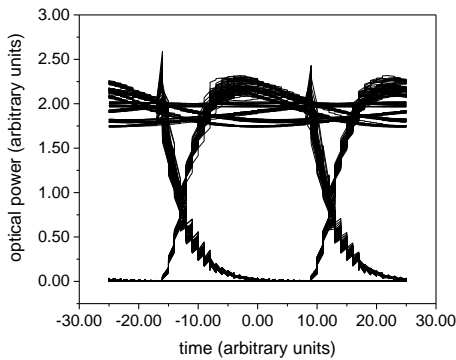


Figure 94: Eye diagram for 32 periods in the intermediate reflector and 19 periods in the top reflector, $I = 10 \text{ mA}$, 40Gbit/s

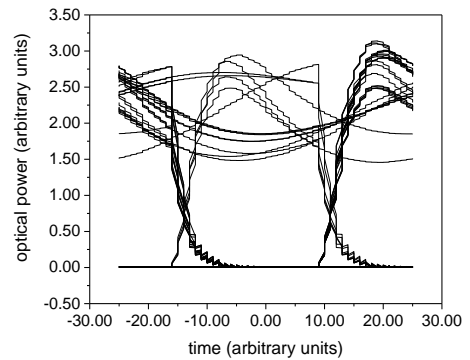


Figure 95: Eye diagram for 31 periods in the intermediate reflector and 19 periods in the top reflector, $I = 10 \text{ mA}$, 40Gbit/s

Figure 93 shows the modulation quality as a function of the number of periods in the *intermediate* reflector. Figure 94 and Figure 95 show eye diagrams for $I = 10 \text{ mA}$, 19 periods in the top reflector, 32 and 31 periods in the intermediate reflector, respectively. This shows again, there is an optimum number of periods, in this case around 32. When the number of periods is increased beyond that value, there is less output power hence low quality factor. When the number of periods is decreased below the optimum level, the active region and the

modulator become more strongly optically coupled, moving from the regime of weak coupling when the modulator cavity works almost as an external modulator to the case of a proper compound cavity, so that the relaxation oscillations effect on the power transients increases. As a result, the eye diagram deteriorates, hence the lower quality factor.

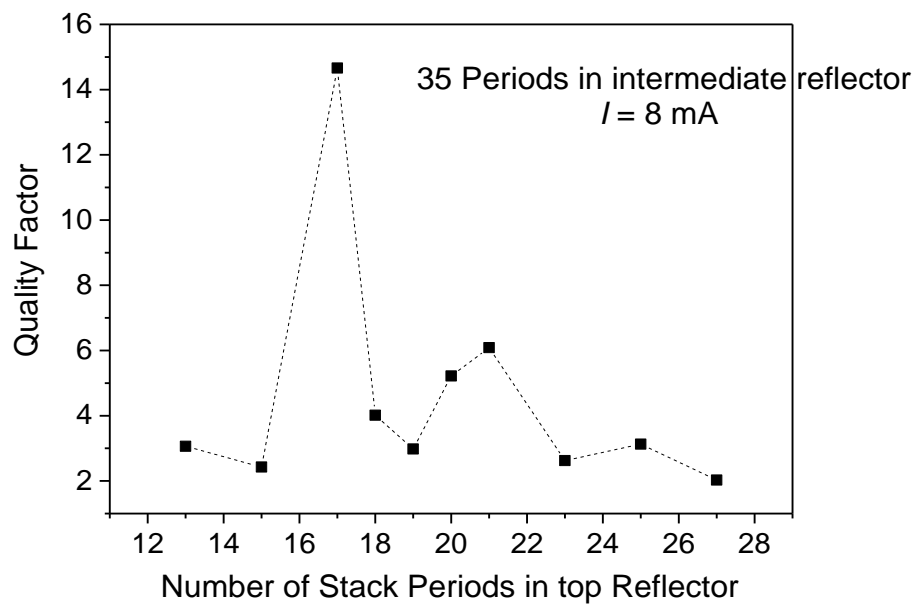


Figure 96: Quality factor when changing number of periods for the top reflector for 8 mA bias current

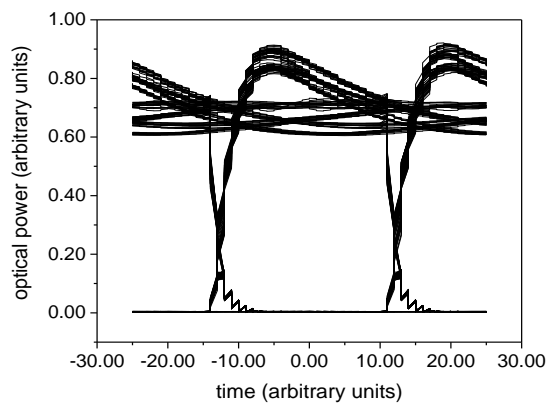


Figure 97: Eye diagram for 35 periods in the intermediate reflector and 17 periods in the top reflector, $I = 8 \text{ mA}$, 40Gbit/s

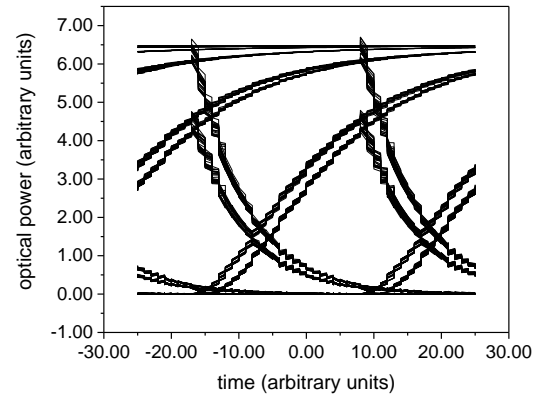


Figure 98: Eye diagram for 35 periods in the intermediate reflector and 23 periods in the top reflector, $I = 8 \text{ mA}$, 40Gbit/s

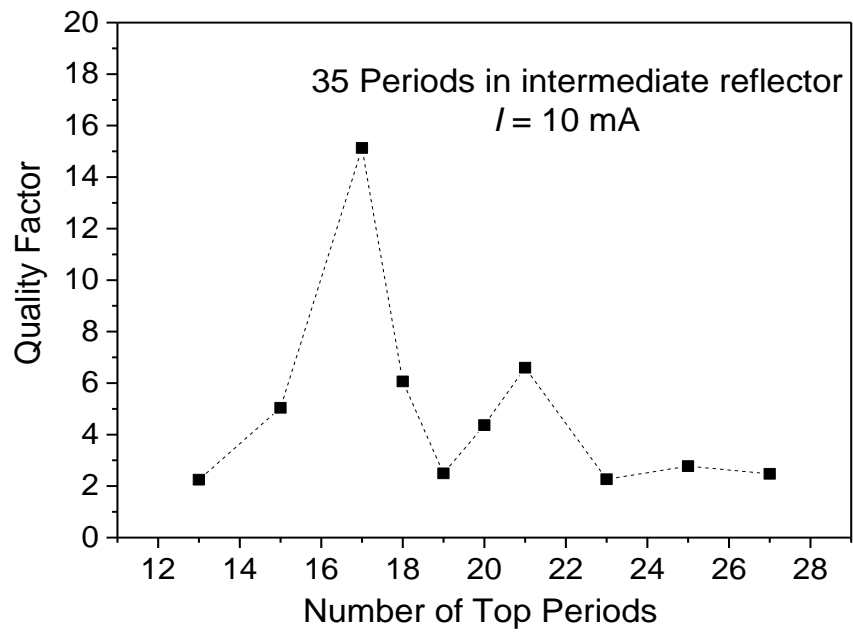


Figure 99: Quality factor when changing number of periods for the top reflector for 10 mA bias current

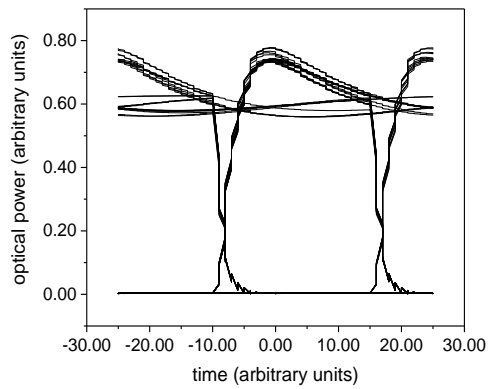


Figure 100: Eye diagram for 35 periods in the intermediate reflector and 17 periods in the top reflector, I= 10 mA, 40Gbit/s

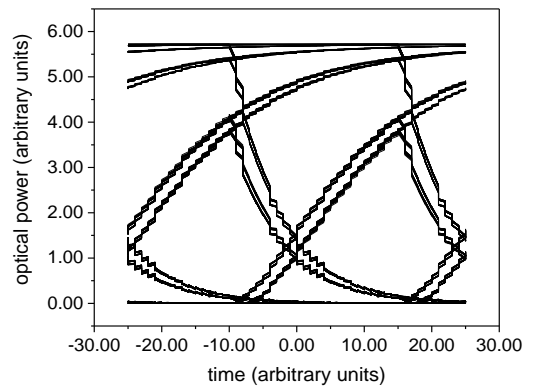


Figure 101: Eye diagram for 35 periods in the intermediate reflector and 23 periods in the top reflector, I= 10 mA, 40Gbit/s

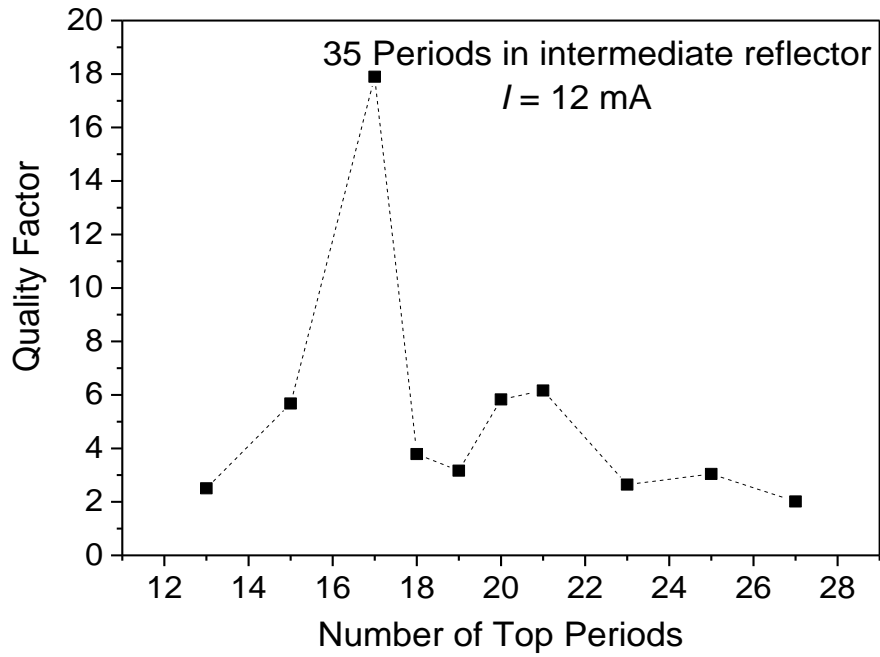


Figure 102: Quality factor when changing number of periods for the top reflector for 12 mA bias current

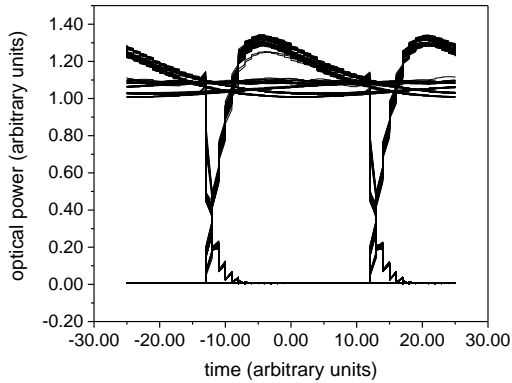


Figure 103: Eye diagram for 35 periods in the intermediate reflector and 17 periods in the top reflector, $I = 12 \text{ mA}$, 40Gbit/s

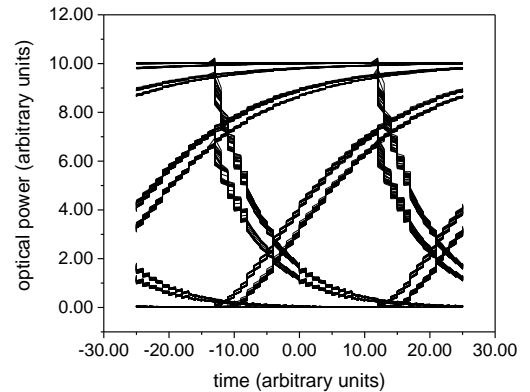


Figure 104: Eye diagram for 35 periods in the intermediate reflector and 23 periods in the top reflector, $I = 12 \text{ mA}$, 40Gbit/s

Figure 96, Figure 99 and Figure 102 show the quality factor as a function of the number of periods in the top reflector for a 35-period intermediate reflector for different bias currents. Figure 97, Figure 98, Figure 100, Figure 101, Figure 103 and Figure 104 show few eye diagrams for currents of 8 mA, 10 mA and 12 mA, respectively. Rather reassuringly, we

observe that the optimum number of periods is not a strong function of the current, so once optimised, a laser should be able to provide good modulation quality at all currents.

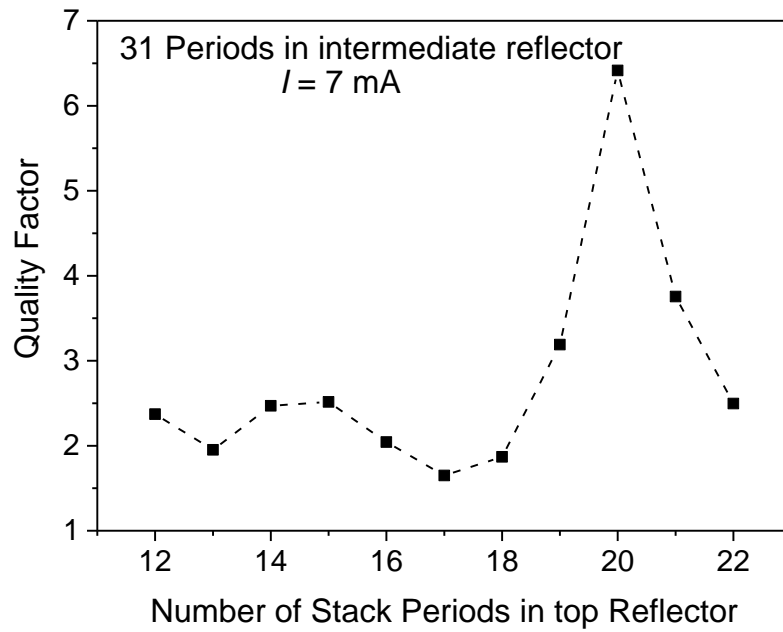


Figure 105: Quality factor when changing number of periods in the top reflector and for 31 periods in the intermediate reflector and 7 mA bias current

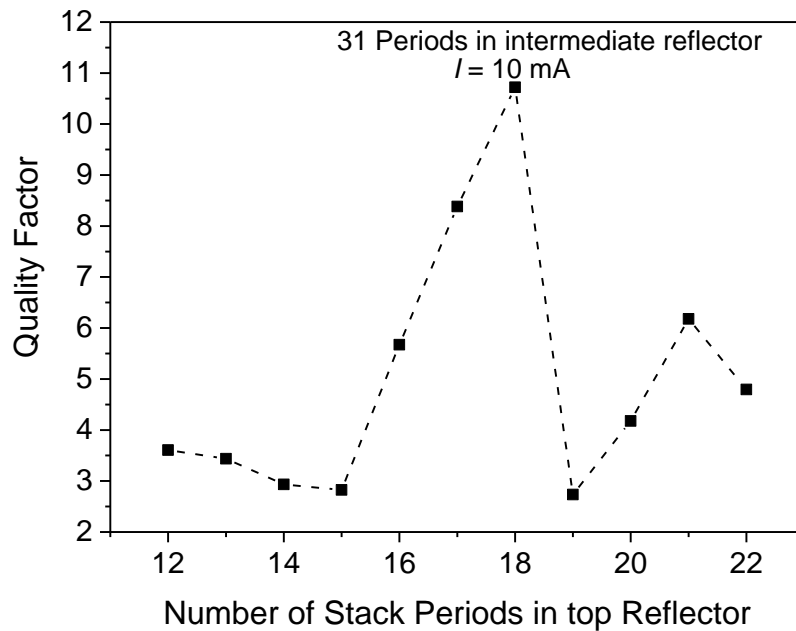


Figure 106: Quality factor when changing number of periods in the top reflector and for 31 periods in the intermediate reflector and 10 mA bias current

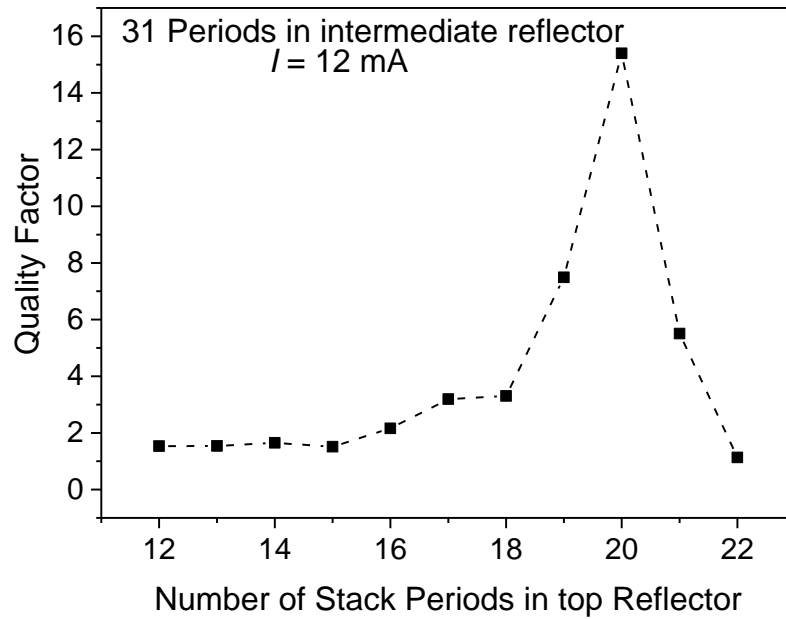


Figure 107: Quality factor when changing number of periods in the top reflector and for 31 periods in the intermediate reflector and 12 mA bias current

Figure 105, Figure 106 and Figure 107 show Quality factor when changing number of periods in the top reflector and for 31 periods in the intermediate reflector and for a bias current of 7 mA, 10 mA and 12 mA, respectively. They show that there is an optimum number of top periods reflector at which there is a maximum quality factor. They show higher quality factors for higher currents.

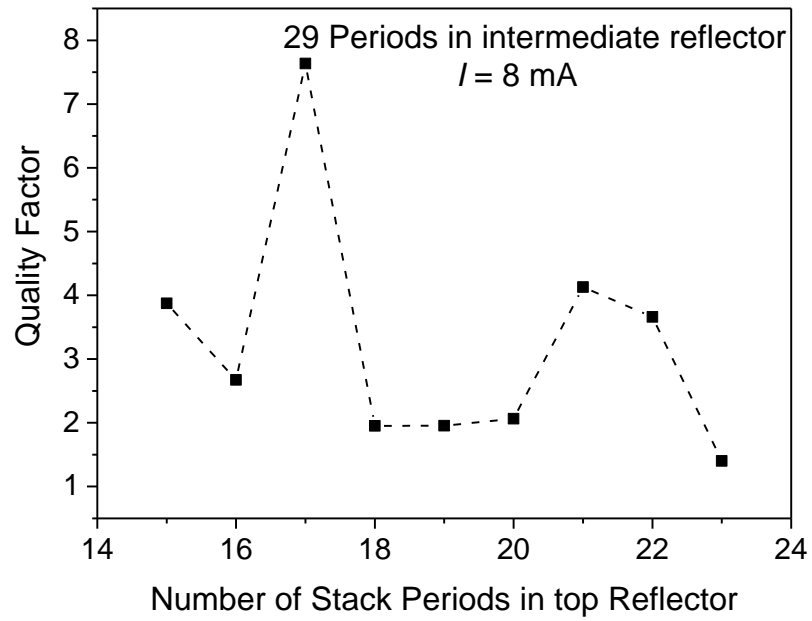


Figure 108: Quality factor when changing number of periods in the top reflector and for 29 periods in the intermediate reflector and 8 mA bias current

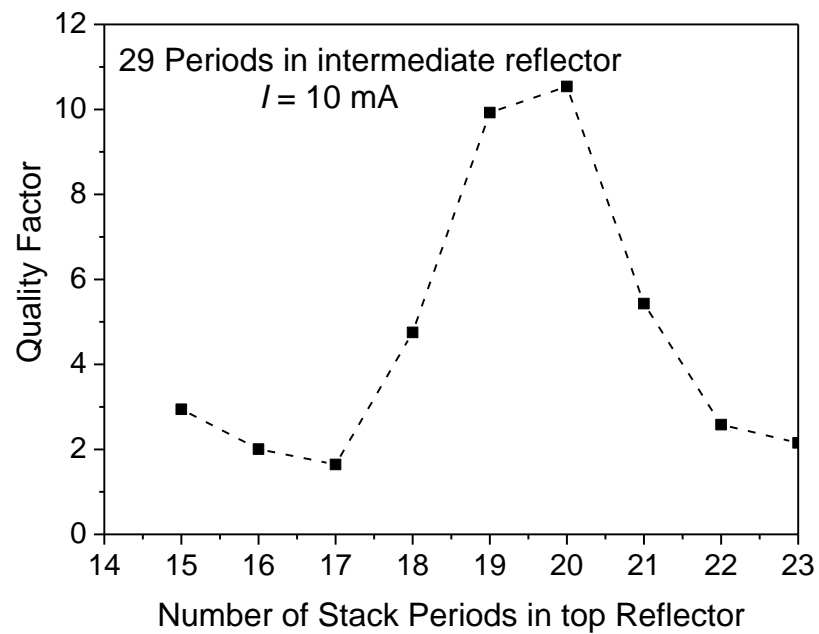


Figure 109: Quality factor when changing number of periods in the top reflector and for 29 periods in the intermediate reflector and 10 mA bias current

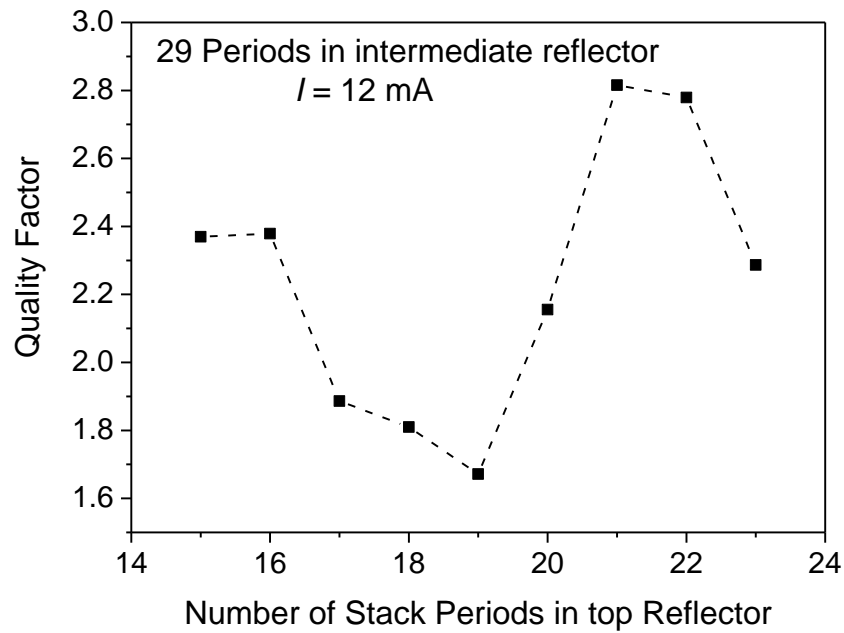


Figure 110: Quality factor when changing number of periods in the top reflector and for 29 periods in the intermediate reflector and 12 mA bias current

Figure 108, Figure 109 and Figure 110 show Quality factor when changing number of periods in the top reflector and for 29 periods in the intermediate reflector and for a bias current of 8 mA, 10 mA and 12 mA, respectively. They show that there is an optimum number of top periods reflector at which there is a maximum quality factor. They show higher quality factors for higher currents.

The above figures show that the best quality factors occur when the intermediate reflector are 35 periods, then 31 periods and 29 periods have the worst quality factor. This might be because when the number of periods is very high (35 periods) there will be almost no electric connection between the active cavity and the modulator cavity which means that there will be no effect for the frequency relaxation oscillation.

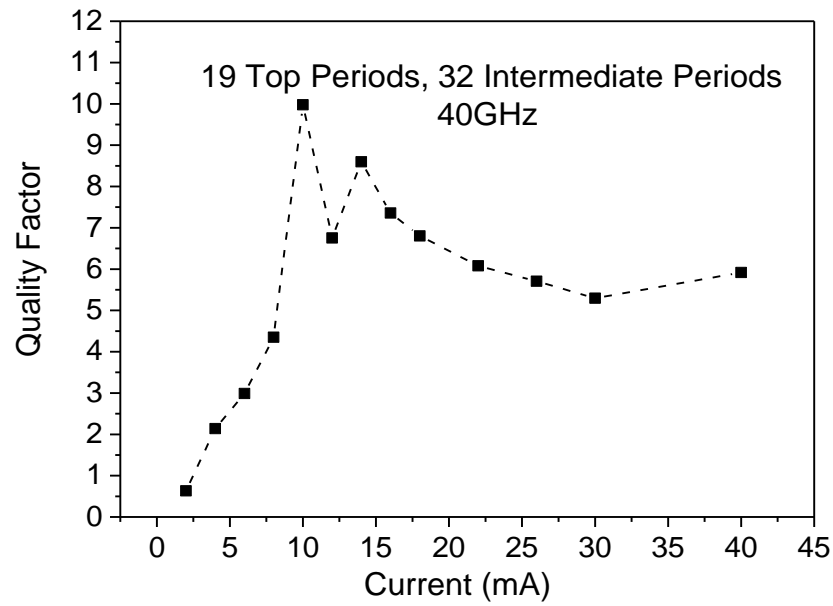


Figure 111: Quality factor when changing the bias current for 40 GBit/s modulation frequency

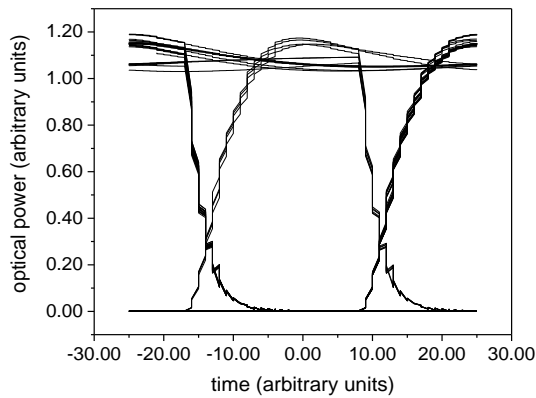


Figure 112: Eye diagram for 35 periods in the intermediate reflector and 19 periods in the top reflector, $I = 8 \text{ mA}$, 40 GBit/s

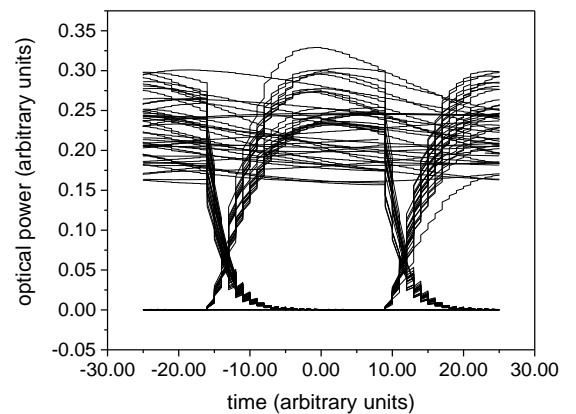


Figure 113: Eye diagram for 35 periods in the intermediate reflector and 19 periods in the top reflector, $I = 2 \text{ mA}$, 40 GBit/s

Figure 111 shows the modulation quality factor as a function of current for 40 GBit/s modulation bit rate. Figure 112 and Figure 113 show eye diagrams for 32 periods in the intermediate reflector and 19 periods in the top reflector, 40 GBit/s, and current of 8 mA and 2 mA, respectively. From 15 - 30 mA bias current, the modulation quality is near constant a large photon density causing fast relaxation oscillations (RO) leads to some decrease in the

modulation quality, though the effect is not large due to the weak coupling between subcavities. Whereas at very high currents, there is a small increase in the quality factor, at very low current values, the modulation quality decreases simply due to lower power, given a similar distribution of the on-state. As a result, there is an optimum (rather modest) current value, though at high currents, the modulation quality is not far below optimum.

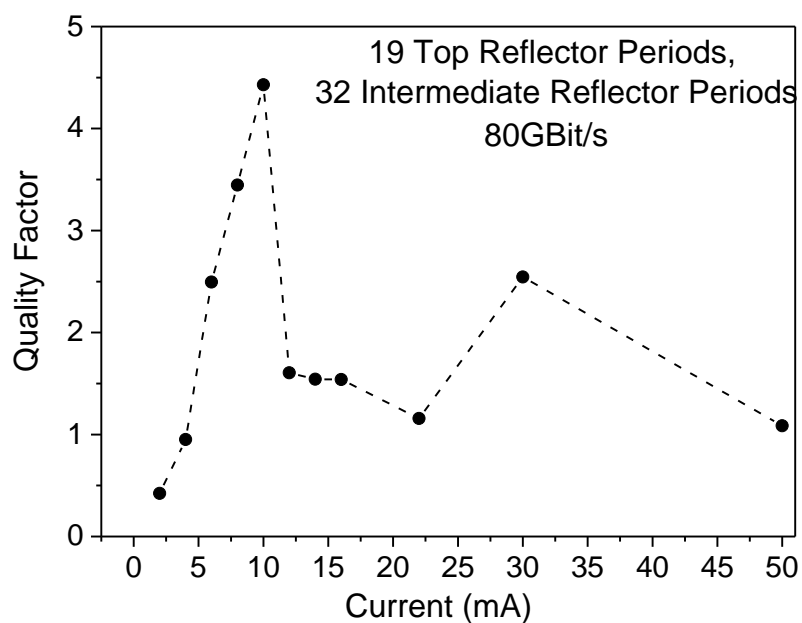


Figure 114: Quality factor when changing the bias current for 80 GBit/s modulation frequency

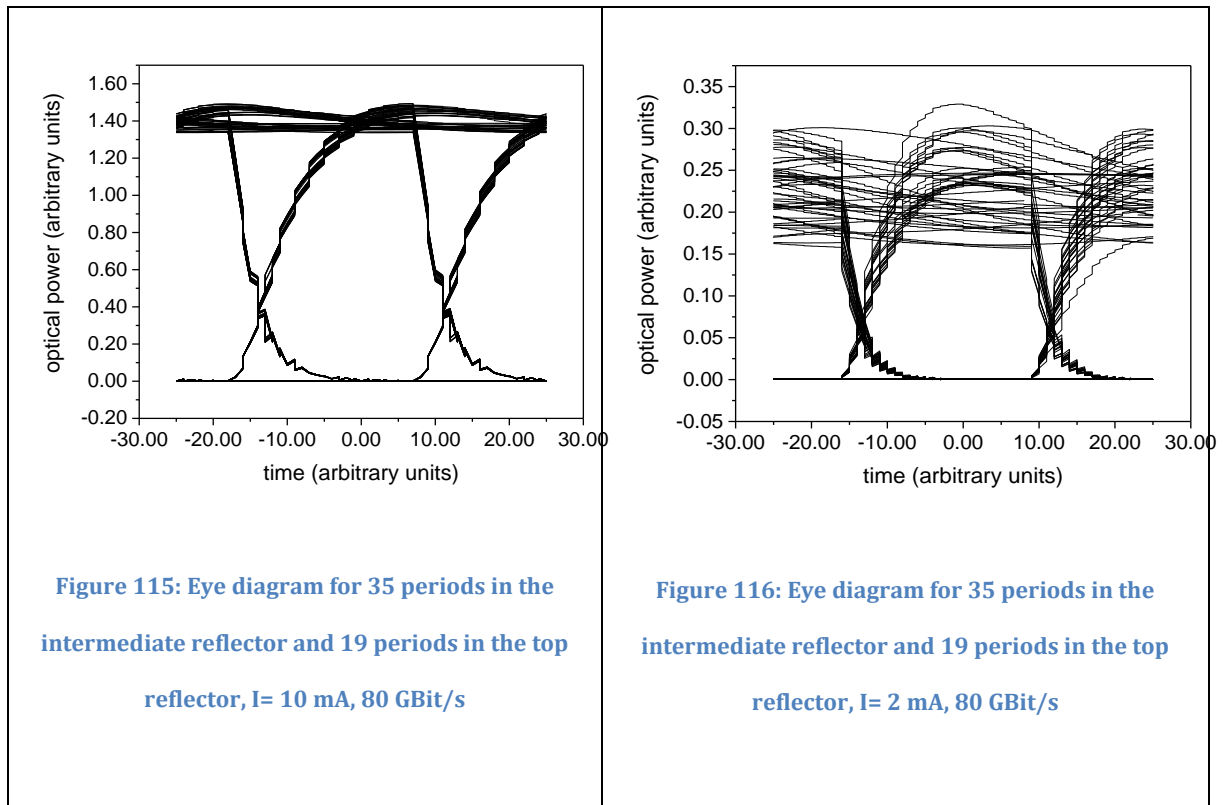


Figure 114 shows a similar curve with a higher modulation rate of 80 GBit/s. Similar qualitative tendencies are observed; quantitatively, the quality factor is smaller than at the lower modulation rate. Figure 115 and Figure 116 show eye diagram for 32 periods in the intermediate reflector and 19 periods in the top reflector, 80GHz and currents of 10 mA and 2 mA, respectively.

Note that in this study, we concentrated on the electromagnetic/carrier kinetic model only, not considering the electrical circuit limitations. Indeed, Zujewski and co-authors [54] [53] have proved that the associated electrical circuit, as studied in [54], of coupled-cavity vertical-cavity surface-emitting laser (CC-VCSEL) can be made to be not a limitation using a traveling wave electrode design [53]. They were also able to make up for the low 50Ω impedance of the modulator which allow the electrical cut-off frequency to go up to 330 GHz [53].

4.5 Chapter summary

After finding some limitations of the the standard rate equation model as detailed in chapter 3, we upgraded the standard rate equations to rate equations with phase, including a new one

for the modulator section. This model is capable of the following (which the standard rate equation model cannot provide):

- a) Deal with modulation of the refractive index, which changes the amplitude and the phase of transmittance and reflectance, rather than with the modulation of photon lifetime, which is a bit artificial.
- b) Calculate the optical spectra (it deals with phase as well as intensity)
- c) Take into account the speed limitations because of the width of the notch in the modulator section transmittance spectrum, which we did not take into account before, by means of the extra rate equation.

The following points can summarize the main findings in this chapter:

0. *As seen in the previous chapter, the standard rate equation model cannot fully describe compound-cavity laser modulation. In this chapter:*
 1. New model has therefore been developed, considering modulation of the refractive index, more accurately describing the electromagnetics of the laser cavity.
 2. The ultimate modulation frequency limit has been identified as determined by the photon lifetime of the modulator cavity (the inverse of the width of the notch in modulator transmittance).
 3. Quality of modulation was found to depend non-monotonically on the numbers of dielectric grating periods in the top and intermediate mirrors (too many periods results in long cavity lifetime, too few periods in weak modulation). This determines the design for optimal performance.
 4. We found there was an optimum number of periods in the top and intermediate reflectors which depends only weakly of current.

Since the purpose of this thesis is to create the most accurate model for advanced high speed semiconductor lasers (and the hypothesis is, effectively, that such a model can be developed by including dynamics of both amplitude and phase), we studied first the

vertical-cavity compound VCSEL's and their limitations, taking into consideration the phase as well as the intensity of the light field in the dynamic model. In the next chapter, the in- plane external cavity laser is to be considered using a fundamentally similar (if somewhat different because of longer cavities), dynamic model and the results will be compared with the vertical compound cavity which I covered in this chapter.

5. IN-PLANE EXTERNAL CAVITY LASER

5.1 Introduction

Advanced semiconductor lasers involving direct modulation of current or photon lifetime, promise substantially higher modulation speed and better dynamic properties than the traditional modulated lasers. In order to create the most accurate model for such advanced high speed semiconductor lasers, it is important to study the limitations and to consider the phase as well as the intensity of the light field in the dynamic model. In this chapter, the in-plane external cavity laser is considered from different current models and analysed theoretically.

A summary of the existing theoretical models used for analysing the dynamics of a VCSEL with an external cavity was given in the review section. Most existing theoretical work, of which the papers by Dalir and Koyama [61] present the most extensive theoretical studies, was performed using the Lang-Kobayashi model, which includes a single delay term.

5.2 Preliminary analysis using the Lang-Kobayashi model

Before developing our own model, we analysed the laser behaviour in the simplified Lang-Kobayashi model used by the previous authors (Equation 14). The question that interests us, which the previous studies did not answer, is how much the cutoff modulation frequency can be increased by increasing the strength of the external feedback, and what limits this increase.

We have therefore performed such a study, for the case of an external cavity with a round trip time of 18 ps (τ_s) which is the time photons travel forward and backward from the oxide stripe amplitude and the reflector terminating the external cavity amplitude (reflectance r_s). In this version of the model, unlike the full one explained later, we set the value of the oxide stripe reflectance r_a to zero for light coming from the external reflector. The complex coupling coefficient was determined as:

$$\kappa \approx \frac{c}{2n_{rs}L_s} \theta_a^2 r_s$$

Where c is speed of light in vacuum, θ_a being the intensity transmittance, r_s is the external cavity amplitude reflectance, n_{rs} is the slow waveguide refractive index and L_s is the external cavity length.

Typical results are shown in Figure 117.

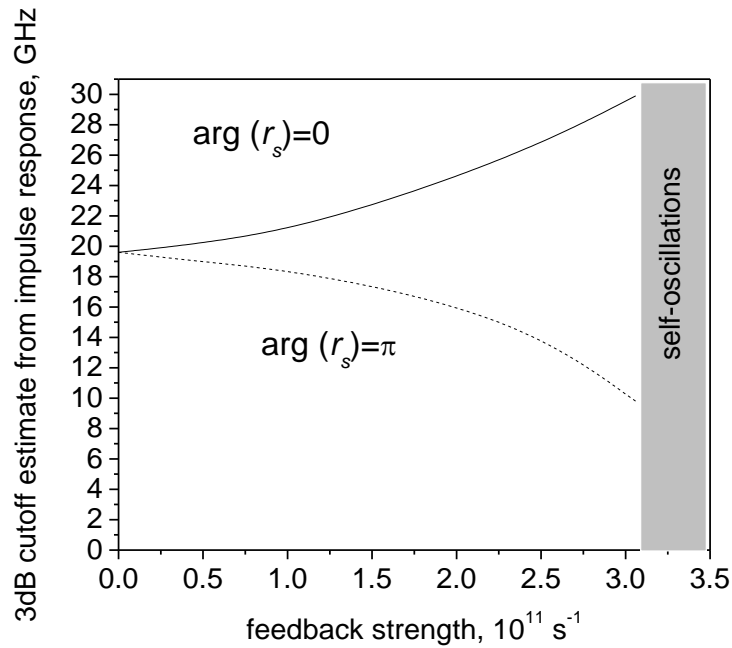


Figure 117: Estimate for 3dB modulation bandwidth using the impulse response method in the Lang-Kobayashi type model for $\tau_s = 18 \text{ ps}$

As in the work by Dalir and Koyama [61], the 3dB frequency is dependent on the phase of the external feedback. Unlike the work by Dalir and Koama, we took the self-phase modulation into account, so it was somewhat more difficult to determine the steady state feedback phase before the simulations. So rather than controlling the feedback phase, we controlled the phase of the external reflector r_s , which is the parameter that can be controlled in fabrication of the laser.

Because the amplitude transmittance of the oxide layer is imaginary (and so θ_a^2 is negative), the case of the $\arg(r_s)=0$ roughly corresponds to out-of-phase feedback (as it gives a negative κ), and the case of $\arg(r_s)=\pi$, to in-phase feedback (as it gives a positive κ).

Simulations show that the nearly out of phase feedback (zero phase of the external cavity amplitude reflectance (r_s) increases the modulation band, and the nearly in phase feedback (π phase of the external reflector) leads to a decrease in the resonance frequency and hence the cutoff frequency, in qualitative agreement with the published work.

The limit to the modulation frequency increase is set by a qualitative change in the laser dynamics. The amplitude of the relaxation oscillations peak increases with the feedback strength, and beyond a certain value the oscillations become undamped, with a self-pulsating regime observed. Clearly, this is not suitable for modulation. Figure 118 shows the intensity for the operating point corresponding to stable laser dynamics. It shows a relaxation oscillation transient settling down to a steady state solution as in a solitary laser, but with a higher relaxation oscillation frequency, promising better modulation behaviour. Figure 119 show the intensity in the unstable operating point, relatively far beyond the critical point for instability ($r_s= 0.99$). Under such conditions, the behaviour of the laser is chaotic (aperiodic), though at smaller reflectances the unstable dynamics can be in the form of periodic oscillations (period 1 dynamics).

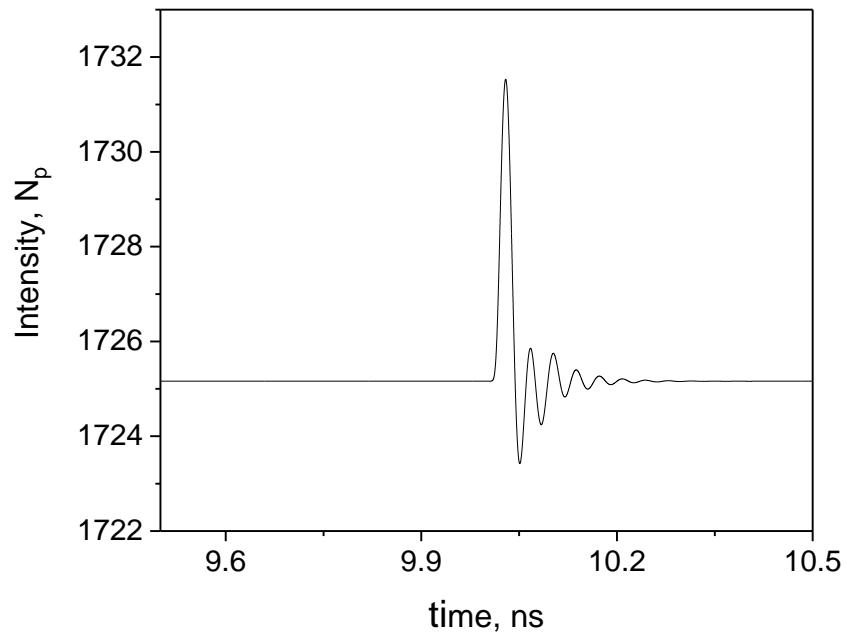


Figure 118: Stable in-plane external cavity laser $r_s=0.6$, bias current =1.5 mA

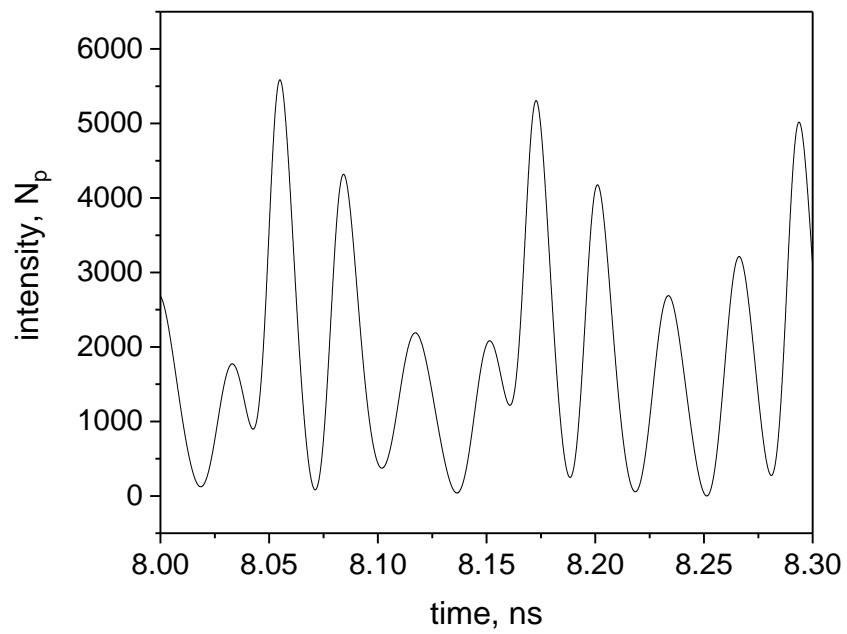


Figure 119: Unstable in-plane external cavity laser $r_s=0.99$, bias current =1.5 mA

The simulations mentioned in the literature in section 2.5.1, show that the modulation frequency can be increased by a factor of 1.5-2 by the external feedback. However, the limitations of the model (see below) does not allow full confidence in this result, so we derived a model of our own.

Figure 120 shows the effect of increasing the feedback strength for Lang-Kobayashi type model for $\tau_s=8$ ps. The figure shows a non-monotonic relationship between the 3dB cutoff frequency and the feedback strength with a peak value at $1.1 \times 10^{11} \text{ s}^{-1}$ feedback strength. The curve goes to instabilities when the feedback strength is more than $2.4 \times 10^{11} \text{ s}^{-1}$. Figure 121 shows the estimate for non-flatness of damping level using the impulse response method in the Lang-Kobayashi type model for a round trip time of 8 ps ($\tau_s=8$ ps).

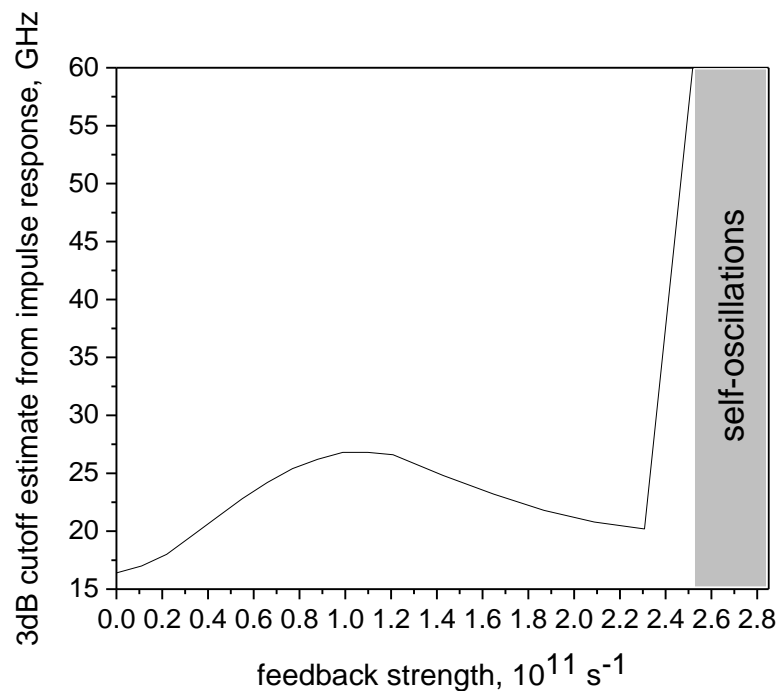


Figure 120: Estimate for 3dB modulation bandwidth using the impulse response method in the Lang-Kobayashi type model or $\tau_s = 8$ ps

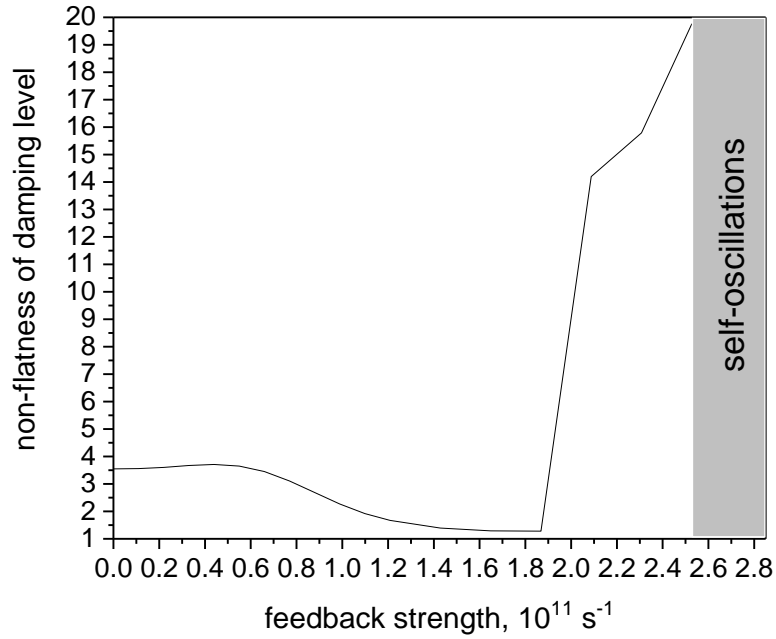


Figure 121: Estimate for non-flatness of damping level using the impulse response method in the Lang-Kobayashi type model for $\tau_s=8 \text{ ps}$

5.3 Electromagnetic Model

As mentioned above, the main problem with using the Lang-Kobayashi model for analysing a VCSEL with the in-plane feedback is that using a single delayed term, even in the case of an edge-emitting laser (which is well described by a one-dimensional model), is only justified if the multiple round-trips in the external cavity give small contributions to the laser dynamics. This can happen either if the external reflectance, denoted r_s in our studies below, is small ($|r_s| \ll 1$ which is the case for which the Lang-Kobayashi model was originally derived) or when the reflectance at the interface between the laser and the external cavity is small (in our notation $|r_a| \ll 1$, which is the case, for example, with external cavity distributed feedback lasers). In a VCSEL with in-plane feedback, neither is the case, so the multiple round-trips in the external cavity should play a part. Therefore, it is preferable to derive a model based on a careful electromagnetic treatment of the cavity to generalise the existing one. The task is made more complex by the fact that in the case of the in-plane cavity, we cannot, from the start, restrict ourselves even approximately to one-dimensional analysis as in the vertical

cavity problem, as the in-plane cavity problem is substantially two-dimensional. We need to distinguish the vertical dimension z and the direction of the in-plane cavity x (the treatment of the third dimension y , the lateral one perpendicular to the external cavity orientation, remains relatively trivial).

The vertical resonator is, as in the case of a one-dimensional cavity, described using a Fabry-Perot type equation:

$$r_t(k_z)r_b(k_z) \exp(-j2k_zL_z)\tilde{G}_z = 1 \quad (53)$$

Here, the complex vertical double pass amplitude gain is:

$$\tilde{G}_z = \exp[(1 + j\alpha_H)\xi g d_a - \alpha_i L_z] \quad (54)$$

Where, as before, ξ is the standing wave factor, g is the material gain in the active layer, d_a is the active layer thickness, α_i is the average internal loss in the vertical cavity. The factors of $\frac{1}{2}$ (amplitude gain) and 2 (double pass) cancel.

As usual in a VCSEL, only the phase of the top and bottom reflectors needs to be taken as k_z -dependent; the amplitude is approximately constant:

$$r_{t,b}(k_z) = |r_{t,b}| \exp \left[j \left(\phi_{t,b}^{ref} + \phi'_{t,b}(k_z - k_{ref}) \right) \right]$$

Allowing us to introduce the effective vertical cavity length as:

$$L_z^{eff} = L_z - \frac{1}{2}(\phi'_t + \phi'_b)$$

(Which is equivalent to the more usually written definition in terms of frequency rather than wave vector derivatives). Then we can estimate the *vertical* wave vector component in the standard form:

$$k_z = k'_z + jk''_z \quad (55)$$

$$k'_z \approx k'_{z0} + \frac{1}{2}\Gamma_z \alpha_H g; \quad k'_{z0} = \frac{\pi q_z - (\phi_t^{ref} + \phi_b^{ref})}{L_z^{eff}}$$

$$k''_z \approx -\frac{1}{2L_z^{eff}} \ln|r_t r_b \tilde{G}_z| = -\frac{1}{2} \left(\Gamma_z g - \alpha_i^{eff} - \frac{1}{L_z^{eff}} \ln \frac{1}{|r_t r_b|} \right)$$

With $\Gamma_z = \xi d_a / L_{effz}$ the vertical confinement factor, and $\alpha_i^{eff} = \frac{L_z}{L_z^{eff}} \alpha_i$ (if necessary, this effective total loss can also include the loss in the mirrors, in which case $r_t r_b$ are to be understood as lossless mirror reflectances).

From this, noting that $k_x^2 + k_y^2 + k_z^2 = k^2 = \left(\frac{n\omega}{c}\right)^2$, we can calculate the in-plane wave vector component. From symmetry considerations, in the case of a square cross-section for simplicity, $k_x = k_y$, so noting that $|\text{Im}(k_z)| = |k''_z| \ll \text{Re}(k_z) = k'_z$, we get:

$$k_x = k'_x + jk''_x$$

$$k'_x \approx \frac{\sqrt{2}}{2} \sqrt{k^2 - k_z'^2} \approx k'_{x0} + \frac{k'_{z0}}{4k'_x} \Gamma_z \alpha_H g, \quad k'_{x0} = \frac{\sqrt{2}}{2} \sqrt{k^2 - k_z'^2} \quad (56)$$

$$k''_x \approx -\frac{k'_{z0}}{2k'_x} k''_z$$

As in the case of vertical wave vector, we can expect $|k''_x| \ll k'_x$ under typical operating conditions of the laser.

Formally speaking, the small k'_x corresponds to a *large* in-plane *phase* velocity $c_x = \omega / k'_x$. However calculating the *group* velocity, we find (for the case of a transparent waveguide, $k''_x = 0$):

$$v_{gx} = \left(\frac{dk_x}{d\omega}\right)^{-1} = \frac{2k'_x}{k} v_g \quad (57)$$

Where as usual $v_g = \left(\frac{dk}{d\omega}\right)^{-1}$ is the total group velocity in the material of the VCSEL cavity.

This value of v_{gx} is a small value ($k'_x \ll k$, so $v_{gx} \ll v_g$) so the in-plane behaviour of the laser does indeed correspond to a *slow wave waveguide*, as discussed by Koyama and co-authors [57].

In the y -direction, the modal profile is a pure standing wave, the lateral mode of the VCSEL cavity, and we shall assume here that the light is entirely in the cavity/waveguide ($\Gamma_y=1$, corresponding to a strong waveguide; a generalisation would be straightforward if needed). In the x -direction, however, we need a more careful analysis.

The geometric picture used is presented in Figure 122. In the in-plane direction, the laser is just a section of the slow-wave waveguide, of a length L_x , with gain or loss due to k''_x . The section is terminated on the left hand side by the outer reflectance r_o (typically $|r_o| \sim 1$ so there is no leakage of radiation in that direction, but we can keep the analysis generic), and on the right, by an oxide stripe separating the laser from the amplifier (slow waveguide external cavity). The oxide stripe is assigned an amplitude reflectance r_a (“ a ” for “*amplifier side*”) and an amplitude transmittance $\sqrt{\theta_a} \exp(j\phi_\theta)$, θ_a being the intensity transmittance and $R_a = |r_a|^2$ the intensity reflectance. If there is no scattering of light out of the slow-waveguide mode in the oxide, $R_a + \theta_a = 1$; in reality it is likely that some scattering is present so $R_a + \theta_a < 1$.

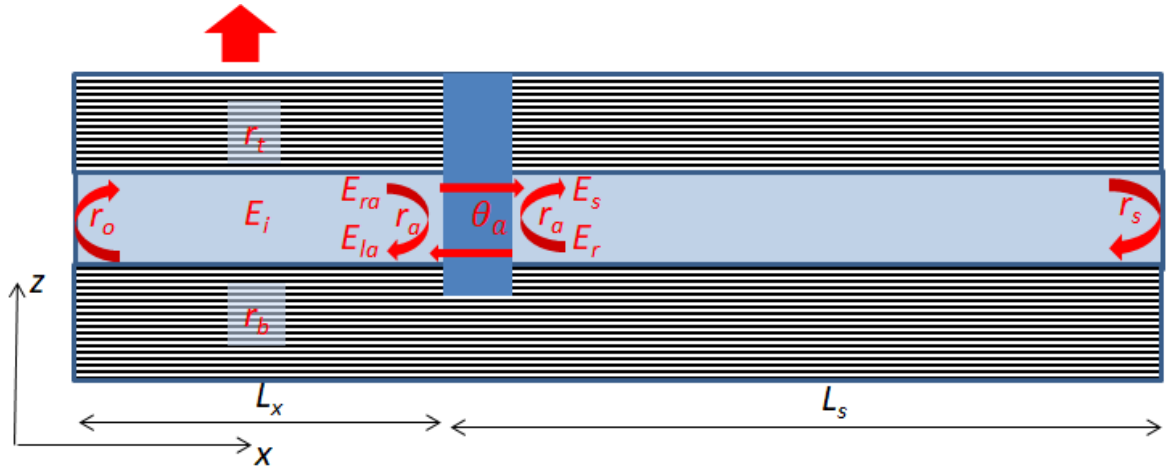


Figure 122: Schematic of the electromagnetic 2D model for a compound in-plane cavity

Without loss of generality, we can assume that r_o and r_a are both real (and negative, so that the fundamental order lateral mode has one antinode at the middle and nodes at either end – this can be expected in a slow wave waveguide because the angle of incidence of the mode on the facet is very large). Reciprocity of linear optics means also that r_a is the reflectance seen by *both* the light incident onto the oxide stripe in the direction from the laser to the slow wave external cavity and by the light in the opposite direction: both the amplitude and the phase of the reflection are the same, since we have the same waveguide either side. This means that we must have the phase of the transmittance $\varphi_\theta = \frac{\pi}{2}$ in order to satisfy energy conservation, as will be discussed in more detail below.

The slow wave is terminated by the equivalent reflectance r_s which is complex and, in our slow amplitude/rotating wave analysis, can have an arbitrary phase, accounting for “subwavelength” ($\ll 1/k'_x$) variations in the external cavity length (given the small value of k'_x , these “subwavelength” variations in the slow waveguide can actually be of the order of micrometers).

For derivation, we shall parametrise the light using the “average light amplitude” inside the cavity E_i , defined in such a way that $|E_i| = \sqrt{N_{pi}}$, where N_{pi} is the longitudinally averaged

photon density. Moreover, we shall denote E_{la} the field at the right side of the laser cavity (facing the slow wave amplifier) and travelling *leftwards* (into the laser).

If a field E_{inj} is incident onto (injected into) the cavity from the slow wave waveguide, then in frequency domain, we have the usual Fabry-Perot type equation:

$$E_{la} = \frac{\sqrt{\theta_a} \exp(j\varphi_\theta)}{1 - r_o r_a \exp(-j2k_x L_x)} E_{inj} \quad (58)$$

Furthermore, we can introduce a parameter $f_x(t) = N_{pi} / |E_{la}|^2$. Without much loss of generality, we can assume that the phase of E_i is the same as that of E_{la} (in particular, in a high quality cavity, with $|r_o r_a|$ of the order of 1 (realistically more than about 0.3-0.5 as in an edge-emitting laser), we have a real and approximately constant $f_x \approx 2$), in which case:

$$E_i = \sqrt{f_x} E_{la} = \frac{\sqrt{f_x \theta_a} \exp(j\varphi_\theta)}{1 - r_o r_a \exp(-j2k_x L_x)} E_{inj}$$

Then, using the definition of the in-plane group velocity, we can set

$$k_x = k_{xm} + \Delta k_x$$

$$k_x = k_{xm} + \frac{1}{v_{gx}} \delta\omega$$

(k_{xm} being the value at the signal frequency corresponding to the laser mode, complex as described by Equation 55). If the reference frequency at the modal frequency, which is a natural choice, then:

$$\text{Re}(k_m) = k'_m = k_0 (1 - r_o r_a \exp(-j2(k_{xm} + \Delta k_x) L_x)) E_i = \sqrt{f_x \varphi_a} \exp(j\varphi_\theta) E_{inj}$$

and using: $\exp(x) = 1 + x, |x| \ll 1$:

$$(1 - r_o r_a \exp(-j2k_{xm} L_x) + j2r_o r_a \exp(-j2k_{xm} L_x) \Delta k_x L_x) E_i = \sqrt{f_x \varphi_a} \exp(j\varphi_\theta) E_{inj}$$

k_{xm} corresponds to the laser lateral mode, so $\exp(-j2L_x k'_{xm}) \approx 1$.

$$k_x'' \approx -\frac{k_z'}{2k_x'} k_z''$$

$$(1 - |r_o r_a| \exp\left(-\frac{k_z'}{2k_x'} k_z'' L_x\right)) E_i + j \frac{2L_x}{v_{gx}} \Delta\omega E_i = \sqrt{f_x \theta_a} \exp(j\varphi_\theta) E_{inj}$$

Then, as in the analysis of the vertical cavity, or in the analysis of mode-locked VECSEL in the literature (see e.g. Mulet and Balle 2005 [106]), we can switch from frequency domain to time domain by substituting $j\delta\omega \rightarrow \frac{d\delta\omega}{dt}$ (after which the index m in k_{xm} can be dropped).

Finally, we obtain a differential equation for the amplitude of light inside the cavity in the form:

$$\frac{dE_i}{dt} \approx \frac{1}{T_x \exp(G_x^{net}(t) T_x)} \left\{ \sqrt{f_x \theta_a} \exp(j\varphi_\theta) E_{inj} + (1 + j\alpha_{Hg}) (\exp(G_x^{net}(t) T_x) - 1) E_i \right\} \quad (59)$$

Where $T_x = 2L_x/v_{gx}$ is the in-plane round-trip time of the laser cavity, and $\tilde{G}_{net}(t)$ is the net in-plane round-trip gain which, after some manipulations, using the expressions for v_{gx} and k_x'' , and noting that that $\frac{k_z'}{k} \approx 1$, can be expressed as:

$$G_x^{net}(t) \approx \frac{1}{2} \left[v_g \Gamma g - \left(\frac{1}{\tau_{ph}^z} + \frac{1}{\tau_{ph}^x} + \frac{1}{\tau_{ph}^{in}} \right) \right] \quad (60)$$

Here,

$$\frac{1}{\tau_{ph}^z} = \frac{v_g}{2L_z^{eff}} \ln \frac{1}{|r_t r_b|^2} \quad (61)$$

$$\frac{1}{\tau_{ph}^x} = \frac{1}{T_x} \ln \frac{1}{|r_a r_o|^2} \quad (62)$$

And

$$\frac{1}{\tau_{ph}^{in}} = v_g \alpha_i^{eff} \quad (63)$$

Determine the lifetimes of photons with respect to vertical and in-plane cavities and internal parasitic loss respectively, α_i being the internal loss.

In the case of weak injection ($|E_{inj}| \ll |E_i|$), we typically have $|\exp(G_x^{net}(t)T_x) - 1| \ll 1$, so the exponential in the denominator of (59) can be neglected, and within Figure 122 braces one gets $\exp(G_x^{net}(t)T_x) - 1 \approx G_x^{net}(t)T_x$, which results in the standard rate equation with an injection term. In the case of strong injection, the laser operates, in-plane, essentially as an optical amplifier, hence the term $\exp(G_x^{net}(t)T_x) - 1$, which is reminiscent of the amplifier theory.

In the case of an external cavity, the *injection* field is the *reflected* field:

$$E_{inj} = E_r$$

The reflected field, in its turn, is determined by the boundary conditions at the outer side of the oxide stripe (the size of which we neglect here – for the purposes of travel time, it is included in the length of the external cavity, and for the purposes of boundary conditions, the oxide is treated as a lumped reflector-transmitter).

To formulate these outside boundary conditions, we notice that the field at the right facet of the laser, inside the laser, is $E_{ra} = E_{la} \frac{\exp(G_x^{net}(t)T_x)}{r_a}$ (going round the cavity and returning to the right, the light sees the normal round-trip gain, but only the reflection at r_o , not r_a)

The field travelling rightwards (out of the laser cavity) *outside* the cavity then is composed of the field coming out of the laser $\sqrt{\theta_a} \exp(j\varphi_\theta) E_{ra}(t)$ and the field returned from the external reflector and reflected back from the oxide stripe $r_a E_r(t)$:

$$E_s(t) = \sqrt{\frac{\theta_a}{f_x}} \exp(j\varphi_\theta) \frac{\exp((G_x^{net}(t)T_x)(t)T_x)}{r_a} E_i(t) + r_a E_r(t) \quad (64)$$

At the outside reflector, in the case of a passive external cavity (or, approximately, for an amplifying one with the gain exactly compensating the loss), we have a simple reflectance condition which for the returned field at the oxide stripe means:

$$E_r(t) = r_s E_s(t - \tau_s) = [r_s] \exp(j\varphi_s) E_s(t - \tau_s) \quad (65)$$

Where $\tau_s = 2L_s/v_{gx}$ is the round-trip delay of the external slow-waveguide cavity, L_s being its physical length. A generalisation for a generic amplifying external cavity can be readily implemented using the reflective amplifier theory developed by Antonelli and co-authors, 2015 [107].

$$\begin{aligned} \frac{dh}{dt} = & \frac{h_u - h}{\tau_{\alpha s}} - \frac{1}{u_s} \frac{h}{h - \alpha_s L} [\exp(h - \alpha_s L) - 1] \left\{ |E_s(t)|^2 \right. \\ & \left. + |r_s|^2 \exp\left(h\left(t - \frac{\tau_s}{2}\right) - \alpha_s L\right) \left| E_s\left(t - \frac{\tau_s}{2}\right) \right|^2 \right\} \end{aligned} \quad (66)$$

Where “ h ” is the integrated single pass gain in the slow waveguide amplifier, ($h_u = g_0 L$) is the unsaturated value given by current, L is the slow waveguide (amplifier) length, and α_s is the effective loss in the amplifier (including vertical emission).

The expression for the returned field then needs to be modified as [107]:

$$E_r(t) = |r_s| \exp(j\varphi_s) \exp\left[\frac{1}{2}\left(h\left(t - \frac{\tau_s}{2}\right) + h(t - \tau_s)\right)(1 + j\alpha_{Ha}) - \alpha_s L\right] E_s(t - \tau_s) \quad (67)$$

The account for amplified feedback was implemented in our model and was investigated in brief (Figure 123). We found it did not make much difference from the passive external cavity ($h=0$) with appropriately adjusted reflectances, at least so long as long as the time of recombination in the amplifier (both stimulated and spontaneous together) remained longer than the bit period, as was the case in all our simulations. For higher values of h , stimulated recombination in the amplifier may have changed the dynamics, but those values of h were not relevant in our work as they led to dynamic instabilities as shown in Figure 132.

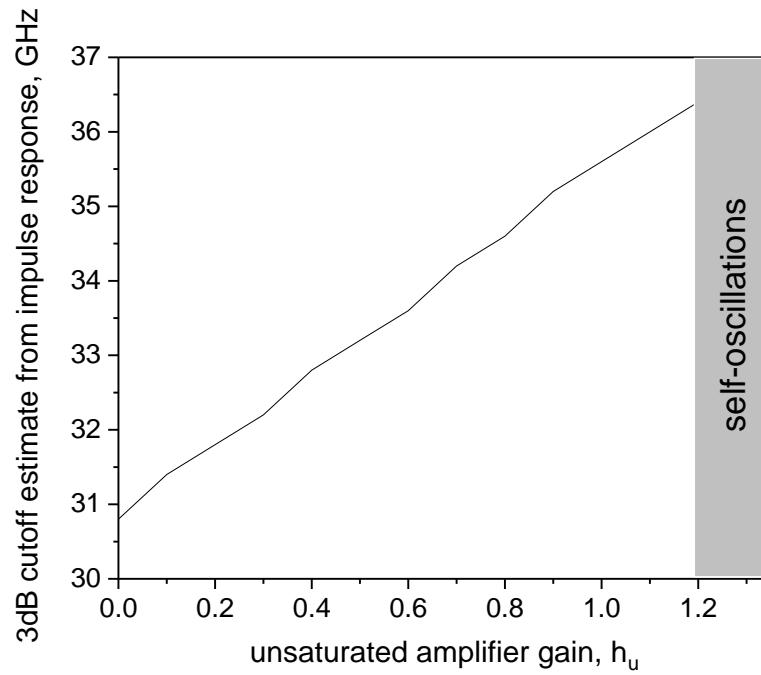


Figure 123: 3dB cutoff frequency vs unsaturated amplifier gain for the full model and $\tau_s=8ps$

Figure 123 shows the 3dB cutoff frequency vs unsaturated amplifier gain for the full model and $\tau_s=8ps$. It shows a monotonic increase for the 3dB cutoff frequency for the increase of the unsaturated gain h_u . When the unsaturated gain is 1.3, the system goes to self-oscillation. Moreover, we found that the non-flatness is increasing with the increase of the unsaturated amplifier gain.

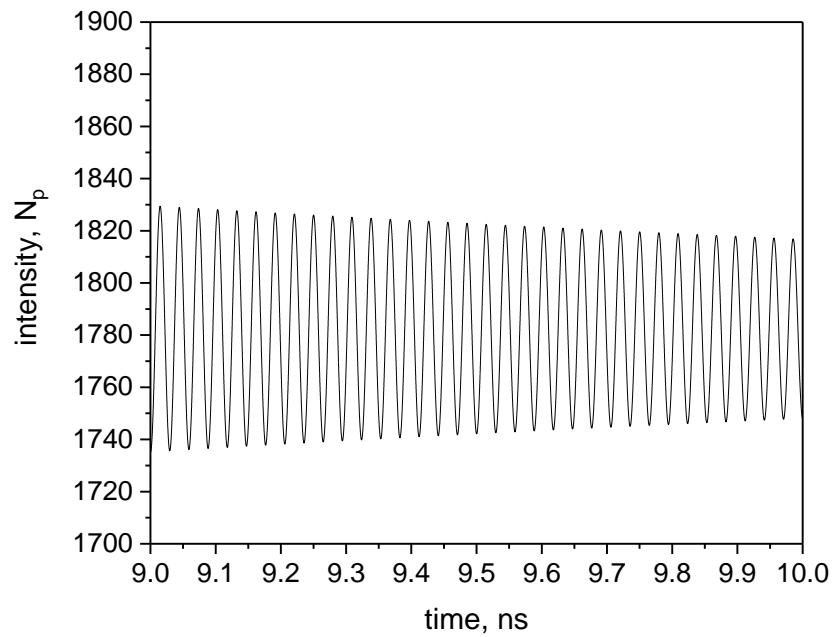


Figure 124: The intensity dynamic unusable system when the reflectance $r_s = 0.6$, $hu = 1.3$ for the full model and $\tau_s = 8ps$

Figure 124 shows the intensity vs time for the full model when the un-stability started when the unsaturated amplifier gain (hu) is 1.3. Figure 125, Figure 126, Figure 127 and Figure 128 illustrate how the modulation modulation index of sinusoidal self-pulsations increases from 78% (Figure 125,) through 90% (Figure 126), 95% (Figure 127), 97%, (Figure 128) to reach 99% (Figure 129) as the unsaturated amplifier gain is increase from $hu=1.4$ to $hu =1.8$. So, this system might be used as an optoelectronic microwave signal generator which can be used, for example, for microwave over fibre generator in this range. Figure 130 and Figure 131 show the irregular self-pulsations of this system when hu is 1.9 and 2, respectively.

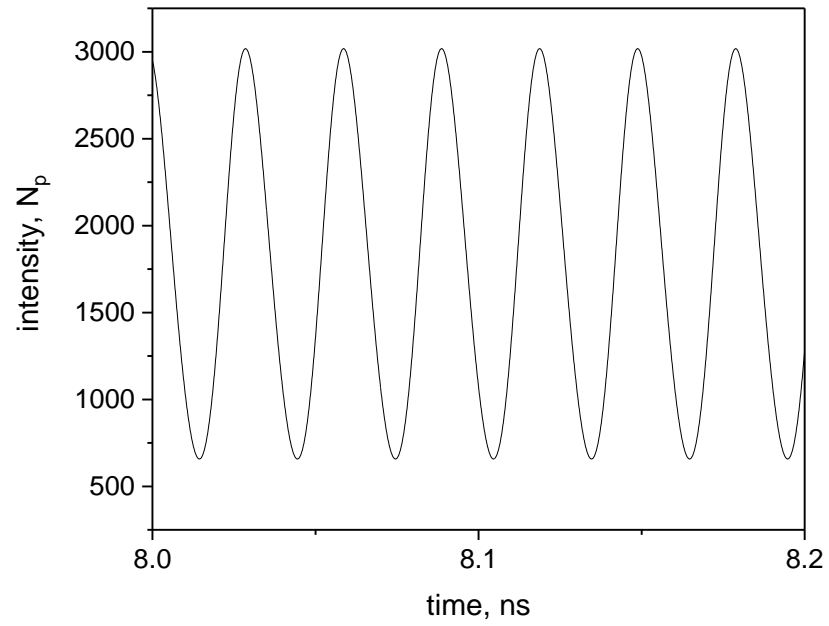


Figure 125: The intensity dynamic unusable system when the reflectance $r_s = 0.6$, $h_u = 1.4$, modulation index = 78% for the full model and $\tau_s = 8ps$

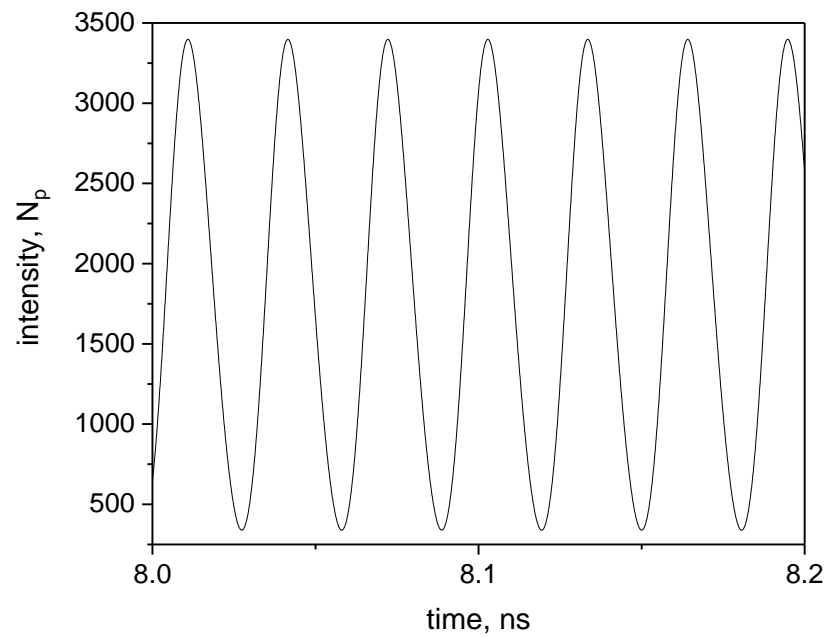


Figure 126: The intensity dynamic unusable system when the reflectance $r_s = 0.6$, $h_u = 1.5$, modulation index = 90% for the full model and $\tau_s = 8ps$

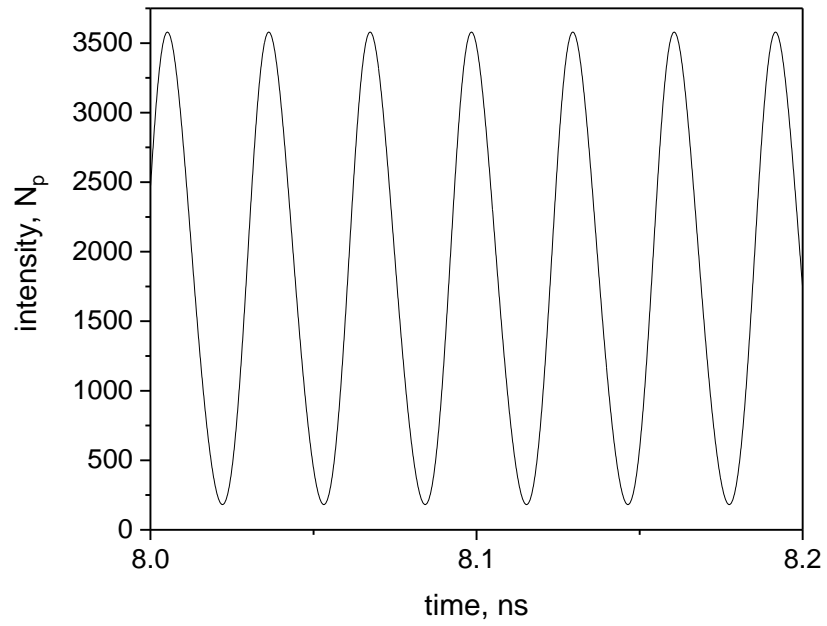


Figure 127: The intensity dynamic unusable system when the reflectance $r_s = 0.6$, $h_u = 1.6$, modulation index = 95% for the full model and $\tau_s = 8ps$

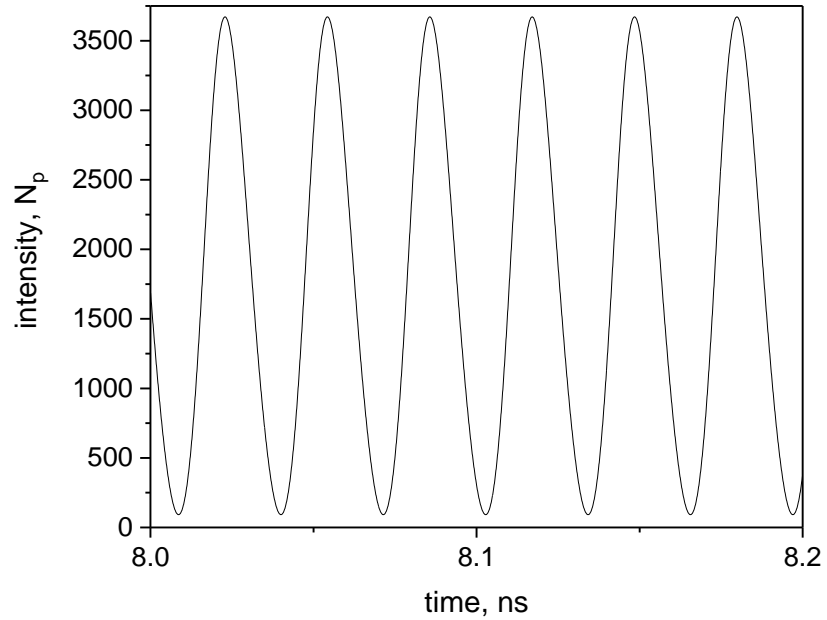


Figure 128: The intensity dynamic unusable system when the reflectance $r_s = 0.6$, $h_u = 1.7$, modulation index = 97% for the full model and $\tau_s = 8ps$

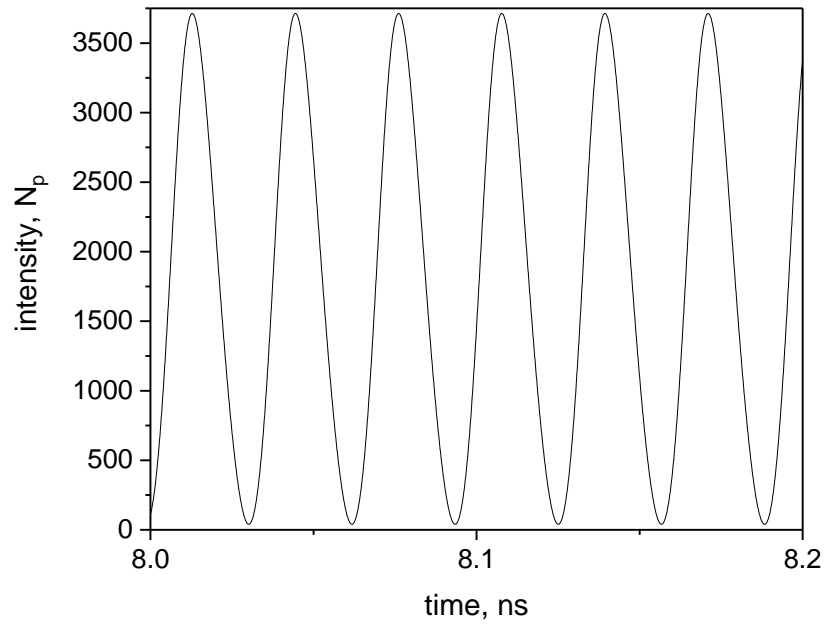


Figure 129: The intensity dynamic unusable system when the reflectance $r_s = 0.6$, $h_u = 1.8$, modulation index = 99% for the full model and $\tau_s = 8ps$

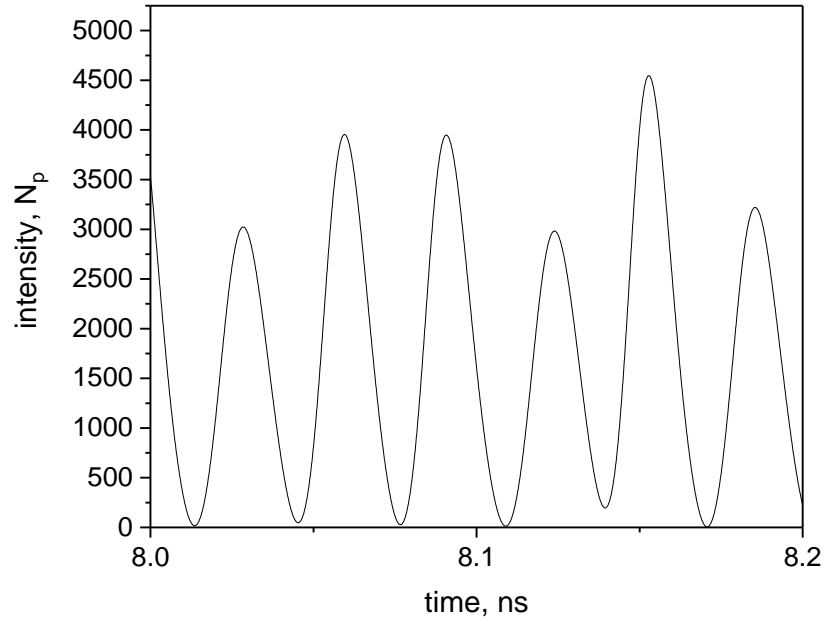


Figure 130: The intensity dynamic unusable system when the reflectance $r_s = 0.6$, $h_u = 1.9$ for the full model and $\tau_s = 8ps$

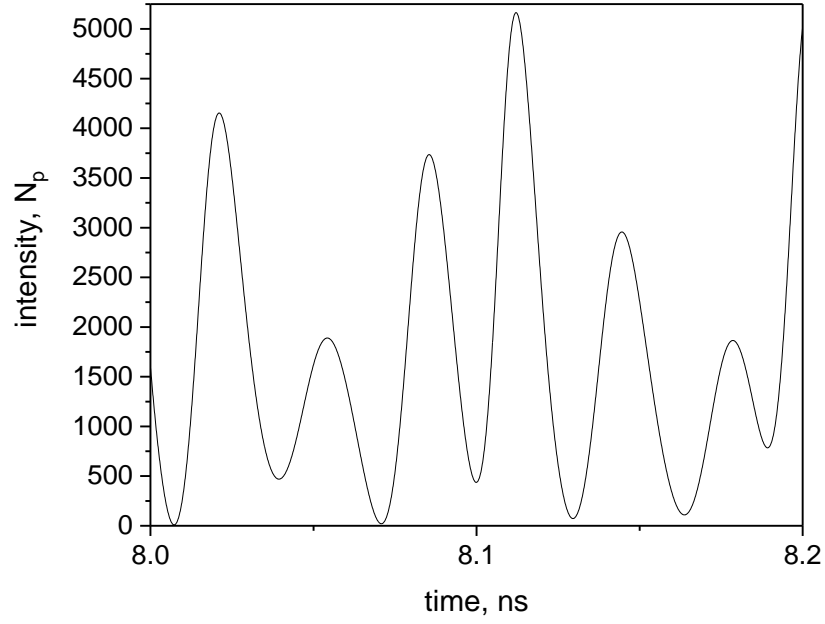


Figure 131: The intensity dynamic unusable system when the reflectance $r_s = 0.6$, $h_u = 2.0$ for the full model and $\tau_s = 8ps$

The rate equation for the carriers which determine the gain, assuming we operate with the average carrier density (the usual assumption in rate equations) is the similar to the standard RE models but (in the case of the laser far from the free laser threshold) with a slightly different stimulated recombination term:

$$\frac{dN}{dt} = \frac{\eta_i I}{eV} - \left(\frac{1}{\tau_{sp}(N)} + \frac{1}{\tau_{nr}(N)} \right) N - v_g \frac{g(N)}{1 + \epsilon N_p} \frac{|\exp(G_x^{net} T_x) - 1|}{G_x^{net} T_x} N_{pi} \quad (68)$$

Here the exponential factor in the stimulated term ensures the balance of photons created by the stimulated emission (Equation (59)) and electrons removed by it. It is similar to the way stimulated recombination is treated in the amplifier (Equation 66).

The output power from the top mirror is then given by:

$$P = v_g \frac{\frac{1}{\tau_{ph}^z}}{\frac{1}{\tau_{ph}^z} + \frac{1}{\tau_{ph}^x} + \frac{1}{\tau_{ph}^{in}}} A_X \hbar \omega N_{pi} \quad (69)$$

Where $A_x = L_x^2$ is the cross-section of the laser area.

The equations (59-66) form a full delay-differential dynamic model of a laser.

At this point, it is worthwhile mentioning the difference between this model and the earlier one developed by Ahmed et al 2015 [67], based on their earlier in-plane laser paper (Ahmed et al 2013 [65]). In both of those papers, the model is presented without derivation and restricted to the laser with a feedback, unlike ours which is derived and is a special case of a more general one of a laser under strong injection.

Both models, in the limit of weak feedback ($|r_s| \ll 1$ in our notations) reduce to the traditional Lang-Kobayashi model with a single delayed term.

Both models, in the limit of steady state solution ($E_i = \text{const}$ in our notations) give the steady state threshold condition of a compound cavity laser formed by the laser resonator and that of the (passive) external cavity. The condition, in our notation, and in the resonant case (real r_s of the same sign as r_a), in other words, the same longitudinal mode shared between the laser and the external cavity is:

$$|r_o r_{as}| \exp\left(\frac{1}{2} \frac{v_g}{v_{gx}} \Gamma g L_x\right) = 1,$$

Where

$$r_{as} = r_a - \frac{\theta_a r_s}{1 - r_a r_s}$$

Is the equivalent reflectance of a compound reflector at the right side of the laser cavity, formed by the oxide stripe and the remote reflector. In particular, with $r_s = 1$ and $R_a + \theta_a = 1$ (no scattering loss at the oxide stripe), we get $r_{as} = 1$, and the reflectance in a passive external cavity can never go above one, as expected.

However, there is a difference between the two models as well. Firstly, the model by Ahmed and co-authors [67] requires a summation of several (in theory, an infinite number, in practical simulations, around 6) terms with delays of $p\tau_s$, $p=1,2,3,\dots$, accounting for multiple

round-trips of light in the external cavity. In our model, these multiple delays are taken into account implicitly and exactly by the “recursive” nature of the boundary conditions (64)-(65) so there is no need for explicit summation, making for more efficient calculations, and also allowing for the amplification in the external cavity to be included.

Secondly, the *functional form* of the model by Ahmed and co-authors [67] seems to be at odds with the physics of the laser with the delayed feedback. Namely, in their equations, the delayed terms modify the *gain* seen by the light in the laser, rather than acting as a free term seeding the laser field, as in ours. Because Ahmed and co-authors present their model without derivation, it is difficult to establish the origin of this functional difference, but we believe our model is both more versatile and more physical, and is likely to be more accurate (to the best of our knowledge neither model has yet been directly compared to experiment). The main parameters used in the simulations, together with their values where appropriate, are summarized in Table 2 and Table 3.

Table 2: VCSEL cavity parameters

Parameter	Symbol	Value	unit
VCSEL top mirror amplitude reflectivity	R_{top}	0.99	-
VCSEL bottom mirror amplitude reflectivity	R_{bottom}	0.999	-
VCSEL internal losses	α_i	0.002	1/ μm
VCSEL effective length in the z direction	L_c	1	μm
QWs cumulative thickness	d_g	0.024	μm
area of the active region	A_a	4	μm^2
spontaneous emission into the mode	β_{sp}	10^{-6}	-
VCSEL group refractive index	n_{rg}	3.5	-
standing wave factor VCSEL gain media	ξ	1.85	-
VCSEL linewidth enhancement factor	A_{Hg}	3	-
ratio of internal intensity to right-propagating light intensity	f_x	2	-
dimensionless coupling (intensity transmittance) between the cavities	θ_a	0.10	-

Table 3: Laser amplifier cavity parameters

Parameter	Symbol	Value	unit
reflectance terminating slow-wave waveguide	r_s	0.6	-
slow waveguide refractive index	n_{rs}	100	-
confinement factor amplifier media	Γ_s	0.02	-
Amplifier linewidth enhancement factor	A_{Ha}	2	-
Amplifier carriers differential lifetime $\left(\frac{1}{\tau_{sp}(N)} + \frac{1}{\tau_{nr}(N)} \right)^{-1}$	τ_n	1	ns μm^3
amplifier absorption coefficient	α_a	10^{-5}	$1/\mu\text{m}$
unsaturated amplifier gain	h_u	0	-
width ratio between amplifier and VCSEL	w_{ratio}	1	-
gain compression factor	ε_a	3×10^{-5}	μm^3
parameter carrier density	N_s	1.1×10^6	$1/\mu\text{m}^3$
transparency carrier density	N_{tr}	1.6×10^6	$1/\mu\text{m}^3$
gain coefficient	g_o	0.3	$1/\mu\text{m}$
time of flight between the VCSEL and reflector	τ	4	ps

5.4 Small Signal Analysis

When analysing the small-signal response, we used the impulse response method, applying a short (~ 2 -5 ps) Gaussian current pulse to the laser and taking a Fourier transform of the resulting transient. This allows to make an express estimate of the 3dB cutoff frequency. The actual estimated modulation curve is calculated as:

$$\text{frequency response} = \left| \frac{\text{FFT}(\text{response of } S_i)}{\text{FFT}(\text{current pulse})} \right|$$

The impulse response method was used instead of the analytical small signal analysis because the optical frequency is not determined from the start and needs very complicated calculations. It has to be noted that the numerical method of small-signal analysis is not absolutely accurate – e.g. the decay of the frequency response at the high-frequency range (above the resonant peak) for a solitary laser is faster than 20 dB/decade which is obtained in analytical studies. However, the fact that the large signal modulation correlates with the small signal results proves that this method of calculation still has some validity in predicting the laser behaviour. It should be noted also that the current pulse duration in the simulations has some effect of the frequency response above the peak but has no effect on the position of the peak.

When comparing the solitary laser (when $|r_s|=0$) and in-plane laser cavity (when $|r_s|=0.6$), the 3 dB cutoff frequency – the main parameter given by the small signal analysis is about 3 times higher in the case of in-plane cavity laser when the as shown in Figure 132 and Figure 133 (which are similar to the experimental results by Ahmed et al 2015 [67] and are discussed in section 2.5.2).

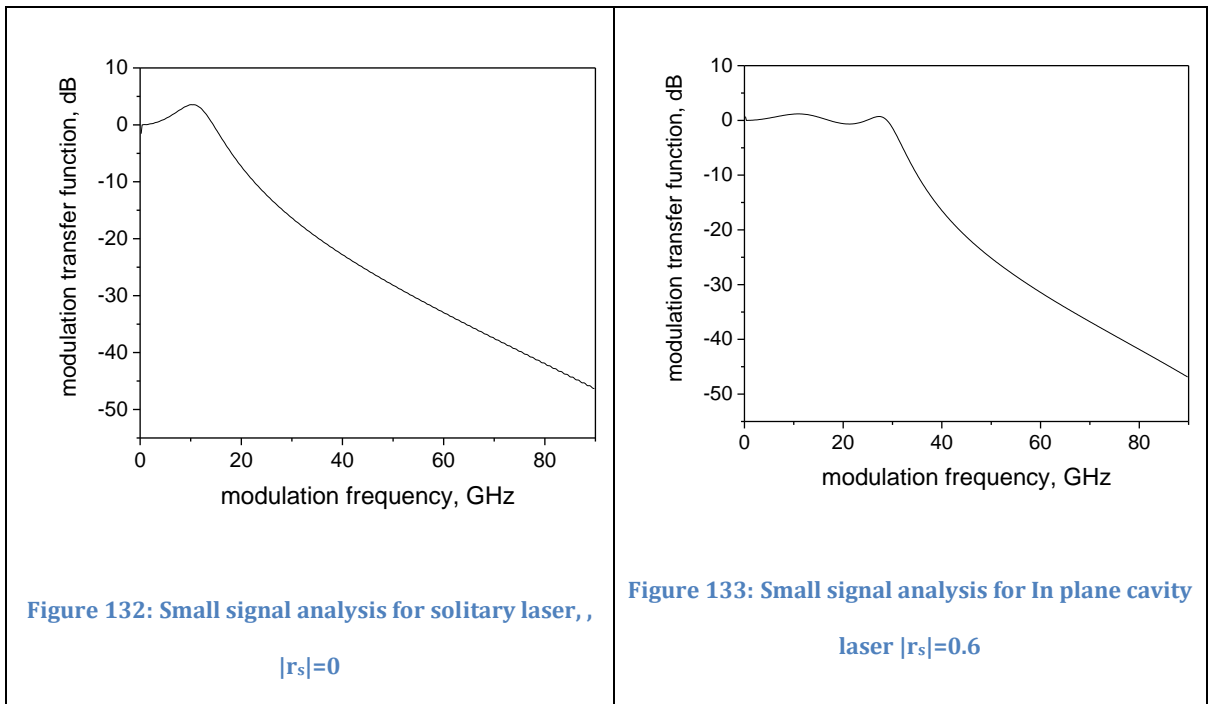


Figure 134 shows the effect of increasing the reflectance terminating slow waveguide (r_s) for the full model for $\tau_s = 8$ ps. When r_s is increasing, the 3dB cutoff frequency is increasing as well before it goes to self-oscillation at $r_s = 0.9$. Figure 135 shows the estimate for non-flatness of damping level using the impulse response method in the full model for $\tau_s=8$ ps. It shows that the non-flatness is very close to zero when $r_s = 0.6$ and it is increasing sharply after that until it goes to self-oscillation. The definition of non-flatness is defined in Figure 136; which is the difference in the transfer function amplitude between maximum and minimum in dB.

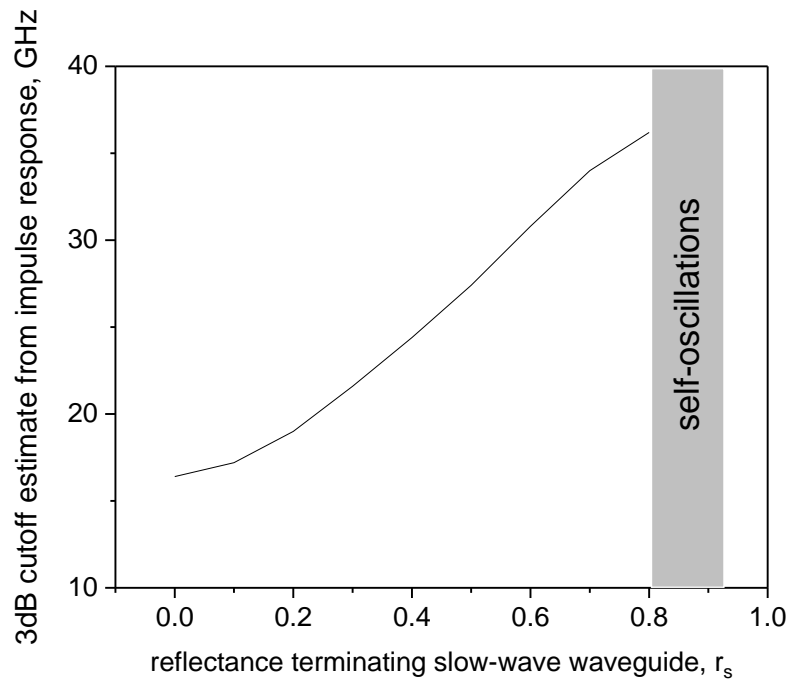


Figure 134: Estimate for 3dB modulation bandwidth using the impulse response method in the full model for $\tau_s=8$ ps

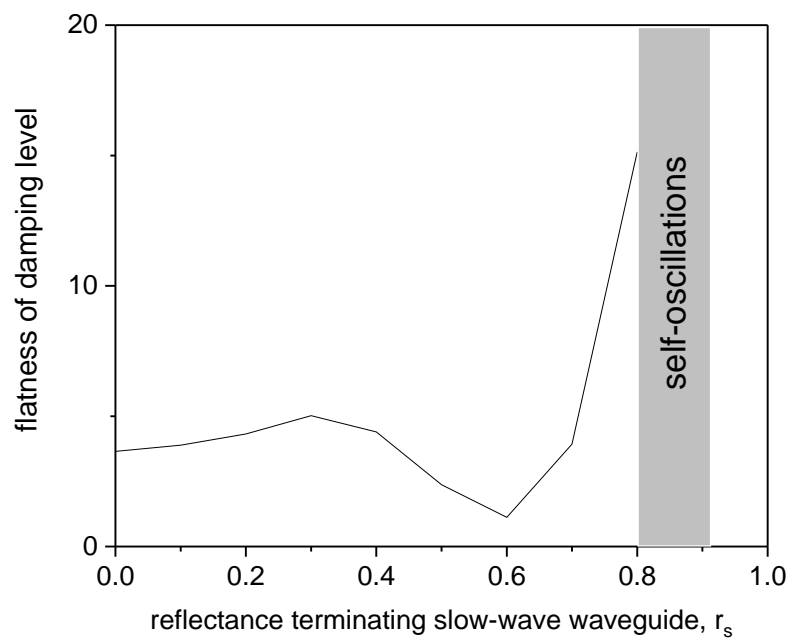


Figure 135: Estimate for non-flatness of damping level using the impulse response method in the full model for $\tau_s = 8$ ps

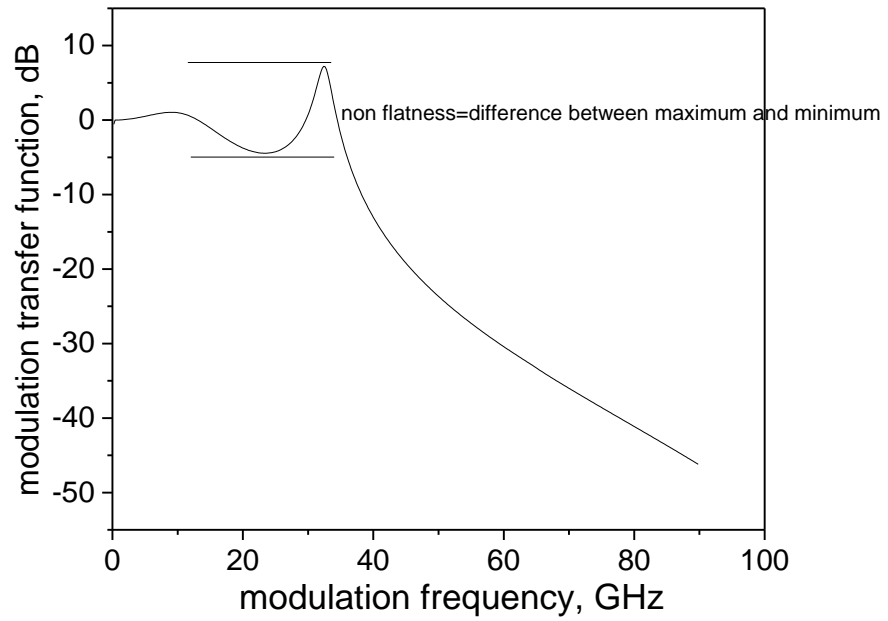


Figure 136: Small signal analysis for In plane cavity laser using the impulse response method in the full model for $\tau_s = 8$ ps and $|r_s| = 0.75$

When the reflectance r_s is 0.6 and the unsaturated amplifier gain is 1.4 for the full model of $\tau_s = 8$ ps, the self-pulsations is sinusoidal (Figure 138) rather than irregular (Figure 141) which is the normal situation in the development of laser instabilities: with increasing the controlling parameter (the reflectance in case of an external cavity laser), first sinusoidal (period one) oscillation are seen, then they become irregular.

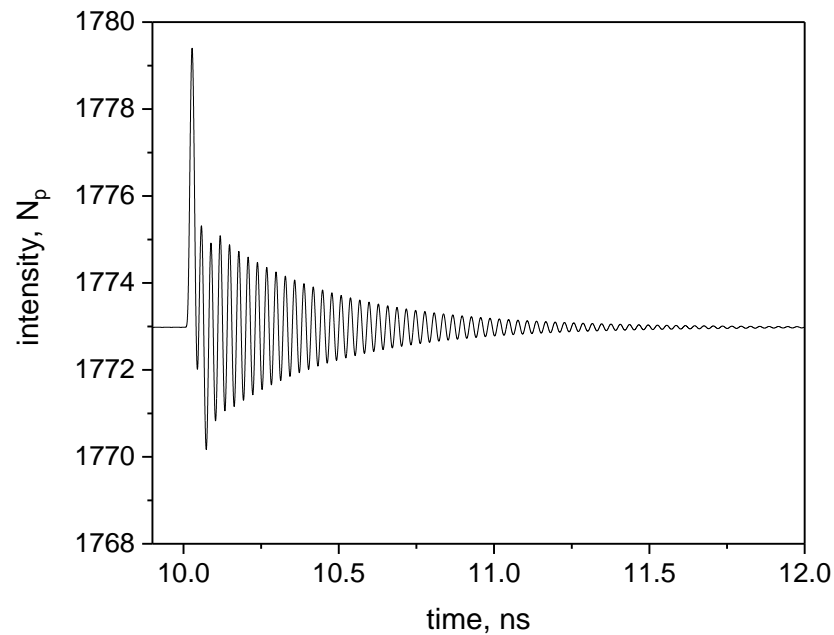


Figure 137: The intensity dynamic unusable system when the reflectance $r_s = 0.8$, $h_n = 0$ for the full model and $\tau_s = 8\text{ps}$

Figure 137 shows the intensity vs time for the full model calculated below, but very near the instability boundary, for the reflectance $r_s = 0.8$. The laser is still stable so the pulsations decay, but the decay decrement is very low and the decay process consequently very long. At higher reflectances, the pulsations become self-sustained, and their modulation depth (index) increases with the value of r_s . Figure 138, Figure 139, and Figure 140, calculated respectively for $r_s = 0.85$, 0.9 , and 0.95 , show sinusoidal self-pulsations with modulation indices of 70%, 93%, and almost 99% respectively. So, this system might be used as an optoelectronic microwave signal generator which can be used, for example, for microwave over fibre generator in this range.

With a further increase in r_s , the dynamics of the laser become chaotic. Figure 141 shows an example of such irregular self-pulsations when r_s is 1.

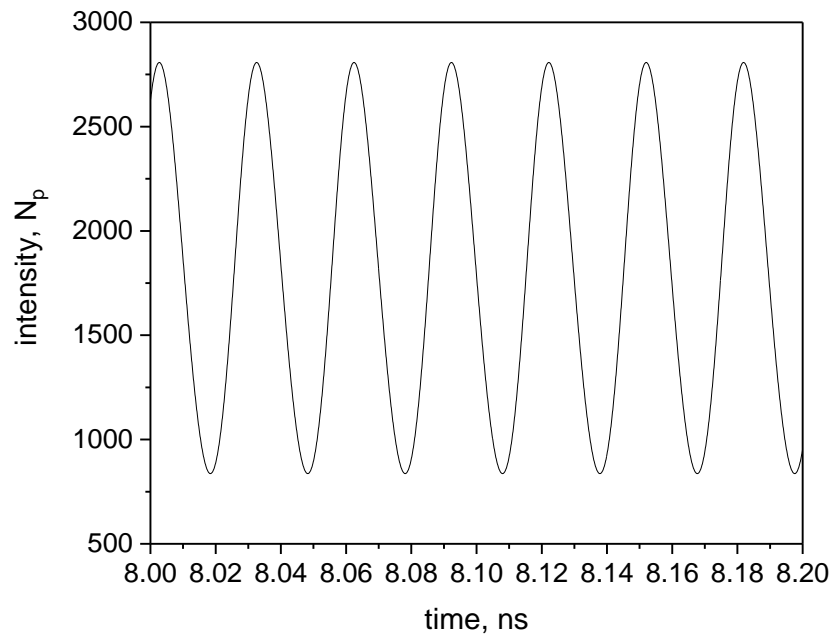


Figure 138: The intensity dynamic unusable system when the reflectance $r_s = 0.85$, $h_u = 0$, modulation index = 70% for the full model and $\tau_s = 8ps$

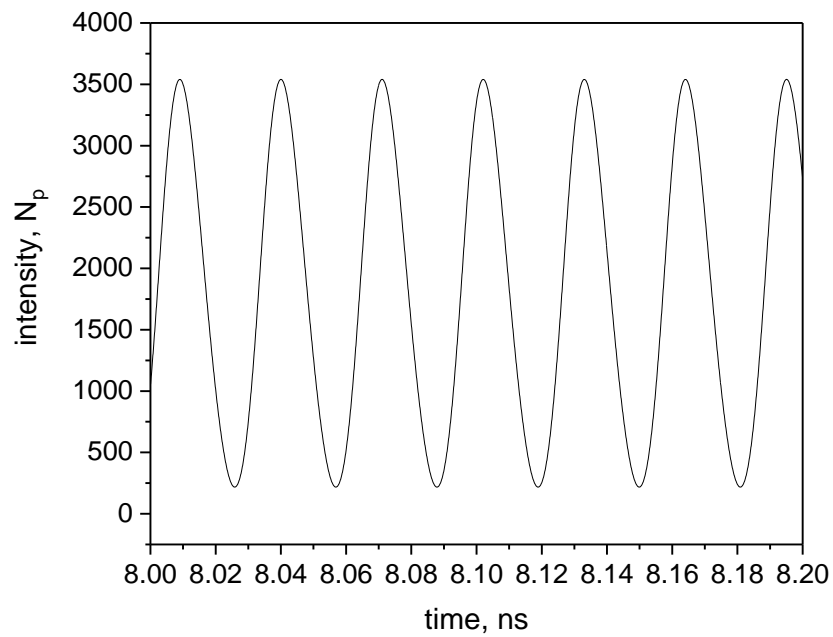


Figure 139: The intensity dynamic unusable system when the reflectance $r_s = 0.9$, $h_u = 0$, modulation index = 93% for the full model and $\tau_s = 8ps$

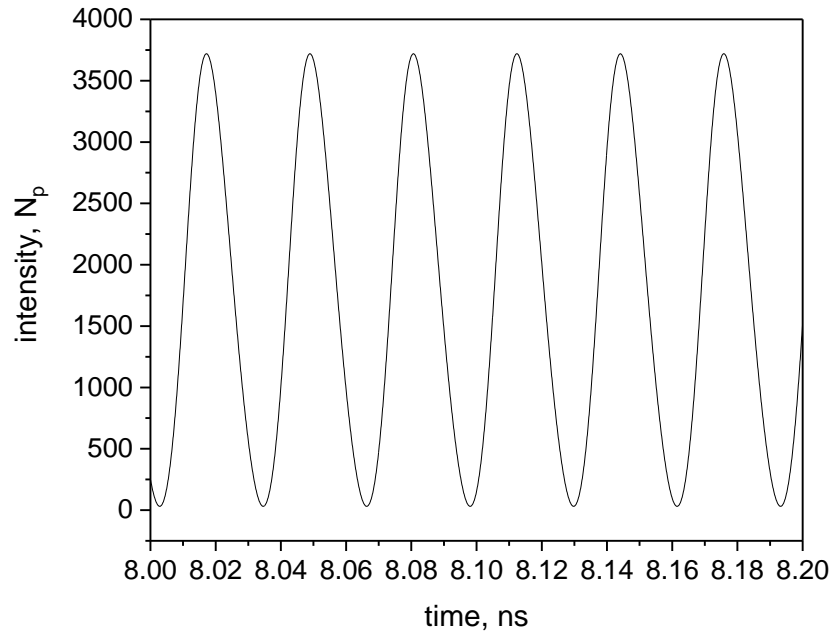


Figure 140: The intensity dynamic unusable system when the reflectance $r_s = 0.95$, $h_u = 0$, modulation index = 99% for the full model and $\tau_s = 8ps$

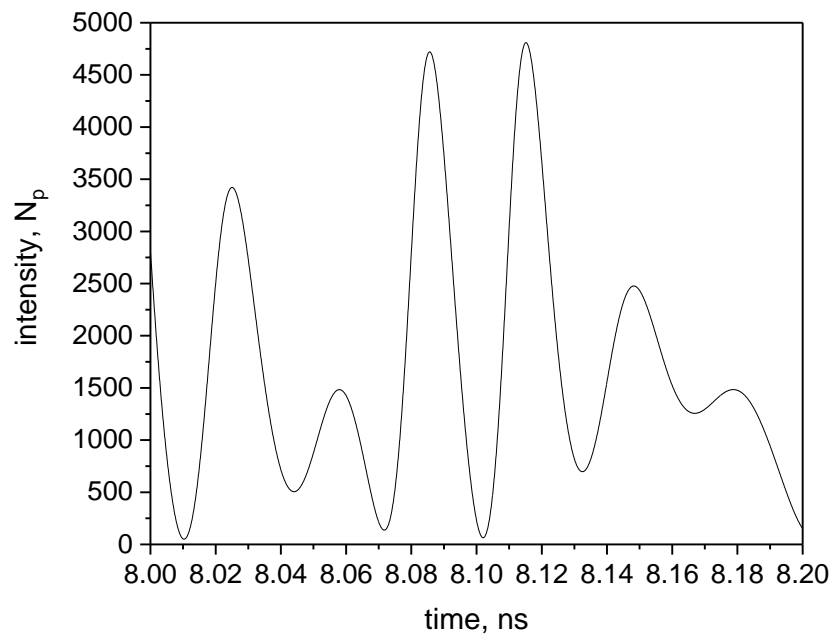
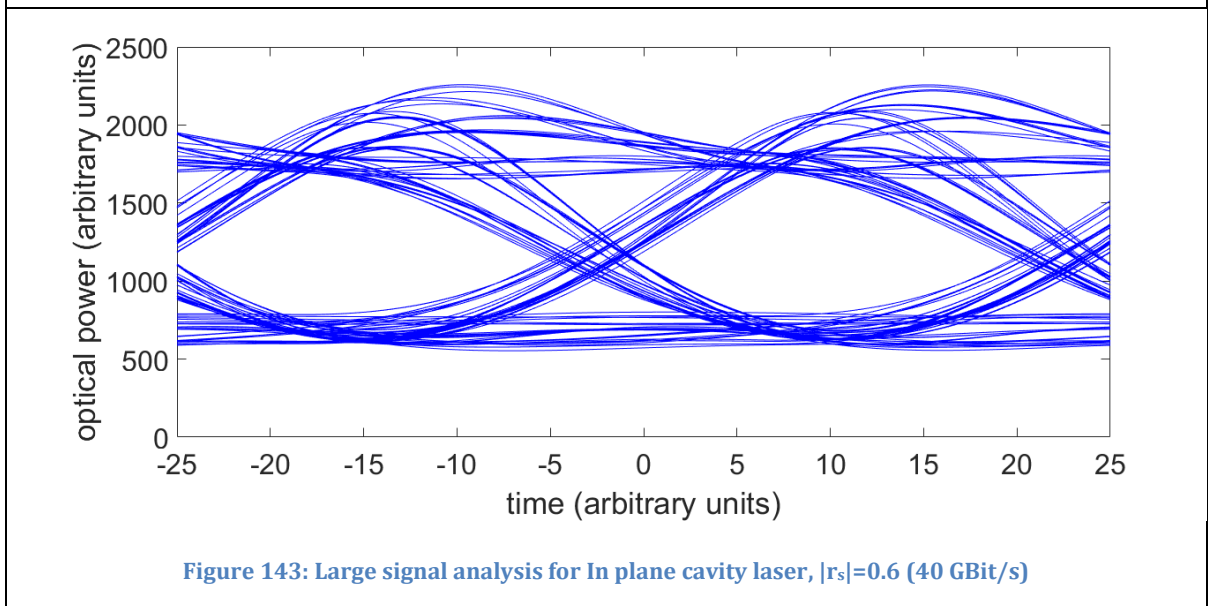
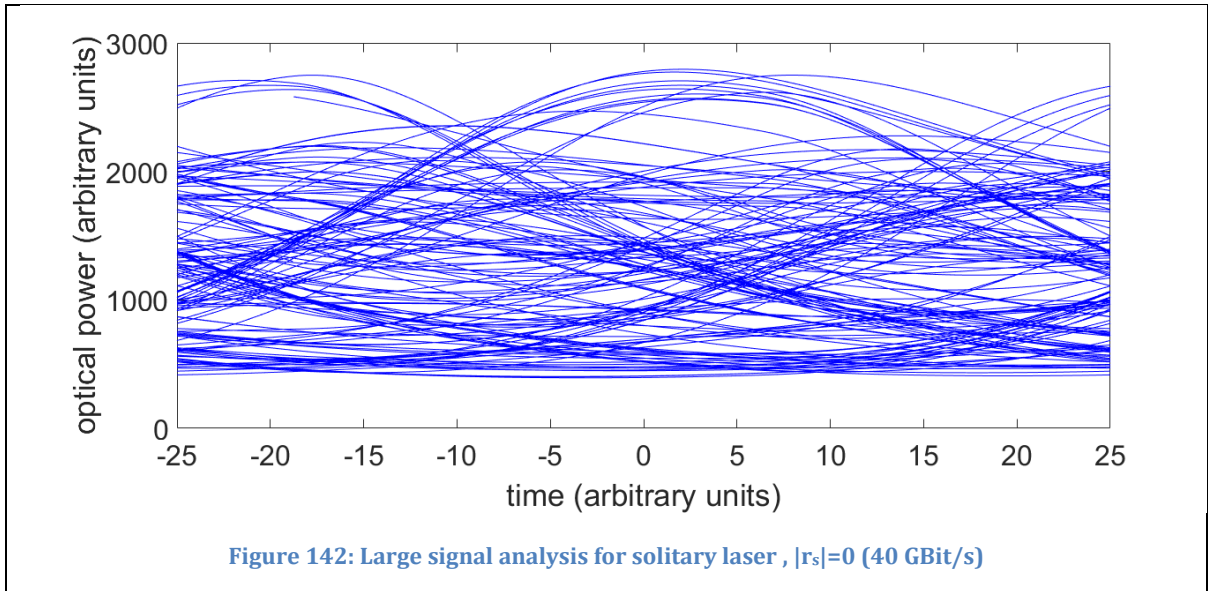
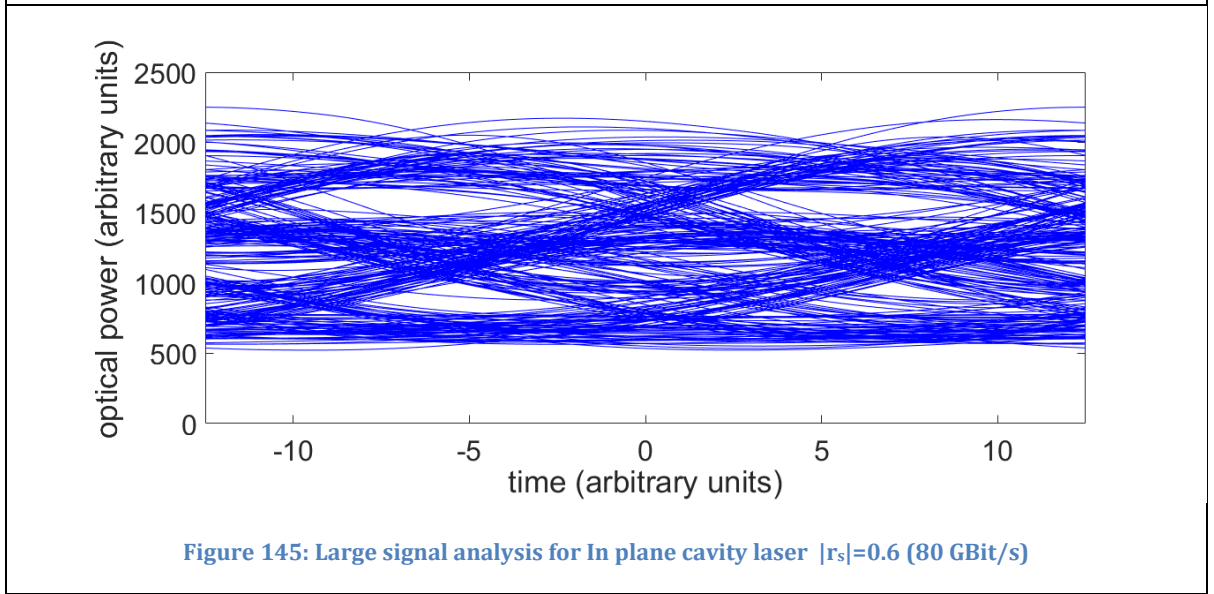
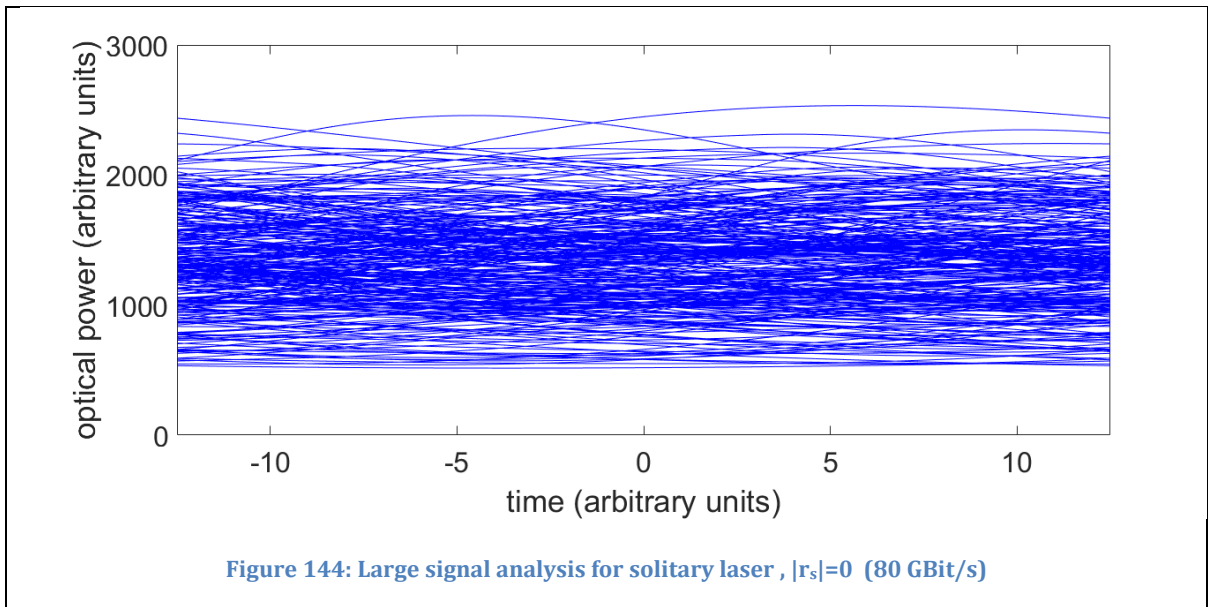


Figure 141: The intensity dynamic unusable system when the reflectance $r_s = 1.00$, $h_u = 0$ for the full model and $\tau_s = 8ps$

5.5 Large Signal Analysis

The eye diagram is open for the in-plane cavity and it is closed for the solitary laser for 40 GBit/s modulation frequency as shown in Figure 142 and Figure 143. However, the eye diagram is closed when doing the large signal analysis and when the modulation frequency is 80 GBit/s for both solitary and in-plane cavity lasers as shown in Figure 144 and Figure 145.





As in the results using the Lang-Kobayashi model, for some values of the feedback phase, the feedback increases the frequency of the relaxation oscillations and hence the 3dB modulation cutoff. The limit to utilising the modulation cutoff frequency increase by increasing the feedback is set by the onset of self-pulsations, with the relaxation oscillations becoming undamped as shown in Figure 117.

Figure 146, Figure 147, Figure 148, Figure 149 and Figure 150 show the relationship between small and large signal analysis. To begin with, bad (fully closed) eye diagrams are simulated for zero external reflectance r_s (Figure 146) when the cutoff frequency of small-signal modulation is known to be small.

Good (with a good opening) eye diagrams are seen when the external reflectance is such that the cutoff frequency is increased, whereas the non-flatness in the small signal analysis is small (Figure 148).

Finally, when r_s is increased so much that the small-signal response becomes non-flat, the eye diagrams begin to close again (Figure 150).

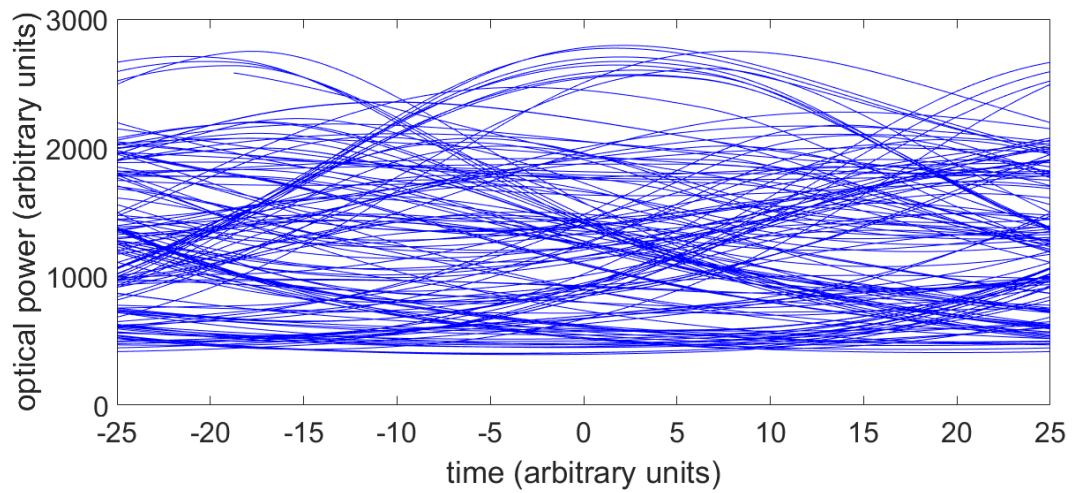


Figure 146: Eye diagram for the full model for $\tau_s = 8$ ps, $|r_s| = 0$ (40 GBit/s) , quality factor = 1.69

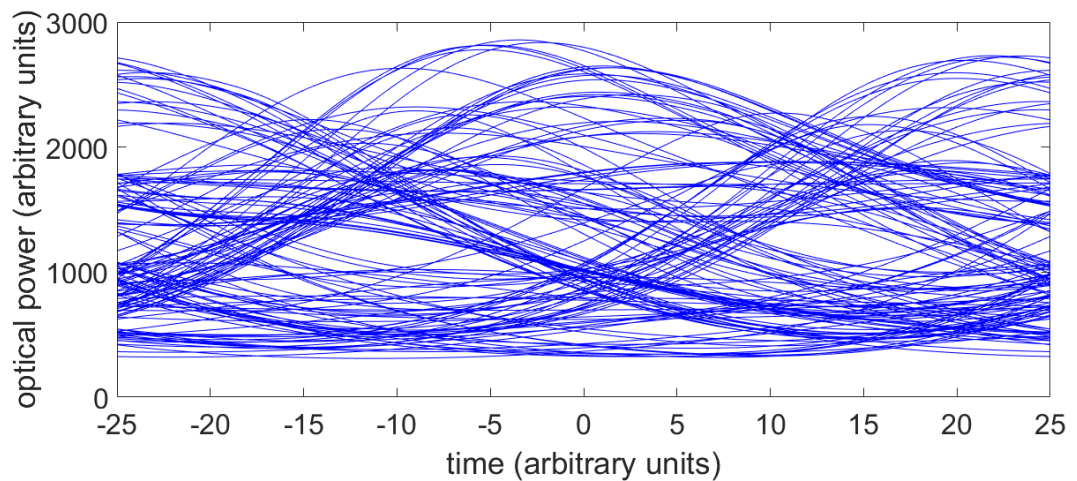


Figure 147: Eye diagram for the full model for $\tau_s = 8$ ps, $|r_s|=0.3$ (40 GBit/s) , quality factor = 1.70

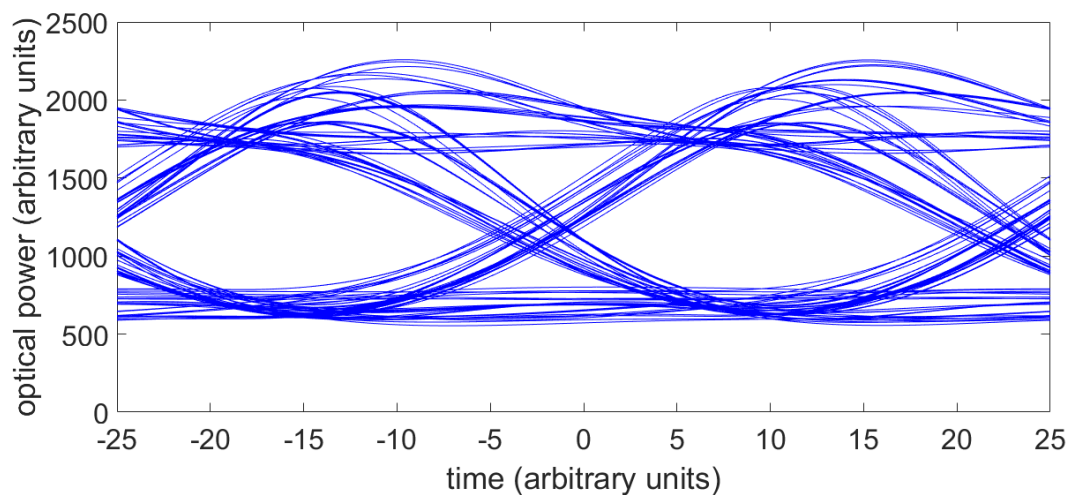


Figure 148: Eye diagram for the full model for $\tau_s = 8$ ps, $|r_s| = 0.6$ (40 GBit/s), quality factor = 2.45

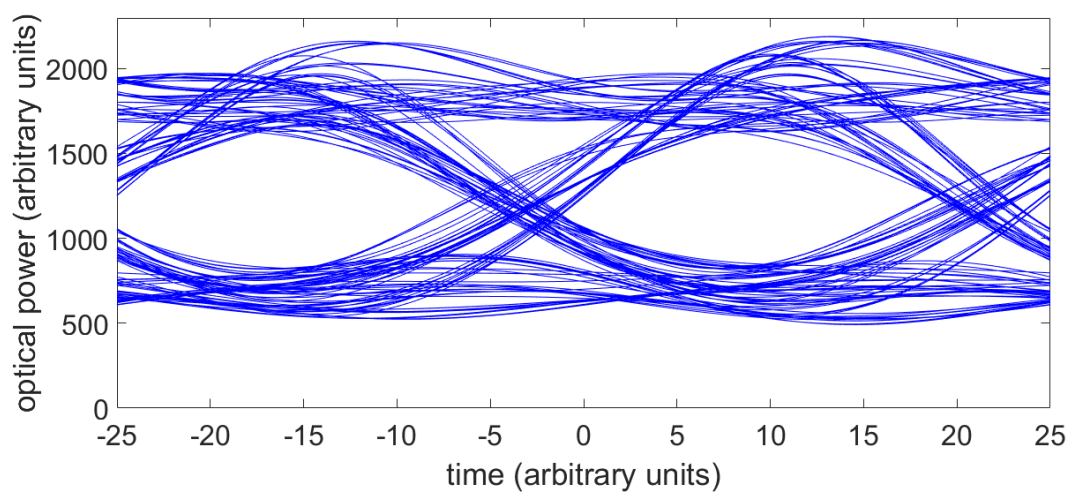


Figure 149: Eye diagram for the full model for $\tau_s = 8$ ps, $|r_s| = 0.7$, (40 GBit/s), quality factor = 2.39

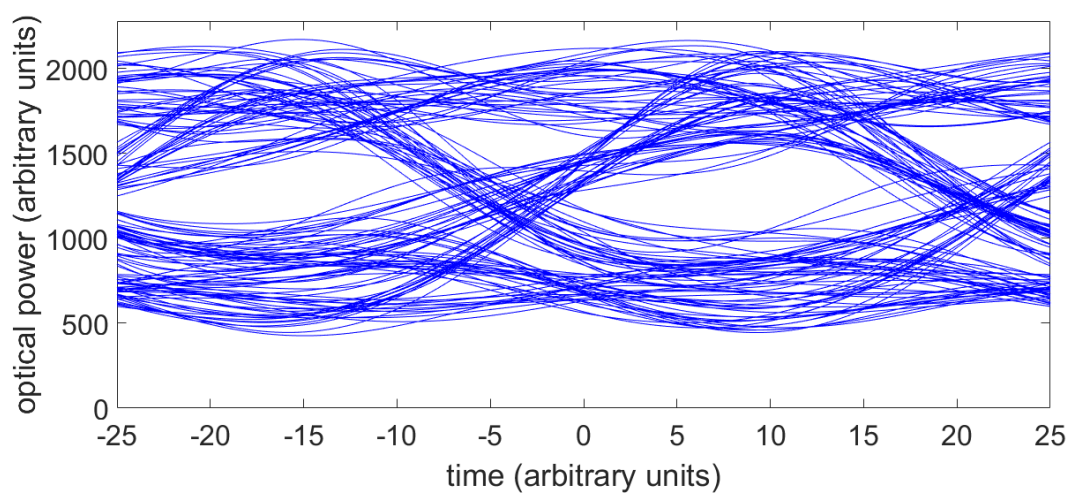


Figure 150: Eye diagram for the full model for $\tau_s = 8$ ps, $|r_s| = 0.8$, (40 GBit/s), quality factor = 2.02

It should be noted that for longer cavities, the instabilities occur at lower reflectance terminating slow-wave waveguide (r_s) values, leading to a smaller increase in the 3dB modulation frequency. For example, Figure 151 and Figure 152 illustrate that for longer cavities ($\tau_s=18$ ps) when r_s is more than 0.3, the laser becomes unstable, and so the cutoff frequencies of just ~ 23 -24 GHz can be achieved, as opposed to more than 30 GHz for shorter cavities.

Thus it can be expected that that this design will work best with short external cavities – the final proof of that will require experimental verification.



Figure 151: Estimate for 3dB modulation bandwidth using the impulse response method in the full model for $\tau_s=18$ ps

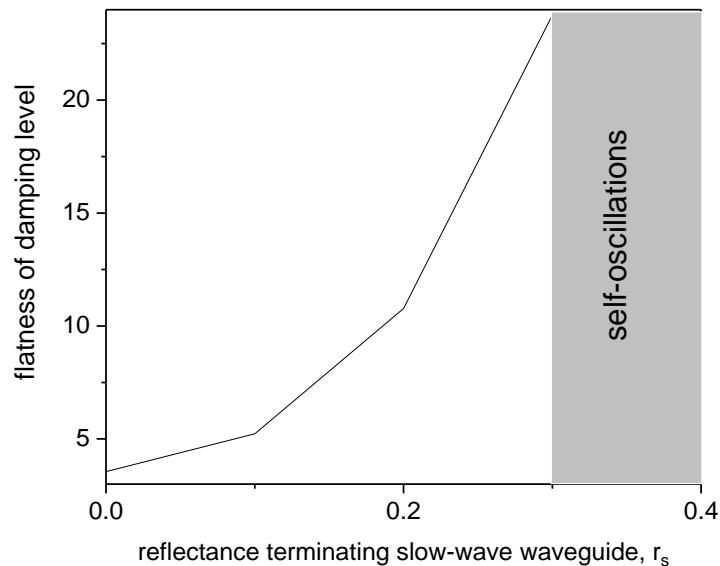


Figure 152: Estimate for non-flatness of damping level using the impulse response method in the full model for $\tau_s=18$ ps

5.6 Chapter summary

In this chapter, we developed a model which could overcome the limitations of both previous approaches to the in-plane compound cavity VCSEL dynamics, the single-pass Lang-Kobayashi model [60, 61] (which is technically speaking valid only for weak feedback but is often used for strong feedback) and the multiple-pass model by Ahmed and co-authors [67] (which represents the external injection field as gain modulation). After conducting initial studies using the Lang-Kobayashi model, a more accurate delay-differential equation model of a transverse compound cavity VCSEL was developed and analysed.

We found that the limits of the modulation performance were set by the dynamic instabilities and the non-flatness of the small-signal modulation curve. We showed that the modulation rate of 40 GBit/s can be achieved in this design but higher ones (80 or 100 GBit/s) do not look likely. If bit rates of the order of 40 GBit/s are adequate, the in-plane compound cavity is preferable, due to the simpler design and alignment, and only one bias and modulation contact.

Comparing the results to those of the previous chapter, we found that a vertical compound cavity appears to promise higher modulation speed than in-plane cavity (but requires very fine tuning of sub-cavities). This new model can also be used to analyse the potential of the laser with a transverse external cavity as an optoelectronic microwave signal generator which can be used, for example, for microwave over fibre generator.

6. CONCLUSIONS AND MAIN RESULTS

The main object of the thesis was to analyse and compare different types of ultrafast VCSEL designs and ascertain the limits of their modulation performance.

In the first part of the thesis, I considered both amplitude and frequency (phase) dynamics of laser emission in an electrooptically modulated compound cavity VCSEL, as well as the spectrally selective nature of the laser cavity. As the standard rate equation model has limitations in describing high-frequency laser modulation, the modified rate equation model considering modulation of the refractive index describing the electromagnetics of the laser cavity more accurately was introduced. It was found that the ultimate modulation frequency limit is determined by the photon lifetime of the modulator cavity. Moreover, simulations have shown that the quality of modulation depends non-monotonically on the numbers of dielectric grating periods in the top and intermediate mirrors, and that the number of periods for the top and intermediate reflectors that gives an optimum quality factors a weak function of current. The maximum quality factor was analysed for a number of device designs and currents, and high quality factors at modulation bit rates of up to 80 Gbit/s were predicted.

In the second part, the performance of a transverse compound cavity VCSEL was studied. The goals of the work were, firstly, to develop a model which could overcome the limitations of both previous approaches, the single-pass Lang-Kobayashi model [60, 61] (which is technically speaking valid only for weak feedback but is often used for strong feedback) and the multiple-pass model by Ahmed and co-authors [67] (which represents the external injection field as gain modulation). Secondly and ultimately, the purpose was to ascertain the limit of modulation performance increase in this laser design and to compare it with the electrooptically modulated design studied in the first part of the work.

After conducting initial studies using the Lang-Kobayashi model, a more accurate delay-differential equation model of a transverse compound cavity VCSEL was developed and analysed.

The limits of the modulation performance were found to be set by the dynamic instabilities and the non-flatness of the small-signal modulation curve. An analytical estimate could not be obtained in this case, but the numerical simulations show that the modulation rate of 40 GBit/s can be achieved in this design but higher ones (80 or 100 GBit/s) do not look likely.

Thus, the vertical cavity electrooptically modulated structure appears to be more promising for ultrafast modulation, at the expense of a somewhat more complex design and bias arrangements (it is important to make sure that the operating point is on the slope of the notch in the modulator section reflectance). If bit rates of the order of 40 GBit/s are adequate, the in-plane compound cavity is preferable, due to the simpler design and alignment, and only one bias and modulation contact.

In this thesis (Chapters 3-4) we conducted a study on the effect of photon lifetime modulation using electrooptic modulators (refractive index modulation). In any future research, more studies can be conducted on the effect of electroabsorption and the comparison between absorption and refraction modulation methods can be included as well.

Alternative high-speed VCSEL-based sources for future high speed long- and medium-haul networks, such as Transistor VCSELS and coupled laser arrays, can also be studied. These new designs can provide 37 GHz modulation bandwidth, narrow spectral width and high output power while the laser array, in particular, can be biased at low current density [2, 108].

After the theoretical investigation of the above designs, having them fabricated according to the design recommendations and measuring their performance should be the final goal of any further work.

7. APPENDIX

7.1 SIOE15 abstract

SIOE'2015, Cardiff, March 2015

Electrooptically modulated coupled-cavity VCSELs: the anomalous small-signal response and the large-signal modulation properties

N. F. Albugami, E. A. Avrutin,

Department of Electronics, University of York, York YO10, 5DD, UK;
emails: na668@york.ac.uk , eugene.avrutin@york.ac.uk

VCSEL constructions capable of direct modulation at bit rates in excess of 40 GBit/s have attracted considerable attention for future high-speed long- and medium-haul networks. The two main approaches to realising this goal are, firstly, the improvement in the direct modulation laser performance, with 40 GBit/s direct modulation having been demonstrated recently (see e.g. [1]), and, secondly, using modulation of the photon lifetime in the cavity as an alternative to current modulation. The latter approach is potentially free from the limitations of the modulation such as the 3dB modulation frequency being limited by the electron-photon oscillation damping, since the photon lifetime modulation, unlike current one, affects the output of the laser directly as opposed to indirectly via carrier density. A possible practical realisation of this principle was suggested a while ago in the form of electrooptic modulation of the reflectance of one of the multistack mirrors forming the VCSEL cavity [2]. Small-signal modulation curves corresponding to this modulation type were analysed and predicted to have a higher 3dB cutoff frequency than the current modulation, owing to the transfer function decaying at high frequency F values as $1/F$ rather than $1/F^2$ as is the case of current modulation. This inspired a large amount of further work, in which the idea of modulating a mirror reflectance has evolved into two possible routes: the coupled-cavity laser with an additional, electrooptically modulated vertical resonator, and a stopband edge-tunable DBR [3]. Experimentally, large-signal NRZ modulation at 40+ GBit/s has been confidently and repeatedly demonstrated (see e.g. [4]). Small-signal modulation at low frequencies has been analysed [5] and showed signs of a broad, large resonant peak consistent with the formula presented in [2]. However, experiments and large-signal simulations show that the best performance of electrooptically modulated VCSELs is realised at moderately small rather than large bias currents [3], which is completely different to the case of current modulation, and not immediately obvious from the published small-signal analysis of photon lifetime modulation [2]. We believe one reason for this is that the small-signal analysis of [2] considered the modulation of the photon density *inside* the laser cavity, rather than the measurable power outside the laser which is also influenced by the outcoupling loss modulation. Here, we present an improved small-signal modulation formula taking into account modulation of both the photon density and the outcoupling loss (Figure 1).

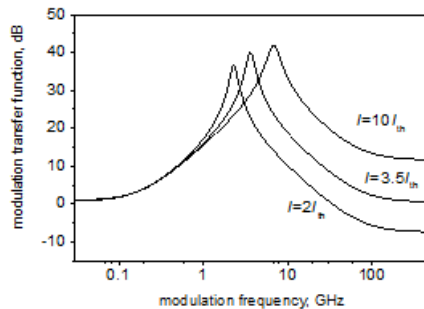


Figure 1. Calculated small-signal response of electrooptic laser modulation at three different values of bias current.

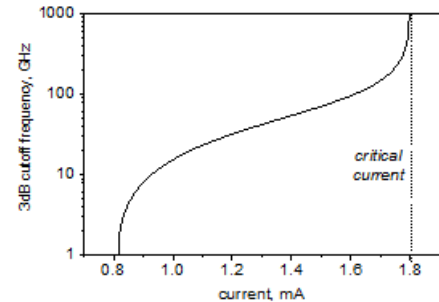


Figure 2. Calculated 3dB cut-off frequency vs bias current for small-signal response of electrooptic laser modulation.

A somewhat unusual result of this analysis is that the concept of 3 dB cutoff frequency as a measure of modulation speed is not applicable to electrooptically modulated coupled-cavity VCSELs as it tends to infinity beyond a certain critical current (Figure 2); their modulation properties are governed instead by the shape and magnitude of the broad resonant peak at the electron-photon resonance frequency. This has implications for future design of such lasers, including possibly the use of Quantum Dot or Dash active media usually considered poorly suited for fast modulation purposes. Detailed discussion of the relation between the small and large signal modulation of electrooptically modulated lasers will be presented at the conference.

1. Blokhin, S. A.; Lott, J. A.; Mutig, A.; Fiol, G.; Ledentsov, N. N.; Maximov, M. V.; Nadochiy, A. M.; Shchukin, V. A.; Bimberg, D. *Electron Lett.* **2009**, *45*, (10), 501-502.

2. Avrutin, E. A.; Gorfinkel, V. B.; Luryi, S.; Shore, K. A. *Applied Physics Letters* **1993**, *63*, (18), 2460-2462.

3. Shchukin, V. A.; Ledentsov, N. N.; Lott, J. A.; Quast, H.; Hopfer, F.; Karachinsky, L. Y.; Kuntz, M.; Moser, P.; Mutig, A.; Strittmatter, A.; Kalosha, V. P.; Bimberg, D. In *Ultra high-speed electro-optically modulated VCSELs: modeling and experimental results*, 2008; pp 68890H-68890H-15.

4. Shchukin, V. A.; Ledentsov, N. N.; Qureshi, Z.; Ingham, J. D.; Panty, R. V.; White, I. H.; Nadochiy, A. M.; Maximov, M. V.; Blokhin, S. A.; Karachinsky, L. Y.; Novikov, I. I. *Applied Physics Letters* **2014**, *104*, (5), 051125.

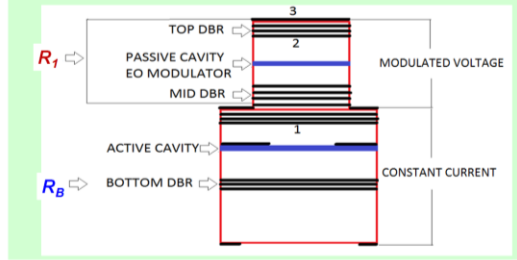
5. Germann TD, H. W., Nadochiy AM, Schulze JH, Mutig A, Strittmatter A, Bimberg D. *Opt Express* **2012**, *20*, (5), 5099-107.

Electrooptically modulated coupled-cavity VCSELs: the anomalous small-signal response and the large-signal modulation properties

Naser Albugami and Eugene Avrutin

na668@york.ac.uk
eugene.avrutin@york.ac.uk

1. Schematic of a Compound Cavity Laser



Top DBR is 31 pairs; mid DBR is 20 pairs (asymmetric cavity).
Bottom DBR reflectivity $R_B = 0.999$.

2. EO Modulation of the Top Cavity Reflectance

Rate Equation Model

$$\frac{dN}{dt} = \frac{\eta I}{qV} \left(\frac{1}{\tau_{sp}(N)} + \frac{1}{\tau_{sp}} \right) N \cdot \frac{G(N)}{1 + \epsilon S}$$

$$\frac{dS}{dt} = \beta_{sp} N + \left(\Gamma \frac{G(N)}{1 + \epsilon S} - (\tau_{ph-m}^{-1} + \tau_{ph-m}^{-1}) \right) S$$

$$\tau_{ph-out}^{-1}(I) = \frac{1}{2L} \ln \frac{1}{R_B R_1(I)}$$

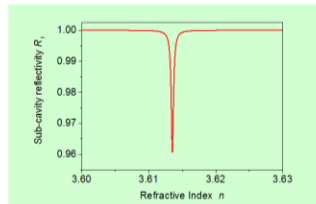
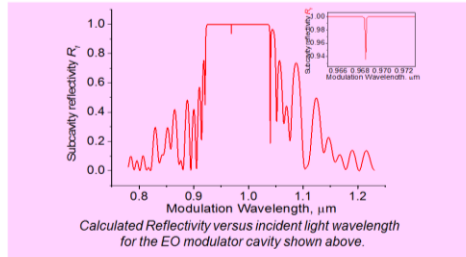
R_1 Reflectance of Modulator Subcavity

$$r_1 = r_{12} + \frac{\theta_{12} \theta_{23} r_{23} e^{j2KL}}{1 - r_{21} r_{23} e^{j2KL}}$$

$$R_1 = r_1 r_1^*$$

r_{im} and θ_{im} are complex amplitude reflectances and transmittances of multistack DBRs, with incidence from layer i towards layer m , $K = 2\pi n/\lambda$, n is the average refractive index of passive (EO) cavity.

Electrorefraction effect plays a dominant role in modulating $R_1(I)$ as compared to electroabsorption [3].

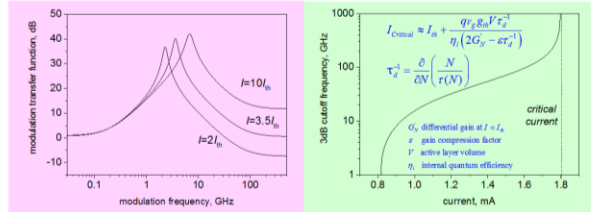


- R_1 changes between 0.994-0.965 as the operating point scans through the notch, which gives $\tau_{ph-out}^{-1} = 1.9 \times 10^{11} - 1.1 \times 10^{12}$.
- The change in the refractive index required is $\sim 10^{-3}$.

3. Small Signal Response

$$\frac{\partial P}{\partial R_1} = -h\omega_{ph} V_{opt} \bar{S} \frac{\nu_g}{2L} \times \frac{-\omega^2 + j(G_N' - \tau_{ph-m}^{-1})\omega + \omega_{rel}^2 - \tau_{ph-m}^{-1}(\tau_{d'}^{-1} + \tau_{st}^{-1})}{-\omega^2 + jG_N'\omega + \omega_{rel}^2}$$

Small-signal analysis of power output with reflectivity modulation (transfer function for the output power)

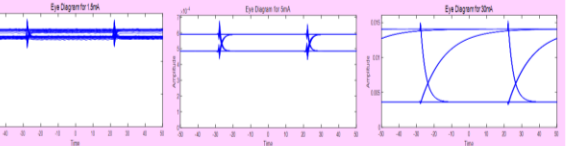
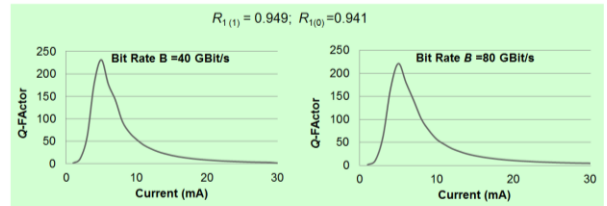


Calculated small-signal response of electrooptic laser modulation at three different values of bias current. Calculated 3dB cut-off frequency vs bias current for small-signal response of electrooptic laser modulation.

- No modulation roll-off at high frequencies beyond a certain current ($I_{critical}$).
- 3 dB cutoff frequency is not defined for those currents.

4. Large Signal Modulation

$$Q = \frac{\overline{P_{(1)}} - P_{(0)}}{\sigma_{(1)} + \sigma_{(0)}} \quad (\overline{P_{(1)}}, \overline{P_{(0)}} \text{ mean}; \sigma_{(1)}, \sigma_{(0)} \text{ standard deviations})$$



- Non-monotonic Q(I)
- A relation between small and large signal properties: (a resonant increase in Q close to the current corresponding to frequency=5 GHz, a subharmonic of the bit rate).
- Large signal needed for high contrast at high bit rates (as in [3])

5. Summary

- No high frequency roll-off in small-signal modulation at $I > I_{critical}$.
- 3 dB cutoff frequency not a valid measure of laser performance.
- Quality of large signal modulation depends non-monotonically on bias current, improves with reflection modulation contrast; attributed to sub-harmonic resonance with relaxation oscillations

References

- Blokhin, S. A.; Lott, J. A.; Mutig, A.; Fiol, G.; Ledentsov, N. N.; Maximov, M. V.; Nadochiy, A. M.; Shchukin, V. A.; Bimberg, D. *Electron. Lett.* **2009**, *45*, (10), 501-502.
- Avrutin, E. A.; Gorfinkel, V. B.; Luryi, S.; Shore, K. A. *Applied Physics Letters* **1993**, *63*, (18), 2460-2462.
- Shchukin, V. A.; Ledentsov, N. N.; Lott, J. A.; Quast, H.; Hopfer, F.; Karachinsky, L. Y.; Kuntz, M.; Moser, P.; Mutig, A.; Strittmatter, A.; Kalosha, V. P.; Bimberg, D. In *Ultra high-speed electro-optically modulated VCSELs: modeling and experimental results*, 2008; pp 68890H-68890H-15.
- Shchukin, V. A.; Ledentsov, N. N.; Qureshi, Z.; Ingham, J. D.; Penty, R. V.; White, I. H.; Nadochiy, A. M.; Maximov, M. V.; Blokhin, S. A.; Karachinsky, L. Y.; Novikov, I. I. *Applied Physics Letters* **2014**, *104*, (5), 051125.
- Germann TD, H. W., Nadochiy AM, Schulze JH, Mutig A, Strittmatter A, Bimberg D. *Opt Express* **2012**, *20*, (5), 5099-107.

7.3 The departmental poster

Advanced ultrafast vertical cavity semiconductor lasers

Theory and design

Naser Albugami (supervisor: Eugene Avrutin)
na668@york.ac.uk

0. Motivation

- Compound cavity electrooptically modulated vertical cavity lasers promise modulation to 80-80 Gbits, ordinary lasers go up to ~40 Gbits
- Many experimental and theoretical studies [1-6] but ultimate performance limitations not clear till now – we are working on establishing them.

1. Schematic of a Compound Vertical Cavity Laser

Top DBR ~ 20 pairs; mid DBR ~ 30 pairs; asymmetric cavity; Bottom DBR reflectivity: RB = 0.999

2. EO Modulation of the Top Cavity Reflectance: the simplest model rate equations [2-4]

$$\frac{dN}{dt} = \frac{\eta I}{qV} \left(\frac{1}{\tau_p(N)} - \frac{GN}{1 + \epsilon S} \right) - \frac{GN}{1 + \epsilon S} S$$

$$\frac{dS}{dt} = \frac{\beta_0 N}{\tau_p} \left(\frac{GN}{1 + \epsilon S} - (r_{p,0}^+ + r_{p,0}^-) S \right)$$

$$r_{p,0}^{\pm}(t) = \frac{1}{2L} \ln \left(\frac{1}{R_1 R_2(t)} \right); \quad P_{in} = r_{p,0}^+ A_0 h\nu_p (1 - R_1) S$$

R1 Reflectance of Modulator Subcavity

$$r_1 = r_{12} = \frac{\theta_1 \theta_2 r_{12} e^{i\beta L}}{1 + r_{12} r_{21} e^{i\beta L}}; \quad R_2 = r_2 r_2^*$$

$$\beta = \frac{\omega m}{c} \approx \beta_{ref} + \frac{\omega_p}{c} \Gamma_m \Delta n + n_{ref} \Delta \phi$$

r_{12} and θ_{12} are complex amplitude reflectances and transmittances of multilayer DBRs, with incidence from layer 1 towards layer m, n is the average refractive index of passive (EO) cavity which is modulated by voltage. Electrorefraction effect plays a dominant role in modulating R1(t) as compared to electroabsorption [3].

3. Small Signal Response [4]

$$\frac{\partial P}{\partial R_1} = -h\nu_p V_{eff} \frac{r_{p,0}^+}{2L} \frac{-\omega^2 + j(\Gamma_{p,0}^+ - \Gamma_{p,0}^-)\omega + \omega_c^+ - r_{p,0}^+ (r_{p,0}^+ + r_{p,0}^-)}{-\omega^2 + j\Gamma_{p,0} \omega + \omega_c^+}$$

Small-signal output power variation under EO reflectivity modulation

Calculated small-signal response of electrooptic laser modulation at three different values of bias current

Calculated 3dB cut-off frequency vs bias current for small-signal response of electrooptic laser modulation

No modulation roll-off at high frequencies beyond a certain current ($I_{roll-off}$). The 3 dB cutoff frequency is not defined for those currents in the rate equation model. Need to improve the model.

4. EO Modulation of the Top Cavity Reflectance: a more complex model: the effective complex frequency

$$\frac{dN}{dt} = \frac{\eta I}{qV} \frac{N}{\tau} G(N) S$$

$$\frac{dS}{dt} = -2 \text{Im}(\Delta\omega(t)) S(t) + \frac{\beta N}{\tau}$$

$$\Delta\omega = \frac{1}{2} \left[\Gamma_g - \frac{1}{L_{ext}} \ln \frac{1}{r_1(A\omega, \Delta n)} \right] - \frac{A\omega_{ref}}{c} \left(\frac{m\pi}{L_{ext}} \frac{n_{ref} \omega_{ref}}{c} \right)$$

$$\frac{dE_{in}}{dt} = \left(\frac{1}{2\tau_{ex}} - j(\delta\omega(t) - \delta\omega_{ex} + \Gamma_m \frac{\Delta n(t)}{n_g} \omega_{ref}) \right) E_{in} + \frac{\sqrt{2} I \tau_p}{4 L_{ext}} \frac{\tau_p}{L_{ext}} \sqrt{S}$$

5. Large Signal Modulation

$$Q = \frac{P_{(1)} - P_{(0)}}{\sigma_{(1)} + \sigma_{(0)}} \quad (P_{(1)}, P_{(0)} \text{ mean}; \sigma_{(1)}, \sigma_{(0)} \text{ standard deviations})$$

6. Summary

- Standard rate equation model cannot describe high-frequency laser modulation
- New model developed, considering modulation of the refractive index, more accurately describing the electromagnetics of the laser cavity
- The ultimate modulation frequency limit is determined by the photon lifetime of the modulator cavity
- Quality of modulation depends non-monotonically on the numbers of dielectric grating periods in the top and intermediate mirrors (too many → long cavity lifetime, too few → weak modulation). Determines the design for optimal performance.

7. Future work

- Alternative designs of vertical cavity lasers for high speed modulation:
 - Integrated extended cavity (photon-photon resonance)
 - Transistor laser
 - Direct modulation with low parasitics
- Compare and decide on the optimum for high bit rate, narrow spectrum.

References

- [1] S.A. Bakhsh, J.A. Lott, A. Matig, G. Fikl, N.N. Ledentsov, M.V. Maximov, A.M. Nedyktylo, V.A. Shchukin, D. Birnberg, *Electronics Letters*, 44(2008) 951-952
- [2] V.A. Shchukin, N.N. Ledentsov, Z. Qureshi, J.D. Ingham, R.V. Perry, I.H. White, A.M. Nedyktylo, M.V. Maximov, S.A. Bakhsh, L.Y. Karashtsky, I. Nisenz, *Applied Physics Letters*, 104(2014) 051125
- [3] E.A. Avrutin, V.B. Gorfinkel, S. Luryi, K.A. Shore, *Applied Physics Letters*, 63(1993) 2460-2462
- [4] V.A. Shchukin, N.N. Ledentsov, J.A. Lott, H. Quast, F. Hopfer, L.Y. Karashtsky, M. Kuntz, P. Moser, A. Matig, A. Strittmatter, V.P. Pavlov, D. Birnberg, 2008, pp. 488304-488305-0815
- [5] D.M. Ganes, D.K. Sarkiss, G.M. Peake, K.M. Gab, K.D. Choquette, *Quantum Electronics, IEEE Journal of* 42(2006) 1548-1554
- [6] C. Chen, K.L. Johnson, M. Hesse-Brenner, K.D. Choquette, *Quantum Electronics, IEEE Journal of* 46(2010) 438-446
- [7] H.W. German, T.D. Nedyktylo, A.H. Schulz, J.H. Magg, A. Strittmatter, A. Birnberg, *Eur. Opt. Express*, 20(2012) 5999-6007

Modelling the Dynamics of Electrooptically Modulated Vertical Compound Cavity Surface Emitting Semiconductor Lasers

N. F. Albugami, E. A. Avrutin

Department of Electronics, University of York, York YO10, 5DD, UK
na668@york.ac.uk , eugene.avrutin@york.ac.uk

Vertical-cavity surface-emitting laser (VCSEL) constructions capable of direct modulation at bit rates in excess of 40 GBit/s have attracted considerable attention for future high speed long- and medium-haul networks. The two main approaches to realising this goal are, firstly, the improvement in the direct modulation laser performance, with 40 GBit/s direct modulation having been demonstrated recently [1], and, secondly, using modulation of the photon lifetime in the cavity as an alternative to current modulation [2]. Advanced semiconductor lasers involving direct modulation of the photon lifetime promise substantially better dynamic properties than current modulated lasers, because their operating speed is not limited by the electron-photon resonance frequency. Several laser designs to implement this principle have been proposed, and initial measurements and theoretical studies using simple rate equation models [3] [4] are all promising.

Our initial work was on advancing such analysis to include small signal analytical approach. A somewhat unusual result of this analysis is that the concept of 3 dB cutoff frequency as a measure of modulation speed is not applicable to electrooptically coupled-cavity VCSELs as it tends to infinity beyond a certain critical current, their modulation properties are governed instead by the shape and magnitude of the broad resonant peak at the electron-photon resonance frequency.

In order to understand the laser performance more accurately, a model involving careful analysis of both amplitude and frequency/phase of laser emission, as well as the spectrally selective nature of the laser cavity, is required. We have developed such a model, based on the analysis for complex eigenvalues (frequency detunings and amplitude variation rates) of the compound cavity modes and used it to describe the laser operation and predict the performance beyond current experimental conditions, under both small- and large signal modulation conditions. The photon lifetime in the modulator cavity was found to be the ultimate limitation of the modulation speed.

1. S.A. Blokhin, J.A. Lott, A. Mutig, G. Fiol, N.N. Ledentsov, M.V. Maximov, A.M. Nadochiy, V.A. Shchukin, D. Bimberg, *Electronics Letters*, 45 (2009) 501-502.
2. V.A. Shchukin, N.N. Ledentsov, Z. Qureshi, J.D. Ingham, R.V. Penty, I.H. White, A.M. Nadochy, M.V. Maximov, S.A. Blokhin, L.Y. Karachinsky, I.I. Novikov, *Applied Physics Letters*, 104 (2014) 051125.
3. E.A. Avrutin, V.B. Gorfinkel, S. Luryi, K.A. Shore, *Applied Physics Letters*, 63 (1993) 2460-2462.
4. V.A. Shchukin, N.N. Ledentsov, J.A. Lott, H. Quast, F. Hopfer, L.Y. Karachinsky, M. Kuntz, P. Moser, A. Mutig, A. Strittmatter, V.P. Kalosha, D. Bimberg, 2008, pp. 68890H-68890H-68815.

adfa, p. 1, 2011.
© Springer-Verlag Berlin Heidelberg 2011

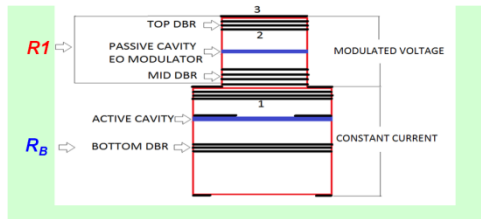
Modelling the Dynamics of Electrooptically Modulated Vertical Compound Cavity Surface Emitting Semiconductor Lasers

Naser Albugami (Supervisor: Eugene Avrutin)
na668@york.ac.uk

MOTIVATION

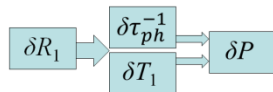
- Whereas ordinary modulation lasers go up to < 40 Gbit/s, the compound cavity electrooptically modulated vertical cavity lasers promise modulation to 60-80 Gbit/s.
- Many experimental and theoretical studies [1;3;5], but ultimate performance limitations not clear till now – we worked on establishing them.
- We considered both amplitude and frequency (phase) of laser emission, as well as the spectrally selective nature of the laser cavity (for the first time according to our knowledge).

1. SCHEMATIC OF A COMPOUND VERTICAL CAVITY LASER

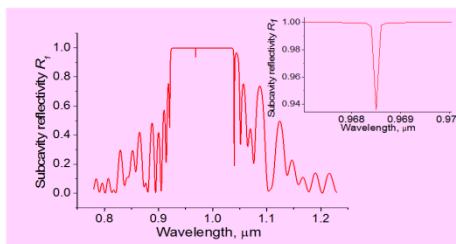


Top DBR ~20 pairs; mid DBR ~30 pairs; asymmetric cavity. Bottom DBR reflectivity $R_B = 0.999$.

2. THE ORIGINAL RATE EQUATION MODEL [2-4]



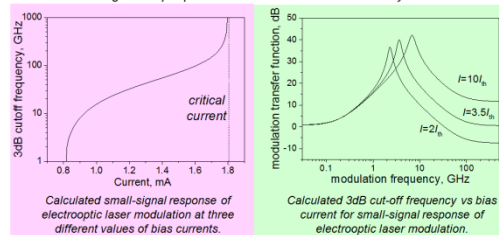
- In this model, we modulate the reflectivity of the modulator subcavity (R_1), which modifies the photon lifetime (τ_{ph-in}) and the transmittance $T_1=1-R_1$, both of which contribute to modulation of the output power (P).



Calculated Reflectivity versus incident light wavelength for the EO modulator cavity shown above.

Electrorefraction effect plays a dominant role in modulating $R_1(t)$ as compared to electroabsorption [3].

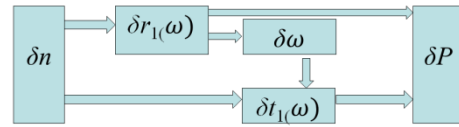
Small-signal output power variation under EO reflectivity modulation



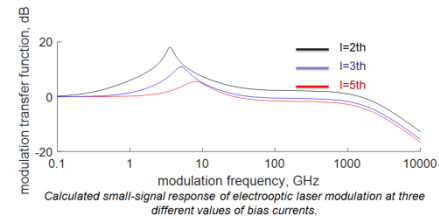
- No modulation roll-off at high frequencies beyond a certain current ($I_{critical}$). The 3dB cutoff frequency is not defined for those currents in the rate equation model.
- Need to modify the model to understand the real limit.

3. THE MODIFIED RATE EQUATION MODEL

- To improve the limitation of the simple model, a more complex model describing the electrodynamics of the complex resonator is created.
- In this model, we modify the refractive index (n) of the modulation layer, which changes the complex reflectance and transmittance and also modifies the operating wavelength of the laser, all of which modulate the output power (P).



3.1 SMALL SIGNAL RESPONSE

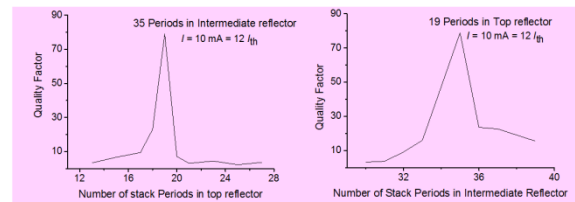


Calculated small-signal response of electrooptic laser modulation at three different values of bias currents.

- While the 3 dB cutoff frequency is not defined for the old model, the photon lifetime of the modulator is the ultimate limitation in the new model.
- The peak at GHz frequencies is due to the photon- electron resonance while the cusp point at hundreds of GHz to THz is due to the photon lifetime in the modulator.

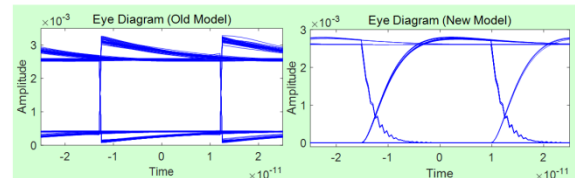
3.2. LARGE SIGNAL MODULATION

$$Q = \frac{P_{(1)} - P_{(0)}}{\sigma_{(1)} + \sigma_{(0)}} \quad (P_{(1)}, P_{(0)} \text{ mean; } \sigma_{(1)}, \sigma_{(0)} \text{ standard deviations})$$



- When number of periods N_{top} is too large, the photon lifetime in the modulator cavity is long, hence low quality factor.
- When N_{top} is too small, low modulation contrast $(P1-P0)/(P1+P0)$ and hence low quality factor.

6. COMPARISON BETWEEN OLD AND NEW MODEL



- The new model is more realistic than the old model and shows more details.
- The new model does not have the sudden change from OFF to ON states.

7. SUMMARY

- A model considering modulation of the refractive index is needed to accurately describe the electromagnetics of the laser cavity. Such a model has been developed.
- The ultimate modulation frequency limit is determined by the photon lifetime of the modulator cavity.
- Quality of modulation depends non-monotonically on the numbers of dielectric grating periods in the top and intermediate mirrors (too many \Rightarrow long cavity lifetime, too few \Rightarrow weak modulation). Determines the design for optimal performance.

8. FUTURE WORK

- Alternative designs of vertical cavity lasers for high speed modulation including Integrated extended cavity (photon-photon resonance), transistor laser and direct modulation with low parasitics.

REFERENCES

1. Blokhin, S. A.; Lott, J. A.; Mutig, A.; Fiol, G.; Ledentsov, N. N.; Maximov, M. V.; Nadochiy, A. M.; Shchukin, V. A.; Bimberg, D. *Electron Lett* 2009, 45, (10), 501-502.
2. Avrutin, E. A.; Gorfinkel, V. B.; Luryi, S.; Shore, K. A. *Applied Physics Letters* 1993, 63, (18), 2460-2462.
3. Shchukin, V. A.; Ledentsov, N. N.; Lott, J. A.; Quast, H.; Hopfer, F.; Karachinsky, L. Y.; Kuntz, M.; Moser, P.; Mutig, A.; Strittmatter, A.; Kalosha, V. P.; Bimberg, D. In *Ultra high-speed electro-optically modulated VCSELs: modeling and experimental results*, 2008; pp 68390H-68391H-15.
4. N. Albugami, E. Avrutin, *Proc. Semiconductor and Integrated Optoelectronics (SIOE)*, Cardiff 2015, p30.
5. Shchukin, V. A.; Ledentsov, N. N.; Qureshi, Z.; Ingham, J. D.; Penny, R. V.; White, I. H.; Nadochiy, A. M.; Maximov, M. V.; Blokhin, S. A.; Karachinsky, L. Y.; Novikov, I. I. *Applied Physics Letters* 2014, 104, (5), 051125.

7.6 PIERS 2017 abstract

Analysis of Fast Electro-optical Modulation of Vertically Integrated Coupled-cavity VCSELs

N. F. Albugami and E. A. Avrutin

Department of Electronics, University of York, York YO10, 5DD, UK

Abstract— There are two main methods of modulating vertical cavity semiconductor emitting lasers (VCSELs) at bit rates exceeding 40 GBit/s which can be used for high speed communication networks. The first one is through advanced developments in current (direct) modulation, which was demonstrated at bit rates up to 40 GBit/s (see, e.g., [1]). The modulation of the photon lifetime in the passive cavity is the second method, alternative to current modulation [2]. This approach promises substantially better dynamic properties than current modulation since it is free from the limitations of the direct modulation such as the the electron-photon resonance. The main laser design that allows this principle to be utilized is the coupled-cavity VCSEL with one of the subcavities acting as an active one, and the other, as an electrooptic modulator [3–5]. Modulation bit rates at least as good as those possible with direct modulation have been demonstrated in the references quoted, and rate equation analysis [2] predicts successful operation at bit rates exceeding 80 GBit/s. However, rather than offering simple modulation of the photon lifetime, this design involves the laser oscillating in complex cavity modes, with the cavity decay time (photon lifetime), instantaneous frequency, and intensity all varying in time in a self-consistent way, which is not captured by rate equations.

Thus, in order to understand the laser performance more accurately, we have implemented a model that includes careful analysis of both amplitude and frequency (phase) of laser emission, as well as the spectrally selective nature of the laser cavity. The model comprises a set of modified rate equations for the complex amplitude of light and carrier densities; the equation for the light involves analysis of complex eigenvalues (frequency detunings and amplitude variation rates) of the compound cavity modes. The modified rate equations, like the standard one, can be, and are, used to describe the laser operation and predict the performance beyond current experimental conditions, under both small- and large signal modulation conditions.

The main conclusion from the (analytical) small signal modulation analysis is that the ultimate modulation frequency limit is determined by the photon lifetime of the modulator cavity and with proper design can be in the range of hundreds of GHz.

Numerical large-signal simulations have shown that the quality of modulation depends nonmonotonically on the numbers of dielectric grating periods in the top and intermediate mirrors, with an optimal design applicable in a broad range of currents. Good quality factors at 80+ Gbit/s modulation frequency were predicted with optimal cavity design.

REFERENCES

1. Blokhin, S. A., et al., "Oxide-confined 850 nm VCSELs operating at bit rates up to 40 Gbit/s," *Electronics Letters*, Vol. 45, No. 10, 501–502, 2009.
2. Shchulkin, V. A., et al., "Digital data transmission using electro-optically modulated vertical-cavity surface-emitting laser with saturable absorber," *Applied Physics Letters*, Vol. 104, No. 5, 051125, 2014.
3. Paraskevopoulos, A., et al., "Ultra-High-Bandwidth (> 35 GHz) electrooptically-modulated VCSEL," *Optical Fiber Communication Conference and Exposition and The National Fiber Optic Engineers Conference*, Optical Society of America, Anaheim, California, 2006.
4. Shchulkin, V. A., et al., "Ultra high-speed electro-optically modulated VCSELs: Modeling and experimental results," 2008.
5. Germann, T. D., W. Hofmann, A. M. Nadtochiy, J. H. Schulze, A. Mutig, A. Strittmatter, and D. Bimberg, "Electro-optical resonance modulation of vertical-cavity surface-emitting lasers," *Opt. Express*, Vol. 20, No. 5, 5099–5107, 2012.



Dynamic modelling of electrooptically modulated vertical compound cavity surface emitting semiconductor lasers

N. F. Albugami¹ · E. A. Avrutin¹

Received: 20 February 2017 / Accepted: 20 July 2017
© The Author(s) 2017. This article is an open access publication

Abstract A generalized rate equation model is used to simulate the interrelated amplitude and frequency modulation properties of Electrooptically Modulated Vertical Compound Cavity Surface Emitting Semiconductor Lasers in both large and small signal modulation regimes. It is shown that the photon lifetime in the modulator subcavity provides the ultimate limit for the 3 dB modulation cutoff frequency. It is shown that there is an optimum design (number of periods) of both the intermediate and top multistack reflectors to maximise the large-signal modulation quality.

Keywords Surface-emitting semiconductor lasers · Electrooptic modulator · High-speed modulation · Modulation bandwidth · Compound cavity · Small-signal response · Large-signal response

1 Introduction

Vertical-cavity surface-emitting laser (VCSEL) constructions capable of direct modulation at bit rates in excess of 40 Gbit/s have attracted considerable attention for future high speed long- and medium-haul networks. There are two main approaches to realizing this goal. The first one is the improvement in the direct modulation laser performance (Blokhin et al. 2009), (Karachinsky et al. 2013). For example, it was possible to have an error-free transmission up to 39 and 40 Gbit/bit/s direct modulation working in a temperature up to 100 °C using oxide-confined 850 nm VCSELs with InGaAlAs based active regions. Another method of improving direct (current) modulation is to modulate two active cavities simultaneously and out of phase (Chen et al. 2010). Reducing the photon lifetime by

✉ E. A. Avrutin
eugene.avrutin@york.ac.uk
N. F. Albugami
na668@york.ac.uk

¹ Department of Electronic Engineering, University of York, York YO10 5DD, UK

MODIFIED RATE EQUATION MODELS FOR UNDERSTANDING PERFORMANCE LIMITS OF VERTICAL AND IN-PLANE COMPOUND CAVITY VCSELs.

Naser F.G. Albugxmi[✉], Eugene A. Arrutim[✉],

Dept of Electronic Engineering, University of York, Heslington, York YO10 5DD, UK

^{✉1} na668@york.ac.uk, ^{✉2} eugene.arutim@york.ac.uk

ABSTRACT

Modified rate equation models including both amplitude and phase properties are developed for advanced vertical cavity surface emitting lasers for multigigahertz modulation, and used to compare the performance of different designs and identify the corresponding limitations.

Keywords: vertical cavity laser, modified rate equation models, ultrafast modulation

1. INTRODUCTION

There are, fundamentally, two main approaches to increasing the modulation frequency range of vertical cavity semiconductor emitting lasers (VCSELs) at bit rates exceeding 40 GBit/s which can be used for high speed communication networks. The first one is through advanced developments in current (direct) modulation, which was demonstrated at bit rates up to 40 GBit/s (see e.g. Blokhin *et al.* 2009, Bobrov *et al.* 2015).

The second approach involves using some form of an advanced cavity structure. At least three solutions falling into the framework of this approach have been discussed. The first of them includes modulation of the photon lifetime in the passive cavity, rather than the current (see e.g. Schchukin *et al.* 2014 and references therein) This approach promises substantially better dynamic properties than current modulation since it is free from the limitations of the direct modulation such as the the electron-photon resonance. The main laser design that allows this principle to be utilized is the coupled-cavity VCSEL, with one of the subcavities acting as an active one, and the other, as an electrooptic modulator (Van Eerden *et al.* 2008, Schchukin *et al.* 2008, Germann *et al.* 2012, Schchukin *et al.* 2014) or electroabsorption modulator (Chen *et al.* 2009) Modulation bit rates at least as good as those possible with direct modulation have been demonstrated in the references quoted, and rate equation analysis (Schchukin *et al.* 2008) predicts successful operation at bit rates up to and exceeding 80 GBit/s. However, rather than offering simple modulation of the photon

lifetime, this design involves the laser oscillating in complex cavity modes, with the cavity decay time (photon lifetime), instantaneous frequency, and intensity all varying in time in a self-consistent way, which is not captured by rate equations and requires more sophisticated mathematical approaches.

A different type of an advanced cavity design involves using photon-photon resonance in some form, which comprises modulation of VCSEL arrays (Fryslie *et al.* 2015) and in-plane compound cavities, with amplified feedback from a slow wave waveguide resonator (see e.g. Dalir and Koyama 2011 and 2014, Park *et al.* 2016, and references therein).

A Lang-Kobayashi type delay-differential equation theory of the latter design has been presented in several papers (Dalir and Koyama 2011, Park *et al.* 2016), in the latter case with a good fit to the experiment achieved. This is despite of the fact that this model is, strictly speaking, intended for the case of weak optical feedback and as such used for the lasers in question (strong optical feedback) outside of its degree of applicability. The model was generalised to be more rigorous for the case of strong feedback, by introducing multiple delays, by Ahmed *et al.* 2015, but the model is presented without derivation and appears to have a somewhat strange feature of the reflected light affecting the net gain rather than acting as an injected signal. Neither of the models includes the amplifying nature of the external feedback, it is not clear whether amplification in the feedback can help achieve further improvement in the laser performance. Finally, the question of what ultimately limits the laser performance does not appear to have been answered.

Thus, in order to understand the performance of both designs more accurately, and to compare those two approaches to improving the modulation properties, we have implemented a set of modified rate equation models each of which includes careful analysis of both amplitude and frequency (phase) of laser emission, as well as the spectrally selective nature of the laser cavity.

REFERENCES

1. Liu, T., T. Katayama, and H. Kawaguchi, *High-Frequency Self-Modulation in Short-External-Cavity VCSEL With Concave Mirror*. IEEE Photonics Technology Letters, 2015. **27**(3): p. 280-283.
2. Fryslie, S.T.M., et al., *37-GHz Modulation via Resonance Tuning in Single-Mode Coherent Vertical-Cavity Laser Arrays*. IEEE Photonics Technology Letters, 2015. **27**(4): p. 415-418.
3. Blokhin, S.A., et al., *Oxide-confined 850 nm VCSELs operating at bit rates up to 40 Gbit/s*. Electronics Letters, 2009. **45**(10): p. 501-502.
4. Chen, C., et al., *Push-Pull Modulation of a Composite-Resonator Vertical-Cavity Laser*. Quantum Electronics, IEEE Journal of, 2010. **46**(4): p. 438-446.
5. Westbergh, P., et al., *Speed enhancement of VCSELs by photon lifetime reduction*. Electronics Letters, 2010. **46**(13): p. 938-940.
6. Westbergh, P., et al., *Impact of Photon Lifetime on High-Speed VCSEL Performance*. IEEE Journal of Selected Topics in Quantum Electronics, 2011. **17**(6): p. 1603-1613.
7. Avrutin, E.A., et al., *Control of surface-emitting laser diodes by modulating the distributed Bragg mirror reflectivity: Small-signal analysis*. Applied Physics Letters, 1993. **63**(18): p. 2460-2462.
8. Stanley, R.P., et al., *Coupled semiconductor microcavities*. Applied Physics Letters, 1994. **65**(16): p. 2093-2095.
9. Panajotov, K., M. Zujewski, and H. Thienpont, *Coupled-cavity surface-emitting lasers: spectral and polarization threshold characteristics and electrooptic switching*. Optics Express, 2010. **18**(26): p. 27525-27533.
10. Shchukin, V.A., et al., *Digital data transmission using electro-optically modulated vertical-cavity surface-emitting laser with saturable absorber*. Applied Physics Letters, 2014. **104**(5): p. 051125.

11. Germann TD, H.W., Nadtochiy AM, Schulze JH, Mutig A, Strittmatter A, Bimberg D., *Electro-optical resonance modulation of vertical-cavity surface-emitting lasers*. Opt Express, 2012. **20**(5): p. 5099-107.
12. Paraskevopoulos, A., et al. *Ultra-High-Bandwidth (>35 GHz) Electrooptically-Modulated VCSEL*. in *Optical Fiber Communication Conference and Exposition and The National Fiber Optic Engineers Conference*. 2006. Anaheim, California: Optical Society of America.
13. Bobrov, M.A., et al., *Ultimate modulation bandwidth of 850 nm oxide-confined vertical-cavity surface-emitting lasers*. Journal of Physics: Conference Series, 2015. **643**(1): p. 012044.
14. Shchukin, V.A., et al., *Ultra high-speed electro-optically modulated VCSELs: modeling and experimental results*. Proc. SPIE, 2008. **6889**: p. 68890H-68890H-15.
15. Albugami, N.F. and E.A. Avrutin. *Electrooptically modulated coupled-cavity VCSELs: the anomalous small-signal response and the large-signal modulation properties*. in *Proc. Semiconductor and Integrated Optoelectronics (SIOE)*. 2015. Cardiff, UK.
16. Lott, J.A., et al. *20 Gbit/s error free transmission with ~850 nm GaAs-based vertical cavity surface emitting lasers (VCSELs) containing InAs-GaAs submonolayer quantum dot insertions*. 2009.
17. Healy, S., et al., *Active region design for high-speed 850-nm VCSELs*. Vol. 46. 2010. 506-512.
18. Tan, F., et al., *Energy efficient microcavity lasers with 20 and 40 Gb/s data transmission*. Applied Physics Letters, 2011. **98**(19).
19. Chang, Y.c., et al., *High-efficiency, high-speed VCSELs with deep oxidation layers*. Electronics Letters, 2006. **42**(22): p. 1281-1282.
20. Al-Omari, A.N. and K.L. Lear, *Low current density, inverted polarity, high-speed, top-emitting 850 nm vertical-cavity surface-emitting lasers*. IET Optoelectronics, 2007. **1**(5): p. 221-225.

21. Mutig, A., et al., *Frequency response of large aperture oxide-confined 850 nm vertical cavity surface emitting lasers*. Applied Physics Letters, 2009. **95**(13): p. 131101.
22. Westbergh, P., et al., *High-Speed, Low-Current-Density 850 nm VCSELs*. IEEE Journal of Selected Topics in Quantum Electronics, 2009. **15**(3): p. 694-703.
23. Coldren, L.A., *Diode lasers and photonic integrated circuits*, ed. S.W. Corzine and S.W. Corzine. 1995, New York, Chichester: Wiley.
24. Gye Mo, Y., et al., *Influence of mirror reflectivity on laser performance of very-low-threshold vertical-cavity surface-emitting lasers*. IEEE Photonics Technology Letters, 1995. **7**(11): p. 1228-1230.
25. Kuksenkov, D.V., H. Temkin, and S. Swirhun, *MEASUREMENT OF INTERNAL QUANTUM EFFICIENCY AND LOSSES IN VERTICAL-CAVITY SURFACE-EMITTING LASERS*. Applied Physics Letters, 1995. **66**(14): p. 1720-1722.
26. Spiga, S., et al., *Single-Mode High-Speed 1.5- μm VCSELs*. Journal of Lightwave Technology, 2017. **35**(4): p. 727-733.
27. Kam, L. and A. Yariv, *Ultra-high speed semiconductor lasers*. IEEE Journal of Quantum Electronics, 1985. **21**(2): p. 121-138.
28. Chao-Kun, L., et al., *High temperature continuous-wave operation of 1.3- and 1.55- μm VCSELs with InP/air-gap DBRs*. IEEE Journal of Selected Topics in Quantum Electronics, 2003. **9**(5): p. 1415-1421.
29. Grasso, D.M., et al., *Direct Modulation Characteristics of Composite Resonator Vertical-Cavity Lasers*. Quantum Electronics, IEEE Journal of, 2006. **42**(12): p. 1248-1254.
30. Chuang, S.L., *Physics of Electronic Devices*. 1995, New York: Wiley
31. Badilita, V., et al., *Rate-equation model for coupled-cavity surface-emitting lasers*. IEEE Journal of Quantum Electronics, 2004. **40**(12): p. 1646-1656.
32. Manning, J., R. Olshansky, and S. Chin, *The carrier-induced index change in AlGaAs and 1.3 μm InGaAsP diode lasers*. IEEE Journal of Quantum Electronics, 1983. **19**(10): p. 1525-1530.

33. Bennett, B.R., R.A. Soref, and J.A.D. Alamo, *Carrier-induced change in refractive index of InP, GaAs and InGaAsP*. IEEE Journal of Quantum Electronics, 1990. **26**(1): p. 113-122.
34. Fischer, A.J., et al., *Coupled resonator vertical-cavity laser diode*. Applied Physics Letters, 1999. **75**(19): p. 3020-3022.
35. Hunsperger, R.G. and J.R. Meyer-Arendt, *Integrated optics: theory and technology*. Applied Optics, 1992. **31**: p. 298.
36. Hasnain, G., et al., *Performance of gain-guided surface emitting lasers with semiconductor distributed Bragg reflectors*. IEEE Journal of Quantum Electronics, 1991. **27**(6): p. 1377-1385.
37. Eisdén, J.V., et al., *Monolithic Integration of an Electroabsorption Modulator into a GaAs-based Duocavity VCSEL for Resonance-free Modulation*, in CS MANTECH 2008: Chicago, Illinois, USA.
38. Van Eisdén, J., et al., *Modulation properties of VCSEL with intracavity modulator - art. no. 64840A*, in *Vertical - Cavity Surface - Emitting Lasers XI*, K.D. Choquette and J.K. Guenter, Editors. 2007, Spie-Int Soc Optical Engineering: Bellingham. p. A4840-A4840.
39. Karachinsky, L.Y., et al., *Reliability performance of 25 Gbit s⁻¹ 850 nm vertical-cavity surface-emitting lasers*. Semiconductor Science and Technology, 2013. **28**(6): p. 065010.
40. Blokhin, S.A., et al., *Stresses in selectively oxidized GaAs/(AlGa)_xO_y structures*. Semiconductors, 2005. **39**(7): p. 748-753.
41. Haisler, V.A., et al., *Micro-Raman studies of vertical-cavity surface-emitting lasers with Al_xO_y/GaAs distributed Bragg reflectors*. Applied Physics Letters, 2002. **81**(14): p. 2544-2546.
42. Blum, O., et al., *Low-voltage-tunable distributed Bragg reflector using InGaAs/GaAs quantum wells*. IEEE Photonics Technology Letters, 1993. **5**(6): p. 695-697.
43. Gorfinkel, V.B. and S. Luryi, *High-frequency modulation and suppression of chirp in semiconductor lasers*. Applied Physics Letters, 1993. **62**(23): p. 2923-2925.

44. Matthijsse, P., et al. *Multimode Fiber Enabling 40 Gbit/s Multi-Mode Transmission over Distances > 400 m*. in *Optical Fiber Communication Conference and Exposition and The National Fiber Optic Engineers Conference*. 2006. Anaheim, California: Optical Society of America.
45. Miller, D.A.B., et al., *Electric field dependence of optical absorption near the band gap of quantum-well structures*. *Physical Review B*, 1985. **32**(2): p. 1043-1060.
46. Lee, Y.H., et al., *Electrodispersive multiple quantum well modulator*. *Applied Physics Letters*, 1988. **53**(18): p. 1684-1686.
47. Nadochiy, A.M., et al., *High-frequency electrical properties of a vertical-cavity surface-emitting laser with a monolithically integrated electro-optical modulator*. *Semiconductors*, 2013. **47**(5): p. 695-700.
48. Ledentsov, N.N. and V.A. Shchukin, *Electrooptically Bragg-reflector stopband-tunable optoelectronic device for high-speed data transfer*. 2007.
49. Hoogland, S., et al., *Passively mode-locked diode-pumped surface-emitting semiconductor laser*. *IEEE Photonics Technology Letters*, 2000. **12**(9): p. 1135-1137.
50. Ledentsov, N.N., et al. *Optical components for very short reach applications at 40 Gb/s and beyond*. 2010.
51. van Eijden, J., et al., *High frequency resonance-free loss modulation in a duo-cavity VCSEL*, in *Vertical-Cavity Surface-Emitting Lasers Xii*, C. Lei and J.K. Guenter, Editors. 2008.
52. Moreau, G., et al., *Enhanced In(Ga)As/GaAs quantum dot based electro-optic modulation at 1.55 μ m*. *Applied Physics Letters*, 2007. **91**(9): p. 091118.
53. Zujewski, M., H. Thienpont, and K. Panajotov, *Traveling wave electrode design of electro-optically modulated coupled-cavity surface-emitting lasers*. *Optics Express*, 2012. **20**(24): p. 26184-26199.
54. Zujewski, M., H. Thienpont, and K. Panajotov, *Electrical Design of High-Speed Electro-Optically Modulated Coupled-Cavity VCSELs*. *Journal of Lightwave Technology*, 2011. **29**(19): p. 2992-2998.

55. Zujewski, M., H. Thienpont, and K. Panajotov, *Electro-optically modulated coupled-cavity VCSELs: electrical design optimization for high-speed operation*, in *Semiconductor Lasers and Laser Dynamics V*, K. Panajotov, et al., Editors. 2012.
56. Lewen, R., S. Imscher, and U. Eriksson, *Microwave CAD circuit modeling of a traveling-wave electroabsorption modulator*. *IEEE Transactions on Microwave Theory and Techniques*, 2003. **51**(4): p. 1117-1128.
57. Shanting, H., et al., *Low chirp and high-speed operation of transverse coupled cavity VCSEL*. *Japanese Journal of Applied Physics*, 2015. **54**(9): p. 090304.
58. Vahala, K., J. Paslaski, and A. Yariv, *Observation of modulation speed enhancement, frequency modulation suppression, and phase noise reduction by detuned loading in a coupled-cavity semiconductor laser*. *Applied Physics Letters*, 1985. **46**(11): p. 1025-1027.
59. Morthier, G., R. Schatz, and O. Kjebon, *Extended modulation bandwidth of DBR and external cavity lasers by utilizing a cavity resonance for equalization*. *IEEE Journal of Quantum Electronics*, 2000. **36**(12): p. 1468-1475.
60. Lang, R. and K. Kobayashi, *External optical feedback effects on semiconductor injection laser properties*. *IEEE Journal of Quantum Electronics*, 1980. **16**(3): p. 347-355.
61. Dalir, H. and F. Koyama, *Bandwidth enhancement of single-mode VCSEL with lateral optical feedback of slow light*. *Ieice Electronics Express*, 2011. **8**(13): p. 1075-1081.
62. Welford, D., *A RATE-EQUATION ANALYSIS FOR THE FREQUENCY CHIRP TO MODULATED POWER RATIO OF A SEMICONDUCTOR DIODE-LASER*. *Ieee Journal of Quantum Electronics*, 1985. **21**(11): p. 1749-1751.
63. Welford, D. and S.B. Alexander, *MAGNITUDE AND PHASE CHARACTERISTICS OF FREQUENCY-MODULATION IN DIRECTLY MODULATED GAALAS SEMICONDUCTOR DIODE-LASERS*. *Journal of Lightwave Technology*, 1985. **3**(5): p. 1092-1099.
64. Mason, S.J., *Feedback Theory-Some Properties of Signal Flow Graphs*. *Proceedings of the IRE*, 1953. **41**(9): p. 1144-1156.

65. Ahmed, M., et al., *Enhancing Modulation Bandwidth of Semiconductor Lasers beyond 50 GHz by Strong Optical Feedback for Use in Millimeter-Wave Radio over Fiber Links*. Japanese Journal of Applied Physics, 2013. **52**(12).
66. Dalir, H. and F. Koyama, *Highly stable operations of transverse-coupled cavity VCSELs with enhanced modulation bandwidth*. Electronics Letters, 2014. **50**(11): p. 823-824.
67. Ahmed, M., et al., *Enhancing the modulation bandwidth of VCSELs to the millimeter-waveband using strong transverse slow-light feedback*. Optics Express, 2015. **23**(12): p. 15365-15371.
68. Dalir, H., et al., *High Frequency Modulation of Transverse-Coupled-Cavity VCSELs for Radio Over Fiber Applications*. IEEE Photonics Technology Letters, 2014. **26**(3): p. 281-284.
69. Ahmed, M. and M. Yamada, *An infinite order perturbation approach to gain calculation in injection semiconductor lasers*. Journal of Applied Physics, 1998. **84**(6): p. 3004-3015.
70. Dalir, H. and F. Koyama, *High-speed operation of bow-tie-shaped oxide aperture VCSELs with photon-photon resonance*. Applied Physics Express, 2014. **7**(2).
71. Dalir, H., et al., *Compact electro-absorption modulator integrated with vertical-cavity surface-emitting laser for highly efficient millimeter-wave modulation*. Applied Physics Letters, 2014. **105**(8): p. 081113.
72. Radziunas, M., et al., *Improving the modulation bandwidth in semiconductor lasers by passive feedback*. IEEE Journal of Selected Topics in Quantum Electronics, 2007. **13**(1): p. 136-142.
73. Feiste, U., *Optimization of modulation bandwidth in DBR lasers with detuned Bragg reflectors*. IEEE Journal of Quantum Electronics, 1998. **34**(12): p. 2371-2379.
74. Bardella, P. and I. Montrosset, *A New Design Procedure for DBR Lasers Exploiting the Photon-Photon Resonance to Achieve Extended Modulation Bandwidth*. IEEE Journal of Selected Topics in Quantum Electronics, 2013. **19**(4).
75. Kjebon, O., et al. *30 GHz direct modulation bandwidth in detuned loaded InGaAsP DBR lasers at 1.55 μm wavelength*. Electronics Letters, 1997. **33**, 488-489.

76. Westbergh, P., et al., *High-speed 850 nm VCSELs with 28 GHz modulation bandwidth operating error-free up to 44 Gbit/s*. Electronics Letters, 2012. **48**(18): p. 1145-U178.
77. Gu, X., et al., *850nm transverse-coupled-cavity vertical-cavity surface-emitting laser with direct modulation bandwidth of over 30GHz*. Applied Physics Express, 2015. **8**(082702): p. 1-4.
78. Lehman, A.C. and K.D. Choquette, *One- and Two-Dimensional Coherently Coupled Implant-Defined Vertical-Cavity Laser Arrays*. IEEE Photonics Technology Letters, 2007. **19**(19): p. 1421-1423.
79. Gallion, P., et al., *CONTRIBUTION OF SPONTANEOUS EMISSION TO THE LINEWIDTH OF AN INJECTION-LOCKED SEMICONDUCTOR-LASER*. Electronics Letters, 1985. **21**(14): p. 626-628.
80. Lau, E.K., L.H. Wong, and M.C. Wu, *Enhanced Modulation Characteristics of Optical Injection-Locked Lasers: A Tutorial*. Ieee Journal of Selected Topics in Quantum Electronics, 2009. **15**(3): p. 618-633.
81. Pan, Z.G., et al., *Optical injection induced polarization bistability in vertical-cavity surface-emitting lasers*. Applied Physics Letters, 1993. **63**(22): p. 2999-3001.
82. Tartwijk, G.H.M.v. and D. Lenstra, *Semiconductor lasers with optical injection and feedback*. Quantum and Semiclassical Optics: Journal of the European Optical Society Part B, 1995. **7**(2): p. 87.
83. Zhong, D., Y. Ji, and W. Luo, *Controllable optoelectric composite logic gates based on the polarization switching in an optically injected VCSEL*. Optics Express, 2015. **23**(23): p. 29823-29833.
84. Simpson, T.B., et al., *Nonlinear dynamics induced by external optical injection in semiconductor lasers*. Quantum and Semiclassical Optics: Journal of the European Optical Society Part B, 1997. **9**(5): p. 765.

85. Kong, H., et al., *Experimental observations on the nonlinear behaviors of DFB semiconductor lasers under external optical injection*. *Chaos, Solitons & Fractals*, 2008. **36**(1): p. 18-24.
86. Zhu, W.Q., et al., *Dynamics of a Monolithically Integrated Semiconductor Laser Under Optical Injection*. *IEEE Photonics Technology Letters*, 2015. **27**(20): p. 2119-2122.
87. Jiang, B., et al., *Polarization Switching Characteristics of 1550-nm Vertical-Cavity Surface-Emitting Lasers Subject to Double Polarization Pulsed Injection*. *IEEE Journal of Quantum Electronics*, 2016. **52**(11): p. 1-7.
88. Olsson, N., et al., *Chirp-free transmission over 82.5 km of single mode fibers at 2 Gbit/s with injection locked DFB semiconductor lasers*. *Journal of Lightwave Technology*, 1985. **3**(1): p. 63-67.
89. Song, J., et al., *Experimental investigations on nonlinear dynamics of a semiconductor laser subject to optical injection and fiber Bragg grating feedback*. *Optics Communications*, 2015. **354**: p. 213-217.
90. Chen, J.-J., et al., *Generation of polarization-resolved wideband unpredictability-enhanced chaotic signals based on vertical-cavity surface-emitting lasers subject to chaotic optical injection*. *Optics Express*, 2015. **23**(6): p. 7173-7183.
91. Chan, S.-C., S.-K. Hwang, and J.-M. Liu, *Period-one oscillation for photonic microwave transmission using an optically injected semiconductor laser*. *Optics Express*, 2007. **15**(22): p. 14921-14935.
92. Sze-Chun, C. and L. Jia-Ming, *Microwave frequency division and multiplication using an optically injected semiconductor laser*. *IEEE Journal of Quantum Electronics*, 2005. **41**(9): p. 1142-1147.
93. Fan, L., et al., *Subharmonic Microwave Modulation Stabilization of Tunable Photonic Microwave Generated by Period-One Nonlinear Dynamics of an Optically Injected Semiconductor Laser*. *Journal of Lightwave Technology*, 2014. **32**(23): p. 4660-4666.

94. Wang, D., et al., *State bistability between pure- and mixed-mode states in a 1550 nm vertical-cavity surface-emitting laser subject to parallel optical injection*. Japanese Journal of Applied Physics, 2017. **56**(7).
95. Yang, C., et al., *IM/DD-Based 112-Gb/s/ λ PAM-4 Transmission Using 18-Gbps DML*. IEEE Photonics Journal, 2016. **8**(3).
96. Zhou, S.W., et al., *Transmission of 2 x 56 Gb/s PAM-4 signal over 100 km SSMF using 18 GHz DMLs*. Optics Letters, 2016. **41**(8): p. 1805-1808.
97. Motaghianezam, R., et al., *52 Gbps PAM4 receiver sensitivity study for 400GBase-LR8 system using directly modulated laser*. Optics Express, 2016. **24**(7): p. 7374-7380.
98. Motaghianezam, R., et al., *Four 45 Gbps PAM4 VCSEL based transmission through 300 m wideband OM4 fiber over SWDM4 wavelength grid*. Optics Express, 2016. **24**(15): p. 17193-17199.
99. Karinou, F., et al., *Directly PAM-4 Modulated 1530-nm VCSEL Enabling 56 Gb/s/ λ Data-Center Interconnects*. IEEE Photonics Technology Letters, 2015. **27**(17): p. 1872-1875.
100. Lu, H.H., et al., *64 Gb/s PAM4 VCSEL-based FSO link*. Optics Express, 2017. **25**(5): p. 5749-5757.
101. Wenzel, H., et al., *Mechanisms of fast self pulsations in two-section DFB lasers*. IEEE Journal of Quantum Electronics, 1996. **32**(1): p. 69-78.
102. Rahman, L. and H.G. Winful, *Nonlinear dynamics of semiconductor laser arrays: a mean field model*. IEEE Journal of Quantum Electronics, 1994. **30**(6): p. 1405-1416.
103. Albugami, N.F. and E.A. Avrutin, *Dynamic modelling of electrooptically modulated vertical compound cavity surface emitting semiconductor lasers*. Optical and Quantum Electronics, 2017. **49**(9): p. 307.
104. Avrutin, E.A., et al., *Analysis of harmonic (sub)THz passive mode-locking in monolithic compound cavity Fabry-Perot and ring laser diodes*. IEEE Proceedings-Optoelectronics, 1999. **146**(1): p. 55-61.

105. Ryvkin, B., E.A. Avrutin, and J.T. Kostamovaara, *Asymmetric-Waveguide Laser Diode for High-Power Optical Pulse Generation by Gain Switching*. Journal of Lightwave Technology, 2009. **27**(12): p. 2125-2131.
106. Mulet, J. and S. Balle, *Mode-locking dynamics in electrically driven vertical-external-cavity surface-emitting lasers*. IEEE Journal of Quantum Electronics, 2005. **41**(9): p. 1148-1156.
107. Antonelli, C., et al., *Analytic Study of the Modulation Response of Reflective Semiconductor Optical Amplifiers*. Journal of Lightwave Technology, 2015. **33**(20): p. 4367-4376.
108. Fryslie, S.T.M. and K.D. Choquette, *Breakthroughs in Photonics 2014: Coherent Vertical-Cavity Surface-Emitting Laser Arrays*. IEEE Photonics Journal, 2015. **7**(3): p. 1-5.